Anterior thalamic-retrosplenial pathways for memory: uncovering a network for theta, head direction and position processing.



Eleonora Lomi

Somerville College

University of Oxford

A thesis submitted for the degree of

Doctor of Philosophy in Experimental Psychology

Hilary 2022

Acknowledgements

Re-use of published material

I, Eleonora Lomi, confirm that the work presented in this thesis is my own. Where information has been derived from other sources, I confirm that this has been indicated in the thesis.

I acknowledge that Chapter 4 has been previously published in: Lomi, E., Mathiasen, M. L., Cheng, H. Y., Zhang, N., Aggleton, J. P., Mitchell, A. S., and Jeffery, K. J. (2021). *Evidence for two distinct thalamocortical circuits in retrosplenial cortex.* Neurobiology of Learning and Memory, 185:107525. I am first author on the publication. I confirm that I have authored, produced and written the material, both text and figures, reproduced in Chapter 4. Contributions of each author are mentioned in the relevant Sections. I confirm that I have obtained permission from all authors to include the published material in my thesis.

I acknowledge that parts of Chapter 2 have been previously published in: Perry, B. A. L., Lomi, E., and Mitchell, A. S. (2021). *Thalamocortical interactions in cognition and disease: the mediodorsal and anterior thalamic nuclei.* Neuroscience Biobehavioral Reviews, 130:162–177. I am joint first author on the publication. I confirm that I have authored, produced and written the material, both text and figures, reproduced in Chapter 2. All authors have contributed equally. I confirm that I have obtained permission from all authors to reuse parts of the published material in my thesis.

Personal

I would like to thank my supervisors, Professors Anna Mitchell and Kate Jeffery for being a source of guidance, support and motivation during and before my DPhil. This thesis would never have been possible had it not been for the fruitful collaboration between labs and institutions, which are the "home" of many inspiring

and brilliant scientists. I have learned a lot from them in the past, and still have much to learn in the future.

I am grateful to the Clarendon Council and Somerville College for the generous support provided, which allowed me to work and study in Oxford. My experience could not have been the same without Somerville's inspiring and welcoming community.

In closing, my thoughts go to my family, who have always encouraged and supported me throughout this journey in innumerable ways. Any results I might have achieved, is also theirs.

Abstract

Many studies have examined head direction (HD) cells along the main circuitry comprising the anterodorsal thalamus (AD) and retrosplenial cortex (RSC). However, little is known about how another region directly upstream of RSC, the anteroventral thalamus (AV), encodes directional information and contributes to RSC processing. By virtue of their anatomical connections and neurophysiological properties, AD and AV are considered to mediate a HD and a theta propagating system to hippocampal formation. In collaboration with University College London (UCL), I recorded single units and oscillatory local field potentials (LFP) from the RSC and AV of freely moving rats as a step towards understanding the function of this thalamocortical pathway.

The work done in this thesis is divided into three experiments. Experiment 1 investigated how the two RSC subregions, granular and dysgranular (gRSC; dRSC), differ with respect to their electrophysiology and thalamic connectivity. The gRSC is more closely connected to the hippocampal formation, in which theta-band LFP oscillations are prominent. The main finding is that there is functional and anatomical segregation within the AV-RSC circuit, whereby only gRSC contains a subpopulation of non-directional cells with spiking activity strongly entrained by theta oscillations. Results suggest the existence of two distinct but interacting RSC subcircuits: one connecting dorsomedial AV (AVDM) to gRSC that may comprise part of the hippocampal cognitive system, and the other connecting ventrolateral AV (AVVL) to both RSC subregions that may link hippocampal and perceptual regions.

Experiment 2 recorded from the two AV subfields to investigate what information is encoded in the firing of AV neurons and whether anatomically-segregated AV projections to RSC could help to explain differences in theta coding between gRSC and dRSC. The main finding is that AV contains multiple functional cell types distributed differentially across the two AV subfields and showing differential responses to theta, orientation and spatial locational, namely place cells, non-rhythmic HD cells and Theta-by-HD cells. A subset of these cells additionally encodes the speed of rotational and translational head movements.

Experiment 3 evaluated the firing of AV cells across trials in light and darkness, showing that most HD and place cells maintained their selectivity of firing in

both conditions. However, there was an increase in drift in darkness, which was stronger for Theta-by-HD than non-rhythmic HD cells. Theta-by-HD cells did not show coherence of firing during drifting, in contrast to the high rotational coherence expressed by non-rhythmic HD cells. This indicates the presence in AV of two separate HD networks: a global continuous HD network attractor, centered in AVDM, and a theta-modulated HD network, centered in AVVL, that does not necessitate attractor connectivity to generate directional tuning.

A topographical organization of HD and place cells within AVDM and AVVL reinforces the notion that the AV-RSC circuitry comprises two anatomically and functionally distinct subcircuits that are differentially involved in the exchange of HD information (via AVDM-gRSC) and in the integration, within a theta frequency range, of HD information with other spatial and sensory representations (via AVVL-dRSC): a convergence that provides foundations for downstream spatial representations in cortical regions. Overall, results emphasize a new, crucial role of AV within the broader neuronal circuitry supporting memory and navigation.

Contents

List of Figures **xix**

List of Tables **xxiv**

List of Abbreviations **xxv**

1 Introduction part 1: General introduction to rodent navigation **1**

1.1 Introduction: rodent navigation and memory 1

1.1.1 Nomenclature 4

1.1.2 Sources of information for navigation 5

1.1.3 Navigation strategies 6

1.2 Neuroanatomy and physiology of the spatial navigation system 7

1.2.1 Place cells 7

1.2.1.1 Place cells combine multimodal metric and contextual inputs to position their fields 8

1.2.1.2 Multimodality of place cells 10

1.2.2 Head direction cells 13

1.2.2.1 Head direction cells provide a global directional code 14

1.2.2.2 Integration of idiothetic and external cues by head direction cells 16

1.2.3 Grid cells 20

1.2.3.1 General properties of grid cells 21

1.2.3.2 Multimodal cue integration by grid cells 23

1.2.4 Boundary related cells 23

1.2.4.1 Allocentric boundary cells 24

1.2.5 How do the spatial systems interact? 27

1.3 Principles of head direction processing 29

1.3.1 Ring attractor model of HD cells 29

1.3.2 Neural mechanisms of cue integration by HD cells 31

1.4 Theta Oscillations, navigation and memory 33

1.4.1 Functional significance of theta oscillations for learning and memory processes 34

1.4.2 Single neurons relationship to theta oscillations and representation of space 36

1.5 Summary 38

2 Introduction part 2: Anterior thalamic-retrosplenial cortex pathways for memory 40

2.1 Introduction 40

2.2 Retrosplenial cortex 41

2.2.1 Anatomy and connectivity of the two retrosplenial cortex subregions 43

2.2.1.1 RSC-(para)hippocampal connections 44

2.2.1.2 RSC-neocortical connections 45

2.2.1.3 RSC-thalamic connections 45

2.2.1.4 RSC-basal forebrain connections 46

2.2.2 Functional and electrophysiological properties of retrosplenial cortex for spatial navigation 48

2.2.2.1 Cognitive mapping 48
2.2.2.2 Visual landmark integration 50
2.2.2.3 Head direction representations 53
2.2.2.4 Spatial coordinate transformations 54
2.3 Anterior thalamic nuclei 57
2.3.1 Anatomy and connectivity of the three anterior thalamic nuclei 59
2.3.2 Neurophysiological properties of anterior thalamic nuclei 61
2.3.3 Functions of the anterior thalamus in spatial navigation 62
2.3.3.1 Head direction processing role of the AD circuit 62
2.3.3.2 Origin and propagation of the HD signal 65
2.3.3.3 Theta propagation role of the AV circuit 66
2.3.3.4 Origin and propagation of the AV theta signal 69
2.4 Summary 70
2.4.1 Road map of the thesis 71

3 General Methods for electrophysiology experiments 73

3.1 Animals 73
3.2 Recording rooms 74
3.3 Electrodes and microdrives 74
3.4 Implant surgery 75
3.4.1 Coordinates 76
3.5 Signal processing and tracking 77
3.5.1 Electrophysiology system 77
3.5.2 Single-unit and LFP recording 78
3.5.3 Position tracking 78

3.6 Data analysis 79
3.6.1 Cell isolation and spike-sorting 79
3.6.2 Waveform Analysis 81
3.6.3 Spectral analysis 81
3.6.3.1 Theta filtering 82
3.6.4 Theta analysis 82
3.6.4.1 Index of phase-coupling 82
3.6.4.2 Index of rhythmicity 83
3.6.4.3 Preferred theta phase analysis 83
3.6.5 Spatial Analysis 83
3.6.5.1 Directional tuning curve plots 84
3.6.5.2 Rayleigh mean vector length 85
3.6.5.3 Tuning curve parameters 85
3.6.5.4 Shuffling 86
3.6.5.5 Ratemap plots 87
3.6.5.6 Locational measures 88
3.7 Histology 88

4 Evidence for two distinct thalamocortical circuits in retrosplenial cortex 90

4.1 Background and Rationale 90
4.2 Aims and Hypothesis 91
4.3 Methods and Materials: Electrophysiology recording experiment 92
4.3.1 Animals and coordinates 92
4.3.2 Behavioural protocol and testing apparatus 93
4.3.3 Data Analysis 93

4.3.3.1 Spike sorting 93
4.3.3.2 Spectral Analysis 94
4.3.3.3 Theta analysis 94
4.3.3.4 Cell identification and inclusion criteria 94
4.3.3.5 Cell-specific temporal firing characteristics 95
4.3.3.6 Statistics 95
4.4 Methods and Materials: Retrograde tracing experiment 96
4.4.1 Animals and tracers 96
4.4.2 Surgery 96
4.4.3 Histology and tracing 97
4.5 Results 98
4.5.1 RSC electrophysiological experiment 98
4.5.1.1 Histology 98
4.5.1.2 The same LFP theta oscillations are recorded from gRSC and dRSC. 99
4.5.1.3 An anatomically organized theta-modulated cell population exists in the RSC. 100
4.5.1.4 gRSC cells have higher firing rate and spike bursting propensity 106
4.5.1.5 Waveform differences: theta phase-locked cells have narrower waveforms 108
4.5.2 Retrograde tracing experiment results 110
4.5.2.1 Injections at the level of recording 113
4.5.2.2 Injections at more rostral and caudal RSC locations. . . 117
4.6 Discussion 121
4.6.1 Increased theta coupling in gRSC 122

4.6.2 Differential AV projections to gRSC and dRSC 124
4.6.3 Two interacting thalamocortical subcircuits 124
4.6.4 Summary and future directions 126
4.6.5 Limitations 127

5 Temporal firing properties of anteroventral thalamic neurons 128

5.1 Background and Rationale 128
5.2 Aims and Hypothesis 130
5.3 Methods and Materials 130
5.3.1 Animals and coordinates 130
5.3.2 Behavioural protocol and testing apparatus 131
5.3.3 Data Analysis 131
5.3.3.1 Spectral analysis 131
5.3.3.2 Theta relationship with running speed 131
5.3.3.3 Analysis of phase precession 132
5.3.3.4 Cell classification 133
5.3.3.5 Classic HD 133
5.3.3.6 Theta-by-HD 133
5.3.3.7 Intermediate HD 134
5.3.3.8 Place cells 135
5.3.3.9 Theta-skipping analysis 135
5.3.3.10 Cell-specific temporal firing characteristics 137
5.3.3.11 Statistics 137
5.4 Results 139
5.4.1 Histology 139

5.4.2 Local field potential signal 141

5.4.3 Overview of the cell data set 142

5.4.3.1 Classic HD cells 143

5.4.3.2 Theta-by-HD cells 145

5.4.3.3 Intermediate HD cells 147

5.4.3.4 Place cells 148

5.4.4 Are there differences in theta-modulation among AV cells? 152

5.4.5 Do different cell groups fire on the same or different theta phases?155

5.4.6 Do cells show phase precession? 157

5.4.7 A subset of Theta-by-HD cells show theta cycle-skipping 159

5.4.7.1 Theta-skipping was coordinated between co-recorded cells 160

5.4.8 Are there differences in firing mode? 162

5.4.8.1 Place cells contain the highest proportion of bursting neurons 162

5.4.8.2 Does burstiness reflect theta strength or cell type? . . . 163

5.4.9 Do cells have different waveform properties? 164

5.4.9.1 Spike waveform shape is variable among AV neurons . 164

5.4.9.2 Are there differences in the firing properties of narrow and broad spiking cells? 166

5.4.10 Qualitative observations on firing mode 168

5.4.11 Are there differences between AV subfields? 171

5.5 Discussion 172

5.5.1 Place cells exist in the AV 174

5.5.1.1 No sign of explanted hippocampal tissue 174

5.5.1.2 Place cells were co-recorded with AV cells and were stable across trials . . . 175

5.5.1.3 Changes in cluster space . . . 175

5.5.1.4 Evidence of place cells in other non-hippocampal related structures . . . 178

5.5.2 Functional properties of hippocampal and AV place cells . . . 179

5.5.2.1 Place cells show similar, but different, firing characteristics . . . 179

5.5.2.2 Origin of the AV place signal . . . 181

5.5.3 Significance and mechanisms of theta-modulation of AV spatial signals . . . 182

5.5.4 Summary . . . 185

5.5.5 Limitations . . . 185

6 Spatial firing properties of anteroventral thalamic neurons 187

6.1 Background and Rationale . . . 187

6.2 Data Analysis . . . 187

6.2.1 Maximum-likelihood method to examine multiple independent spatial influences . . . 188

6.2.1.1 Position times direction correction . . . 188

6.2.2 Analysis of anticipatory firing . . . 189

6.2.2.1 Decomposition of standard tuning function into CW and CCW . . . 190

6.2.2.2 Optimal-time shift analysis . . . 191

6.2.3 Analysis of directional signal instability . . . 191

6.2.3.1 Linear drift analysis . . . 192

6.2.3.2 Statistical considerations . . . 193

6.2.3.3 Non-linear shifts analysis 195

6.2.4 Analysis of motor correlates 196

6.2.4.1 Running speed calculations 197

6.2.4.2 Speed-rate relationship 197

6.2.4.3 Angular head velocity calculations 197

6.2.4.4 Angular head velocity-rate relationship 198

6.3 Results 198

6.3.1 Qualitative observations on signal stability 198

6.3.2 Are there differences in directional tuning curve properties? . . 200

6.3.3 Are there differences in the strength of spatial influences? 202

6.3.3.1 Some Theta-by-HD cells met the place cell threshold based on locational information 203

6.3.3.2 Some place cells met the head direction threshold based on the tuning curve R-vector 205

6.3.4 Directional and locational influences on cell firing rate, corrected for the sampling bias 207

6.3.4.1 Effects of the *pxd* correction: only Theta-by-HD cells show true conjunctive coding 207

6.3.5 Do cells anticipate the animal's heading direction? 213

6.3.5.1 Theta-by-HD cell firing is less anticipatory 213

6.3.5.2 Optimal time-shift method 216

6.3.5.3 Tuning curve shape is not affected by the animal's turning behaviour 219

6.3.6 Are Theta-by-HD cells more directionally unstable? 220

6.3.6.1 Linear drift analysis 220

6.3.6.2 Non-linear shifts analysis 222

6.3.7 Do cells represent information about head movements? 224

6.3.7.1 Linear and angular speed modulate cell firing rates . . 224

6.3.7.2 Angular speed modulation is symmetric and does not depend on the turning direction 226

6.4 Discussion 228

6.4.1 Theta-by-HD cells have broader directional correlates due to intra-trial directional instability 228

6.4.2 Spatial cells are conjunctively modulated by linear and angular head movements 230

6.4.3 Summary 232

6.4.4 Limitations 232

7 Stability of anteroventral thalamic representation across trials and in darkness 233

7.1 Background and rationale 233

7.2 Aims and Hypothesis 234

7.3 Methods and Materials 235

7.3.1 Behavioural protocol and testing apparatus 235

7.3.2 Data Analysis 236

7.3.2.1 Cross-trial stability 236

7.3.2.2 Directional cross-correlation 237

7.3.2.3 Locational cross-correlation 237

7.3.2.4 Increased drifting in darkness 238

7.3.2.5 Rotational coherence of the PFDs 238

7.4 Results 239

7.4.1 Are cells controlled by room cues? 239

7.4.2 Are directional cells stable across trials and in darkness? 240

7.4.2.1 Similarity of directional firing 240

7.4.3 Do cells drift in darkness? 242

7.4.4 Is there evidence of coherence of PFD drifting in cell pairs? . . . 243

7.4.5 Are place cells stable across trials and in darkness? 245

7.4.5.1 Similarity of locational firing 245

7.4.5.2 Qualitative observations 247

7.5 Discussion 248

7.5.1 Persistence and gradual drift of directional cells in darkness . . . 249

7.5.2 Place cell stability across trials and in darkness 250

7.5.3 Conclusion 251

7.5.4 Limitations 251

8 General Discussion **253**

8.1 Summary of the three experiments 253

8.2 How do directional cells in AV acquire their specific response properties and what are they for? 255

8.2.1 Formation of non-rhythmic HD cells 257

8.2.2 Formation of Theta-by-HD cells 259

8.2.3 What is the functional relevance of a theta-modulated directional signal for spatial processing? 259

8.3 Two-stream model of the AV-RSC circuit 261

8.4 Future works 263

Appendices

A Appendices **266**

A.1 General methods 266

A.1.1 Coordinates verification for AV implants 266

A.2 Experiment 1: electrophysiology recording experiment 268

A.2.1 Histological considerations 268

A.2.2 Phase preference analysis 269

A.3 Experiment 1: retrograde tracer experiment 272

A.3.1 Injection coordinates 272

A.3.2 Injection sites for injections made at more rostral and caudal RSC locations 274

A.4 Experiment 2 275

A.4.1 Theta-by-HD do not show phase coding of HD 275

A.4.2 Differences in firing properties between narrow and broad spiking cells 277

A.4.3 Visualization of spatial firing distributions 279

Bibliography **281**

List of Figures

1.1 Tolman's apparatus used to investigate the existence of an internal cognitive map of space in rats. 2

1.2 Place cell recorded from hippocampus of a rat foraging for food inside a squared box. 8

1.3 HD cell recorded in the anterior thalamic region as the rat foraged for food inside a squared box. 14

1.4 Grid cell recorded in MEC inside a squared box. 20

1.5 Boundary vector cell (BVC) model. 26

1.6 Schematics of continuous attractor ring dynamics. 30

1.7 Simplified diagram of the head direction (HD) circuit. 33

2.1 Schematic diagram of the main cortical and subcortical connections of the retrosplenial cortex in rats. 44

2.2 Conjunctive EBC-HD cells used to explain the formation of allocentric boundary related cells. 56

2.3 Graphical representation of the main cortical and subcortical connections of the three ATN nuclei in rats. 58

2.4 Schematics of the "extended hippocampal-diencephalic system" for memory. 61

3.1 2-compartment box used in Experiment 1. 74

3.2 Photograph and schematic drawing of an Axona microdrive. 75

3.3 Basic elements of the recording system. 79

3.4 Spike-sorting procedure. 80

3.5 Analysis of spatial firing properties. 84

4.1 Histology of RSC recordings. 99

4.2 Theta oscillations have the same power and frequency. 100

4.3 Differences in theta-phase locking. 103

4.4 Two types of theta cells: theta coupled and rhythmic vs theta coupled and non-rhythmic. 105

4.5 Two types of temporal firing modes: (A) non-bursting vs (B) bursting. 107

4.6 Theta-modulated cells are concentrated in the granular subregion of the RSC (gRSC). 108

4.7 Broad and narrow spiking cells display differences in theta-modulation strength. 110

4.8 Injections in retrosplenial cortex (RSC) made at the electrode recording levels. 115

4.9 Ventrolateral AV (AVVL) projects to both gRSC and dRSC, dorsomedial AV (AVDM) projections are more restricted to superficial layers of gRSC. 116

4.10 Contrasting patterns of AV retrograde label from separate gRSC and dRSC injections. 117

4.11 Injections involving both gRSC and dRSC produce label across AVDM and AVVL, while dual dRSC injections leave label restricted to AVVL. . 119

4.12 Tracer injection confined to deep gRSC layers resulted in AVVL cell labelling, akin to dRSC injections. 121

5.1 Flowchart of theta-skipping cell identification 136

5.2 Histology of anteroventral thalamic recordings 140

5.3 Theta oscillations were modulated by running speed. 142

5.4 Basic characterization of classic head direction cells 145

5.5 Basic characterization of Theta-by-head direction cells 147

5.6 Basic characterization of intermediate head direction cells 148

5.7 Basic characterization of place cells with a single firing field 151

5.8 Basic characterization of place cells with multiple firing fields. 151

5.9 Example of place cells co-recorded on the same tetrode with an anteroventral thalamic cell. 152

5.10 Only Theta-by-HD cells and place cells showed rhythmic modulation of their firing rates at theta frequency. 154

5.11 All cell groups have different preferred theta phases from each other. . 156

5.12 Place cells phase precess relative to the local theta oscillations. 158

5.13 Examples of Theta-by-HD cells showing theta cycle-skipping in the autocorrelogram. 159

5.14 Theta-skipping HD cells maintain fixed temporal relationships to the theta cycle over time. 161

5.15 Cells have a variable extracellular waveform duration. 165

5.17 Differences between broad- and narrow-spiking place cells. 168

5.18 Specific temporal firing profiles can be visualized by inter-spike interval scatterplots. 170

5.19 Different anatomical distribution of neurons within AV. 171

5.20 Spatial cells in AV are well segregated in a 3D-scatter plot. 173

5.21 Changes in cluster space and spike waveform of place cells over consecutive days recording. 177

6.1 Example of analysis comparing intra-trial direction shifts. 195

6.2 Directional and locational fields verified by recording across trials. . . . 199

6.3 Theta-by-HD cells have broader directional correlates. 202

6.4 A subset of Theta-by-HD cells formed larger place fields. 204

6.5 A subset of place cells met the directionality threshold. 208

6.6 The *pxd* correction disrupts directional correlates of all the place cells. 210

6.7 The *pxd* correction does not alter Theta-by-HD cell directional correlates: example of conjunctive Theta-by-HD cell. 211

6.8 The *pxd* correction does not alter Theta-by-HD cell directional correlates: example of non-conjunctive Theta-by-HD cell. 212

6.9 Angular head velocity has a consistent effect on the direction but not on the actual shape of the tuning curves. 214

6.10 Theta-by-HD cells are less anticipatory. 216

6.11 Illustration of the optimal time shift method. 218

6.12 Cells are relatively stable but a higher number of Theta-by-HD cells have fast drift rates compared to non-rhythmic HD cells. 222

6.13 Theta-by-HD cell tuning curves shifted more but were not inherently broader. 223

6.14 Spatial cells modulated by linear and angular head movements. 225

6.15 Analysis of motor correlates and dependency on turning direction. . . . 227

7.1 No influence of uncontrolled room cues during the Baseline trial in the Light. 240

7.2 Similar directional firing across Light-Light and Light-Dark conditions. 241

7.3 Theta-by-HD cells are more impaired in integrating movement cues. . 244

7.4 Similar place cell firing across Light-light and Light-Dark conditions. . 246

7.5 Examples of "dark-off" place cells. 248

8.1 Model schematic of the main features and connectivity of AV directional cells. 256

8.2 Theta-by-HD cells as building blocks for allocentric spatial representations in hippocampus: model schematics. 261

A.1 Implant coordinates verification. 267

A.2 Additional RSC histology for R602 and R887. 269

A.3 Distribution of preferred phases of single neurons. 270

A.4 Dual retrograde tracer injections at different AP levels in the RSC. . . . 274

A.5 Single retrograde tracer injection in either gRSC or dRSC. 275

A.6 Plots of theta phase vs HD for two representative Theta-by-HD cells. . 276

A.7 Broad and narrow spiking cells have distinct firing properties. 278

A.9 Analysis of locational firing for different orientations compared between cell groups. 280

List of Tables

3.1 Electrode implant coordinates. 77

4.1 Distribution and electrophysiological properties of non-directional RSC neurons. 102

4.2 List of all retrograde tracer injections. 113

5.1 Summary of statistical tests, their abbreviations and software used. . . 138

5.2 Summary of recording locations and cell distribution in AV for all animals.139

5.3 Numbers and percentages of AV cell types recorded in each animal. . . 143

5.4 Statistical analysis on the temporal properties and relation to the local LFP theta of AV cells with spatial profiles. 153

6.1 Summary statistics for the three groups of AV neurons expressing directional properties. 201

6.2 Summary statistics of spatial properties for AV cells with spatial profiles.206

6.3 Analysis of tuning curve shape for CCW (left) and CW (right) turns, and standard. 220

A.1 List of all injection coordinates. 273

List of Abbreviations

AD . . . . . Anterodorsal Thalamic Nucleus

AV . . . . . Anteroventral Thalamic Nucleus

AVDM . . . . . Dorsomedial Area of Anteroventral Thalamic Nucleus

AVVL . . . . . Ventrolateral Area of Anteroventral Thalamic Nucleus

AM . . . . . Anteromedial Thalamic Nucleus

AHV . . . . . Angular Head Velocity

ATI . . . . . Anticipatory Time Interval

ATN . . . . . Anterior Thalamic Nuclei

BVC . . . . . Boundary Vector Cell

CW . . . . . Clockwise

CCW . . . . . Counterclockwise

dLGN . . . . . Dorsal Lateral Geniculate Nucleus

DTN . . . . . Dorsal Tegmental Nucleus

EBC . . . . . Egocentric Boundary Cell

EC . . . . . Entorhinal Cortex

HD . . . . . Head Direction

KDE . . . . . Kernel Density Estimate

LD . . . . . Laterodorsal Thalamic Nucleus

LM . . . . . Lateral Mammillary Nucleus

LP . . . . . Lateroposterior Nucleus

LMN . . . . . Lateral Mammillary Nucleus

MEC . . . . . Medial Entorhinal Cortex

MMN . . . . . Medial Mammillary Nucleus

MVN . . . . . Medial Vestibular Nucleus

nPH . . . . . Nucleus Prepositus Hypoglosi

NRe . . . . . Nucleus Reuniens

PaS . . . . . Parasubiculum

PFD . . . . . Preferred Firing Direction

POR . . . . . Postrhinal Cortex

PoS . . . . . Postsubiculum

PPC . . . . . Posterior Parietal Cortex

PrS . . . . . Presubiculum

RSC . . . . . Retrosplenial Cortex

dRSC . . . . . Retrosplenial Dysgranular Area; Brodmann Area 30

gRSC . . . . . Retrosplenial Granular Area; Brodmann Area 29

Sub . . . . . Subiculum

V1 . . . . . Primary visual cortex

V2 . . . . . Secondary visual cortex

TPD . . . . . Theta-by-Place-by-Position Cells

VTN . . . . . Ventral Tegmental Nucleus

1

Introduction part 1: General introduction to rodent navigation

1.1 Introduction: rodent navigation and memory

Spatial navigation is a vital cognitive function for the survival of several mammalian species, allowing animals to find and remember the location of food or mates, and avoid predators. In his early behavioural work, Tolman (1948) suggested that the brain achieves this function by constructing an internal, map-like representation of the external environment, or cognitive map, which encodes the spatial relationships between external cues. Mammals like rats can use this map to navigate flexibly in their environment, for instance by using shortcuts behaviors to reach a goal location. The existence of an internal cognitive map was first investigated by Tolman, who trained rats to follow a path between a start point and a goal location (Figure 1.1 left). After training, rats were able to choose the shortest route to reach the same goal's location in a sun-burst maze, despite no prior experience of this environment (Figure 1.1 right). Later behavioural work by Morris (1981) provided evidence compatible with Tolman's original idea that rats use a mental representation of space to solve spatial tasks. Rats were trained to swim to a hidden platform starting from a specific location inside a water maze. After training, rats were able to locate the platform when released from random starting locations, suggesting that they were not using a

simple associative-response strategy to solve the task, for instance based on body turns or swimming duration.

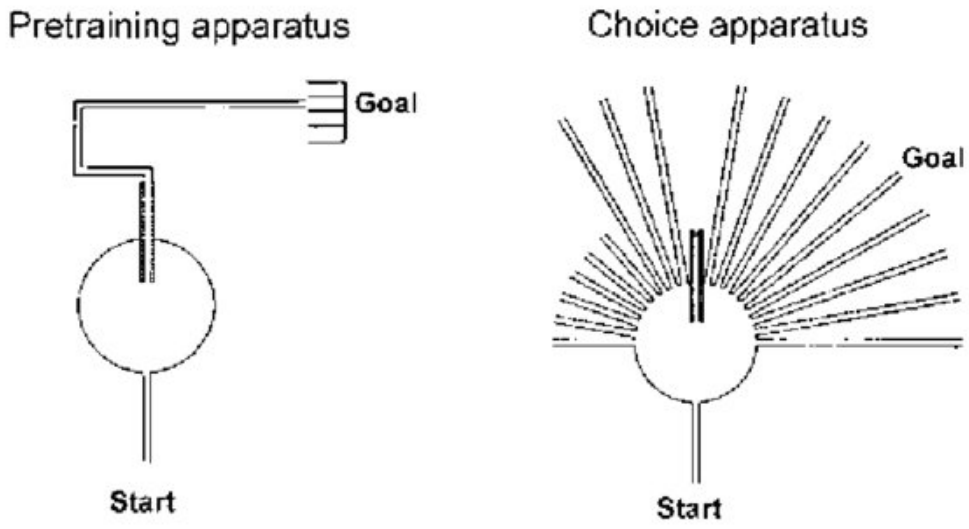


Figure 1.1: **Tolman's apparatus used to investigate the existence of an internal cognitive map of space in rats.** Left, maze used in the training phase, in which rats learned to run from a start point and a goal location. Right, sun-burst maze used in the test phase, in which the original path was blocked. Most animals were able to choose the shortest route to the previously learned goal location. Adapted from Tolman (1948).

O'Keefe and Nadel, in their book "The Hippocampus as a Cognitive Map" (O'Keefe and Nadel, 1978), proposed that Tolman's cognitive map resides in the hippocampus, based on the discovery by O'Keefe and Dostrovsky (1971) of place cells in the dorsal hippocampus of foraging rats. These cells became active only when animals explored a specific region of the environment, being silent everywhere else. Important behavioural findings have followed to suggest that hippocampus and related areas play a crucial role for storing and using the cognitive map. For example, rats with hippocampal and subicular damage were more impaired than controls in the acquisition of place learning in the Morris water maze task, although they were able to eventually reach similar levels of performance as the controls after extensive training (Morris et al., 1990).

Since this early work, the cognitive map has been investigated by several single unit recording studies in rodents during free exploration (see review by McNaughton et al., 2006a). These studies discovered a broad range of neurons, across the wider limbic system, that respond to different elements of space in allocentric

coordinates. First, head direction (HD) cells were discovered in the dorsal presubiculum (PrS) of rats, also known as the postsubiculum (PoS) (Taube et al., 1990a). HD cells did not form firing fields at specific locations but fired selectively when the animal was facing a specific direction in the horizontal plane, irrespective of its position. Subsequent investigations reported HD cells also in related parahippocampal structures, as well as in retrosplenial cortex (RSC) (Cho and Sharp, 2001) and in lower diencephalic structures, in particular the dorsal tegmental nucleus of Gudden (DTN), lateral mammillary nucleus (LMN) of the mammillary bodies, and anterodorsal thalamic nucleus (AD) of the thalamus (Sharp et al., 2001; Stackman and Taube, 1998; Taube, 1995; Taube and Muller, 1998), suggesting the presence of a thalamocortical HD system. Several years after HD cell discovery, grid cells were found in all regions of the parahippocampal cortex, namely medial entorhinal cortex (MEC) (Hafting et al., 2005; Sargolini et al., 2006), PoS, PrS, parasubiculum (PaS), and subiculum (Sub) (Boccara et al., 2010), having a hexagonal pattern of firing fields across the environment. Most recently, boundary related cells were found mostly in Sub (Lever et al., 2009; Barry et al., 2006) and MEC (Boccara et al., 2010; Savelli et al., 2008; Solstad et al., 2008), responding to the presence of geometric boundaries at a specific distance and direction from the animal. Further recordings from parahippocampal areas revealed many other spatial cell types that respond to a conjunction of two or more sets of spatial inputs, namely heading direction, self-position, boundaries, as well as egocentric cues (for example Cacucci et al., 2004), whose functions are just starting to be understood.

The discovery of different types of spatially-modulated neurons led to the notion of an extended hippocampal cognitive system for allocentric navigation, which comprises the hippocampus proper (O'Keefe and Dostrovsky, 1971), as well as extensive limbic cortical and subcortical regions (Aggleton and Brown, 1999). Existence of place and grid cells in hippocampus and MEC was also confirmed in other mammalian species besides rodents, namely bats (Rubin et al., 2014; Ulanovsky and Moss, 2007; Yartsev et al., 2011; Yartsev and Ulanovsky, 2013), non-human primates (Yin et al., 2018; Robertson et al., 1999), and humans (Miller et al., 2013; Doeller et al., 2010; Jacobs et al., 2013; Ekstrom et al., 2003).

In rodents, spatial exploration is associated to another electrophysiological signature in the hippocampus, beside place cell firing. That is, the presence in the local field potential (LFP) of highly coherent theta oscillations, characterized by a large-amplitude rhythmic fluctuation (6-12Hz) (Buzsáki, 2002, 2005). Hippocampal

theta oscillations are closely coupled to two fundamental aspects of spatial exploration: locomotion behaviour (running speed of the animal) and self-position (place cell firing). These correlations led O'Keefe and Nadel (1978) to propose that theta might represent a mechanism necessary for cognitive mapping functions.

Before moving to a description of our three experiments, we need to understand the current state of knowledge about how the brain encodes spatial and theta signals, and what is their functional significance. In this first part of the Introduction we will review our understanding of what constitutes the neural basis of the cognitive map, with a a particular focus on the HD and theta systems, which are the focus of this thesis. In the second part of the Introduction (next Chapter), we will review the anatomy, connections, electrophysiology and functions of RSC and anteroventral thalamic nucleus (AV) and explain why we conducted our experiments. We will conclude the next Chapter with a summary of the three Experiments, which will then be presented in each of the subsequent experimental Chapters.

1.1.1 Nomenclature

Different definitions of hippocampus and hippocampal formation have been adopted in the past (Amaral and Lavenex, 2007). This thesis adopts the nomenclature whereby hippocampus comprises the cornu ammonis (CA) fields (CA1, CA2, CA3) and the dentate gyrus. The hippocampal formation includes the hippocampus and the subiculum (Sub), both having a three-layered organization. Parahippocampal regions (para = near/adjacent in latin) consist of the PrS, PoS, PaS, and entorhinal cortex, all having a multi-layered organization. The hippocampal formation, together with the adjacent parahippocampal cortex, make up the medial temporal lobe. In this thesis, the term "hippocampal cognitive system" is used to refer to this extended network of brain regions that serves a critical function in memory, navigation, and cognition. The cognitive spatial map is encoded by neurons across these regions with specific functional properties.

The limbic system (limbo = transition/intermediate in latin) comprises the hippocampal formation, parahippocampal cortex, amygdala, medial septum, cingulate cortex, postrhinal and perirhinal cortex. In this case, the transition is between the neocortex and the diencephalon (including mammillary nuclei and anterior thalamic nuclei − ATN).

Papez (1937) first described connections between these core limbic structures. He suggested the presence of a loop linking the hippocampal formation to the medial diencephalon, cingulate cortex, parahippocampal cortex, and back again to the hippocampal formation (Papez, 1937). The Papez circuit, also known as the hippocampal "limbic system", was regarded as vital for emotions. We now know that this original concept of a loop that starts and ends in the hippocampus, needs to be regarded as a much more complex system of direct and indirect interconnections, referred to as an "extended hippocampal-diencephalic network". Spatial and memory functions of the hippocampus and related cortical areas are now known to rely on these diencephalic inputs (Aggleton and Brown, 1999).

1.1.2 Sources of information for navigation

Different coordinate systems can be used by the brain to encode local sensory information. The cognitive map is allocentric, since the location of external cues is defined relative to each other. By contrast, egocentric spatial information is encoded so that location of external cues is defined relative to the agent, and thus depends on the agent's orientation relative to the cues (in our case, a rat). We start with a description of the various types of information used by spatially-modulated neurons of the allocentric cognitive map to modify their activity. The first broad distinction can be defined in relation to spatial (metric) or contextual (non-metric) inputs. Spatial inputs are derived from local sensory information while contextual inputs provide information about the general properties of an environment (Jeffery and Anderson, 2003; Jeffery, 2007). Sensitivity of spatial neurons to both global contextual and local metric information highlights the complexity of a map-based system, whose role is not restricted to the spatial domain.

Spatial inputs can then be subdivided based on the type of information they convey into idiothetic (generated due to movements) and external (reference points in the environment). Idiothetic information includes angular head velocity (AHV) from vestibular signals and, during locomotion, self-motion cues in the form of optic flow (rotation and translation of the visual scene), efference copies of motor commands and proprioceptive signals from muscle joints. External information present in the environment includes landmarks and geometric boundaries in the form of visual, auditory, tactile, olfactory and auditory cues (Etienne et al., 1996; McNaughton et al., 2006a; Jeffery, 2007). A conceptually important aspect of the cognitive map is its ability to integrate these different sources of information, to generate unified, multimodal and unambiguous spatial representations (McNaughton et al., 1996, 2006a).

1.1.3 Navigation strategies

On the basis of available sensory information, animals can adopt two different navigation strategies, path integration and landmark-based navigation. Through path integration, animals can rely solely on a combination of internally-generated cues without explicit guidance from environmental cues (Gallistel, 1990). Animals continuously monitor idiothetic cues during movement to calculate the direction and length of the path traveled from a known starting location and orientation, to compute self-position and orientation based on translational and rotational movements. At the same time, through landmark-based navigation, animals can infer their position and orientation from salient reference points in a familiar environment (Etienne et al., 1996; Etienne and Jeffery, 2004). In rats, vision provides the most reliable source of external information for navigation (Gallistel, 1990). Hence, knowledge about the spatial relations between visual cues or landmarks can be combined with linear and angular path integration to compute self-position and orientation during cognitive mapping.

The ongoing interaction between these two mechanisms, one conveying sensory information from the external environment and another based on idiothetic cues, is required to update and maintain a correct spatial estimate through time. This updating mechanism is a bidirectional process: landmarks (or boundaries) intermittently correct errors accumulated during linear and angular path integration. In turn, path integration sets the internal reference to assign a specific direction or location to external cues, so that they can establish landmark references to correct cumulative path integration noise during movement, while simultaneously filtering other unstable cues (Jeffery and O'Keefe, 1999; McNaughton et al., 1996, 2006a). This is reflected in the dynamic response properties of spatially-modulated neurons, which do not depend on a single sensory modality but are determined by the integration of path integration and landmark information. Supramodality of responses is discussed next and accounts for animals' ability to incorporate these different sources of information for effective navigation.

1.2 Neuroanatomy and physiology of the spatial navigation system

Four main types of spatially-responsive neurons have been discovered so far and form the neural basis of the allocentric cognitive map. This Section provides a general overview of these cells in order of discovery, their general firing properties and how their activity is influenced by various types of sensory stimuli.

1.2.1 Place cells

Hippocampal place cells (Figure 1.2) are principal (pyramidal) neurons that fire with low/irregular background firing rates, and exhibit peaks in activity that are highly specific to a unique location within an environment, or place field (O'Keefe and Dostrovsky, 1971). Firing rates increase gradually as the rat enters the place field, peaking at its centre, and decrease moving away from it. Place cells are typically omnidirectional and so this spatial firing pattern is seen across all heading directions faced by the animal while exploring the place field. The population activity of hippocampal place cells provides a global representation of the animal's spatial location that is independent of heading direction and overall behaviour of the animal (Muller et al., 1994).

Place cells have been mostly described in CA1 and CA3 fields of hippocampus (O'Keefe and Dostrovsky, 1971). The hippocampal axis presents a gradient of spatial scales, whereby place fields become larger and increase in number moving from dorsal to ventral hippocampus (Moser and Moser, 2008; Kjelstrup et al., 2008; Royer et al., 2010). This is paralleled by a reduction of theta-modulated firing and LFP theta power, possibly reflecting a decrease in spatial function specialization from dorsal to ventral hippocampus (Poulter et al., 2021).

Later studies in rats reported place cells in the dorsal Sub and MEC, both receiving a dense CA1 input. Compared to CA1 place cells, subicular and entorhinal place cells were proposed to form broader fields less sensitive to environmental shape (Sharp, 1999; Quirk et al., 1992). Place cells with highly compact fields were also recorded in rats from brain regions outside the hippocampal system, in the anteromedial thalamic nucleus (AM), nucleus reuniens (NRe), parataenial nucleus (Jankowski et al., 2015), anterior claustrum (Jankowski and O'Mara, 2015), somatosensory cortex

(Long and Zhang, 2021). Preliminary evidence suggests place cells may also exist in dorsal lateral geniculate nucleus (dLGN) (Hok et al., 2018). Extra-parahippocampal place cells show a much weaker relationship to theta compared to place cells in CA fields. (Hok et al., 2018).

To understand how place cells compute spatial location, we now describe their firing characteristics, and how external and internally-generated cues are combined to determine where a place field should be located. This interaction between multiple sources of information constitutes a general principle of all spatial neurons, accounting for the flexibility of the map-based system.

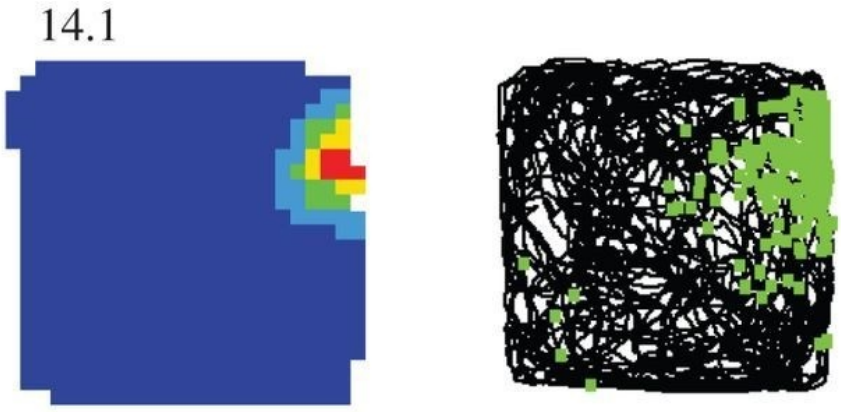


Figure 1.2: **Place cell recorded from hippocampus of a rat foraging for food inside a squared box.** Left, spatial ratemap showing firing rate as a function of location. Heat colours denote firing rate (Hz). Peak firing rate is at the top. Right, spikemap showing the rat's spatial trajectory (black) with superimposed spikes (green) at locations along the rat's path at which the cell fired. Spikes are clustered at a specific location. Adapted from Hartley et al. (2014), first reported by O'Keefe and Dostrovsky (1971).

1.2.1.1 Place cells combine multimodal metric and contextual inputs to position their fields

Hippocampal place fields are remarkably stable over time and during re-exposure to a familiar environment (Lever et al., 2002), but remap in sufficiently different environments (Lever et al., 2002; Muller and Kubie, 1987; Leutgeb et al., 2005; O'Keefe and Burgess, 1996). Remapping refers to changes in location, size/shape and scale of the firing fields, in response to changes in metric and contextual properties of an environment. Two types of remapping occur, depending on the extent of changes. Minor changes (like changing box colour or odour) cause partial remapping, in which

only some place cells change their field locations and metrics, or rate remapping, whereby some cells change their firing rate but not field metrics (Leutgeb et al., 2005). Larger changes (like box shape) lead to global remapping, in which all cells show a complete reorganization of the their field locations and metrics, as well as rate of firing (O'Keefe and Conway, 1978; Jeffery and Anderson, 2003). Based on this notion, investigating the dynamics of remapping is indicative of the types of information used by the hippocampus to identify spatial location.

The hippocampus uses different spatial maps to represent environments having different metric properties. For example, place fields become stretched along the longest wall of a square box when it is stretched along one dimension into a rectangular box, and a small subgroup starts firing at a second location in the larger shape (O'Keefe and Burgess, 1996). A similar rescaling effect is seen when place cells are recorded from a small to a larger cylinder (or rectangular box), although some cells also shift their field locations unpredictably in the larger shape (Muller and Kubie, 1987). When the recording box is changed in shape, from cylinder to square, all place cells show very different firing locations, which cannot be predicted from knowledge of the firing pattern in the other shape (Lever et al., 2002; Muller and Kubie, 1987). Different maps can also be used by hippocampus to represent the same spatial layout having different non-metric properties. For example, CA1 place fields remap in identical boxes in response to changes in global contextual cues, both external, such as the colour and odour of the walls (Jeffery and Anderson, 2003), and idiothetic, specifying behavioural (McNaughton et al., 1983) or motivational (Moita et al., 2004; Markus et al., 1995) variables associated to that environment. In response to multimodal contextual changes, remapping is unpredictable and heterogeneous across the place cell population, since place and rate of firing are rearranged independently between place cells when recorded in identical square boxes characterized by unique brightness/odours or walls/floors combinations (Anderson and Jeffery, 2003; Jeffery and Anderson, 2003).

Despite the heterogeneous repositioning effect in response to geometric and contextual manipulations, firing fields maintain a constant distance to the two nearest adjacent walls, leading to theories that metric information about distance and direction of boundaries represents the strongest spatial reference for determining where a place cell should fire (O'Keefe and Burgess, 1996; Barry et al., 2006). Studies indicate the importance of non-perimeter boundaries as well: barrier insertion in the box causes place fields near the barrier to disappear, duplicate or addition of new place fields near the barrier, without affecting fields at the perimeter of the

box (Muller and Kubie, 1987). There is strong speculation that this geometric input is supplied to the place cell system by upstream interconnected parahippocampal structures that contain boundary related neurons, like the MEC (Solstad et al., 2008; Hartley et al., 2000).

During active movement, when 6-12Hz theta oscillations emerge in the hippocampal LFP, place cells show firing rates strongly modulated at theta frequencies (O'Keefe and Recce, 1993). This has been seen in head-fixed mice navigating a virtual environment, and in freely moving rodents. In CA1 and CA3 pyramidal layers, cells display strong coherence between their spike times and the phase of local oscillations, preferentially firing on descending and ascending phases in CA1 and CA3, respectively (O'Keefe and Recce, 1993; Dragoi and Buzsáki, 2006; Csicsvari et al., 1999; Cacucci et al., 2004; Fox et al., 1986). In addition to the spike time-theta phase relationship, hippocampal place cells display a negative correlation between theta phase of spiking and the location of the animal within their firing field, known as theta phase precession (O'Keefe and Recce, 1993; Skaggs et al., 1996; Royer et al., 2010). The precession of firing phases during field traversal, combined with increased and decreased firing rate when entering and leaving the field, is a key feature of the rodent hippocampus, allowing spatial location to be inferred from ensemble activity of the place cell population.

1.2.1.2 Multimodality of place cells

Place cell firing is primarily driven by path integration, but is modulated by external cues, in particular landmarks and geometric boundaries, as reviewed above (Muller and Kubie, 1987; O'Keefe and Speakman, 1987; Zhang et al., 2014). The sufficiency of idiothetic cues is suggested by evidence that firing rate of hippocampal place cells correlates with running speed (McNaughton et al., 1983) and, following initial exposure to environmental cues, idiothetic cues can maintain place cell activity, which continue to fire selectively at the same location in darkness (Zhang et al., 2014; Markus et al., 1994), during blindfolding (Hill and Best, 1981; Save et al., 1998) and after landmark removal (O'Keefe and Conway, 1978; Markus et al., 1994). However, reliance on path integration alone is less efficient, since place fields can be maintained for only brief periods, after which error accumulation in the path integrator drives a slight place field drift, which can be rectified by the use of geometric boundaries or proximal non-visual cues i.e., tactile from contact with the arena walls (Zhang et al., 2014) or olfactory when the arena is not cleaned prior to the recording trial

(Save et al., 2000). Evidence that non-visual cues from the environment influence place cell firing comes from recordings of CA1 place fields that follow rotations of olfactory, visual, auditory or tactile cues rotated around a cross maze while rats perform a working memory task (O'Keefe and Conway, 1978). This is consistent with CA1 place cells being activated by multimodal sensory stimuli, including olfactory (Wood et al., 1999), tactile (Gener et al., 2013) and auditory (Aronov et al., 2017), reinforcing a role of hippocampus in integrating local sensory cues within and across modalities for cognitive mapping.

Visual cues are considered to be particularly important to stabilize the spatial firing pattern, by providing directional inputs to place cells, directly or via the MEC. The typical experimental setup used to investigate the influence of visual cues consists of a symmetric cylinder containing a single polarizing white cue card on its wall. Other extra-maze room cues such as distal landmarks and room geometry are controlled by placing the cylinder in the centre of a curtained enclosure, to ensure that the card provides the only salient source of directional information. To induce a change in the perceived sense of orientation (as specified by the cue card), the cylinder is rotated in the presence of the rat or after removing the rat from the arena. This generates a conflict between the orientation as specified by idiothetic and visual information. If place cells use the proximal visual cue to map spatial location, then the rotation of the card should lead to a similar place field rotation. If on the other hand, place fields are primarily controlled by idiothetic cues, then place fields should not follow the card rotation. Rotation of the single-cued cylinder has become the standard paradigm for investigating how spatial neurons integrate idiothetic and visual landmark information. In these experiments, place fields can rotate in the same direction as the card inside the cylinder, when it is rotated to alter the animal's sense of direction. Similarly, place fields shift after removal of the card, suggesting sensitivity to visual changes (Muller and Kubie, 1987; O'Keefe and Conway, 1978; O'Keefe and Speakman, 1987). Firing is influenced by both distal visual cues (cue cards on the lab room walls) and proximal ones (cue card inside the cylinder). When both are available and conflicting with each other (rotated in opposite directions), place fields either split or rotate with one or the other (Shapiro et al., 1997; Yoganarasimha et al., 2006), whereas changes in spatial relations between distal cues leads to place field remapping, having the same effect as changing relations between box walls (O'Keefe and Conway, 1978). This suggests that knowledge about local and distant landmarks or visual cues and their spatial relations is crucial for self-localization, whereby landmarks are integrated to maintain and update estimates of distance traveled from path integration to derive a unified locational estimate.

When idiothetic and landmark information are placed in conflict through cylinder rotations, place cells (and HD cells) weigh different sources of local sensory information and select the most reliable (most invariant) one to position their firing fields (Knierim et al., 1995; Jeffery and O'Keefe, 1999; Knill and Pouget, 2004; Jeffery et al., 2016). The strength of landmark control on place cells (and HD cells) depends on learning of cue reliability as compared to path integration, and prior experience of cue stability (Knierim et al., 1995). Reliability of each cue can be manipulated by using different extents of cylinder rotations, to generate different levels of cue conflict. During small conflicts between the visual card and the path integrator (rotations less than 45° performed in the presence of the animal), landmark control is strong and so place fields rotate by similar amounts as the card. During larger conflict on the other hand (180° rotations), place fields do not rotate with the card or show a radical rearrangement (remapping) (Knierim et al., 1995). Small conflicts between the landmark and path integration are supposedly attributed to path integration noise, and so the landmark can reliably capture the spatial signal. If the card is visibly and abruptly rotated by larger amounts, discrepancies are too large and sudden to result from cumulative path integration noise, and so path integration predominates in controlling the spatial signal. This is reflected at the behavioural level in the homing behaviour of hamsters (Etienne et al., 1990), whose responses rely on visual or self-motion components depending on their degree of conflict.

Similar findings have been obtained from place cell recordings on a linear track. Gothard et al. (1996) generated a conflict between the path integration and the visual landmark by training rats to run between two reward locations, while the starting box was being shifted to different positions during the trial. The main finding was that place cell fields were most strongly controlled by the most reliable cue: cells fired at fixed distance from the starting box during the first part of the journey (controlled by path integration), but started firing in relation to the visible goal in the second half (predominance of vision). The dynamics of this transition from idiothetic to visual control were determined by the extent of cue conflict: when the starting box was moved by a small amount, place fields transitioned gradually up the track to compensate for this shift, while during larger displacements, fields abruptly switched to single-cue, idiothetic dominance. Experimental evidence has led to computational models proposing that small spatial conflicts require weighted cue integration in order to derive a single, optimal locational estimate, where individual weights are determined by the reliability (inverse of the variance) of each cue. Larger conflicts lead to all or none responses because a weighted average of the two cues would not

yield accurate locational information (Knierim et al., 1995; Jeffery and O'Keefe, 1999; Jeffery et al., 2016). A discussion of the different models that seek to explain spatial cue integration is beyond the scope of this thesis, although most models suggest that cues are integrated in a statistically optimal fashion according to principles of Bayesian integration (Knill and Pouget, 2004) by place and HD cells, to reduce uncertainty in the perceived position (Madl et al., 2014; Jeffery and O'Keefe, 1999) and orientation (Jeffery et al., 2016), even in conditions of conflict.

1.2.2 Head direction cells

The functional role of the HD signal is to provide a global code for head orientation (Figure 1.3). Cells discharge only as a function of the animal's instantaneous heading direction in the horizontal plane. Firing is independent of the animal's position within the environment and behaviour in general (Taube et al., 1990a; Taube and Muller, 1998; Stackman and Taube, 1998; Knierim et al., 1998).

HD cells form a widely distributed network. The first discovery of HD cells was in the PoS (Taube et al., 1990a). Since then, these cells were described in a wide number of interconnected cortical and subcortical brain areas, including AD, LMN, DTN, RSC, and all parahippocampal areas. Although regions of the HD circuit are densely interconnected to hippocampus, directly or via the MEC (Giocomo et al., 2014), HD cells are not typically found in the hippocampus proper (Leutgeb et al., 2000). These areas forming the thalamocortical HD network are responsible for generating, updating and resetting the HD signal. Along this circuit, vestibular input ascending from subcortical areas is required for HD signal generation and for updating it on the basis of movement. Visual input descending from PoS/RSC is required for resetting the HD signal based on landmarks.

We now describe general firing properties of classic HD cells, followed by an overview of the studies seeking to dissect the influence of landmark and idiothetic information on their discharge activity. The theoretical model proposed to explain how the HD signal is generated by vestibular inputs and updated based on the integration with visual inputs is discussed in Section 1.3, along with attractor network models.

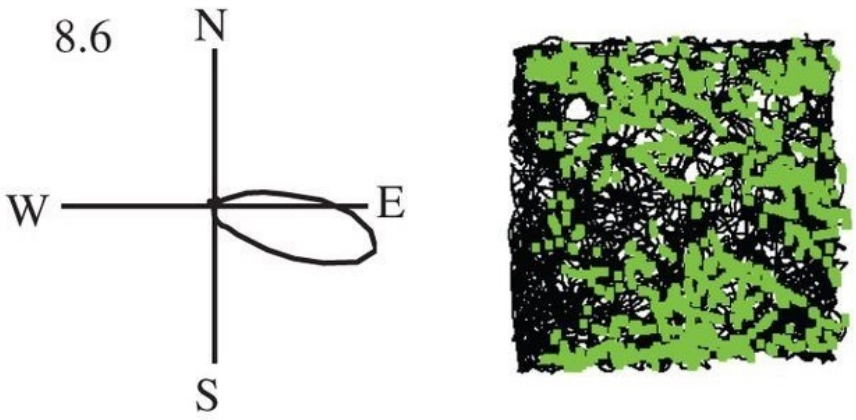


Figure 1.3: **HD cell recorded in the anterior thalamic region as the rat foraged for food inside a squared box.** Left, directional tuning curve expressed as a polar plot, showing firing rate (Hz) as a function of heading direction (degrees). The cell has a single directional peak. Directional peak firing rate is at the top. Right, spikemap showing the rat's trajectory with superimposed spikes. Spikes occurred when the rat was facing within a specific range of directions, corresponding to the tuning curve width. Adapted from Hartley et al. (2014), first reported by Taube et al. (1990a).

1.2.2.1 Head direction cells provide a global directional code

The HD system functions as a compass: each cell fires maximally when the animal faces a specific compass direction, known as the cell's preferred firing direction (PFD), and firing rates decline gradually as the animal turns away from the PFD (Taube et al., 1990a). As a population, all HD cells evenly signal the full 360° compass range. Unlike a real compass however, HD cell orientation is not geocentric and is constantly updated by the animal's own movements, as evidenced by the existence of HD cells modulated by angular head velocity (AHV) (Stackman and Taube, 1998; Blair and Sharp, 1995; Taube et al., 1990a; Taube, 1995; Stackman and Taube, 1998; Taube and Muller, 1998; Lozano et al., 2017).

A typical HD cell has an activity profile that follows a Gaussian distribution, the circular analogue of a normal distribution, both being unimodal and symmetric. The peak is at the PFD and activity is silent (approximately 0Hz background firing rate) outside of the directional firing range. The directional firing range defines the range of directions inside the activity curve at which the cell fires. In the adult rat, there is large variability in the peak firing rate and firing range of HD cells across brain regions, ranging between 5-120Hz and 60-150°, respectively. A general trend is visible whereby HD cells from subcortical regions, for example LMN and AD (Stackman and

Taube, 1998), display broader tuning curves and higher peak rates compared to cells located downstream in cortex, for example PoS (Stackman and Taube, 1998; Sharp et al., 2001) and RSC (Cho and Sharp, 2001). However, there is no specific topological organization of tuning curve properties, except for an increase in directional firing range along the dorsal-ventral axis of MEC layer III (Giocomo et al., 2014).

HD cells provide a global directional metric. This is because, unlike place cells, whose firing fields are strongly environment-specific, HD cells are active in all environments and generally maintain their relative directional preferences in different environments (Taube et al., 1990a,b; Taube and Muller, 1998). HD cell activity is only weakly modulated by geometry: PFDs rotate with geometric cues only in the absence of alternative sources of visual and idiothetic information, for example after disorientation of the animal or when landmarks are removed (Knight et al., 2011). In disoriented animals, Golob and Taube (1997) found that changing the shape of the environment leads to PFD shifts in only 20% of HD cells from PoS and AD. Since geometric cues provide a strong reference for updating the activity of place cells, but constitute only a weak orienting signal for HD cells, recognition of geometry is likely to require first the extraction and processing of linear distance information about geometric boundaries downstream of the HD system, in parahippocampal structures including MEC (Solstad et al., 2008; Hartley et al., 2000).

Despite the environment-invariant responses of HD cells to both geometric and contextual changes, environmental manipulations that induce a shift in the animal's sense of direction lead to equal rotations of PFDs, suggesting sensitivity to visual landmarks. Landmark learning is rapid, as one-minute exposure to a stable cue card in the cylinder is sufficient to develop cue control of HD cells in AD and PoS when the card is rotated (Goodridge et al., 1998). HD cells always maintain fixed spatial and temporal correlations between their activity. That is, co-recorded HD cells from the same or different brain regions always rotate their PFDs by similar amounts (Taube et al., 1990b; Taube and Burton, 1995; Peyrache et al., 2015; Yoganarasimha et al., 2006; Knierim et al., 1998; Hargreaves et al., 2007; Goodridge et al., 1998; Zugaro et al., 2001) and maintain fixed temporal intervals between their spiking, which follows the animal's turning direction (Muir et al., 2009). This coherence has led to computational models proposing that the HD cell system expresses a rigid internal network connectivity in a continuous attractor network (Skaggs et al., 1995; Zhang, 1996).

1.2.2.2 Integration of idiothetic and external cues by head direction cells

Like place cells, HD cells compute global head orientation using information primarily from idiothetic cues, derived from the vestibular and proprioceptive/self-motion systems. The sufficiency of idiothetic cues to generate HD signal is evidenced by results that HD cells maintain direction-specific discharge in darkness (Blair and Sharp, 1996), after removal of familiar landmarks (Goodridge and Taube, 1995; Taube et al., 1990b), blindfolding (Goodridge et al., 1998) and before eye opening (Tan et al., 2015). However, PFDs drift more in the absence of vision, indicating that reliance on path integration alone is not sufficient to maintain a stable orientation over time (Goodridge et al., 1998; Mizumori and Williams, 1993; Taube et al., 1990b; Goodridge and Taube, 1995; Save et al., 2000).

For landmark stabilization, HD cells can use both distal (cue cards on the lab room walls) and proximal visual cues (cue card in the cylinder) but distal cues control HD cells more than proximal ones (Zugaro et al., 2001). In the presence of conflicting directional information from proximal and distal cues, when they are rotated in opposite directions, place cells form split representations, whereas HD cells always rotate as an ensemble following the most distal cue (Yoganarasimha et al., 2006). Further away cues serve as more reliable directional reference because they are associated to a more narrow range of directions i.e., perceived to be more invariant by the animal. This is due to a lower degree of parallax error: proximal cues, even when stable, are associated to many different directions in moving animals (Gallistel, 1990).

When a continuously viewed cue is rotated inside the cylinder in the presence of the rat, in the absence of more distal room cues, a conflict is generated between directional information provided by the intra-maze card and that provided by vestibular inputs. As already explained for place cells, HD cells perform experience-dependent weighted cue integration so that PFDs are more strongly controlled by the most reliable input (more stable). In this way, PFDs follow the card rotation only for small rotations (45°), when it is perceived as stable (Taube et al., 1990b; Knierim et al., 1998). In these trials, PFDs rotate by similar amounts as the card, with a tendency towards under-rotations (Knierim et al., 1995, 1998; Taube et al., 1990b; Goodridge and Taube, 1995; Taube, 1995). Such corrective responses suggest that the final PFD reflects the weighted average of all conflicting stimuli (visual, idiothetic and non-visual). If rotations are progressively increased above 45°, PFD under-rotations show a non linear increase, but PFDs remain stationary after the 180° shift, indicating a switch to complete idiothetic capture (Knierim et al., 1998). In some cases, after 180°

rotations, HD cell behaviour is less predictable and PFDs rotate by 180° smoothly over the course of two minutes as a consequence of path integration noise (Knierim et al., 1998; Chen et al., 1994b). In these trials, the conflict is presumably too large for the card to be considered as stable and reset the internal path integrator, and so idiothetic input predominates over the landmark. Similar results have been reported for hippocampal place cells recorded during continuously viewed cue rotations in the cylinder. In these studies, the visual cue exerted robust control over place cells during small rotations (45°). When the mismatch was increased above 180°, place fields either remapped to generate new spatial representations (Knierim et al., 1998), or remained stationary, aligned with idiothetic cues (Rotenberg and Muller, 1997). Hence, HD and place cells are similarly influenced by the rotations, given that PFD shifts correspond to equal shifts or remapping of place fields (Knierim et al., 1995, 1998), implying that the hippocampal map is oriented relative to the world by landmark information received from the HD system.

Other studies have removed the animal from the cylinder and disoriented it during hidden cue rotations (90°). In this case, the card lost control over HD and place cells (Knierim et al., 1995), since larger PFD under-rotations were observed compared to trials in which animals were not removed from the cylinder during the rotations (Knierim et al., 1998; Taube, 1995). Supposedly in these trials, the card was associated to a different direction every time the rat experienced it due to unstable self-motion signals and so was learned to be unreliable i.e., the relation between the landmark and the internal sense of direction was altered by the disorientation procedure on each trial. Crucially however, disorientation was not deleterious for landmark control if preceded by training trials in which the experimental manipulation was covered from the rat's sight but no disorientation was performed (Dudchenko et al., 1997). It has been proposed that weightings of internal and external cues are dynamic, modified by prior experience so that they can shift even within a single trial (Jeffery, 1998; Jeffery et al., 2016; Knight et al., 2014). This has been demonstrated by Knight et al. (2014) by recording AD HD cells in the cylinder when a light was being continuously shifted along the walls in 20° intervals (20 to 100°) during the course of an experimental session. HD cell responses were found to be dependent on the trial: for displacements of less than 120°, PFDs shifted by at least 50% of the light shift, while for greater displacements, under-rotations progressively increased (less than 50%), indicating a gradual shift toward idiothetic control as a consequence of reduced landmark stability. Landmark control vanished in a longer time compared to naive animals exposed to the same level of conflict, implying experience-dependent weighted integration by

HD cells. In agreement with this notion, abrupt 180° rotations of a familiar cylinder in the presence of the rat cause equal shifts (or remapping) of HD and place cells, but this is not seen in novel environments (McNaughton et al., 1995).

There is some evidence that HD cells can use external non-visual cues to anchor their PFDs, although vision provides a much stronger directional reference. For instance, Goodridge et al. (1998) found that olfactory and tactile stimuli, but not auditory, rotated inside a cylinder in blindfolded rats could trigger PFD shifts (Goodridge et al., 1998), with larger under-rotations compared to visual cues. The influence of tactile and olfactory intra-maze cues has been further studied by Zugaro et al. (2000) by performing independent rotations of floor and walls of a cylinder containing a white cue card. When the floor was stable, card rotations reliably shifted the PFDs. The small under-rotations observed are consistent with the idea that idiothetic and floor's cues can be used to partially correct PFD shifts. Rotations of the floor alone failed to shift the PFDs, suggesting that olfactory and tactile cues on the floor exert weaker landmark control than the visual card. However, there is still some debate regarding whether non-visual processes or path integration supersede in the absence of a more reliable visual reference. For instance, in rats exploring a radial arm maze in darkness, HD signal quickly drifted if animals were placed in the centre of the maze, given the lack of salient tactile and olfactory stimuli, but the signal was maintained for up to 30 minutes if animals were confined at the end of each arm, where food wells provided tactile and olfactory information (Mizumori and Williams, 1993). Future experiments need to investigate the influence of physical properties of three dimensional objects, like their smell or texture, to maintain HD cells in darkness.

Vestibular inputs provide the driving signal for HD cells, as shown by studies comparing HD cell responses in rats during active foraging and passive rotation. Passive rotation abolishes efferent copies and proprioceptive cues, while leaving vestibular and optic flow stimuli intact (see definitions in Section 1.1.2). In these studies, the absence of locomotion was shown to reduce the peak firing rate of HD cells by up to 27% compared to activity during active foraging, but PFDs remained constant, indicating the sufficiency of vestibular inputs (Zugaro et al., 2001; Taube et al., 1990b; Taube, 1995; Golob et al., 1998). This is consistent with the observation that HD cell firing is largely maintained in unrestrained animals when stationary despite reduced peak rate (Taube et al., 1990a). Although other experiments have reported an almost complete silencing of HD cells during passive rotation of restrained rats (Knierim et al., 1995), this could be due to higher levels of stress/restraint of the rat.

During angular path integration, self-motion is required to update the HD signal generated based on vestibular inputs, as evidenced in rats performing path integration tasks in the dual chamber apparatus. The animal was required to move from the familiar cylinder containing a single orientation cue to a new rectangular box devoid of familiar landmarks, following a U-shaped corridor. Path integration maintained a stable sense of direction in the new shape and across the corridor, as polarizing cues were not available to provide a directional reference. If the animal was allowed to walk into the new box (Taube and Burton, 1995; Stackman et al., 2003), for most HD cells the PFDs remained relatively constant between the cylinder and the rectangle, with only a small (6-30°) shift in the novel environment. If the animal was simply placed there or it was passively transported there, the drifting error increased up to 36° and 70°, respectively (Stackman et al., 2003; Taube and Burton, 1995). This suggests that efference copies and proprioception derived from locomotion are important for angular path integration. When the rectangular box was located in a different room connected to the cylinder by a much longer corridor (Yoder et al., 2011a), drifting error increased to 45°, although PFDs remained relatively constant, in line with path integration being degraded by cumulative errors over time. This also suggests that, in the original set up of the dual chamber apparatus, the rat did not use extra maze room cues to solve the task. A similar shift (30°) was seen during recordings in darkness (Stackman et al., 2003), implying a complementary role of optic flow in updating HD cell orientation in the absence of polarizing external cues. To test whether optic flow alone controls HD cell activity, Arleo et al. (2013) recorded from rats in a circular platform surrounded by black curtains. Rotating arrays of dots were projected on the curtains to provide moving optic flow stimuli. PFDs shifted at one-third of the speed of the stimuli rotation, but returned to their original direction in almost all the sessions after cessation of rotation. This indicates that global optic flow stimuli only weakly control HD cell signal, reinforcing the need for single landmark processing instead.

In conclusion, similar to self localization, cortical and subcortical HD cells perform weighted integration of various types of sensory information, both within and across modalities. Neural mechanisms for how HD cells are anchored to landmarks and attractor dynamics are described in Section 1.3.

1.2.3 Grid cells

Whereas place cells in the hippocampus usually form a single firing field, grid cells have multiple compact fields that are regularly arranged forming a hexagonal grid pattern across the whole environment (Figure 1.4). The location of a cell's grid fields is called the grid phase, while distance between fields is the grid scale. The relationship between field locations of one cell with the others is called the offset. The periodic fields of neighbouring grid cells are offset relative to each other so that the entire surface of the environment is represented within the grids of multiple cells. Grids of neighbouring cells share a common orientation and spacing, but their field locations (phases) and offset between cells differ (Hafting et al., 2005).

Grid cells were first recorded in the rat MEC, where grid scale and field size are topographically organized and increase along the dorsoventral axis, while the phase of the grid and offset vary randomly among cells and are not topographically organized (Hafting et al., 2005). Since then, grid cells were reported also in dorsal Sub, PrS and PaS (Boccara et al., 2010; Gardner et al., 2022), where they co-localize with HD cells.

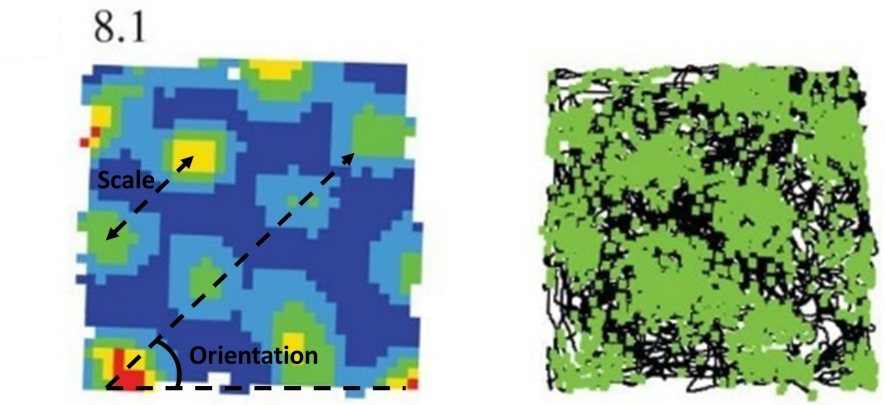


Figure 1.4: **Grid cell recorded in MEC inside a squared box.** Left, spatial ratemap showing regularly spaced firing fields that collectively form a hexagonal grid pattern. Orientation, scale and peak firing rate (Hz) are noted. Right, spikemap showing firing of the cell at multiple locations. Adapted from Hartley et al. (2014), first reported by Hafting et al. (2005).

1.2.3.1 General properties of grid cells

Grids from different parahippocampal regions are clearly distinguishable. Grid cells in MEC layer II show the highest grid periodicity (gridness) and theta rhythmicity, whereas grid cells in PrS/PaS show reduced theta and gridness, but stronger directional selectivity (Boccara et al., 2010). Differences in firing properties and theta phase locking preferences (Newman and Hasselmo, 2014) are also present within MEC, between layers II and III, providing afferents to different hippocampal areas (dentate gyrus-area CA3 and area CA1, respectively) (Mizuseki et al., 2009). Precession is more commonly observed among grid cells in layer II than layer III but direction preference is more common in layer III or IV (Sargolini et al., 2006; Giocomo et al., 2014; Newman and Hasselmo, 2014; Hafting et al., 2008).

The periodicity of grid fields allows cells to represent and update self-position by keeping track of the animal's translational movements in all environments (McNaughton et al., 2006a; Hafting et al., 2005). In this respect, the firing field arrays (grids) are stable across trials in the same familiar environment and grid cells are are active in all environments. Their firing structure (offset between cells) is independent of environmental manipulations (Hafting et al., 2005; Fyhn et al., 2007) and behavioural states (Gardner et al., 2022). For instance, metric environmental changes caused by changing the box shape (square; cylinder) cause extensive shifts in place cell field locations, while MEC grid cells translate their grid locations together, and sometimes rotate together, but maintain the same grid scale and offset (Fyhn et al., 2007). Furthermore, changing the environment size from small to larger cylinder leads to a higher number of grid fields and only a partial increase in field size, without affecting grid scale (Hafting et al., 2005). Another study reported that grid fields maintain fixed size but partially rescale to match the size and geometric shape (large square; small rectangle) of a familiar, but not novel, environment (Barry et al., 2007). Rescaling occurs in the same direction as the change in the length of the wall, but by a lesser amount. The incomplete rescaling and the fact that the original grid metric is rapidly restored following exploration of the environment (Barry et al., 2007) suggest that grid cells depend primarily on mechanisms for path integration, but geometric cues about environmental boundaries exert a specific influence on their field locations and orientations. Further evidence that grid cells are modulated by boundaries comes from the observation that wall removal results in grid cells translating their field locations, without changes in grid orientation and offset between grid cells and co-recorded HD cells in MEC (Solstad et al., 2008).

Cells can also use purely non-metric contextual information to position and orient their grids. Similar to the effects of metric changes, exposure to two identical square boxes characterized by unique odour/brightness combinations results in global place cell remapping and causes grid cells to translate or rotate their field locations together (Marozzi et al., 2015). When the contextual manipulation only causes rate remapping in place cells, there is no translation/rotation of the grids, suggesting that MEC grid and hippocampal place cell networks may receive contextual information from one another (Fyhn et al., 2007).

The rigid grid structure, resembling the internal coherence across environments expressed by HD cells, points to the existence of two interconnected "hardwired networks" that may interact with each other (Hafting et al., 2005; Gardner et al., 2022). According to computational models, continuous attractor networks in a one-dimensional ring and two-dimensional torus could provide the mechanism to explain HD and grid cell firing patterns, respectively (Burak and Fiete, 2009). While there is no direct biological evidence in the mammalian brain that HD cells follow a specific topological organization, simultaneous recordings of grid cells from MEC/PaS of exploring rats revealed that the grid cell population activity resides on a torus. Position of each cell on the torus matches the position of their receptive fields in the environment, and it is maintained between environments and behavioural states (Gardner et al., 2022). As the animal moves in space, activity can be smoothly shifted along the torus by speed and directional inputs, as well as by external sensory cues from boundaries and landmarks.

Computational models indicate that the overall grid pattern is formed from the combination of two types of internally-generated input: a speed-related input, conveyed by theta oscillations via speed cells within MEC, and a direction-related input, conveyed by HD cell inputs to MEC (Burgess et al., 2007). In MEC, speed cells encode the animal's running speed through their firing rates (Kropff et al., 2015) and through the frequency of their rhythmicity (Hinman et al., 2016). As predicted, firing rates of individual grid cells show strong theta rhythmic modulation, which correlates with gridness (Boccara et al., 2010; Giocomo et al., 2014; Kornienko et al., 2018) and, in the deeper MEC layers, a subset of speed cells displays conjunctive grid-HD properties (Sargolini et al., 2006). These cells are well suited to send linear and angular self-motion inputs for grid cell formation. This is consistent with disrupted MEC grid cell periodicity and lowered grid cell number after damage to the subcortical HD system (Winter et al., 2015), and with disrupted MEC gridness when the LFP theta is suppressed by medial septum inactivation, despite preserved spatial properties

of boundary vector cells (BVC), HD cells and hippocampal place cells (Koenig et al., 2011; Brandon et al., 2011, 2014). Furthermore, passive transport abolishes grid cell periodicity and speed-modulation of theta activity in MEC (Boccara et al., 2010), reinforcing the notion of grid cells as part of a path integration-based system.

1.2.3.2 Multimodal cue integration by grid cells

Within MEC, periodic grid cell activity is maintained during visual deprivation in familiar environments, implying independence from external information (Hafting et al., 2005), but cells show a weak drift in their field locations, expressed as a lowered auto-correlation of spatial ratemaps (Pérez-Escobar et al., 2016). This supports the notion that the periodic firing structure is independent of external information and primarily based on linear and angular self-motion signals combined by grid cells within the MEC. However, path integration requires corrective mechanisms from environmental cues, including boundaries and landmarks. Neural mechanisms for how the MEC path integrator is reset by these stimuli and contributes to self-localization together with place cells are poorly understood. It is thought that visual landmarks supply directional input to the grids in MEC, via projections from RSC/PoS HD cells (Hafting et al., 2005; Jacob et al., 2017). This is evidenced by the fact that rotating a visual landmark causes grid field arrays to rotate similarly, without changing grid spacing, size and offset relative to one another — much like HD cell rotations in the cylinder (Hafting et al., 2005; Boccara et al., 2010; Fyhn et al., 2007; Barry et al., 2007). Grid field rotations always occur in concert with one another and with co-recorded HD cells (Hafting et al., 2005), highlighting the interconnected dynamics between these networks. It may also be that place cells provide anchoring of the grids to the geometrical reference (boundaries) via direct feedback projections from hippocampal CA1 to MEC (Moser and Moser, 2008; Bonnevie et al., 2013) or alternatively this could occur via non-grid parahippocampal cells, like boundary related cells, described next.

1.2.4 Boundary related cells

Boundary related cells provide vector-based representations of the spatial layout. There are two types of these cells, both forming vectorial firing fields which can be either allocentric or egocentric. Allocentric boundary cells, including BVC, border

cells and vector trace cells, have been recorded mostly from dorsal Sub and parahippocampal areas. These cells encode distance and direction from boundaries, that is an allocentric vector, and are the focus of this Section.

Egocentric boundary cells (EBC) have been mostly recorded in parahippocampal/retrosplenial/parietal areas. Briefly, cells encode distance and direction of prominent environmental cues or boundaries in relation to the animal's heading direction. In this sense, both allocentric and egocentric vectorial receptive fields anchor to the animal, but only egocentric ones also rotate with the animal's head. This is why border/BVC typically respond to one or two of the box's walls, whereas EBC respond to all walls indiscriminately (Bicanski and Burgess, 2020). Cues encoded by EBC are, for example, boundaries in RSC (Alexander et al., 2020a; van Wijngaarden et al., 2020), PoS (Peyrache et al., 2017), PaS, MEC, postrhinal cortex (POR, Gofman et al., 2019), secondary motor cortex, posterior parietal cortex (PPC, Alexander et al., 2020a), dorsomedial striatum (Hinman et al., 2019), the arena's centre in POR (LaChance et al., 2019), objects in the lateral entorhinal cortex (Wang et al., 2018), visual landmarks and a moving visual target in PPC (Wilber et al., 2014; Alexander et al., 2020b).

1.2.4.1 Allocentric boundary cells

The existence of a BVC type was predicted from recordings of place cells in boxes of various shape and size (Muller and Kubie, 1987) showing that, despite a shift in place field locations and sizes, fields always maintained a constant distance from the two nearest adjacent walls. Moreover, recordings of place cells in a stretched rectangular environment (O'Keefe and Burgess, 1996) revealed that place fields stretched and a small subgroup developed a second field. This evidence has led to computational models stating that place field sizes and locations are determined primarily by the intersection of linear distance inputs from the two nearest boundaries (O'Keefe and Burgess, 1996). To account for the source of geometric inputs to place cells, Burgess et al. (2000) and Hartley et al. (2000) outlined a "boundary vector cell model", in which place cells receive inputs from a hypothetical cell type, the BVC (Figure 1.5), and the thresholded sum of activity of BVCs with different allocentric boundary preferences can model place field characteristics and explain effects of geometric changes (Hartley et al., 2000; Burgess et al., 2000).

Barry et al. (2006) simulated BVC activity, and generated a number of predictions to test the validity of the BVC model to explain place cell responses. The

first prediction was that BVC receptive fields would expand along the entire length of a boundary. Second, the insertion of a barrier would cause a BVC to develop a new field along the barrier. For place cells, fields tend to occur more often along the environment walls (Hartley et al., 2000) and barrier insertion leads to either place field deletion, doubling or addition along the barrier, without affecting periphery fields (Muller and Kubie, 1987). The third prediction was that BVC fields should stretch during environmental extension, similar to place fields. The fourth prediction was that BVC should be active in all environments and preserve the same boundary preference across differently shaped environments. Finally, BVC should fire maximally when a boundary is at a preferred allocentric distance and direction from the animal, in all allocentric directions, given that place cell activity does not show directional selectivity in the open field.

Barry et al. (2006) and Lever et al. (2009) provided the first recordings of the predicted BVC type from the dorsal Sub of the hippocampal formation. Cells met the functional requirements of the BVC model. Unlike place cells, showing strong remapping in different environments, BVC were found to retain the same boundary preference irrespective of shape and visual appearance of the environment, and after wall removal, ruling out a purely visual basis for BVC firing. Firing was solely dependent on the animal's position relative to boundaries, independently of the animal's allocentric heading direction. Finally, cells did not only signal perimeter walls but boundaries more generally, as field doubling occurred after barrier insertion in the box (Figure 1.5).

Subsequent experiments uncovered a second type of allocentric vector-based representation, the border cell, recorded from all layers of MEC and other parahippocampal areas, namely PrS/PaS (Solstad et al., 2008; Savelli et al., 2008; Boccara et al., 2010). Like BVC, cells encoded boundaries in all allocentric directions, their receptive fields stretched with environment extension and boundary tuning was maintained across different environments. However, border cells reacted more variably to barriers insertion, with only a subgroup demonstrating field doubling. Border and BVC can be primarily distinguished based on the range of encoded distances. BVC signal both proximal and distant boundaries, with preference for proximal compared to distant ones, and receptive field size increasing with tuning distance. Border cells signal only proximal boundaries that need to physically block the animal's path. BVC respond to both external barriers as well as external cues that are traversable, like gaps or objects (Bicanski and Burgess, 2020).

A third type of allocentric vectorial representation has been recently discovered in the dorsal Sub, the vector trace cell. Cells fire maximally when the animal is at a specific allocentric distance and direction from external cues, including boundaries, much like BVC. However, they immediately generate a new vectorial field when a new cue is encountered, and maintain this field also after cue removal for up to 3 hours, thus generating a vector-based memory trace (Poulter et al., 2021). Vector trace cells and BVC with non-trace properties form distinct subpopulations within the Sub, being more common in distal vs proximal Sub, and showing preference for distal vs proximal cues (Poulter et al., 2021). Trace properties have been suggested to arise from feedback projections from place cells to BVC. BVC could be reactivated in the post-cue trial via pattern completion in the hippocampus, whereby the same spatial firing pattern is reactivated in the presence of incomplete sensory cues caused by activity only in a subset of place cells (Bicanski and Burgess, 2020).

In the Sub, the existence of BVC and vector trace cells, recorded alongside a large population of place cells with sparse locational fields, emphasizes the importance of these cells for anchoring place fields to the geometric reference. However, since the Sub does not project directly to CA1 (Witter and Moser, 2006), border cells in parahippocampal areas, rather than the Sub, could also supply a direct geometric input to hippocampus (Solstad et al., 2008). This information can be mediated by MEC projections to CA1. The respective contribution of different allocentric boundary cell types to localize allocentric position in the hippocampus remains to be investigated.

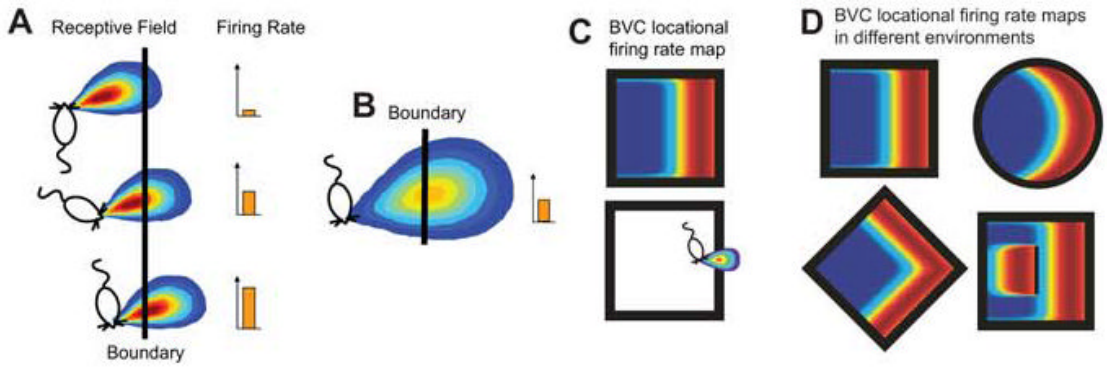


Figure 1.5: **Boundary vector cell (BVC) model.** A BVC responds maximally when a boundary is at a preferred distance and allocentric direction from the animal, irrespective of its allocentric orientation. First reported by Barry et al. (2006). **(A)** The BVC cell shows preference for proximal wall to the east of the rat. **(B)** The BVC shows preference for more distal wall to the east, and so the receptive field is broader.

(C) For cell (A), this results in the east wall falling inside the receptive field of the cell, as shown in the ratemap at the top. **(D)** Receptive field of the cell (A) across different environments. Boundary distance and direction preference is maintained, but barrier insertion causes field doubling. BVC model: summing BVC responses explains the characteristics of place fields and remapping in different environments. Taken from Lever et al. (2009).

1.2.5 How do the spatial systems interact?

From the above discussion, it can be speculated that grid cell networks interact with place cells by supplying path integration inputs to the hippocampus, while boundary related cells (BVC or border cells) supply environmental information about geometric boundaries (Burgess and O'Keefe, 2011; Moser and Moser, 2008). In the hippocampus, the movement-based (idiothetic) representation of space derived from MEC becomes associated with information about landmarks or boundaries to specify place field locations, derived from HD and BVC, respectively. Anchoring of the grids to the environment's geometrical reference could then occur via feedback projections from hippocampus (McNaughton et al., 2006a; Moser and Moser, 2008).

In support of this model, Bonnevie et al. (2013) showed that muscimol inactivation of the hippocampus leads to a gradual loss of MEC grid field periodicity and a drift in the grid pattern, arguing in favor of models that require a hippocampal excitatory drive to anchor the grids (Moser and Moser, 2008). One interpretation is that associations between path-integration and environmental elements are stored in hippocampus and conveyed to the MEC via hippocampal back projections, to correct errors in the MEC path integration. On the other hand, grid cells are not necessary for place cell formation and to generate new spatial representations in response to geometric change, given that place cells keep firing at a specific location and remap in new environments after muscimol inactivation of the medial septum that abolishes theta oscillations and grid cells (Brandon et al., 2014). While grid cells alone are not necessary to drive place cell firing, they are nonetheless required to maintain a stable spatial pattern when animals have to rely exclusively on self-motion, as evidenced by the fact that excitotoxic MEC lesions do not abolish the spatial selectivity of CA1 place cells but impair firing stability only in darkness (Jacob et al., 2020).

HD cells interact with place and grid cell systems by supplying directional information to orient and maintain their field activity. Direct evidence is represented by the fact that place and grid firing fields are oriented relative to visual landmarks

(Knierim et al., 1998; Hafting et al., 2005) and place cells develop directional selectivity in linear tracks (McNaughton et al., 1983). The existence of conjunctive theta-by-grid-by-direction cells that co-localize with HD neurons in middle and deep layers of MEC (Boccara et al., 2010; Sargolini et al., 2006), is also consistent with this notion. Their directional modulation could be driven by projections from the subcortical HD network to MEC. HD cells co-localize with a vast population of conjunctive neurons also in other parahippocampal areas, namely theta-by-place-by-direction cells (Cacucci et al., 2004) and theta-by-border-by-HD cells (Peyrache et al., 2017), although a bias in the animal's position and orientation sampling due to the physical constrains of the box should be taken into account when evaluating conjunctive responses (Burgess et al., 2005; Cacucci et al., 2004). More indirect evidence comes from juxtacellular recording studies. HD cells in PrS layer III project directly to MEC layer III, which contains the largest proportion of grid cells within MEC (Preston-Ferrer et al., 2016). Through this projections the HD system could influence grid cells directly or be mediated by an intermediate layer of conjunctive directional neurons (Boccara et al., 2010; Sargolini et al., 2006).

It is clear from lesion and inactivation data that cells in higher cortical regions cannot normally express their spatial patterns in the absence of subcortical directional input. Specifically, temporary inactivation of the HD system via the AD leads to lowered grid cell number, widespread loss of grid-like firing as well as directional firing in MEC (Winter et al., 2015). Lesions and inactivation of ATN, including AD, produce a loss of all spatial activities recorded from the dorsal Sub, including HD, place and grid cells, while sparing CA1 place cells (Frost et al., 2021). Likewise, hippocampal place cells continue to fire in the same location after AD lesion, despite reduced locational information content and emergence of directional tuning (Calton et al., 2003). One interpretation is that subcortical HD cell discharge is necessary for the maintenance and function of spatial neurons outside of hippocampus, including place and grid cells, but not in hippocampus proper. In contrast to the effects of AD damage, damage to cortical HD circuit components like the PoS only produce a loss of visual landmark control of hippocampal place cells, which start to shift randomly rather than following landmark rotations (Calton et al., 2003). This effect is only mild after AD damage, suggesting that landmark information conveyed directly from PoS/RSC, rather than from subcortical HD components, provides environmental anchoring of place cells.

1.3 Principles of head direction processing

The previous Section summarised the large body of experimental work, derived from neurophysiological experiments, available to explain how local sensory cues from different modalities are combined by spatially-modulated neurons through numerous interrelated subcortical and cortical structures. The advantage of combining these different sources of information is that the spatial pattern is maintained across different environments and persists in the absence of sensory cues from the environment.

We now focus on the HD cell system. Since HD cells were discovered in the PoS (Taube et al., 1990a), a vast body of work has focused on elucidating the characteristics of these cells, how they respond to various sensory inputs and the network that generates the HD signal. We have already covered their relevant properties. In this Section, we will first review attractor network models that have been proposed in the literature to simulate HD cell activity, and explain how the HD signal is generated. We will then discuss how this network integrates visual and idiothetic cues so that the neuronal compass always maps a single, well-defined direction, to enable HD system functioning. Discussion is made in relation to what is known about the neural pathway that comprises the HD system.

1.3.1 Ring attractor model of HD cells

How are HD cells generated and how do they develop their specific response properties? Theoretical models of HD cells typically locate them in a hypothetical one-dimensional ring with continuous attractor network properties (Figure 1.6). Each cell is active only at a narrow range of directions (90°) (Taube, 1995). As in a compass, all heading directions in the horizontal plane are homogeneously distributed, since the HD cell population as a whole covers the entire 360° range and cells are arranged in the ring according to their PFDs: neighbouring cells have similar PFDs, distant ones encode more distant directions (Skaggs et al., 1995; Zhang, 1996; Redish et al., 1996). Here, we note salient features of these models.

Connectivity in the ring is organized so that each cell forms excitatory connections with all other cells, whose strength decreases with distance between PFDs, and forms inhibitory connections only with distant cells. Given this connectivity, neighboring cells with similar PFDs are mutually excited and are activated

simultaneously, while distant cells with different PFDs inhibit each other. This combination of local excitation and global lateral inhibition gives rise to continuous attractor dynamics (Zhang, 1996), ensuring that only one cell is activated at any given time i.e., the neuronal compass always points toward one direction. Activity is maintained as a single localized "packet", represented by a Gaussian distribution, consistent with the Gaussian-shaped activity profile of individual HD cells. The activity packet is shifted without deformation as the animal turns its head and can stabilize at any one position along the ring, corresponding to the specific direction being faced by the animal. The existence of an internally organized HD cell attractor is evidenced by the sequential activation of HD cells as the animal turns its head, which persists in mice during sleep (Peyrache et al., 2015) and in rats after vestibular damage (Stackman and Taube, 1997; Muir et al., 2009; Yoder and Taube, 2009) or before eye opening (Tan et al., 2015), despite the absence of stable directional signalling and landmark stabilization. The fact that PFDs always remain "in register" during landmark rotations is also consistent with attractor dynamics (Taube et al., 1990b).

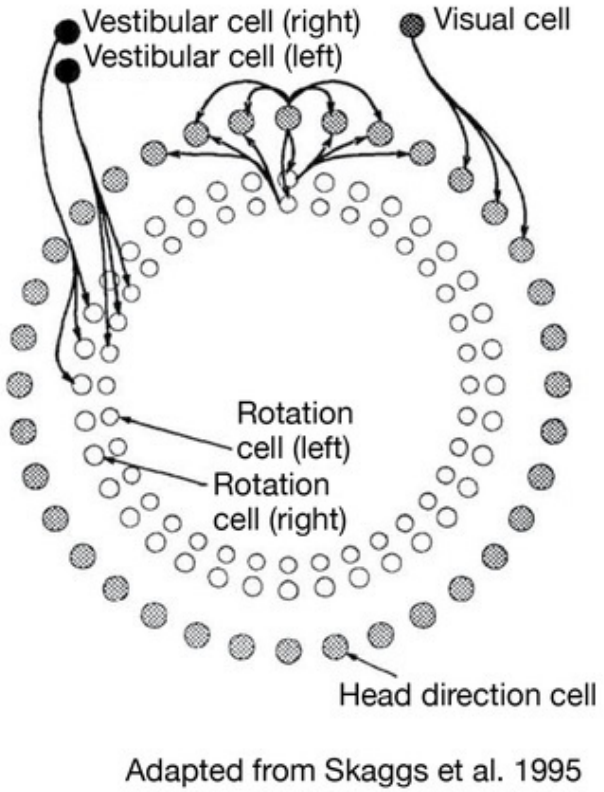


Figure 1.6: **Schematics of continuous attractor ring dynamics.** HD cells are arranged in a ring structure set up by strong local excitatory connections and weak global lateral inhibition. There are two additional rings (inner empty dots) of rotation

cells that receive inputs from vestibular cells (i.e., angular head velocity; AHV) and from the HD ring (outer black dots). As the animal turns its head, these cells receive clockwise (CW) and counterclockwise (CCW) velocity signals and project to the right and to the left of HD cells, respectively. Visual cells project to HD cells and can rotate activity along the ring to reset drifting. Synaptic weights of vestibular and visual inputs are adjusted via Hebbian plasticity to determine their relative influence on HD cells. Adapted from Skaggs et al. (1995).

1.3.2 Neural mechanisms of cue integration by HD cells

To encode global orientation, the neural compass requires not only an intrinsic ring architecture, but also it needs to receive sensory signals generated by movements and landmarks corresponding to stable cues in a familiar environment (McNaughton et al., 1991). Whereas an interconnected network structure (attractor ring) is required to generate the HD profile defined by a unitary, localized Gaussian peak, the strength of excitation and inhibition is calibrated by vestibular inputs carrying AHV information during head movements (McNaughton et al., 1991), as well as visual inputs carrying landmark information (Skaggs et al., 1995). Then, through experience-dependent learning, the weights of these different inputs (synaptic weights) converging onto the ring are modulated and control network activity (Knierim et al., 1995; Jeffery et al., 2016).

The system is initially set up by idiothetic inputs, provided by two additional rings of clockwise (CW) and counterclockwise (CCW) "rotation cells" (McNaughton et al., 1991; Skaggs et al., 1995). Each ring of rotation cells receives AHV inputs from upstream vestibular cells (i.e., AHV cells) about CW and CCW head movements, respectively. Rotation cells are simultaneously sensitive to HD and AHV. Connectivity is organized so that there are one-to-one projections from the HD ring to rotation cells, based on similarity between their PFDs. Feedback projections from rotation cells are asymmetric, meaning that rotation cells receiving the CW input project to the right of the HD cells, and those receiving the CCW input project to the left of the HD cells. This allows the activity packet to be rotated by upstream rotation cells in the same direction as the turning movement, and stabilize at a specific direction when rotation stops. Cells that encode HD, AHV, and a conjunction of the two have been mostly recorded from brainstem areas, namely DTN and LMN (Sharp et al., 2001), and in lower proportions in AD and PoS Taube and Muller (1998). Reciprocal inhibitory and excitatory connections between DTN-LMN are considered to provide

the reciprocal excitation and lateral inhibition required to set up global attractor dynamics for HD signal generation (Yoder and Taube, 2014).

To address the issue of drifting along the ring, models rely on a stable mapping system between HD cells and learned visual inputs (from cells in visual cortices) (Skaggs et al., 1995). Visual inputs are assumed to be distal. As mentioned before, distal cues mask the need to correct parallax errors derived from the simple association between proximal external and idiothetic cues (Gallistel, 1990; Bicanski and Burgess, 2016). Hebbian plasticity in the efferent inputs to the ring (i.e., visual and iditoehtic) allows asymmetric reweighing of these different inputs, so that the final activity packet, modeled by a Gaussian distribution, stabilizes in a position that reflects the weighted average of these inputs (Knierim et al., 1995; Jeffery et al., 2016). Landmark anchoring occurs when a visual input to the ring is consistently associated with a single HD cell, representing directional information derived from idiothetic inputs. This consistency between externally- and internally-derived orientations allows the network to develop stable firing associations between simultaneously active presynaptic and postsynaptic cells. When these connections are strengthened by long-term potentiation (LTP), rotation of the visual landmark will cause an equal shift of the activity packet, reflecting the new orientation of the animal. If on the other hand the visual input is associated to a different HD each time the visual input is activated, for instance in the presence of drastically unstable visual cues or after disorientation of the animal, repeated mismatches lead to weakening of connections and the system cannot learn stable firing associations (Jeffery et al., 2016). Longer-term plasticity in the efferent inputs implement experience-dependent re-weighting of visual cues (Jeffery et al., 2016), explaining why familiar landmarks previously experienced as invariant exert a stronger positioning effect during later rotations (McNaughton et al., 1995; Knight et al., 2014). Vice versa, disconnecting unstable landmarks from the network might require long-term depression (LTD) (Knierim et al., 1995; Jeffery et al., 2016). These re-weighting mechanisms are thought to occur in RSC/PoS (Page and Jeffery, 2018), where visual landmarks gain control of the HD signal (Yoder et al., 2015, 2011b). This is evidenced by the presence of visually driven HD cells whose synaptic plasticity with the main HD ring mediates integration of visual landmarks into the allocentric HD signal(Zhang et al., 2021). Interconnected cortical structures relay landmark information to other HD components and downstream spatial networks. The HD pathway is described in the next Chapter and is summarized in Figure 1.7. Attractor models described here represent a useful theoretical framework to model HD system structure and biological

properties, and successfully capture the the dual nature of spatial multisensory integration, in which simultaneous anchoring to stable landmarks and filtering of unstable ones occur, allowing animals to only use reliable landmarks for navigation.

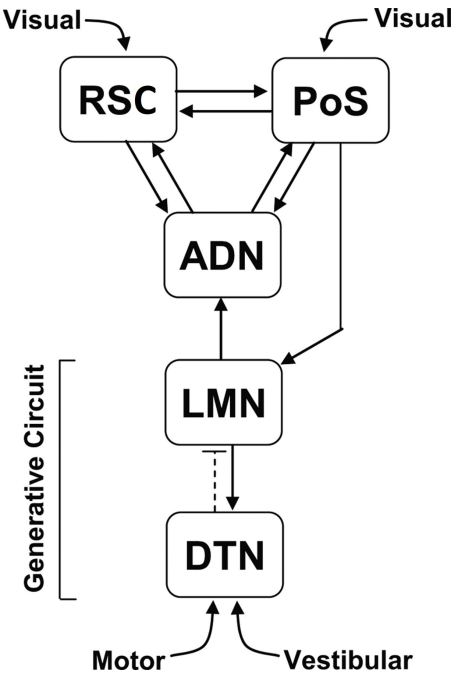


Figure 1.7: **Simplified diagram of the head direction (HD) circuit.** HD cells in dorsal tegmental nucleus (DTN) and lateral mammillary nucleus (LMN) receive inputs from vestibular and proprioceptive/self-motion systems. HD signal is generated within the DTN-LMN loop and is then conveyed to anterodorsal thalamic nucleus (AD), then to cortex. In retrosplenial cortex (RSC) and postsubiculum (PoS), the signal becomes associated with visual information from visual cortices. The integrated HD signal is transmitted via feedback projections to the subcortical HD attractor and to medial entorhinal cortex (MEC). Note that HD cells have been reported in medial mammillary nucleus (MMN) (Sharp and Turner-Williams, 2005). Solid lines are excitatory connections, dashed lines are inhibitory connections. Adapted from Clark et al. (2010). Note that the focus of this thesis is RSC in Experiment 1, and anteroventral thalamic nucleus (AV; not shown as it is not part of the main HD circuit) in Experiments 2-3.

1.4 Theta Oscillations, navigation and memory

In rodents, highly coherent oscillations at theta frequency range (Type-1 theta, 6-12Hz) appear in the hippocampus when it is actively supporting spatial exploration (Buzsáki, 2002). Theta activity is strongly associated with locomotion and voluntary

movements, even in tasks with no specific memory requirement, such as random foraging in the open field (Vanderwolf, 1969). Theta power and frequency positively correlate with the animal's running speed (McFarland et al., 1975; Richard et al., 2013; Belchior et al., 2014; Dillingham et al., 2019) and decrease with familiarization with a novel environment (Young and McNaughton, 2009; Sambeth et al., 2009). These correlations indicate that theta is behaviourally important, highlighting the importance of studying its function.

In species other than rodents, hippocampal theta oscillations have been described during a range of active behaviours that supposedly involve mnemonic processing. These include real-world navigation in non-human primates (Stewart and Fox, 1991), and real-world (M. Aghajan et al., 2017; Bohbot et al., 2017) and virtual navigation (Caplan et al., 2001, 2003; Bohbot et al., 2017) as well as working memory tasks (Addante et al., 2011) in humans. In bats, MEC and hippocampus show a much less less robust LFP theta (Yartsev et al., 2011; Yartsev and Ulanovsky, 2013; Ulanovsky and Moss, 2007), raising questions on whether theta could be crucial for spatial cognition in all mammalian species. In humans, LFP theta frequency is slower (4-8Hz) than in rodents due to the lack of actual movement during virtual tasks (Bohbot et al., 2017). Likewise, in rodents a lower frequency theta component (Type-2 theta, 4–6Hz) can be seen during periods of immobility in the presence of arousing stimuli (Vanderwolf, 1969), during rapid eye movement (REM) sleep (Bassant and Poindessous-Jazat, 2001; Buzsáki, 2002), and during sensory stimulation (tail pinch) under urethane-anesthesia (Kocsis et al., 2001; Vertes et al., 2001; Albo et al., 2003).

In the rodent hippocampal system, studying the temporal relationships between neuronal spiking and LFP signals by multi-electrode extracellular recordings has revealed another important relationship between spatial navigation and the LFP pattern, beyond that with movements. Individual neurons that underlie spatial mapping functions, including place and grid cells, fire in a way that is highly correlated with theta oscillations. Given this, theta is at the base of several theories of hippocampal functions (Buzsáki and Moser, 2013; Burgess et al., 2002, 2007; Buzsáki, 2002, 2005; Hasselmo et al., 2002; Hasselmo, 2005).

1.4.1 Functional significance of theta oscillations for learning and memory processes

The notion that theta supports learning has been extensively investigated by single unit recordings in rodents. In the rodent hippocampus, it has been shown that

(1) tetanic burst stimulation delivered at peaks or troughs of CA1 theta oscillations preferentially induces opposite signs of synaptic plasticity, LTP and LTD, respectively, both *in-vitro* and *in-vivo*, in urethane anesthetized and freely moving animals (Hyman et al., 2003; Hölscher et al., 1997; Huerta and Lisman, 1995; Pavlides et al., 1988); (2) stimulation delivered in the presence of theta oscillations more effectively potentiates population responses (Huerta and Lisman, 1996, 1993); (3) LTP is more efficiently induced with burst stimulation delivered at theta frequency compared to the same stimulation at other frequencies (Greenstein et al., 1988; Larson et al., 1986; Larson and Lynch, 1986; Larson and Munkácsy, 2015). A current hypothesis is that, during theta oscillations, synapses are "in a state of heightened plasticity" (Huerta and Lisman, 1993), with peaks and troughs corresponding to phasic changes in the magnitude of synaptic potentiation.

Behavioural effects associated with the presence or blockade of hippocampal theta also imply a role of theta in information processing by the hippocampus. For example, in humans, hippocampal theta power during a virtual spatial memory task correlates with maze difficulty (Caplan et al., 2001). There is also emerging evidence that theta activity correlates with performance during non-spatial memory, given that theta power before stimulus presentation predicts whether the stimulus will be successfully remembered in the recall phase of a working memory task (Addante et al., 2011). Similar findings in rats are that place-based, but not cue-based, learning in the Morris water maze modifies and increases hippocampal theta power (Olvera-Cortés et al., 2002). Furthermore, lesions (Mitchell et al., 1982; Borst et al., 1987; Winson, 1978) and inactivation (Mizumori et al., 1990; Jeffery et al., 1995; McNaughton et al., 2006b) of the medial septum impair learning in a range of spatial memory tasks, and disrupt theta oscillations and theta rhythmic unit activity in hippocampus and MEC. Similar to the effects of medial septum lesions, damage to the fornix also abolishes theta oscillations and theta rhythmicity in hippocampus (Buzsáki et al., 1983).

A groundbreaking discovery is the fact that theta rhythmicity actively enhances memory in rats. Particularly, when medial septum is inactivated with tetracaine, which blocks the sodium channels, hippocampal theta rhythm and spatial memory in the Morris water maze are restored by electrical stimulation of the fornix at theta frequencies (McNaughton et al., 2006b). More recently, Barnett et al. (2021) showed that theta-burst optogenetic stimulation (8.5Hz) of glutamatergic neurons in the AV restores spatial working memory in the radial maze after mammillothalamic tract lesions. These findings provide clear evidence that theta supports hippocampal functions and shine light on the neuronal pathways that influence hippocampal

theta. As we will discuss in the next Chapter (Section 2.3.3.4), it is well accepted that hippocampal theta is under complex control of several structures, including medial septum via the fornix (Unal et al., 2015; Hangya et al., 2009) and brainstem regions via the mammillothalamic tract (Vertes and Kocsis, 1997), although how this interaction occurs remains poorly understood.

Inhibition of inhibitory neurons in the medial septum not only abolishes the hippocampal theta output and spatial memory, suggesting a functional link between the two, but also disrupts MEC grid cells (Koenig et al., 2011; Brandon et al., 2011). Although theta may be required for periodic spatial firing (Burgess et al., 2007), it may not be necessary for the generation and function of other spatial neurons with single-field activity, given that medial septum inactivation that compromises MEC grid cells does not affect spatial selectivity of BVC and directional tuning of HD cells (Koenig et al., 2011; Brandon et al., 2011). Likewise, hippocampal place cells keep firing at a specific location and remap in new environments in the absence of LFP oscillatory activity (Koenig et al., 2011; Brandon et al., 2014). Nevertheless, there is evidence, discussed next, that synaptic plasticity occurs between sequentially-activated hippocampal place cells during individual theta cycles (O'Keefe and Recce, 1993; Skaggs et al., 1996; Mehta et al., 2002), and theta has been used by computational models to explain how place cells encode spatial location.

1.4.2 Single neurons relationship to theta oscillations and representation of space

Across the hippocampal system, individual neurons display the same intrinsic frequency as the LFP pattern (rhythmic firing) and maintain fixed spike time-theta phase relationships (phase locking), suggesting that LFP oscillations arise from the combined, synchronized activity of functionally-related neurons (Fox et al., 1986; Climer et al., 2015; Csicsvari et al., 1999). For each neuron, spikes are not distributed uniformly across the theta cycle but preferentially occur at a specific phase of the cycle, known as the preferred theta phase (O'Keefe and Recce, 1993). Based on these observations, there are multiple ways in which theta oscillations could influence learning and computations by the hippocampus, and they are the focus of the present Section.

The first group of theories states that theta coordinates information flow in the hippocampus via spike time-theta phase relationships between neurons

(Alexander et al., 2018; Mizuseki et al., 2009; Hasselmo et al., 2002). Theta cycles could provide temporal windows for timing neuronal activities and allow theta-rhythmic oscillatory interactions between brain regions that contain cells locked to this rhythm. For example, theta-paced information transfer occurs between individual neurons in RSC and hippocampus, since they fire phase locked to a common CA1 theta phase (Young and McNaughton, 2009; Alexander et al., 2018). Another example is the fact that grid cells in MEC layers II and III, projecting mostly to dentate gyrus-CA3 and CA1, respectively, preferentially fire at peaks and troughs of local LFP theta, respectively. Their phase preference is opposite to that of their respective target neurons in hippocampus (Mizuseki et al., 2009), and such phase offset across brain regions could allow for local computation to occur before information is passed to the next processing stage.

In addition to coordinating the timing of neuronal spiking and inter-regional communication, a second group of theories emphasizes a role of theta in encoding spatial location. In this respect, place cells not only carry spatial information in their firing rate (rate coding) but also in the timing of spikes relative to phase of oscillations (phase coding) (Mehta et al., 2002; Bush et al., 2022). A cell fires only when the animal enters its place field and spikes occur at progressively earlier phases during successive theta cycles as the field is traversed, so that there is a negative correlation between location of the animal inside the place field and firing phase (phase precession) (Skaggs et al., 1996; O'Keefe and Recce, 1993). Because phase precession is coordinated among cells, it leads to "theta sequences" of place cell firing at the network level. During the course of a single theta cycle, cells fire sequentially according to the behavioural order of their firing fields, and this encodes sequential information. Because of phase precession, population activity of place cells provides an estimate of location and distance traveled through the place field that is additional to the rate code (O'Keefe and Recce, 1993). Phase precession also appears in recordings of MEC grid cells (Hafting et al., 2008).

Theta phase at which cells fire influences synaptic plasticity: when two place cells fire sequentially at similar locations because they have adjacent firing fields, phase precession enables them to also fire at similar phases of the theta cycle, and in turn become functionally linked via Hebbian plasticity (O'Keefe and Recce, 1993; Mehta et al., 2002). This leads to offline replay of place cell firing during periods of quiescent waking and sleep, associated to the emergence of high-frequency sharp-wave ripple events in the hippocampal LFP (SWR; 150-250Hz). Sequential re-activation of place cell firing, due to plasticity between co-active cells during

navigation, could consolidate recently encoded spatial information (Skaggs and McNaughton, 1996; Bush et al., 2022).

Consistent with the notion that theta phase regulates hippocampal plasticity (Hölscher et al., 1997; Hyman et al., 2003), a third hypothesized role for theta is to separate encoding and retrieval phases of episodic and spatial memories at different phases (Hasselmo et al., 2002; Douchamps et al., 2013; Hyman et al., 2003). Because MEC and CA3 neurons fire maximally at peaks and troughs of CA1 theta, respectively, the strength of their relative inputs onto CA1 at different times has been hypothesized to drive encoding and retrieval in CA1 pyramidal layer at theta peaks and troughs, respectively (Hasselmo et al., 2002), corresponding to the arrival of inputs from MEC and CA3, respectively (Fernández-Ruiz et al., 2017). According to Hasselmo et al. (2002), at CA1 theta peaks (encoding phase), excitatory synapses from MEC show strong transmission, whereas synaptic transmission arising from CA3 is weak, but LTP preferentially occurs in these synapses. Strong transmission from MEC optimizes encoding of new information derived from the external environment without interference from information retrieved from memory (CA3 input). At CA1 theta troughs (retrieval phase), MEC is relatively weak and CA3 input is strong, but LTD preferentially occurs in these connections. Strong transmission from CA3 optimizes retrieval of previously learned information, while preventing further encoding of this information. The fact that CA3 synapses undergo depotentiation on opposite phases compared to the entorhinal input could result in the extinction of old information that is no longer present during encoding (Hasselmo et al., 2002; Douchamps et al., 2013). The notion that different learning stages need to be separated within each cycle is consistent with recordings of subicular vector trace cells (Poulter et al., 2021) that develop a new vectorial firing field in the presence of a new object (encoding) and spikes inside the field occur at earlier theta phases compared to post-cue trials (retrieval). A similar temporal segregation of neuronal computations by theta could also occur across cycles, rather than within. One example is the simultaneous recording of place and HD cell assemblies that represent different spatial trajectories (Kay et al., 2020) and heading directions (Brandon et al., 2013) on opposite alternating cycles (theta skipping), pointing to theta cycles as temporal units of information.

1.5 Summary

Spatial behaviour recruits hippocampal circuits that operate in theta mode. Along this system, highly coherent LFP fluctuations at theta frequencies reflect widespread

coordination and interactions between individual neurons. Interfering with theta rhythms causes memory deficits, similar to hippocampal damage, implying a crucial role of theta in hippocampal-related processing. For reviews on theta functions in spatial navigation and memory see Buzsáki (2005, 2002); Buzsáki and Moser (2013).

2

Introduction part 2: Anterior thalamic-retrosplenial cortex pathways for memory

2.1 Introduction

ATN and RSC are fundamental components of the extended hippocampal circuit supporting learning and memory (Vann et al., 2009). As identified in rats, around this circuit, two important signals for spatial behaviour are propagated, HD and theta oscillations. The general consensus has been that different, parallel pathways ascending via the ATN provide the biological basis for the relay of HD information between AD and RSC (HD system), and theta information between AV and RSC (theta system). In this thesis, we will utilize a combination of electrophysiology and tracing techniques in rats to further study how theta and HD signals are encoded and integrated by neurons along the AV-RSC circuit (theta), whose electrophysiological properties and functional involvement in spatial cognition are relatively less well characterized in the rodent literature compared to the parallel AD-RSC circuit (HD). Before explaining our specific experimental aims and objectives, this Chapter is divided into two main parts. The first part provides an overview of the anatomy and connections of the RSC, its functional cell types, and the main theories on RSC functions in spatial cognition. The second part reviews anatomical, electrophysiological

and behavioural properties of the different ATN nuclei, AD, AV and anteromedial (AM), to discuss evidence for the existence of anatomically and functionally distinct thalamocortical pathways, AD-RSC and AV-RSC.

2.2 Retrosplenial cortex

Research into the neurobiological basis of learning and memory has shown that a widespread network of hippocampal-diencephalic regions is required for memory functions, with much of this evidence coming from lesion studies in humans and animals. Hippocampus, RSC and ATN are core brain areas within this extended network, given that damage to either of these regions can induce severe memory deficits associated with diencephalic amnesia (Perry et al., 2021; Mitchell et al., 2018; Mitchell and Dalrymple-Alford, 2005, 2006; Aggleton et al., 1996, 2016; Harding et al., 2000) and they are also linked to neurodegeneration in Alzheimer's disease (Braak and Braak, 1991; Raji et al., 2009).

Spatial memory is a prominent component of this system: selective RSC damage in humans or animals results in memory deficits and also spatial disorientation (Reed and Squire, 1997; Sutherland and Hoesing, 1993; Whishaw et al., 2001; Vann and Aggleton, 2002, 2004; Pothuizen et al., 2008, 2009, 2010; Buckley and Mitchell, 2016; Cooper and Mizumori, 1999; Cooper et al., 2001). Human functional imaging studies provide further evidence of the spatial functions attributed to the RSC (Maguire, 2001; Auger et al., 2012). Moreover, ATN damage (Sutherland and Rodriguez, 1989; Aggleton et al., 1996; Mitchell and Dalrymple-Alford, 2005, 2006; Perry et al., 2018; Barnett et al., 2021) impairs performance in a range of hippocampal-dependent spatial memory tests in rats. Not only are these behavioural tests sensitive to hippocampal lesions, but also to RSC-ATN and RSC-hippocampus disconnections in contralateral hemispheres, suggesting the conjoint importance of these sites to support spatial memory (Sutherland and Hoesing, 1993; Warburton et al., 2000, 2001). In agreement with behavioural data, ATN damage in rats disrupts neuronal activation in limbic structures that are involved in spatial memory: bilateral and unilateral ATN damage reduce the expression of functional gene markers c-fos and zif268 in RSC (Perry et al., 2018; Jenkins et al., 2002b,a), and zif268 in hippocampal CA1 (Perry et al., 2018), to a greater extent than mammillothalamic tract damage (Perry et al., 2018). This suggests that ATN lesion deficits are due to a loss of direct connections of ATN with hippocampal/retrosplenial areas, rather than ATN being

just a relay of mammillary inputs to these cortical structures. Marked decreases in the expression of phosphorylated cAMP response element-binding protein (pCREB) are also found after bilateral ATN lesions in granular RSC and hippocampus during spatial exploration of a new environment (Dumont et al., 2012), and in granular RSC, hippocampus and amygdala after completion of a contextual fear test (Dupire et al., 2013), reinforcing the notion of an extended hippocampal system in which ATN supports hippocampal functions.

The interdependent function of RSC and hippocampus in spatial memory is also consistent with neurophysiological data demonstrating strong oscillatory interactions between these regions during different phases of learning. Alexander et al. (2018) recorded LFPs from RSC and CA1 during track running in rats and observed strong coordination of neuronal oscillations during run and rest phases across three time frames (theta, gamma, sharp wave ripples). During run, RSC units are strongly phase-locked to hippocampal theta and local gamma oscillations, and the power of RSC gamma is phase-locked to hippocampal theta (phase-amplitude coupling), implying coordination of information transfer from hippocampus to RSC during memory encoding. During rest, sharp wave ripple events appear simultaneously in RSC and hippocampus, and this coincides with increased or decreased activation of RSC units, suggesting modulation of RSC activity by hippocampal sharp waves ripples during memory consolidation. In agreement, Opalka et al. (2020) combined electrophysiology and optogenetic in mice to show that pyramidal neurons in superficial layers of granular RSC display increased activation 100-500ms before the onset of hippocampal sharp wave ripples, while inhibitory interneurons are activated immediately after ripples, thereby inhibiting excitatory neurons. Similar results were reported using calcium imaging and optogentic in mice by Chambers et al. (2021), who showed that pyramidal neurons and inhibitory interneurons in superficial layers of granular RSC undergo a reduction in activity 1-2s before hippocampal ripples and this pre-ripples silence can be attributed to a reduction of excitatory thalamocortical inputs from ATN. From these results, hippocampus-RSC circuit synchronization appears to be important for memory, and ATN may have a regulatory role in hippocampus-RSC communication, one way being via reduced subcortical interference during memory consolidation.

The question that emerges now is how these different interconnected cortical and subcortical regions interact with one another to support spatial learning. To answer this question, it is first necessary to explore their anatomical interconnections. To this end, we now review anatomical studies that have described RSC anatomy and

connectivity to discuss how relevant connections enable RSC functions within the hippocampal-diencephalic memory network. A discussion on these RSC functions will follow.

2.2.1 Anatomy and connectivity of the two retrosplenial cortex subregions

In rodents, RSC is a multi-layered cortical region located along the midline of the posterior cingulate cortex. The cingulate cortex contains two major divisions: the anterior cingulate cortex comprises Brodmann areas 24 and 3, whereas the RSC comprises areas 29 and 30 — along with areas 23 and 31 in primates, referred to as posterior cingulate cortex (Vogt et al., 1987; Vogt and Miller, 1983; Bubb et al., 2017).

The RSC has two main subregions, granular (gRSC; Brodmann area 29) and dysgranular (dRSC; Brodmann area 30), resembling hippocampal and neocortical architecture, respectively. There is a progressively defined lamination moving from the four/five-layered granular subregion to a six-layered dysgranular subregion. In gRSC layer II, neurons are densely packed while dRSC has wider and poorly defined layers II-IV (van Groen and Wyss, 1992). gRSC is located more ventrally adjacent to the Sub, while dRSC occupies a more dorsal position, laterally adjacent to visual cortices. Some researchers further divided gRSC into two subregions, granular a cortex and granular b cortex, based on connectivity differences (van Groen and Wyss, 1990b,c; Van Groen and Wyss, 2003). For simplicity, this thesis only considers the anatomical division of RSC into granular and dysgranular.

While RSC has critical connections with three main areas, the hippocampal formation, ATN, and visuospatial neocortical areas, these connections are not equally shared between the two RSC subregions (van Groen and Wyss, 1990b,c, 1992; Vogt and Miller, 1983; Sugar et al., 2011; Vogt et al., 1987). gRSC connectivity is strongly coupled with subcortical regions of the HD system and with hippocampal formation that are involved in spatial navigation and memory processes. dRSC connectivity is strongly coupled with visual regions. The considerations on RSC anatomy (reported below and summarized in Figure 2.1) portray RSC as a multimodal region for the integration of idiothetic and external information, which is also part of both the HD and theta systems. We will now review these different patterns of connections to discuss how gRSC and dRSC map onto different aspects of information processing. For more detailed reviews see Mitchell et al. (2018) and Sugar et al. (2011).

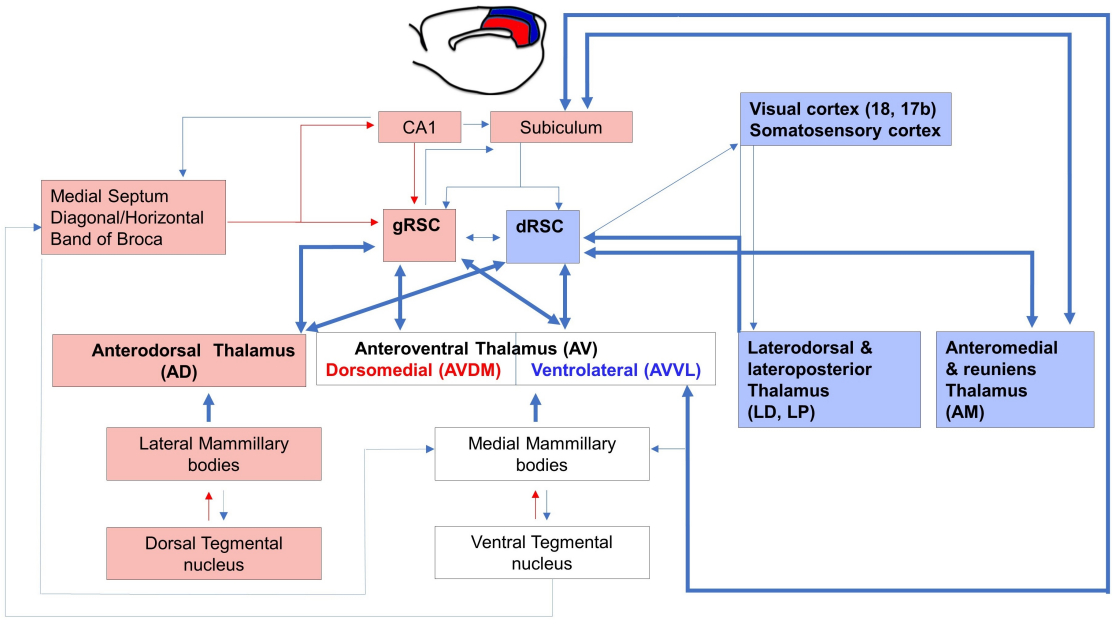


Figure 2.1: **Schematic diagram of the main cortical and subcortical connections of the retrosplenial cortex in rats.** A feature of the retrosplenial cortex (RSC) is its connectivity with hippocampal formation, anterior thalamus and neocortex. RSC is situated at the interface between the brain's navigational (via gRSC) and perceptual (via dRSC) systems, mediating between the two via intrinsic gRSC-dRSC interconnections. In the figure, arrows denote anatomical connections. Thick arrows are thalamic connections, thin arrows are other connections. Blue arrows are excitatory, red are inhibitory. A schematic of the rat's brain is at the top, illustrating the anatomical location of gRSC (red) vs dRSC (blue). The same colour scheme will be used to represent the two RSC subregions throughout this thesis. Note than AD and AV provide the neural substrate for the exchange of head direction and theta information to RSC (mostly gRSC), respectively.

2.2.1.1 RSC-(para)hippocampal connections

RSC has extensive reciprocal connections with all parahippocampal regions, namely PrS, PoS, PaS, MEC and POR (Shibata, 1994; Jones and Witter, 2007; van Groen and Wyss, 1990b, 1992; Van Groen and Wyss, 2003; Vogt and Miller, 1983; van Wijngaarden et al., 2020; Czajkowski et al., 2013). RSC projections to parahippocampal regions follow a topographic organization, in which neurons along RSC rostro-caudal axis terminate along the septo-temporal axis (Sugar et al., 2011). All regions of the parahippocampal cortex reciprocate inputs from dRSC, while only PrS and MEC project back to gRSC, with a similar topographic organization.

Compared to dRSC, gRSC connectivity is more strongly coupled with regions of the the hippocampal formation that are involved in spatial navigation and memory processes. gRSC layers II-III receive direct inputs from the dorsal hippocampus, primarily from Sub (Yamawaki et al., 2019; van Groen and Wyss, 1992; Opalka et al., 2020), and secondarily from CA1 (Shibata et al., 2009; van Groen and Wyss, 1990b), both glutamatergic (Haugland et al., 2019; van Groen and Wyss, 1990b) and GABAergic Opalka et al. (2020); Jinno et al. (2007); Yamawaki et al. (2019); Unal et al. (2015). These projections follow a similar topographic organization to parahippocampal ones, with distal Sub targeting the caudal gRSC, and proximal Sub targeting the rostral gRSC (Sugar et al., 2011). In contrast, dRSC layer I-II only receives a very sparse input from Sub and no direct CA1 input (van Groen and Wyss, 1990b; Vogt and Miller, 1983; Witter et al., 1990). Anatomical evidence is consistent with single-cell recordings from Opalka et al. (2020), showing that optogenetic stimulation of dorsal hippocampal projections into superficial layers of gRSC activates inhibitory neurons and, as a result, inhibits excitatory neurons (Opalka et al., 2020).

2.2.1.2 RSC-neocortical connections

RSC is reciprocally interconnected with several neocortical sensory, cognitive and motor areas, including prefrontal (Shibata et al., 2004), auditory (Vogt and Miller, 1983), PPC (Olsen et al., 2017)) and secondary motor cortex (Yamawaki et al., 2016). Instead of the strong hippocampal inputs, dRSC connectivity is more strongly dominated by visual inputs, given that only dRSC receives monosynaptic inputs directly from primary/secondary visual cortices in the occipital lobe (Brodmann areas 17 and 18a/b) as well as from somatosensory cortex in the parietal lobe. Only dRSC reciprocates the visual cortex projections to area 18b, which primarily terminate in layer I (van Groen and Wyss, 1990b, 1992; Van Groen and Wyss, 2003; Vogt and Miller, 1983).

2.2.1.3 RSC-thalamic connections

The main subcortical connections of RSC are with ATN (van Groen and Wyss, 1990b, 1992). ATN is subdivided into three nuclei, AD, AV and AM, based on anatomical and cytoarchitectonic properties (Jankowski et al., 2013), and each of these nuclei has a distinct pattern of connectivity with each of the two RSC subregions. However overall, both AV and AD appear to have a stronger relationship with gRSC compared to dRSC

(mostly gRSCb; van Groen and Wyss, 1990c; Van Groen and Wyss, 2003; van Groen and Wyss, 1992; Shibata, 1993b; Mathiasen et al., 2017; Witter et al., 1990). AM displays a unique pattern of connectivity that is not shared by other ATN nuclei, since it has only sparse interconnections with dRSC (Shibata, 1994; van Groen and Wyss, 1992). While the majority (56%) of AD neurons are HD cells (Taube, 1995), the majority of AV neurons (approximately 75%) have firing entrained by the theta oscillations (Vertes et al., 2001; Albo et al., 2003), suggesting that AD and AV provide the principal source of HD and theta information entering gRSC, respectively. In contrast, AM contains only small numbers of HD and theta cells, and instead contains neurons encoding the animal's spatial location, including place and border cells (Jankowski et al., 2015; Shibata, 1994; van Groen and Wyss, 1992).

Instead of the extensive ATN inputs, dRSC is characterized by stronger subcortical inputs from two visual thalamic nuclei, namely laterodorsal (LD) and lateroposterior nuclei (LP, or pulvinar in primates), with only few LD terminals additionally observed in gRSC (Buckwalter et al., 2008). dRSC, and to a lesser extent gRSC, reciprocates the LD input. Both LD, involved in visual landmark processing (Mizumori and Williams, 1993), and LP, supporting visual attention, receive direct inputs from primary visual cortex (area 17), and thus provide an additional route for visual inputs to reach dRSC. dRSC additionally receives a sparse input from the NRe of the thalamus (Shibata, 1994; van Groen and Wyss, 1992). Other minor connections shared by both RSC subregions are with the claustrum, locus coeruleus, reticular, mediodorsal (MD) and intralaminar thalamic nuclei (Buckwalter et al., 2008; Vantomme et al., 2020).

2.2.1.4 RSC-basal forebrain connections

gRSC receives extensive inputs from basal forebrain structures that are involved in the generation of hippocampal theta, namely the medial septum and diagonal and horizontal band of Broca (Unal et al., 2015; Van Groen and Wyss, 2003). Across limbic regions, theta oscillations are clearly present in the LFP and are believed to reflect the relaying of information (and perhaps timing) related to hippocampal function (Burgess et al., 2002; Buzsáki, 2002, 2005). Rhythmic disinhibition from the medial septum is thought to pace hippocampal theta activity (Hangya et al., 2009) and could similarly drive theta oscillatory activities in gRSC, given that GABAergic neurons in medial septum and diagonal band expressing theta-rhythmic firing project to both gRSC and hippocampal CA1, with an overall similar projection pattern (Unal et al.,

2015, 2018; Viney et al., 2018). In both structures, neurons selectively target, and rhythmically inhibit, GABAergic interneurons, resulting in a rhythmic disinhibition of the principal neurons, whose activity can become theta-synchronized and phase-locked to septo-hippocampal theta. Moreover, hippocampal inputs co-localize with ATN inputs in superficial gRSC layers, targeting pyramidal neurons that are required for spatial functions (Yamawaki et al., 2019; Brennan et al., 2020, 2021), in agreement with a role of ATN in optimizing hippocampal-RSC plasticity, discussed above (Chambers et al., 2021; Opalka et al., 2020).

Theta oscillations are distinguishing features of brain regions that are linked to the hippocampal spatial system. This notion, together with reviewed anatomical evidence (summarized in Figure 2.1), makes the picture of RSC as mediating between two different systems in the brain. Processing of visual landmarks and the local visual scene mainly occurs via connections between dRSC and sensory cortices, whereas connections between gRSC, ATN and the hippocampal formation mainly ensure the exchange of internally-generated spatial information between these regions. Integration of these two information streams, landmark processing and processing of HD/theta self-motion cues, is made possible by the extensive interconnections between the two RSC subregions (Shibata et al., 2009).

The notion of a visual/external and a self-motion/internal stream interacting within the RSC, while also being kept largely separate in the brain, provides the background for conducting Experiment 1, presented in Chapter 4 of this thesis and recently published (Lomi et al., 2021). We investigated differences in theta-modulation between RSC subregions to provide support for the notion that the anatomical segregation of gRSC and dRSC is related to differences in their involvement in hippocampal functions. Another crucial question relates to which RSC inputs, other than the septo-hippocampal ones, could explain the observed differences in theta coding between the two RSC subregions. The AV is a possible candidate, given the large concentration of neurons entrained by theta oscillation and its differential inputs to the two RSC subregions (Lomi et al., 2021). This hypothesis provided the motivation for then conducting AV recordings in Experiments 2 and 3, presented in Chapters 5 to 7 of this thesis. Chapter 8 is the General Discussion and brings together RSC and AV results from all the experiments.

2.2.2 Functional and electrophysiological properties of retrosplenial cortex for spatial navigation

We now discuss theories on RSC functions, with a focus on its role in spatial navigation. These functions can be grouped as: cognitive mapping (via gRSC-hippocampal connectivity), visual landmark integration (via dRSC-sensory cortex connectivity), directional processing (via AD-gRSC connectivity) and spatial coordinate transformations (via gRSC-hippocampal and dRSC-parietal cortex connectivity).

2.2.2.1 Cognitive mapping

RSC plays a crucial role in the updating and retrieval of stored spatial knowledge for goal-directed navigation. Patai et al. (2019) found that RSC was selectively active during navigation towards goal locations, tracking the distance to the goal, in familiar but not recently learned environments. This is consistent with other fMRI studies that have reported increased RSC activation during acquisition of spatial knowledge about an environment (Auger et al., 2012, 2015; Auger and Maguire, 2018) and with lesion studies in rats. Generally, when tested in spatial memory tasks, RSC lesions do not abolish memory of external information, but rather the ability to coordinate information available to the animal and stored mnemonic representations of the environment. For example, bilateral RSC lesions (Vann and Aggleton, 2002; Whishaw et al., 2001), as well as RSC-anterior thalamus and RSC-hippocampus disconnections (Sutherland and Hoesing, 1993), impair spatial working memory performance in the Morris water maze. Completion of this task requires integration of currently available sensory cues with memory of landmarks that were available in the learning trials. Other studies reported overall milder impairments after inactivation or bilateral lesions of RSC in radial (Cooper and Mizumori, 2001; Pothuizen et al., 2008; Vann and Aggleton, 2004) and T-maze tasks (Pothuizen et al., 2008), which can be successfully completed using a single spatial strategy (visual or self-motion cues). Deficits in these tasks become more evident when rats are required to rely on path integration during task performance in darkness (Cooper and Mizumori, 2001; Pothuizen et al., 2008; Vann and Aggleton, 2005; Nelson et al., 2015), given that path integration involves tracking translational and rotational movements, and forming association with landmark-based memory (Cooper et al., 2001). Interestingly, hippocampal place fields remapping in the radial maze occurs in both light and dark trials after RSC temporary inactivation, irrespective of behavioural impairments (only present in

dark testing) (Cooper and Mizumori, 2001). Place field instability suggests that RSC may supply mnemonic information about the environment to the hippocampus, for updating place fields and facilitating path integration. Other studies observed that learning impairments in radial and T-maze tasks are unmasked following bilateral RSC lesions when intra- and extra-maze cues are placed in conflict by rotating the maze mid-trial, despite spared sequential alternation behaviour (Pothuizen et al., 2008, 2010; Nelson et al., 2015; Vann and Aggleton, 2005). Similarly to testing in darkness, during maze rotation successful performance relies on prior experience of external cues to disregard unstable intra-maze ones and switch to an alternative directional reference. Likewise, RSC lesion impairments emerge in rats performing a place avoidance task only when useful and misleading sensory information need to be segregated in order for one of them to be ignored (Wesierska et al., 2009). These behavioural observations are also consistent with reports in primates of impaired retrieval of positional information for objects after RSC damage despite spared anterograde memory (Buckley and Mitchell, 2016).

The notion that RSC contributes to navigation and hippocampal spatial processing receives additional support from neurophysiological studies in rodents. RSC neurons exhibit directionally selective firing and place fields, and many RSC neurons respond to complex combinations of location, heading direction and head movements (Cho and Sharp, 2001; Chen et al., 1994a; Lozano et al., 2017). A calcium imaging study by Mao et al. (2018) recorded place cells with highly selective firing fields in superficial layers of dRSC in head fixed mice running on a treadmill. Place fields only developed after repeated experience of the linear track environment and were partially impaired by bilateral (but not unilateral) dorsal hippocampus lesions. During unrestrained navigation, although RSC encodes spatial location, it seems to generate more complex spatial representations that may be useful for goal-directed navigation and planning. Miller et al. (2019) showed that spatial representations gradually developed in the RSC of rats over the course of learning a T-maze task, including information about spatial location, trajectory to the reward location and future reward locations. Their emergence coincided with the time at which neurotoxic (NMDA) lesions of the RSC caused deficits in alternation task performance. This is coherent with the numerous reports of route-centric RSC representations. For example, neurons representing specific sequences of turns forming a trajectory on a w-shaped track (Alexander and Nitz, 2015) and neurons with spatially-periodic, sparse place fields either across the full route of a plus maze, or that repeated across sub-routes of the maze (Alexander and Nitz, 2017). These complex representations

could code self-position within a route and sub-routes. Full-route periodicity could also provide a metric for signalling distance of each route position to all others, given that their activation pattern was continuous and cyclic across the whole track, reinforcing the notion of RSC in storing spatial relations for cognitive mapping (Alexander and Nitz, 2017).

2.2.2.2 Visual landmark integration

The notion that RSC is important for the experience-dependent integration of mnemonic spatial information about the environment with currently experienced sensory cues is consistent with a specific involvement of RSC in landmark learning. Landmark learning is achieved by integrating idiothetic and visual cues with knowledge about landmark stability, which can only be derived from prior experience of the landmark in time (Cooper et al., 2001; Knierim et al., 1995; Page and Jeffery, 2018). Visual landmarks correct spatial computations derived from movement and are important for HD and place cell orientation (Burgess and O'Keefe, 2011).

A special role of RSC in relating visual landmark and idiothetic information was first suggested by clinical human studies of amnesic cases. As these studies show, lesions comprising Brodmann's area 30 (dRSC) lead to impairments in locating landmark positions on a map, impairments in using familiar landmarks for orientation (Takahashi et al., 1997; Suzuki et al., 1998), as well as reports of disorientation in highly familiar environments (Maguire, 2001). Since then, several imaging studies in humans and behavioural studies in humans and rats have demonstrated a functional link between RSC and landmark computations for goal directed behaviour. In humans, RSC is preferentially activated during virtual navigation when viewing permanent features of the environment rather than temporary objects, which would be less useful for orientation behaviour (Auger et al., 2012; Auger and Maguire, 2013). Rats with bilateral RSC lesions are impaired in flexibly using visual cues for place discrimination (Hindley et al., 2014; Vann and Aggleton, 2005), and are unable to use distal visual cues to discriminate two opposing room views (Hindley et al., 2014).

Although RSC as a whole plays a role in landmark processing, it is believed that visual landmark information first reaches dRSC, and is then routed to gRSC and to subcortical areas of the HD circuit, whereas internal/mnemonic information derived from subcortical/hippocampal networks mostly reaches gRSC. This notion comes from a combination of anatomical and behavioural studies that considered

RSC subregions in separation. Selective damage to dRSC is not sufficient to induce learning impairments in the radial maze, but rats solve the task by using a simple motor-turn strategy instead of relying on visual landmarks (Vann and Aggleton, 2005). Selective gRSC and complete RSC lesions equally disrupt learning in the radial maze, and lead to milder spatial alternation impairments in the T-maze (Pothuizen et al., 2010). However, when the use of intra-maze cues is prevented by using two different T-mazes between learn and test trials, gRSC lesions result in larger impairments than complete lesion, likely due to an over-reliance on visual landmarks represented in dRSC, which are particularly misleading for spatial alternation learning (Pothuizen et al., 2010). In contrast, selective gRSCb lesions are sufficient to impair spatial learning in the water maze (van Groen et al., 2004). To complement behavioural data, genetic evidence revealed increased expression of immediate early gene c-fos in dRSC during a spatial working memory task in the light, but not when the same task was performed in darkness (Pothuizen et al., 2009).

At the neuronal level, both single-cell and 2-photon calcium imaging experiments from RSC have reported a variety of visually-driven responses. In mice, these include neurons responsive to visual inputs (Vedder et al., 2017; Powell et al., 2020; Murakami et al., 2015), landmarks (Fischer et al., 2020), and a minority of landmark-encoding neurons modulated by spatial location (Mao et al., 2020). Landmark-related activation, predominantly observed in dRSC (Fischer et al., 2020), is driven by a combination of external and idiothetic information, rather than purely visual inputs. This is because activation was disrupted when visual and locomotion cues were uncoupled, or coupled in non-spatially-meaningful ways, during treadmill running in head-fixed mice (Mao et al., 2020; Fischer et al., 2020). When recorded in the same treadmill setup, excitatory pyramidal neurons in RSC of mice displayed supralinear integration of visual and locomotion signals, whereas inhibitory interneurons were more locomotion-modulated (Powell et al., 2020).

An influential study by Jacob et al. (2017) extended this idea by demonstrating a functional difference in the electrophysiological recordings between RSC subregions in freely-moving rats. While global HD cells encoding the animal's orientation were recorded in both gRSC and dRSC, a directional signal more sensitive to local visual landmarks was present only in dRSC (Jacob et al., 2017), suggesting that visual landmarks first gain access of the HD system via dRSC. These cells, later named multidirectional cells, exhibited a bimodal activity profile, firing at two opposite directions across two connected environments that presented identical cue-cards in opposite directions, and with distinct odor cues in each environment (environment

with 180° symmetry). See Figure 3.1 for an illustration of the two-compartment box (Jacob et al., 2017).

In a follow-up investigation, Zhang et al. (2021) recorded dRSC multidirectional cells in a range of more complex, visually-symmetric environments. Cells that expressed bidirectional tuning in the two-compartment box, expressed tetra-directional tuning in a four-compartment box and unidirectional tuning in the open field. Two types of multidirectional cells were observed. One showed multidirectional peaks, one per compartment, the other showed multidirectional peaks also when restricted in a single compartment. Notably, multidirectional cells were solely found in dRSC, since gRSC, AD and PoS HD cells always remained unimodal. Authors speculated that HD cells primarily utilize vestibular inputs to maintain their globally stable directionality in environments that are visually conflicting, whereas multidirectional cells are more sensitive to visual inputs. Based on dRSC anatomy, multidirectional cells are likely to be HD cells with inputs from visual cortices stronger than the subcortical HD input, given that AD is primarily interconnected with gRSC (Page and Jeffery, 2018).

Based on these findings, modeling work on HD cells considered dRSC as the site of experience-dependent landmark integration (Yan et al., 2021; Page and Jeffery, 2018). Hebbian-dependent synaptic plasticity between global HD cells in RSC (derived from thalamic HD cells to gRSC) and multidirectional cells in dRSC (driven by visual inputs from cortex to dRSC) mediates landmark learning by enabling the system to develop strong links only with stable visual cues — when HD and bidirectional cells are consistently activated at the same direction. In turn, RSC HD cells send feedback projections to the subcortical attractor, allowing the integrated HD signal to be transferred to the rest of the circuitry to correct path integration computations (Yoder et al., 2011b). Since in the two-compartment box the animal is exposed to two landmarks, 180° apart, the same multidirectional cell (reversing PFD between compartments) becomes associated with two opposite HD cells, thereby preventing stable firing associations for learning of a landmark reference. Within-compartment multidirectionality can be explained as between-compartment multidirectional cells acquiring inputs from oppositely tuned HD cells in each compartment (Page and Jeffery, 2018). See related modeling work on multidirectional cells by Yan et al. (2021).

The existence of landmark-dominated HD cells was corroborated in other parahippocampal regions outside of the main HD generative circuit, in MEC/PaS (Kornienko et al., 2018; Brandon et al., 2013). When a visual cue was alternated

between two different walls of a square box, some HD cells displayed bidirectional tuning curves (Kornienko et al., 2018). The majority of these cells (63%) fired rhythmically at theta frequency (6-10Hz), the remaining showed no intrinsic spike rhythmicity. Most interestingly, visually-driven tuning curve changes induced by the landmark manipulation were strongest among the non-theta rhythmic HD cells, and these responses were often non-coherent between co-recorded cells (Kornienko et al., 2018). It is likely that non-theta rhythmic HD cells escaping attractor dynamics receive stronger visual input, directly or via dRSC, as compared to subcortical HD (AD) and theta (AV) inputs. In this respect, theta-modulation of MEC/PaS HD cells is not driven by the septo-hippocampal system, given that medial septum inactivation disrupts grid cells without affecting theta and HD properties of MEC/PaS HD cells (Brandon et al., 2013). The necessary source of HD and theta inputs is likely to be provided by different ATN efferents (AD and AV), directly or via gRSC (van Groen and Wyss, 1990b,c; Shibata, 1993a).

2.2.2.3 Head direction representations

It is now well established that AD and RSC (mostly via gRSC) form the canonical thalamocortical HD system for encoding global directional signals. Canonical HD cells are present in both gRSC and dRSC and arguably represent the most extensively investigated neurophysiological property of RSC in rodents. These cells, first described by Chen et al. (1994a), show unimodal directional tuning curves that anchor to local visual landmarks (Chen et al., 1994a; Lozano et al., 2017), like those originally reported in PoS (Taube et al., 1990b). The more highly variable responses of RSC HD cells to visual landmark rotations, some being visually controlled, other relying entirely on idiothetic cues, and the rest displaying combined responses with significant under-rotations, support the simultaneous processing of visual landmark and idiothetic information, discussed above (Chen et al., 1994b; Jacob et al., 2017). Cue integration is likely to be a key feature of directional coding in RSC, being achieved via synaptic interactions between canonical HD cells in RSC and inputs from neocortex via dRSC.

While canonical HD cells make up about 10% of RSC neural population (Chen et al., 1994b), most of the directional neurons exhibit more conjunctive profiles, as compared to subcortical HD components. Cho and Sharp (2001) recorded HD cells modulated by spatial location, that is, cells with distinct PFDs at different locations within the environment. Other studies reported HD cells that additionally encode

egocentric signals, namely head turning direction, head movements (speed and AHV; Lozano et al., 2017), distance and direction from boundaries (Alexander et al., 2020a), and the orientation of local visual landmarks (Jacob et al., 2017). In addition to HD neurons, RSC contains AHV cells whose firing depends on a combination of vestibular cues and optic flow, given that the reliability and strength of the AHV code improved when both inputs were provided during passive rotations of mice in the light, as compared to single cue conditions (Keshavarzi et al., 2021a). The overlap in RSC of HD and AHV cells presupposes an important function of RSC in orientation behaviour, and makes it crucial for future experiments to investigate whether RSC could generate and update the HD signal locally, or whether it requires subcortical vestibular inputs.

2.2.2.4 Spatial coordinate transformations

Extensive experimental and theoretical work suggests that successful navigation requires coordination of egocentric and allocentric spatial reference frames. This is because, for the cognitive map to be useful to guide behaviour, it needs to be anchored to the local visual scene (spatial layout or landmarks), which is perceived in viewpoint-dependent egocentric coordinates, while the hippocampal spatial code is allocentric, or viewpoint-independent (McNaughton et al., 1995; Byrne et al., 2007; Hinman et al., 2019). The importance of RSC in egocentric-allocentric spatial coordinate transformations was first suggested by its connectivity with parietal and hippocampal regions known to process both egocentric and allocentric elements of space, namely PPC (Wilber et al., 2014), POR (Jones and Witter, 2007; Olsen et al., 2017), and hippocampal formation (Lever et al., 2009; Boccara et al., 2010). Anatomy is consistent with reports from fMRi studies in humans that RSC, PPC and hippocampus become active together during tasks that require translation or switching between spatial coordinates, for example when participants make mnemonic associations between previously available visual landmarks experienced in a map-like representation of the environment, and self-motion cues derived from optic flow during first-person virtual navigation (Sherrill et al., 2013). RSC activity is also associated to tasks that require participants to re-orient in space from different imagined viewpoints (Epstein et al., 2017; Lambrey et al., 2008), and activity tracks distance to a goal location in familiar, but not new, environments (Patai et al., 2019). These tasks supposedly require switching between egocentrically perceived visual cues and the stored allocentric representation, but the latter is less available in newly learned environments.

At the single cell level, transforming the local visual scene into allocentric cognitive map representations that can be used for efficient navigation in complex environments is thought to require vectorial computations in relation to external cues (McNaughton et al., 1995; Byrne et al., 2007; Burgess et al., 2002). Models presuppose a spectrum of vectorial cell types (Barry et al., 2006; Peyrache et al., 2017; Hinman et al., 2019; Byrne et al., 2007; Gofman et al., 2019), including experimentally observed subicular/entorhinal BVC and border cells (allocentric), and parietal/retrosplenial/parahippocampal EBC (egocentric; see Section 1.2.4). In a similar way, theories on spatial coordinate transformations presuppose a third vectorial cell type that integrates egocentric and allocentric information, as found in several regions along the EBC network. These cells, termed conjunctive HD-EBC, encode egocentric boundaries but additionally show allocentric directional tuning, and serve as building blocks for transforming egocentric boundary information into allocentric representations that capture the spatial layout of complex environments. Many theoretical models show specifically how this can be applied to the formation of border/BVC (Figure 2.2; Gofman et al., 2019). Both EBC and conjunctive HD-EBC responses have been recorded in the rat dRSC (Alexander et al., 2020a). One experiment reported EBC in both gRSC and dRSC, whose response properties depended on intact MEC afferents (van Wijngaarden et al., 2020). However, these cells differed from classic EBC recorded from dRSC given that they encoded only proximal walls at a specific distance, but at all directions, from the animal, and only a subgroup developed egocentric directional preference toward the closest wall (van Wijngaarden et al., 2020). While we do not currently know whether egocentric boundary responses necessarily originate in RSC, the presence of these cells highlights a role of RSC in mediating at least some initial spatial translations. This framework is consistent with the notion that RSC acts as an integrator of allocentric spatial inputs (via AD-gRSC and hippocampus-gRSC) and incoming sensory information (via visual cortex-dRSC and parietal cortex-dRSC), which become related within dRSC. Further corroborating this function, single unit recordings from the RSC of rats in a w-shaped track revealed the presence in both RSC subregions of neurons signalling multiple forms of spatial information, allocentric, egocentric and route-centric (Alexander and Nitz, 2015). These cells encoded a conjunction of the animal's self-position within the environment, turn direction and the sequence of turn behaviours through a specific route.

From the discussed evidence, it is difficult to tell whether severe spatial learning impairments following RSC lesions in rats and humans stem from the

inability to integrate different sensory information, processing orientation or perform coordinate transformations. Furthermore, other studies revealed a role of the RSC for multimodal association among spatial and non-spatial information. For instance, electrolytic RSC lesions impairs contextual fear conditioning, which is a form of associative learning (Keene and Bucci, 2008), and RSC damage prevents the formation of associations between a tone and a visual cue presented simultaneously (Robinson et al., 2014) or in series (Robinson et al., 2011). We have reviewed anatomical, neurophysiological, and the main functional properties of RSC. We will now focus on the ATN, providing one of the main sources of thalamic afferents to RSC.

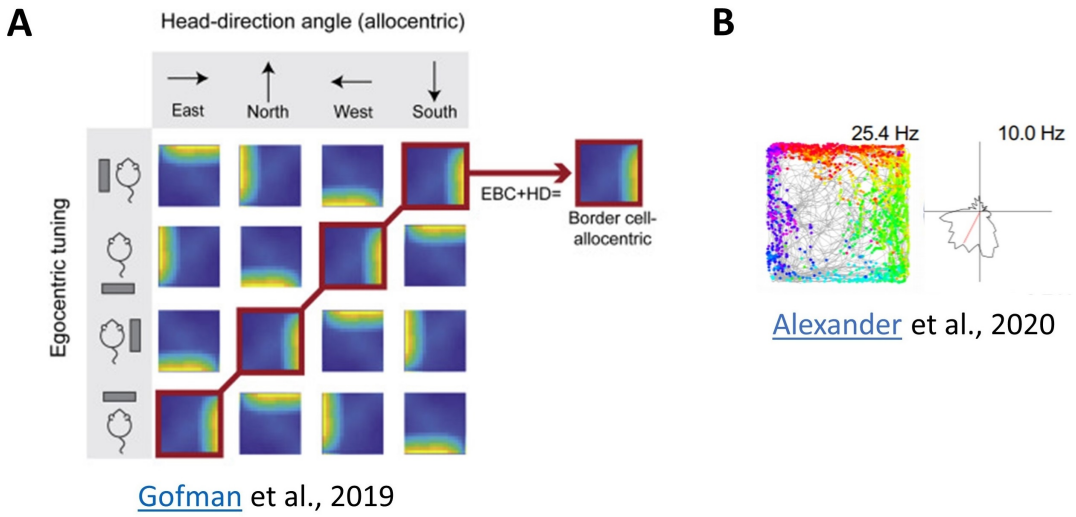


Figure 2.2: **Conjunctive EBC-HD cells used to explain the formation of allocentric boundary related cells.** **(A)** Border/BVC cells with no allocentric HD-component arise from the output of multiple conjunctive HD-EBC with different directional and egocentric properties. Conjunctive HD-EBC have egocentric vectorial receptive fields but additionally are modulated by allocentric HD. Row represent the egocentric tuning of these cells (each cell has firing fields when boundary is at a specific distance and direction relative to the animal's head direction). Columns represent the allocentric tuning of their HD component. Adapted from Gofman et al. (2019). **(B)** Example of conjunctive HD-EBC recorded from dRSC. Egocentric preference is for nearby boundaries to the left of the rat (spikemap, left). Allocentric directional preference is toward south west (polar plot of firing rate (Hz) vs head direction (degrees), right). Apated from Alexander et al. (2020a).

2.3 Anterior thalamic nuclei

The ATN is a diencephalic nucleus located in the rostral part of the dorsomedial thalamus. It comprises three main nuclei, AD, AV and AM, which can be identified based on their cytological properties in humans, whereby AD and AV contain densely-packed small cells, while AM cells are larger and more widely dispersed (Morel et al., 1997; Jankowski et al., 2013). In rodents and primates, a defining feature of ATN nuclei is their strong connections with RSC, hippocampal formation and mammillary bodies. It is assumed that these structures are part of an extended neuronal network for learning and memory, given that damage to either structure is consistently associated with anterograde amnesia in humans (Harding et al., 2000; Tsivilis et al., 2008). This proposal has received extensive support from lesion studies in rodents (Aggleton and Brown, 1999; Aggleton et al., 1996; Mitchell and Dalrymple-Alford, 2006; Perry et al., 2018; Vann, 2005). Although ATN nuclei are all connected to the same structures, they are connected to different subregions within those structures, supporting the idea of each nucleus being integrated into a different functional subcircuit, which underlies its differential contribution to learning and memory functions. These connections are summarized in the diagram of Figure 2.3 and are reviewed next.

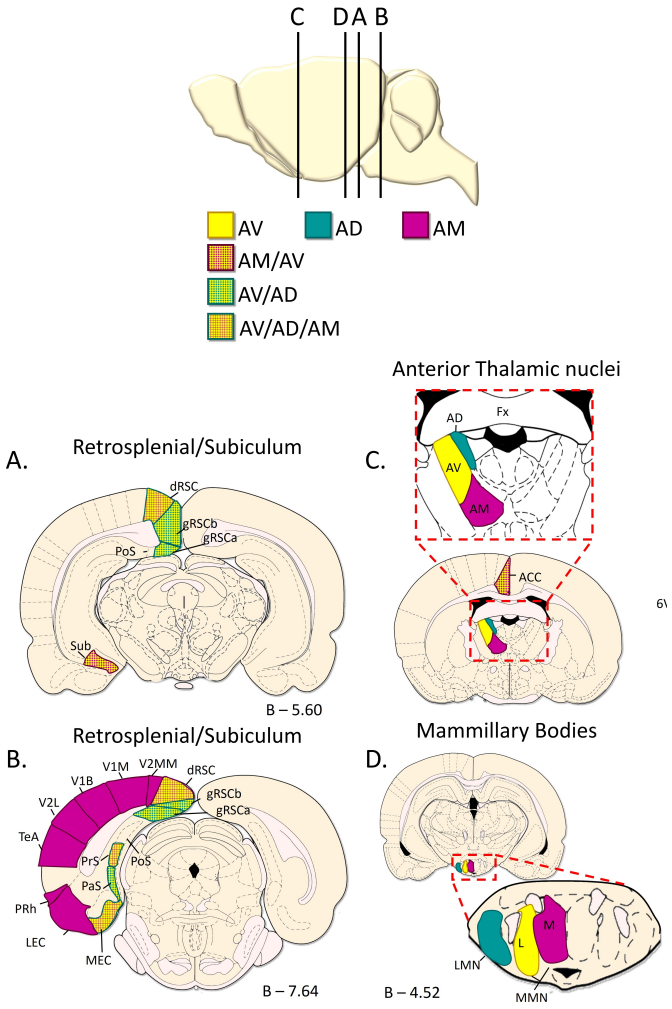


Figure 2.3: **Graphical representation of the main cortical and subcortical connections of the three ATN nuclei in rats.** The atlas plates have been adapted from Paxinos and Watson (2007) and the anterior-posterior (AP) coordinate given is relative to bregma. The approximate location of each coronal plate relative to each other is indicated in the sagittal plane in the top illustration. Anterodoral (AD), anteroventral (AV), anteromedial (AM) thalamic nuclei are colour-coded as indicated. **(A)** Connections with retrosplenial cortex and hippocampal formation. AD and AV are have extensive connections to both retrosplenial cortex subregions (gRSC; dRSC) and postsubiculum (PoS), whereas AM only sends a sparse input to dRSC. Only AM and AV are interconnected with subiculum (Sub). **(B)** AM has a distinctive profile of cortical connectivity that is not apparent for either the AV or AD. There are considerable connections between AM and visual (V1 and V2), temporal association (TeA) and parahippocampal cortices (Perirhinal (PrH) and lateral entorhinal (LEC). All three ATN nuclei connect to the medial entorhinal cortex (MEC). **(C)** There appears to be some overlap between AV and AM in the frontal pole and anterior cingulate cortex (ACC). **(D)** ATN nuclei have a distinctive profile of connectivity with the mammillary bodies. Lateral mammillary bodies (LMN) project to AD, while medial mammillary

bodies (MMN) medial and lateral parts (marked as M and L in figure) project to AM and AV, respectively. Adapted from Perry et al. (2021) (joint first author paper).

2.3.1 Anatomy and connectivity of the three anterior thalamic nuclei

In both rodents and macaque monkeys, hippocampal formation and mammillary bodies forms three different pathways with each of the ATN nuclei (Aggleton et al., 2010; Vann et al., 2007; Wright et al., 2010; Christiansen et al., 2016). These pathways follow the same, but parallel, organization, delineated as follows: hippocampal formation-tegmental nucleus of Gudden-mammillary bodies-ATN-retrosplenial/subicular/entorhinal cortices-hippocampal formation. Based on this parallel connectivity, (Aggleton and Brown, 1999) first advanced the idea of an "extended hippocampal-diencephalic network" for memory processing, having the ATN at its centre (Figure 2.4). To understand how different ATN nuclei work in concert with their different mammillary and hippocampal components to influence limbic system functions, we first need to consider their interconnections in finer details.

As reviewed by Aggleton et al. (2010), the three pathways linking hippocampal formation to ATN and mammillary bodies are highly segregated: different nuclei of the same structure project to each component of the respective downstream structure, reinforcing the notion that different pathways convey parallel information. The main subcortical input to ATN is from the mammillary bodies, via the mammillothalamic tract. In turn, mammillary bodies are in receipt of ascending projections from the tegmental nuclei of Gudden, via the tegmentomammillary tract. Mammillary bodies comprise a lateral (LMN) and a medial (MMN) mammillary nucleus, while the tegmental nuclei comprise a dorsal (DTN) and a ventral (VTN) tegmental nucleus. The LMN receives tegmental inputs mostly from DTN, and projects exclusively to AD. In contrast, MMN receives inputs only from VTN, with dorsal VTN projecting to the medial part of MMN (pars medialis centralis), and ventral VTN projects to the lateral part of MMN (pars medialis dorsalis and pars lateralis), in turn projecting to AM and AV, respectively (Seki and Zyo, 1984; Shibata, 1992). Within the MMN, projecting to AV, dorsal MMN projects predominantly to the medial AV division, while ventral MMN projects predominantly to the lateral AV division (Seki and Zyo, 1984), suggesting that a further functional division exists within the AV-mediated pathway i.e., medial vs lateral AV; commonly referred to as magnocellular and parvicellular AV subnuclei (Gabriel, 1993) or, as we will refer to them in this work, as dorsomedial

(AVDM) and ventrolateral (AVVL) AV subfields, following the rat atlas nomenclature (Paxinos and Watson, 2007).

Both mammillary bodies and ATN receive descending projections from parahippocampal-hippocampal areas, and display contrasting patterns of connectivity with these areas (van Strien et al., 2009; Seki and Zyo, 1984; Shibata, 1993a). Within the mammillary bodies, LMN receives descending projections mostly from PoS/PaS, while MMN receives projections mostly from PrS/Sub. The strongest connections of AV and AD are with PrS/PaS/PoS/MEC and with RSC (van Groen and Wyss, 1990b; Van Groen and Wyss, 1995; van Groen et al., 1999; Van Groen and Wyss, 2003). Most of these connections are reciprocal (Shibata and Naito, 2005). AM has only sparse reciprocal connections with RSC and PrS (van Groen et al., 1999; Shibata, 1993a), having more extensive connections with structures beyond the hippocampus instead. The strongest are with prefrontal areas, including anterior cingulate and prelimbic cortices, and visual cortex area 18b (van Groen et al., 1999).

Additionally, AV and AM are reciprocally connected with dorsal and ventral Sub (van Strien et al., 2009; Seki and Zyo, 1984; Shibata, 1993a) and MEC (van Groen and Wyss, 1990c; Wright et al., 2010; Shibata, 1993a), and receive projections from different cell populations within the Sub: proximal subicular axons terminate in AM, distal axons terminate in AV (Christiansen et al., 2016). ATN inputs to Sub follow a similar topographic organization, whereby AM and AV mostly target ventral and dorsal Sub, respectively. Likewise, subicular projections to ATN and mammillary bodies arise from different cell population within the Sub: pyramidal cells in deep layers project to ATN, while those projecting to mammillary bodies are more superficially placed within the Sub (Wright et al., 2010). The Sub is considered as the main hippocampal output structure, and so this organization, as well as collateral projections, could support the relay of different, parallel hippocampal information to mammillary bodies and ATN, as well as to different ATN nuclei (van Strien et al., 2009; Seki and Zyo, 1984; Shibata, 1993a).

Overall, the hippocampal formation, via the fornix, forms with ATN and mammillary bodies three interdependent circuits vital for diencephalic memory mechanisms, which explains why damage to any of these structures and to the fornix is associated to dense diencephalic amnesia (Tsivilis et al., 2008; Harding et al., 2000; Sutherland and Rodriguez, 1989; Gaffan et al., 1991).

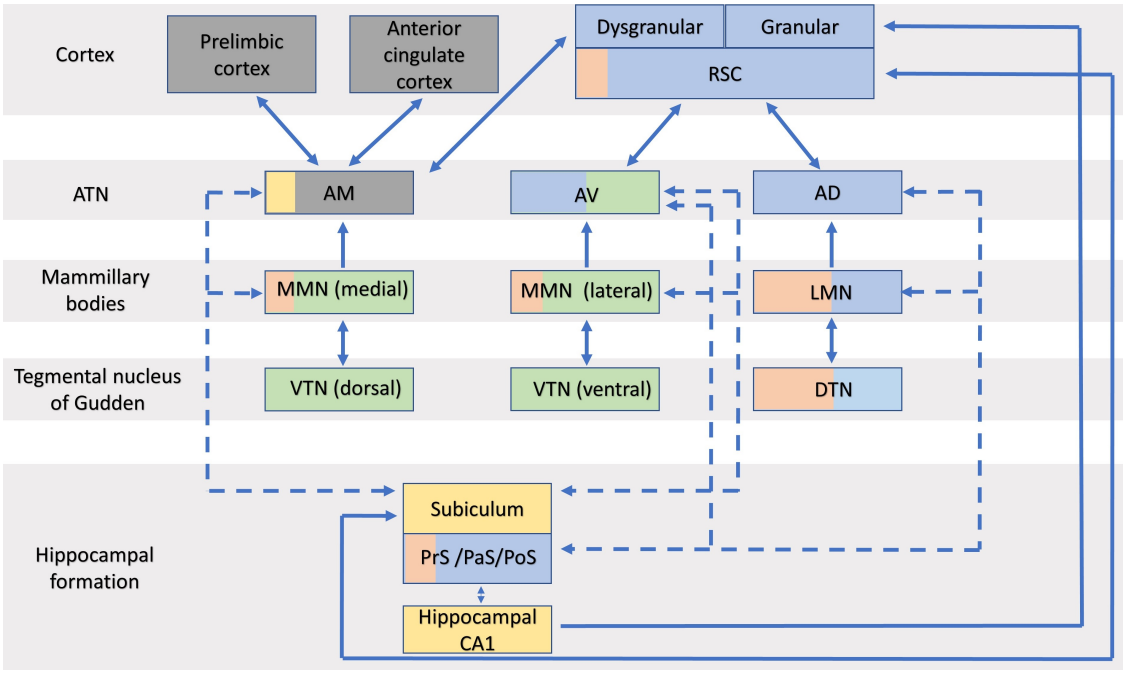


Figure 2.4: **Schematics of the "extended hippocampal-diencephalic system" for memory.** Proposed by Aggleton and Brown (1999). Three direct, parallel pathways link hippocampal formation to ATN and mammillary bodies, and contain different cell types: angular head velocity (AHV) cells (orange), HD cells (blue), theta-modulated cells (green), spatial cells including place and border cells (yellow). Arrows denote anatomical connections, dashed arrows are conveyed by the fornix. AD and AV mediate HD and theta signals to the hippocampal formation, respectively, while AM is more weakly interconnected with hippocampal formation. Putative HD circuit: DTN-LMN-AD-retrosplenial/subicular/entorhinal cortices. LMN-DTN loop forms the HD generative circuit, driven by inputs from vestibular nuclei. Theta circuit: VTN-MMN-AV-retrosplenial/subicular/entorhinal cortices. Not shown: AM-to-PrS projection and hippocampal-to-prelimbic/ACC.

2.3.2 Neurophysiological properties of anterior thalamic nuclei

Contrasting anatomical patterns of ATN nuclei also extend to their neurophysiological properties, described in the remaining parts of this Chapter. While the majority of cells in AD and AV are HD neurons (60-69%; Taube, 1995; Tsanov et al., 2011), AM contains only a marginal proportion of HD neurons (9.7%, Jankowski et al., 2015), recorded alongside small subsets of cells responsive to spatial location, namely place (6.2%) and border cells (0.5%), which have not so far been reported in other ATN nuclei (Jankowski et al., 2015). Despite high numbers of HD cells in AV, a fundamental property of this nucleus is the presence of neurons showing prominent rhythmic

activation at theta frequencies (6-12Hz), classified as slow- and fast-spiking theta-bursting neurons (75%; Tsanov et al., 2011, 2010; Welday et al., 2011; Vertes et al., 2001; Albo et al., 2003). Crucially, a subset (32%) of these theta-bursting cells additionally display a significant directionality (Tsanov et al., 2011). Much smaller proportions of cells modulated at theta frequencies have been reported in other ATN nuclei of anesthetized and freely-moving rats (6-10%; Albo et al., 2003; Vertes et al., 2001; Jankowski et al., 2015). The conclusion is that, subcortical inputs ascending to the hippocampus via AD and AV are predominantly HD and theta (or combined HD-theta) in nature, respectively.

2.3.3 Functions of the anterior thalamus in spatial navigation

Since the initial proposal of an "extended hippocampal-diencephalic network", several subsequent models have proposed that the three ATN nuclei, and their respective cortical and subcortical components, can be functionally dissociated, and form separate systems that differently contribute to limbic functions (Aggleton et al., 2010). AD encompasses the HD system conveying global directional inputs to hippocampal formation, whereas AV is part of a theta system that perpetuates theta activity to the hippocampal formation (Jankowski et al., 2013). AM mediates transfer of hippocampal-diencephalic information to prefrontal areas and contributes to other higher cognitive functions outside of the spatial domain (Perry and Mitchell, 2019; Aggleton et al., 2010).

In light of discussed anatomical and electrophysiological evidence, the two systems mediating HD (AD) and theta (AV) signals to hippocampus ascend along the following parallel projections (more lateral vs more medial), delineated as follows: tegmental nuclei of Gudden (dorsal vs ventral; DTN vs VTN) → mammillary bodies (lateral vs medial; LMN vs MMN) → anterior thalamic nuclei (dorsal vs ventral; AD vs AV) → retrosplenial/subicular/entorhinal cortices → hippocampus (Witter et al., 1990; Shibata, 1993b; Van Groen and Wyss, 1995). We will now dive further into the functional properties of these pathways and their neurophysiological outputs.

2.3.3.1 Head direction processing role of the AD circuit

By virtue of its anatomical and electrophysiological properties, the AD is part of an interconnected circuit for HD signal propagation, organized hierarchically along the

following projections: DTN-LMN-AD-RSC/PoS-MEC. This is known as the main HD system (Figure 1.7), given that all these structures contain neurons that discharge as a function of heading direction, AHV or a combination of the two (Taube, 1995; Lozano et al., 2017; Stackman and Taube, 1998; Bassett and Taube, 2001). Within this circuit, AD contains the largest proportion of HD cells (60%; Taube and Burton, 1995; Yoganarasimha et al., 2006.

As reviewed in the previous Chapter, spiking activity of HD cells is highly multimodal and depends on a multi-level convergence of external (visual) and idiothetic (self-motion and vestibular) information (Taube, 2007). Vestibular inputs carry information about AHV and are critical for HD signal generation (Stackman et al., 2002; Stackman and Taube, 1997), whereas landmark information and self-motion cues are important for updating it (Taube et al., 1990b; Knierim et al., 1995; McNaughton et al., 1991; Stackman et al., 2003; Zugaro et al., 2001). The importance of vestibular inputs for generating the HD signal is highlighted by the existence of AHV cells in brainstem vestibular nuclei, projecting to the HD network, as well as in DTN (75%; (Bassett and Taube, 2001)) and LMN (44%; (Stackman and Taube, 1998)). AHV signals are present at a smaller extent in RSC (Keshavarzi et al., 2021b). HD cells conjunctively modulated by AHV are present in DTN (Bassett and Taube, 2001; Sharp et al., 2001), LMN (Blair et al., 1999; Bassett and Taube, 2001), AD (Taube, 1995; Blair and Sharp, 1995), RSC (Lozano et al., 2017) and parahippocampal cortices (MEC/PaS/PoS; Spalla et al., 2021).

The notion of a hierarchical HD system first came from lesion studies in rodents, showing that disrupting lower circuit components abolishes HD cells at higher levels. Specifically, AD HD cells are abolished by bilateral, but not unilateral, lesions of LMN or DTN (Blair et al., 1998, 1999; Bassett et al., 2007). In animals with unilateral LMN lesions, AD HD cells persist but develop AHV-modulation, similar to HD cells normally seen in LMN (Blair et al., 1999). These results implicate a role of LMN in mediating AHV inputs, and a more indirect role (in conjunction with DTN) in establishing attractor dynamics for HD signal generation. AD lesions disrupt HD cells in cortical areas like PoS (Goodridge and Taube, 1997) and superficial MEC layers (Winter et al., 2015), but HD cells can still be recorded in AD and LMN after lesions of PoS (Goodridge and Taube, 1997) and RSC (Yoder et al., 2015). RSC and PoS lesions only impair landmark control and stability of HD cells in AD and LMN, suggesting a role in visual landmark integration (Clark et al., 2010; Yoder et al., 2011b, 2015). MEC sits at the top of the hierarchy and receives a highly integrated directional input from the ascending HD network, given that MEC lesions only mildly affect AD HD cells

and do not impact landmark processing nor angular path-integration of these cells (Clark and Taube, 2011). It follows that AHV information, representing the major input for driving HD cell orientation during path integration, is transmitted from the brainstem to subcortical HD components, whereas visual information, required to update HD cell orientation and correct path integration errors, is first associated with the HD signal in cortical regions, and is then transferred to subcortical HD components via corticothalamic pathways. See review by Yoder et al., 2011b.

A hierarchy of directional processing is also based on regional differences in HD cell anticipatory firing relative to the animal's heading direction (Blair et al., 1997, 1998; Stackman et al., 2003). Along the HD circuit, anticipatory firing is achieved through integration of information about the present heading direction and AHV inputs, and so it varies according to the direction in which vestibular inputs are propagated along the circuitry. Generally, subcortical HD cells (i.e., closer to vestibular inputs) tend to display longer anticipatory time intervals (ATI) compared to HD cells in cortical regions, receiving more indirect vestibular inputs (Stackman and Taube, 1998; Sharp et al., 2001). More specifically, LMN HD cells have broader tuning curves and larger ATIs of approximately 95ms (Stackman and Taube, 1998) or 40ms (Blair et al., 1998). The intervals reported in the AD are 49ms (Stackman et al., 2003) and 20ms Blair et al., 1998; Taube and Muller, 1998; Blair and Sharp, 1995; Blair et al., 1997), in the RSC they are 25ms (Cho and Sharp, 2001) and 48ms (Lozano et al., 2017)). PoS HD cells have slightly narrower tuning curves than RSC ones and encode more current or past heading direction, with intervals of about 15ms (Lozano et al., 2017) or 0ms (Blair and Sharp, 1995; Blair et al., 1997; Taube and Muller, 1998). The stepwise decrease in ATI values along the ascending HD system means that, as the animal turns its head, HD cells are updated first in the LMN, than 20ms later in the AD and RSC, and 20ms after that in PoS, where HD cells code for the instantaneous directional heading. Finally, bridging results from lesion studies and ATI analysis, prior work showed that RSC damage in rats not only impairs directional stability and weakens visual landmark control of AD HD cells, but also increases the time interval by which these cells anticipate the future heading direction (ATI between 40 and 75ms). This increase reflected an increased reliance on vestibular inputs due to disrupted integration of visual inputs via RSC (Clark et al., 2010). Indeed, directional stability was not impaired in a dual-chamber test, which tests path integration abilities (Clark et al., 2010).

2.3.3.2 Origin and propagation of the HD signal

How is HD cell activity generated and updated within this hierarchy? It is generally accepted that the HD generative network is anatomically localized within the excitatory-inhibitory connections between DTN and LMN, given that lesions to either structure abolishes AD HD cells (Blair et al., 1998, 1999; Bassett et al., 2007). This network depends on vestibular inputs derived from brainstem vestibular nuclei, namely nucleus prepositus hypoglossi (NPH) and medial vestibular nucleus (MVN), which in turn encode AHV signals derived primarily from horizontal semicircular canals in the inner ear. This is because, vestibular damage, in the form of neurotoxic lesions of the vestibular labyrinth in rats (Stackman and Taube, 1997) and semicircular canals occlusion in chichillas (Muir et al., 2009), abolishes HD cell activity in AD, but generates a pattern of bursting activity unrelated to heading direction. Similarly, a small number of bursting cells were identified in AD of transgenic mice with specifically disrupted otholith organ, but not in control mice Yoder and Taube (2009). HD neurons with unstable directionality could still be recorded in transgenic mice, suggesting that semicircular canals but not the otolith organ, both located in the vestibular labyrinth, are required for HD signal generation. Furthermore, AD HD cells become unstable after optogenetic inactivation of DTN-projecting neurons within the NPH (Butler et al., 2017). As mentioned before, LMN and/or DTN lesions abolish AD HD cells, while lesions to cortical HD components, namely RSC and PoS, only impair landmark control and stability of HD cells in AD and LMN.

The conclusion is that vestibular and landmark information flow in opposite direction along the HD circuit, and converge at each hierarchical level to establish a unitary directional peak (Figure 1.7). Vestibular information is propagated in an ascending manner, delineated as follows: information about head rotations in the horizontal plane arises mainly from semicircular canals, and then travels to MVN, then to NPH, and is then projected to DTN, which is reciprocally connected with LMN. The HD signal is generated within the LMN-DTN loop by integrating AHV inputs (Redish et al., 1996; Yoder and Taube, 2014), and is transferred to AD, and thence to cortical areas, mainly RSC/PoS, and finally MEC (Winter and Taube, 2014). Visual signals are propagated in a descending manner, delineated as follows: RSC/PoS receive projections directly from primary visual cortex (Vogt and Miller 1983; Van Groen and Wyss 1990) and are responsible for the integration of visual landmarks and their relay to MEC and other subcortical HD components, via return projections from RSC/PoS to AD, and from PoS to LMN (Huang et al., 2017; Yoder

et al., 2015; Allen and Hopkins, 1989; Shibata, 1989; van Groen and Wyss, 1990b). PoS projections to LMN and AD arise from segregated populations (layer IV bursting cells vs layer V-VI regular-spiking cells), allowing for convergent visual information to reach AD simultaneously, via a slower but direct PoS-AD and a faster but more indirect PoS-MMN-AD route (Huang et al., 2017)).

We end by noting that small proportions of HD cells have been reported in thalamic regions outside the generative circuitry of the attractor, that receive few, if any, tegmentomammillary directional inputs. These regions are the AV (69%; Tsanov et al., 2011; Yoganarasimha et al., 2006), AM (10%; Jankowski et al., 2015), LD (30%; Mizumori and Williams, 1993), and NRe (11%; Jankowski et al., 2014). Cells are likely to inherit directional modulation from the subcortical HD system via an indirect corticothalamic route, mediated by descending projections from RSC/PoS, although this theory remains to be verified by studies recording from these regions when the HD pathway is lost, or by comparing respective ATI values. Further considerations on the origin of the AV directional signal are presented below.

2.3.3.3 Theta propagation role of the AV circuit

Contrary to AD, AV receives massive projections from a more medial pathway to the HD one, ascending to hippocampus along the following projections: VTN-MMN-AV-RSC/PoS-MEC. Strong entrainment of unit activity by theta oscillations is seen at all levels of this circuitry, in VTN (Kocsis et al., 2001; Bassant and Poindessous-Jazat, 2001), MMN (Sharp and Turner-Williams, 2005) and AV (Vertes et al., 2001; Albo et al., 2003). By comparison, only small numbers of cells entrained by theta are found along the AD circuitry (Albo et al., 2003; Vertes et al., 2001), where units predominantly function as HD and AHV cells.

As discussed before in this thesis, theta propagation is considered to serve spatial and mnemonic functions of the limbic system by optimizing synaptic plasticity and inter-regional communication (Buzsáki and Moser, 2013; Burgess et al., 2002; Buzsáki, 2002, 2005). The presence of theta in the AV, together with its widespread direct and indirect interconnections with hippocampus, suggests a neuronal network crucial for spatial navigation and memory. One crucial hint for this function comes from Barnett et al. (2021), who showed that theta-burst optogenetic stimulation of AV glutamatergic neurons restores spatial working memory performance in rats after mammillothalamic tract lesions, and also increases theta activity and expression

of immediate early gene zif268 in gRSC and hippocampal formation during open field exploration. This provides clear evidence that theta activity driven from the AV nucleus actively supports hippocampal functions.

Initial experiments aimed at uncovering the functional properties of the AV axis recorded single-units from the VTN of urethane-anesthetized rats (Kocsis et al., 2001). LFP theta oscillations in VTN and hippocampal CA1, elicited by sensory stimulation (tail pinch), display high levels of coherence, but VTN theta precedes hippocampal theta by approximately 2s. During strong theta states, all VTN units switch from irregular discharge to rhythmic bursting coherent with hippocampal theta. These results were later confirmed by recordings in unanesthetized rats during wakefulness and REM sleep (Bassant and Poindessous-Jazat, 2001). VTN units show theta-bursting activity coherent with hippocampal theta, but switch to burst mode approximately 1-2s before the onset of hippocampal theta. Like in the VTN, almost all MMN units in awake and urethane-anesthetized rats synchronize their bursting activity in the theta range (Sharp and Turner-Williams, 2005). Theta oscillations simultaneously recorded from VTN, MMN and hippocampus (Bland et al., 1995; Kocsis and Vertes, 1994; Sharp and Turner-Williams, 2005), as well as from AV and hippocampus (Vertes et al., 2001; Tsanov et al., 2011, 2010), are always highly coherent with each other.

Only limited recordings have been conducted from AV so far. Initial experiments in urethane-anesthetized rats showed that up to 75% of AV cells discharge rhythmically and coherently with local and hippocampal CA1 theta, with a much smaller subset of these neurons reported in AD (12%) and AM (6%) (Vertes et al., 2001; Albo et al., 2003). These findings were confirmed also in unanesthetized rats during free exploration and naturally occurring sleep (Tsanov et al., 2010). By recording from the most medial part of AV using drivable microdrives similar to the ones used in this thesis, Tsanov and colleagues identified theta-bursting units (23.7%). Their rhythmic spike discharge directly contributes to the local LFP theta, given that theta spectral power depends on the proximity of these units to the LFP electrode within AV. Theta oscillations recorded simultaneously from hippocampal CA3 and AV display high levels of coherence in the 7-10Hz range, but AV theta precedes hippocampal theta by 7-10ms (Tsanov et al., 2011).

Despite initial recordings of HD cells in both AD and AV nuclei of the ATN (Taube, 1995; Yoganarasimha et al., 2006), Tsanov et al. (2011) provided the first, and to our knowledge the only, detailed investigation and quantification of a

directional signal in AV. By recording from the medial AV part, at the border with AD, Tsanov and colleagues found that 69% of the recorded units express a significant directionality, and 39% of these units display conjunctive theta- and HD-modulation (Theta-by-HD cells), discharging rhythmic spike trains at theta frequency at the PFD. Further evidence that theta and HD processing interact at the subcortical level comes from the existence of neurons with theta frequency-modulation that varies with the cosine of the animal's movement direction in dorsally-located ATN regions, including in AV (Welday et al., 2011). The convergence of theta-HD signals is a property that is missing theoretical understanding. One functional explanation is that theta-modulation via AV primes RSC HD cells (via AV-gRSC) to increase their responsiveness to AD-mediated directional information (via AD-gRSC) during locomotion (Vertes et al., 2001; Tsanov et al., 2011). Alternatively, Yan et al. (2021) proposed a model of landmark learning in dRSC whereby theta-modulation of HD cells from AV gates feedforward and feedback information transfer between visual and hippocampal cortices via dRSC, by firing on different phases. Other studies suggested that subcortical directional information may need to be transformed into a theta signal in order to be integrated and compared with entorhinal-hippocampal networks that contain theta-modulated spatial neurons (Cacucci et al., 2004).

Although directional information is represented in AV, both as a pure HD code and in conjunction with theta, there is no evidence of HD cells in MMN and VTN, situated upstream of AV. Within MMN however, about one third of the cells display conjunctive modulation by linear speed and AHV, and almost all the cells are modulated by theta (Sharp and Turner-Williams, 2005). This can be contrasted with the AHV signal recorded from LMN, which often occurs in conjunction with HD and is unrelated from theta (Stackman and Taube, 1998). Given that conjunctive HD-AHV cells are a prerequisite for driving and updating HD cells during head turns (Skaggs et al., 1995), questions remain on how AV could develop its directional profiles i.e., inherited from thalamo-cortico-thalamic pathways dependent on AD, or generated via mechanisms independent of the main HD attractor.

In the next Section, we review evidence that cortical and subcortical structures, including hippocampal, septal and tegmental areas, act synergistically to drive and/or modulate AV theta, which in turn is part of a return loop propagating integrated theta activity to hippocampus.

2.3.3.4 Origin and propagation of the AV theta signal

The AV is considered to be a central hub within a complex hippocampal-diencephalic-cortical-hippocampal system for theta propagation. The main AV output is to retrosplenial/subicular/entorhinal cortices (van Strien et al., 2009; Shibata, 1993a; Christiansen et al., 2016). The main subcortical afferent to AV is from MMN (Seki and Zyo, 1984), which receives converging inputs from medial septum and VTN (Shibata, 1989), both being implicated in modulating hippocampal theta (King et al., 1998; Vertes et al., 2004). In addition to the MMN input, AV theta is in the position to be influenced by a descending hippocampal input, via the Sub (Seki and Zyo, 1984). In this sense, AV receives a theta signal that integrates reciprocal tegmental, septal and hippocampal theta activity (Jankowski et al., 2013; Vertes et al., 2004; Vertes and Kocsis, 1997; Kirk et al., 1996).

Lesion and inactivation experiments in rodents provide strong support for the theory that the ascending pathway via AV cannot be considered as a simple hippocampal theta relay, but also provides subcortical control of hippocampal theta. Specifically, pharmacological inactivations of MMN and AV reduce hippocampal theta power in the lower theta frequency (3-5Hz) and theta frequency (6-8Hz), respectively (Zakowski et al., 2017). Medial septum inactivation typically suppresses theta-rhythmic discharge and theta oscillations in hippocampus and MMN, providing major afferents to AV (Kirk et al., 1996; Ruan et al., 2017). However, medial septum inactivation does not always eliminate theta rhythmicity in parahippocampal regions (Brandon et al., 2013), suggesting that the AV pathway may be able to maintain theta oscillations in the absence of a descending septo-hippocampal influence. One interpretation is that AV receives two main types of theta signals: one mainly descending from the septo-hippocampal system and another ascending from brainstem regions, the two being under a complex bidirectional control. This idea was first advanced by Kocsis et al. (2001), who suggested that reciprocal VTN-MMN connections form an inhibitory-excitatory recurrent network, comparable to the adjacent HD generative network (DTN-LMN), whose properties are sufficient to maintain oscillatory behaviour. Descending septo-hippocampal projections to VTN can then set the baseline excitation to initiate this behaviour, or set coherence between tegmental and septo-hippocampal theta (Kocsis et al., 2001). This could provide an explanation for the occasional reports in rats of theta oscillations in gRSC that persist, or are enhanced, in the absence of hippocampal theta i.e., during hippocampal large amplitude irregular activity (Young and McNaughton, 2009), or

electrolytic medial septum lesions (Borst et al., 1987). It could also explain why, in rabbits, hippocampus is not required for theta rhythmic discharge in AV, given that theta rhythmicity persists in gRSC and AV after dorsal hippocampus lesion (Talk et al., 2004), and firing rate and theta rhythmicity are enhanced in AV after Sub and gRSC lesions (Gabriel et al., 1987).

2.4 Summary

The pattern of AD and AV connectivity with hippocampal areas, and their specific cell types, suggest the existence of parallel HD (AD) and theta (AV) circuits. This notion provides the road map for this thesis, aimed to uncover the unique contribution of the AV-RSC circuit to spatial processing. Extensive previous efforts to characterize neurophysiological properties of AD HD cells (Taube, 1995) have had a tendency to mask the specific properties and contribution of AV to hippocampal-dependent spatial and memory functions (Aggleton et al., 2010). ATN damage disrupts parahippocampal spatial activities including HD, place and grid cells (Calton et al., 2003; Goodridge and Taube, 1997; Frost et al., 2021; Winter et al., 2015). Extensive studies demonstrate that rodents with ATN lesions are impaired in spatial learning and memory performance (Perry et al., 2021; Mitchell and Dalrymple-Alford, 2005, 2006). Although this is generally believed to reflect a loss of AD directional signalling, given its importance for path integration and downstream spatial networks (Sharp, 1999; McNaughton et al., 1995, 1996), arguably this is not enough to account for the importance of ATN in cognition (Nelson, 2021). In fact, damage of the subcortical HD system alone has little effect on spatial memory tasks presumed to involve an element of orientation (Dillingham and Vann, 2019; Vann, 2018, 2005). Given the importance of theta for memory, and the view of AV as a central hub of an interconnected circuit of regions linked to theta and hippocampal formation, it is likely that AV prominently contributes to these tasks. Nevertheless, so far only limited AV recordings have been conducted in freely-moving rats (Tsanov et al., 2010, 2011) and the question of what AV might add to the main HD signal ascending to RSC via AD remains open. This question constitute an important motivation for our AV and RSC recordings.

2.4.1 Road map of the thesis

The general aim of this thesis is to investigate neurophysiological and anatomical properties of the AV-RSC "theta" circuit. There are three main Experiments, each addressed by a separate Chapter.

Experiment 1 (Chapter 4) investigates how the two RSC subregions differ with respect to their electrophysiology and thalamic connectivity. RSC lies at the interface between external/sensory and internal/cognitive networks in the brain and mediates between the two, although it is not yet known how. gRSC is more closely connected to hippocampal formation, in which theta-band LFP oscillations are prominent. We, therefore, compared theta-rhythmic single-unit activity between the two RSC subregions and found, mostly in gRSC, a subpopulation of non-directional cells with spiking activity strongly entrained by theta oscillations, suggesting a stronger coupling of gRSC to the hippocampal cognitive system. As mentioned above, the hippocampal cognitive system comprises medial temporal lobe structures, where functional neurons embody the spatial cognitive map. Formation of this map relies on the use and integration of external sensory input and idiothetic input from subcortical regions, an integration that may occur in RSC, where the two networks converge. We then used retrograde tracers to test for differential inputs to RSC from the AV. We found that gRSC and dRSC differ in their afferents from two AV subfields, dorsomedial (AVDM) and ventrolateral (AVVL). Specifically: (1) as a whole AV projects more strongly to gRSC; (2) AVVL targets both gRSC and dRSC, while AVDM provides a selective projection to gRSC, (3) the gRSC projection is layer-specific: AVDM targets specifically gRSC superficial layer I. These same AV projections are topographically organized with ventral AV neurons innervating rostral RSC and dorsal AV neurons innervating caudal RSC. These combined results suggest the existence of two distinct but interacting AV-RSC subcircuits: one connecting AVDM to gRSC, which is part of the more spatial hippocampal system, and the other connecting AVVL to both RSC regions that may link hippocampal and perceptual regions.

Experiment 2 replicates and extends the work of Tsanov et al. (2011) to perform a detailed investigation of the temporal (Chapter 5), spatial and motor (Chapter 6) characteristics of AV neurons. We showed the existence in AV of neurons modulated by theta oscillations, the animal's heading direction (non-rhythmic HD), and a combination of the two (Theta-by-HD cells). Unexpectedly, we also discovered neurons modulated by spatial location (place cells). Compared to non-rhythmic HD, Theta-by-HD cells carried weaker directionality but additionally carried

some small amount of spatiality to their firing, which was however significantly weaker than that of place cells, which more strongly encoded spatial location. Some of these cells showed conjunctive tuning to self-motion derived from linear and angular head movements. The surprising overlap of neural signals related to spatial navigation discovered in AV is consistent with it being anatomically located to mediate bidirectional communication between RSC, MMN, and hippocampal formation. There were anatomical differences in cell types between the two AV subfields, which may be relevant for clarifying the RSC subregion electrophysiological differences.

Experiment 3 (Chapter 7) investigates the stability of AV neurons across trials and in the absence of visual inputs. All spatial cell types, namely non-rhythmic HD, Theta-by-HD and place cells, were stable and continued processing elements of space in darkness. Absence of vision did not disrupt coding of orientation and spatial location, although there was an increase in drift in darkness which was stronger and more incoherent for Theta-by-HD cells.

3

General Methods for electrophysiology experiments

In all the electrophysiology experiments of this thesis, animals, methods for tetrodes and microdrives making, surgeries, and recordings followed the same general principles and are described in this Chapter. Animals and techniques used in the anatomical tracing experiment will be described in the relevant experimental Chapter (Chapter 4, Section 4.4).

3.1 Animals

A total of 15 male Lister Hooded rats weighing between 420 and 480g at time of surgery (Charles River, UK) were used for electrophysiology recordings. Five animals were later discarded from analysis due to inconclusive histology. Prior to the implant surgery, rats were handled for up to 10 days and familiarized with transportation to the recording lab and open field square arena. After the implant surgery, rats were housed individually in transparent Plexiglass cages in a temperature and humidity-controlled environment (21°C). Testing was conducted in the light phase of a 12h light/dark cycle (lights on at 7am). Ten days after recovery from surgery, food regulation started (20g/day/rat), with water freely available in the home cage. After one week, rats were food restricted to maintain 85-90% of free-feeding body weight and testing began. All

experiments were carried out in accordance with UK Animals (Scientific Procedures) Act, 1986 and EU directive (2010/63/EU), complying with ARRIVE guidelines for the care and use of laboratory animals.

3.2 Recording rooms

Electrophysiological recordings were conducted in a 2-compartment box in Experiment 1 (Figure 3.1), or in an open field, square box in Experiments 2-3. Details of each one are provided in the relevant experimental Chapters. The recording rooms for the two sets of experiments were different but shared common features. Both were rectangular, with the testing box placed in the center and above the center of each box a video camera was attached to the ceiling.

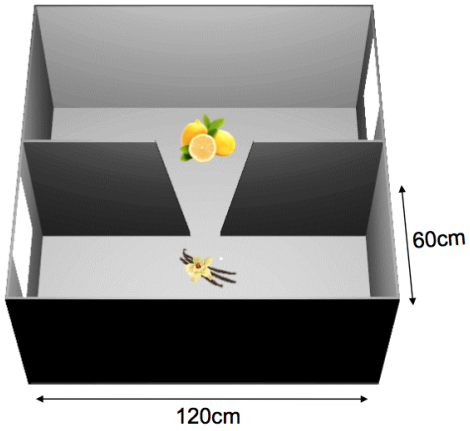


Figure 3.1: **2-compartment box used in Experiment 1.** A 120x120cm square box with 60cm high walls was placed inside a curtained enclosure of 260cm in diameter. The box was divided into two equal rectangular compartments by a wall. A 10 cm-wide opening on the wall allowed the animal to move between compartments. The two compartments were visually identical and symmetric by 180° relative to the doorway (opposite orientation). Symmetry was established by two white cue-cards attached on opposite walls in each compartment. Each compartment had a different smell (lemon or vanilla) to allow the rat to distinguish between them.

3.3 Electrodes and microdrives

Rats were anesthetized and implanted with a custom-built microdrive that was configured with either four or eight tetrodes threaded inside a guide cannula. Each

tetrode was made of individual 90:10 platinum–iridium wires (California Fine Wire) of diameter 25μm. A precision screw embedded into the microdrive allowed electrodes to be lowered dorso-ventrally in the brain (Figure 3.2). The tetrode configuration was selected because it provides a way to isolate extracellular spikes of multiple cells (McNaughton et al., 1983).

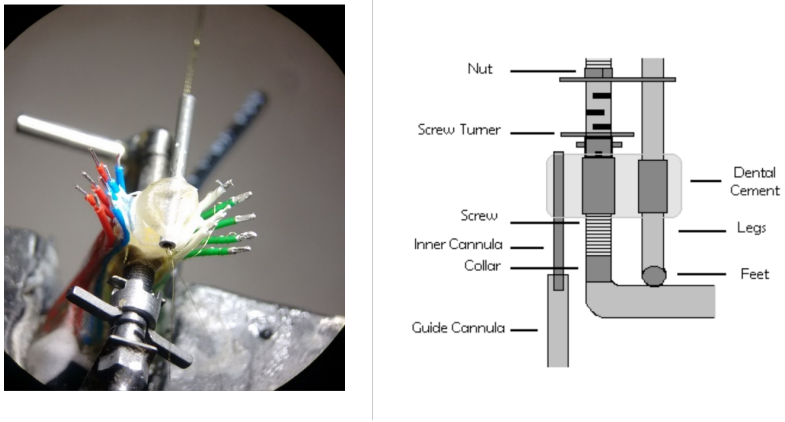


Figure 3.2: **Photograph and schematic drawing of an Axona microdrive.** The screw is held fixed on the microdrive. Turning the screw moves up and down the nut, which is connected to the electrical connector and the electrodes.

Electrode wires were attached to the electrical contacts on the microdrive by hand. First, insulation was removed from the top part of each tetrode with a flame, to expose the four individual wires. The tetrode was then passed through a 21-gauge cannula previously mounted onto the microdrive with dental acrylic. Each separated wire was connected to an individual electrical contact on the drive. This connection was sealed with silver-paint for electrical conduction. The assembly was covered with Plastidip (Plastidip UK Limited, UK) for protection and insulation. The tip of each tetrode was manually cut to optimize single unit isolation. Prior to surgery, tetrodes were impedance-tested using NanoZ device (Neuralinx, USA).

3.4 Implant surgery

Surgery followed standard stereotaxic surgery techniques for chronic recording of extracellular activity in behaving animals (Szymusiak and Nitz, 2003). Rats were anesthetized by isoflurane and oxygen mix (4% induction, 1.8–2% maintenance), and given analgesia in subcutaneous injections of 0.05mg/kg buprenorphine (Vetergesic; 0.3g/ml) and 1mg/kg Metacam (Meloxicam; 5mg/ml). Hair over the skull was shaved

to expose surgical sites and rats were secured to a stereotaxic frame (Kopf). Viscotears was applied to protect the eyes. Body temperature was monitored and kept constant throughout surgery using an internal rectal thermometer probe and a heat pad. Warmed sterile saline (1ml/100g) was administered subcutaneous into the scruff of the neck every one hour.

A midline skull incision was performed to expose bregma and lambda, and the implant coordinates were calculated relative to bregma. Using a dental drill (0.1mm drill bits), 4 holes were created and 1.6mm diameter screws were inserted into the occipital, parietal and frontal cranial bones. One of the supporting screws made contact with dura in the frontal cortex and was connected to the microdrive ground wire via soldering. A craniotomy was then drilled over the implant site in RSC or AV (2.7mm trephine bit).

The rat's skull was prepared using Metabond treatment. Dura was removed at the implant site, and the electrodes were lowered inside the craniotomy to the correct DV. A guide cannula was lowered around the tetrodes for protection against bending. Vaseline was applied around the cannula to fill the remaining space between the cannula and the skull, prior to dental acrylic being used to attach the microdrive to the skull and implanted screws. A ground wire was soldered to the drive for electrical grounding. After surgery, each animal was monitored until awake, and 1mg/kg Metacam (Meloxicam, 1.5mg/ml) was given in jelly for three consecutive days as pain relief. All animals were allowed to recover for one week prior to the start of recording.

3.4.1 Coordinates

In Experiment 1, four rats were implanted with microdrives in RSC. In Experiments 2-3, eleven rats were implanted with microdrives in AV, but five were removed from analysis after histological verification of electrodes placement. RSC implant coordinates were based on a previous study by Jacob et al. (2017). AV coordinates were tested using a neurotoxic lesion prior to conducting the recording experiments in one non-experimental animal by doing a non-recovery surgery (See Supplementary Figure A.1, Appendices), based on previous coordinates published in Mitchell and Dalrymple-Alford (2006). Coordinates are reported in Table 3.1.

Table 3.1: **Electrode implant coordinates.**

Implant coordinates			
Brain Area	AP	ML	DV
RSC (n=4)	-5.5 − -5.8	±1.0 − 0.80	0.4 − 0.65
AVVM (n=4)	-1.7	±1.4 − 1.5	3.6
AVVL (n=2)	-1.7	±1.8 − 1.7	3.4

Table 3.1: Values represent the range of coordinates used for tetrode placement in different animals. All coordinates are in mm from Bregma. Anterior-Posterior (AP) and Medio-lateral (ML) coordinates were taken from Bregma. Dorsal-ventral (DV) coordinates were taken from brain surface after removal of dura. RSC, retrosplenial cortex; AVDM, dorsomedial field of the anteroventral thalamic nucleus; AVVL, ventrolateral field of the anteroventral thalamic nucleus.

3.5 Signal processing and tracking

This section describes the structure and functioning of the multichannel recording equipment (DacqUSB, Axona, UK) that I set up in Oxford to conduct extracellular recordings in freely moving rats, in Experiments 2 and 3 of this thesis (Figure 3.3). Electrophysiology data in Experiment 1 was collected using the same recording setup that was previously available in Professor Kate Jeffery's Lab (University College London; UCL) and recordings followed the same principles.

3.5.1 Electrophysiology system

Signal from each electrode was recorded using a AC-coupled, unity-gain operational amplifier embedded on the headstage device connected to the microdrive. The headstage was connected to the multichannel recording system (DacqUSB, Axona) via a flexible lightweight cable. Signal buffering by a headstage amplifier allows the signal detected by high-impedance electrodes to be transmitted by low-impedance cables, making it less susceptible to noise. The buffered signal was relayed to a preamplifier and a system unit (Figure 3.3). In the preamplifier, the signal is amplified; in the system unit the signal is filtered for different frequencies, and digitized via an analog-to-digital signal converter. The system unit also provides an audio-video

output that allows monitoring of the animal's position within the box, while listening to threshold-triggered spikes.

3.5.2 Single-unit and LFP recording

Single unit activity was continuously sampled (48kHz sampling frequency), amplified 15-50K times and band-pass filtered from 300Hz to 7kHz. The Nyquist theorem states that the sampling frequency must be at least double that of the maximum frequency component of the signal recorded. The band-pass filter was chosen to reject slow oscillations and frequencies that approached our sampling frequency (Jeffery et al., 2018).

The signal from each electrode was differentially recorded against the signal from an electrode on a different tetrode with low spiking activity, and so subtracting the two signals removes their common noise (improves signal-to-noise ratio of the recording electrode). The voltage signal was also referenced against the animal's electrical potential, referred to as the ground. The ground voltage was recorded by the jeweler's screw inserted through the skull. In addition, because as the animal moves it may accumulate charge which generates electrical noise, the animal was grounded by connecting the testing arena to the grounded wire in a mains socket. Spikes were defined as events exceeding a user-defined voltage threshold. Each spike was time-stamped and stored together with a 1ms of surrounding signal (200μs pre- and 800μs post-threshold interval). Tetrodes were lowered by 25-150μm to locate single-unit spiking activity.

The output of 8 arbitrarily-selected channels was split and routed to 8 empty channels, so that the local LFP could be recorded simultaneously with single spikes from the same channel. This can be achieved by filtering the neural signal for the slow- or the high-frequency components (Jeffery et al., 2018). The LFP signal was collected single-ended (250Hz sampling frequency), amplified 5k times, filtered with a 500Hz low-pass filter and stored with the unit data. A 50Hz notch filter was applied to remove local mains noise.

3.5.3 Position tracking

Two light-emitting diodes (LEDs), one large and one small and separated by 5cm, were attached to the headstage to provide the position and the orientation of the rat's

head. The LEDs were imaged with an overhead camera (50Hz sampling frequency). Position was determined based on the x/y coordinates of the large LED. Orientation was derived from the angle between the two LEDs. Compared to video-tracking, this method was chosen because it allows for tracking in darkness for Experiment 3. Position in x/y coordinates (cm) and heading direction in degrees were saved for offline analysis.

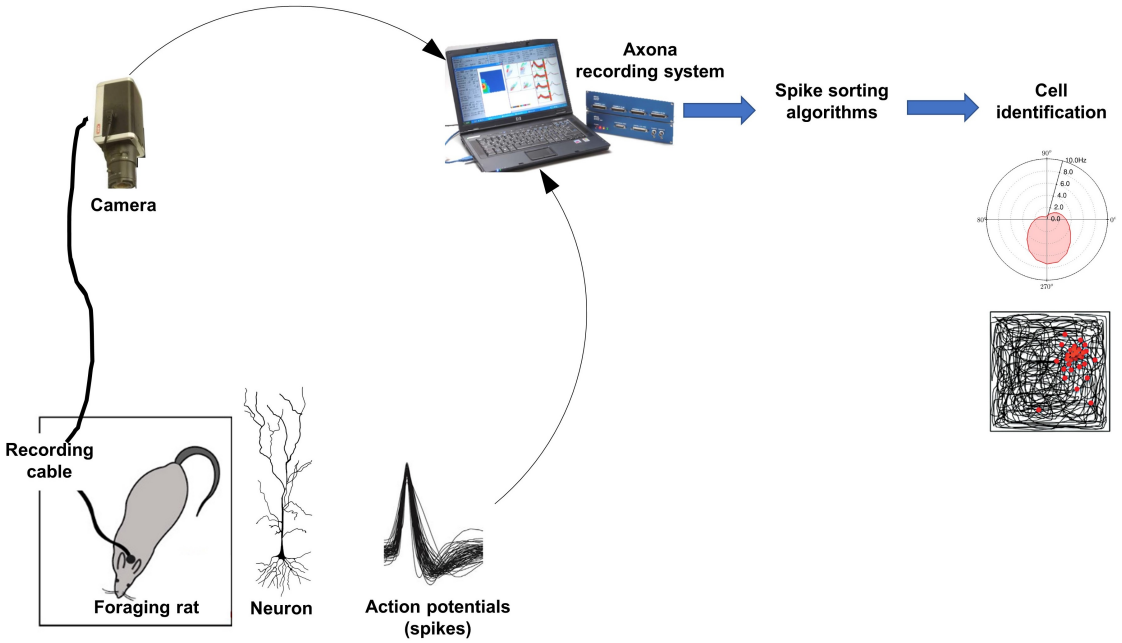


Figure 3.3: **Basic elements of the recording system.** Recordings were conducted from freely-moving rats, implanted with custom made 16- or 32-channel microdrives in RSC (Experiment 1; 4 implanted animals) or AV (Experiments 2 and 3; 11 implanted animals), using Axona recording equipment (headstage, preamplifier, system unit). Position and orientation of the rat's head were tracked by an overhead camera. Spike and position data were synchronized, and offline spike sorting algorithms were used to identify single units.

3.6 Data analysis

Data were analyzed using TINT (Axona, UK) and MATLAB R2018a (MathWorks, USA) with custom-made programs and functions. CircStat toolbox was used for analysis using circular statistics (Berens, 2009).

3.6.1 Cell isolation and spike-sorting

Spike-sorting was performed using automatic spike sorting algorithm KlustaKwik (Kadir et al., 2014) followed by manual refinement using TINT software package

(Axona). Spike-sorting involves isolating action potentials (spikes) belonging to different neurons recorded on a tetrode during a trial (Lewicki, 1998). Because the four electrodes that form a tetrode have a small spatial separation, the spike waveform will have slightly different features depending on which electrode records it. One of the most prominent feature is waveform amplitude, which is inversely proportional to the distance between a neuron and the electrode tip. Spikes were therefore isolated based on peak-to-trough amplitude differences for each pair of electrodes within one tetrode. This resulted in six scatter plots of waveform amplitude recorded on one electrode, against waveform amplitude recorded on a different electrode within the same tetrode (Figure 3.4). Spikes with similar waveform features were grouped together. To confirm that an isolated cluster of spikes resulted from single unit activity, we adopted the following inclusion criteria: (1) average spikes waveform displaying the classical action potential shape, and (2) less than 10% of spikes occurring in the first 2ms of the autocorrelogram (action potential refractory period). Only cells meeting these criteria were accepted into further analysis.

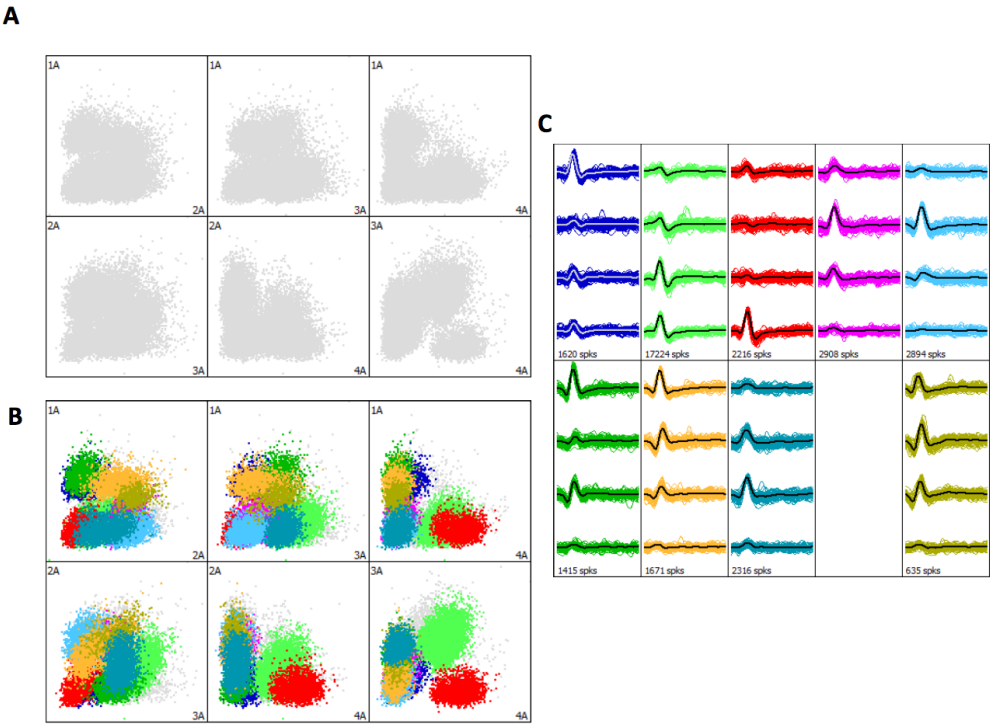


Figure 3.4: **Spike-sorting procedure.** **(A)** All spikes recorded on one tetrode were isolated based on peak-to-peak amplitude differences between electrodes within the same tetrode, resulting in 6 cluster space plots. The neuron nearest to the electrode produces larger spikes on that electrode. By contrast, further neurons produce smaller spikes. In this way, spikes with the same waveform amplitude are clustered

together. **(B)** Spikes were assigned to different clusters manually or using KlustaKwik algorithms. Each color represents spikes belonging to a different cluster (n=9). **(C)** For each of the 9 isolated clusters, average waveform for all spikes was plotted across the four channels of the tetrode. Note that different clusters are associated to waveforms of different shapes, indicating a different unit.

3.6.2 Waveform Analysis

The average spikes waveform was constructed for each isolated unit. Waveforms are typically described using two parameters: (1) peak-to-trough amplitude (μv), representing the voltage difference between waveform peak and trough, and (2) peak-to-trough width (μs), representing the time interval between the peak and the trough.

The width of the average spike waveform was used to separate narrow from broad spiking cell types (Lewicki, 1998). We followed methods reported in Ardid et al. (2015), using the open source code from the public Git repository: https://bitbucket.org/sardid waveformanalysis. Briefly, a two-Gaussian model was applied to the distribution of waveform widths. We defined two cutoffs on this model that divided waveforms into three groups: narrow, broad and in-between. Broad waveforms were those for which the likelihood to be considered broad was larger than 10 times the likelihood to be narrow. Narrow waveforms were those for which the likelihood to be considered narrow was larger than 10 times the likelihood to be broad. Unclassified waveforms were those falling into the dip of the bimodal distribution. The bimodality of the distribution was tested using the calibrated version of the Hartigan dip test (p<0.01).

3.6.3 Spectral analysis

The LFP signal, recorded by low-pass filtering the raw neural signal, was analyzed using a fast Fourier transform (FFT). The power of each frequency component was defined as the square of the magnitude of the output of the FFT. To compare across trials, power measures within each trial were normalized to z-scores. The power spectrum for a trial shows z-scores vs frequency smoothed with a Gaussian kernel (bandwidth=2Hz; standard deviation=0.5Hz). The power of theta frequency is the maximum z-score within 6-12Hz. The theta frequency is the frequency value associated to peak theta power.

3.6.3.1 Theta filtering

In addition to considering spikes and LFP in isolation, an important aim of this thesis was to investigate their relationship. To investigate spikes-LFP coupling, the LFP signal was bandpass-filtered at theta frequency range (6-12Hz) with a 4^{th} order Butterworth filter. A zero-phase filtering was applied to prevent the phase shift introduced by the filter. The Hilbert transform was applied to the bandpass-filtered LFP to derive instantaneous theta phases. Each theta cycle was defined such that peaks occurred at 0 and 360°, and trough at 180°. To determine at which point to apply the Hilbert Transform, the LFP signal (Hz) was linearly interpolated with spike time (s), with each spike being assigned to the phase of the theta cycle at which it occurred.

To visualize the spikes-LFP relationship of a cell, firing phases were double-plotted in a frequency histogram. The probability distribution of spikes relative to theta phases was derived by smoothing the spike-phase histogram using a circular kernel density estimation (KDE) method, with an automatically selected bandwidth parameter using the plug-in rule of Taylor (2008). Spike-phase histogram and the associated probability were plotted on the same graph and gave a useful visual indicator of whether the firing of a neuron was locked to the local theta cycle.

3.6.4 Theta analysis

In all experiments of this thesis, spike-LFP coherence and rhythmicity were assessed by computing an index of theta phase-coupling (IC) and an index of rhythmicity (IR), respectively. Coupling refers to the phase of theta at which spikes occurred; rhythmicity refers to the frequency of the temporal modulation of the spike-time autocorrelogram. We used both measures (IC and IR) to examine the theta behaviour of a cell, as spikes may be emitted with a timing coupled to theta (phase-locked) even if there is no overt rhythmicity on the autocorrelogram (Eliav et al., 2018; Alexander et al., 2020)

3.6.4.1 Index of phase-coupling

For each cell, a firing phase distribution was plotted by binning phases binned between 0-360° with 6° bins. We computed the index of theta phase-coupling (IC) as the associated mean vector length (Rayleigh vector, CircStat toolbox) (Climer et al.,

2015; Frank et al., 2001). IC values are bound between 0 and 1, with higher values indicating more unimodal concentration of spikes around a single phase value, and hence stronger phase locking. For each cell, an IC value that was above 99^{th} or 99.9^{th} percentile of a shuffle distribution was used to sort cells into theta-modulated vs not.

3.6.4.2 Index of rhythmicity

The index of rhythmicity (IR) additionally quantifies the temporal modulation of a cell's firing, at theta frequency range (6-12Hz). It was derived from the spike-time autocorrelogram, displaying correlation of the signal with itself under different time lags. A cell firing theta-rhythmically at 8Hz will show peaks at ~125ms in its autocorrelogram, reflecting the most frequently occurring spike interval. Autocorrelograms of the spike trains were plotted between 500ms using 10ms bins, normalized to the maximum value (between 0-10ms) and smoothed (20 bins boxcar). Following methods outlined in Lozano et al. (2017), the IR was calculated as the difference between the expected theta modulation-trough (autocorrelogram value between 60-70ms) and the theta-modulation peak (autocorrelogram value between 120-130ms), divided by their sum. It takes values between -1 and 1. Positive values indicate an ascending probability of the cell to fire again after the duration of one theta cycle (~125ms). A cell was considered as theta-rhythmic if it had an IR>0.001.

3.6.4.3 Preferred theta phase analysis

For each cell with a significant IC, the preferred theta phase was estimated as the circular mean firing phase. Preferred theta phases for all cells were plotted in a circular histogram binned between 0 and 360° with 6° bins. The length of the associated Rayleigh vector was taken as a measure of phase preference consistency across cells, its direction as the mean preferred theta phase across cells. A Rayleigh test was conducted on the phase distribution to assess the significance of this phase preference across cells.

3.6.5 Spatial Analysis

The following paragraphs provide a description of the analysis performed to assess the pattern of spatial activity for each isolated unit.

3.6.5.1 Directional tuning curve plots

In order to determine whether a cell was directionally tuned, the spike times and position samples of the animal's heading direction were recorded in parallel and sorted into bins of 60 x 6°. The mean firing rate for each directional bin (Hz) was calculated by taking the sum of the spikes divided by the total amount of time (s) that the animal's heading direction was located in that bin, as follows:

$$\text{Mean firing rate in bin}_i(Hz) = \frac{\sum \text{spikes in bin}_i}{\sum \text{dwell time in bin}_i(s)}$$

Tuning curves were constructed as the histogram of firing rates (Hz) as a function of head direction (degrees) (Figure 3.5 A). The resulting histograms were smoothed using a Gaussian kernel (Matlab function *imfilter*; smoothing factor =5-bins or 30°) to minimize random fluctuations of the firing rates. Polar plots of the smoothed histograms were generated (Figure 3.5 B).

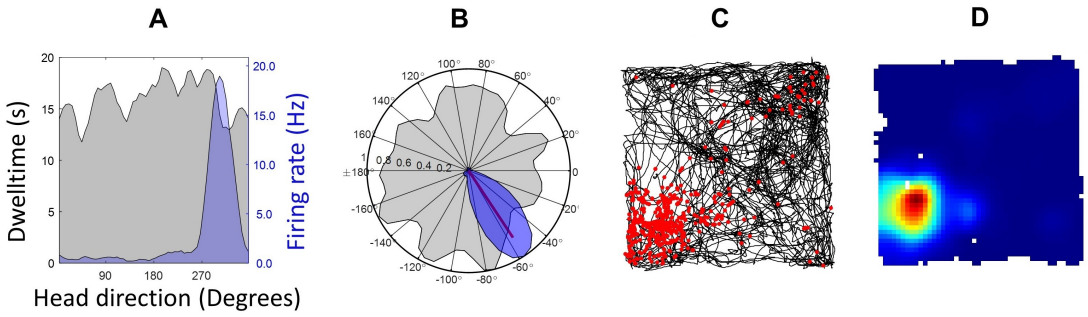


Figure 3.5: **Analysis of spatial firing properties. (A)** The tuning curve (blue curve) allows to visualize directional tuning of a cell. It was derived as the smoothed histogram of firing rate (Hz) vs head direction (HD; degrees). The dwelltime curve (gray curve) was derived as the smoothed histogram of dwelltime (s) vs HD (degrees) and shows the sampling of the animal. Histograms were constructed using bins of 6°, smoothed by a Gaussian kernel (smoothing factor=5 bins; 30°). **(B)** The tuning curve was converted to polar coordinates. This allowed to derive a single vector (Rayleigh vector, red line) to describe the relation between firing rate and the animal's heading. The cell in the figure has significant directional tuning, as suggested by the single firing rate peak. The cell has a peak firing rate of 6.8Hz (normalized to 1Hz in the plot, see axis). The preferred firing direction (PFD) is at 310°, corresponding to the direction where the peak rate occurred. The tuning width is 70°, corresponding to the directional firing range. **(C)** The spikemap allows to visualize the locational specificity of a cell. The path of the animal was smoothed with a 400ms window

and overlaid with spikes at the appropriate times and locations. **(D)** Spikemap data was binned (2x2cm bins), smoothed with a Gaussian kernel (smoothing factor=5cm) and dwelltime-normalized to generate a ratemap, expressed as a heatplot. Colors represents 20% bands of the peak firing rate (blue, 0-20%; red, 80-100%). The cell in the figure has a single place field in the southwest corner.

3.6.5.2 Rayleigh mean vector length

Two factors were considered to identify neurons significantly tuned to HD: (1) directional peak firing rate surpassing a pre-defined threshold of 1Hz, and (2) the extent to which the tuning curve was directional. The peak rate (Hz) was defined as the directional bin of the smoothed circular histogram associated with the maximal firing rate. The mean vector length, or Rayleigh vector (R-vector, CircStat toolbox) of the smoothed histogram was used as a measure of directionality for each cell (Zar, 2010). To derive the R-vector, the mean firing rate in each directional bin i was considered as a complex unit vector pointing toward the direction corresponding to that bin, α_i, with x and y coordinates defined as:

$$r_i = (\cos\alpha_i, \sin\alpha_i)$$

The sum of all the unit vectors r_i was averaged to obtained the mean resultant vector, $\overline{r}$, with an associated mean direction ($\overline{\phi}$):

$$\overline{r} = \frac{1}{n}\sum r_i$$

The mean vector length (R-vector) was derived as the absolute value of $\overline{r}$:

$$R = |\,\overline{r}\,|$$

Values of R close to 1 indicate that the spikes were closely clustered around a single value and values close to 0 indicate that the spikes were distributed across all directions. After filtering cells based on peak firing rate and R-vector, tuning curves parameters were calculated.

3.6.5.3 Tuning curve parameters

The parameters that were used to quantify tuning curve characteristics were (1) R-vector, (2) peak firing rate, (3) preferred firing direction (PFD), (4) tuning width, and (5) concentration parameter k. Parameters were estimated by fitting smoothed polar histograms (polar plots) by a Gaussian function, or Von Mises distribution, the

circular analogue of a normal distribution (Fisher, 1993). In Experiment 1, given that some tuning curves were clearly bimodal, an angle-doubling procedure was performed before computing the R-vector of the firing rate distribution (see relevant Chapter). In Experiment 2, no sign of multimodality/bidirectionality was seen while screening for cells.

The PFD of a cell was derived as the directional bin associated with the peak firing rate; that is, the mode of the polar histogram. We did not use the circular mean direction ($\overline{\phi}$) to estimate the PFD, as this measure can be biased by how well the polar histogram is fitted by a Von Mises distribution. The cell's tuning width, or directional firing range, was determined by computing two standard deviations from the circular mean direction ($\overline{\phi}$) . The concentration parameter k quantifies circular spread around the circular mean and was derived using the Matlab function *circ_k*. See Figure 3.5 for an example. Directional information content in bits/spike was also computed following the method of Skaggs et al. (1992), and computes the amount of directional information carried by each spike.

3.6.5.4 Shuffling

A shuffling procedure was used to derive a control distribution and chance-level criteria for each cell in the theta-phase coupling and directionality analyses. In the theta analysis, the entire spike train of each cell was time-shifted by random intervals ranging from 20s to the trial duration minus 20s relative to the phase data. Spike times shifted past the end of the trial were wrapped around to the beginning to preserve the same number of spikes and the temporal structure of the spike sequence. This was repeated 1000 times for each cell, and the IC was computed for each repetition. All IC values were pooled together to derive a control distribution. The same procedure was used in directionality analysis, but the spike time sequence of each cell was time-shifted relative to the HD data. For each repetition, a directional tuning curve was constructed as outline above, and the associated R-vector was computed to build the control distribution against which single cells can be tested. Chance-level criteria that a cell would be theta- or HD-modulated were identified from the control distribution of IC and R-vector (99^{th} percentile in Experiment 1; 99.9^{th} percentile in Experiments 2 and 3).

3.6.5.5 Ratemap plots

Locational firing of a cell was investigated in the standard manner. First, we examined the spatial distribution of spikes by plotting spikemaps like the one of Figure 3.5 D. Path data of the animal were extracted by smoothing the position points with a boxcar algorithm (400ms window) and spikes were overlaid as points onto the path data at their corresponding times and locations.

Ratemaps (Figure 3.5 E) were generated from the spike data, using the Gaussian approach described in Leutgeb et al. (2005) and Grieves et al. (2020). Briefly, position and spikes data were binned using 2x2cm bins, and smoothed separately using a weighted Gaussian kernel (smoothing factor=5cm), such that spikes and position data closer to a bin's center had more influence on that bin's firing rate. Bins that were >10cm away from the current bin had no influence (weight=0), and were not included in the Gaussian smoothing process. If the rat did not explore within 2cm of a bin's center, or if he spent less than 1s there, the bin was considered as unvisited and discarded. The smoothed ratemap was generated by dividing the smoothed spikemap by the smoothed dwelltime map. Mean firing rate in each locational bin x was found as:

$$f(x) = \frac{\sum_{i=1}^{n} g(S_i - x)}{\int_0^T g(y(t) - x)}$$

where x is the bin's center, n is the spike count, S_i is the location of the i-th spike, y(t) is the location of the animal at time t, and 0-T are the periods of recording. g is the Gaussian kernel used to weight each position and spike point. The overall spike count, divided by session duration gave the mean firing rate (Hz) of the cell. The locational bin with the highest firing rate gave the locational peak firing rate. A place field was defined as a group of at least 9 adjoining pixels in which firing rate was at least 20% of the peak firing rate, and peak firing rate was at least 1Hz.

3.6.5.6 Locational measures

Four factors were considered to identify neurons significantly tuned to spatial location, in the same way as is usually done for hippocampal place cells: (1) locational peak firing rate >1Hz; (2) mean firing rate >0.1Hz but <10Hz; (3) the extent to which the animal's location could be successfully predicted by the cell's firing rate (locational information content >0.8 bits/spike), and (4) the percentage of the arena's surface over which a cell fired (sparsity score <0.2). That is, a cell should fire over less than 20% of the arena. The following formulas were used:

$$\text{Locational information content} = \sum_i (\frac{\lambda_i}{\lambda}) * log_2(\frac{\lambda_i}{\lambda}) * \sum p_i$$

$$\text{Sparsity score} = \frac{(\sum p_i \lambda_i)^2}{\sum p_i (\lambda_i)^2}$$

where p_i=probability of occupancy of the locational bin i; λ_i=firing rate in bin i, and λ=overall mean firing rate (Skaggs et al., 1992).

3.7 Histology

After completion of electrophysiology recordings, rats were anesthetized with isofurane and received an overdose of sodium pentobarbital (Euthatal, Merial, Harlow, UK). Rats were perfused transcardially using saline (0.9% sodium chloride solution) followed by 10% formalin perfusion (10% formalin in 0.9% sodium chloride solution). The brains were removed and post fixed overnight in 10% formalin, transferred to a 25-30% sucrose solution (25-30% in 0.1M PBS) for a minimum of 48h for cryoprotection, and finally frozen with dry ice. Brains were sliced coronally into sections of variable thickness (20 to 50μm) on a freezing microtome. Sections were mounted on glass slides. Tetrode locations were histologically verified from cresyl violet-stained brain section.

This method involves stepping slides through an ascending ethanol series, a descending ethanol series followed by immersion in cresyl violet dye for 12 minutes, and a final ascending ethanol series. After staining slides were left in Histoclear for

10 minutes, and then coverslipped. Photomicrographs of the Nissl-stained brain sections were captured using a camera mounted on a Leica DMR microscope (Leica Microsystems, UK) or an Olympus microscope (Olympus Keymed, UK) using a x1.6 objective.

4

Evidence for two distinct thalamocortical circuits in retrosplenial cortex

4.1 Background and Rationale

RSC is a brain region lying between primary sensory cortices and the hippocampal spatial memory system. It has two component subregions, dRSC and gRSC, that may serve different, albeit related, functions (Aggleton et al., 2021). In order to shed light on these functions, in Experiment 1 we first explored how gRSC and dRSC differ electrophysiologically and then traced the thalamic afferents, which form some of the most prominent inputs to RSC, to try to determine what may account for these differences. This Chapter has been published as a paper (Lomi et al., 2021) [1].

Hippocampus, RSC and ATN form an interconnected neuronal system supporting learning and memory (Vann et al., 2009). While rodent and human studies have extensively characterized the spatial functions of the RSC (Vann et al., 2009) the details are far from complete (Mitchell et al., 2018; Aggleton et al., 2021), although directional processing is a prominent feature (Chen et al., 1994a; Cho and Sharp, 2001;

[1] Lomi, E., Mathiasen, M. L., Cheng, H. Y., Zhang, N., Aggleton, J. P., Mitchell, A. S., and Jeffery, K. J. (2021). *Evidence for two distinct thalamocortical circuits in retrosplenial cortex.* Neurobiology of Learning and Memory, 185:107525

Lozano et al., 2017; Alexander et al., 2020a). The topography of connections of each of the major RSC subregions, gRSC and dRSC, represents a key aspect for functional considerations on the RSC involvement in navigation and memory. While the two RSC subregions have connections with three main areas, the hippocampal formation, ATN, and visuospatial neocortical areas, these connections are not equally shared between the two subregions (van Groen and Wyss, 1990b,c, 1992; Van Groen and Wyss, 2003; Cenquizca and Swanson, 2007; Sugar et al., 2011; Vogt and Miller, 1983). gRSC connectivity is weighted toward regions of the hippocampal formation that are involved in spatial navigation and memory processes, as it receives a direct input from dorsal subiculum and CA1 (Meibach and Siegel, 1977; Yamawaki et al., 2019; Opalka et al., 2020). gRSC is also interconnected with basal forebrain structures that are involved in the generation of hippocampal theta oscillations (6-12Hz), namely medial septum and diagonal and horizontal band of Broca (Unal et al., 2015).

By contrast, instead of these limbic inputs, dRSC is characterized by stronger connections directly from primary/secondary visual cortices and LD/LP visual nuclei of the thalamus (van Groen and Wyss, 1990, 1990b, 1992), which are considered to endow dRSC with a privileged role in visuospatial processing (Vann and Aggleton, 2005). Jacob et al. (2017) extended this idea by showing different functional properties of HD cells between the two RSC subregions in rats. While global HD cells were present in both gRSC and dRSC, a directional signal more sensitive to local visual landmarks was found only in dRSC (Jacob et al., 2017). Conjunctive HD and landmark coding in dRSC has been accounted for by reference to its stronger visual inputs as compared to global directional inputs ascending from the ATN (Yan et al., 2021; Page and Jeffery, 2018). Finally, ATN has strong reciprocal connections to the two RSC subregions. Different ATN nuclei, namely AD and AV, mediate two information streams, HD vs theta (Vertes et al., 2001; Albo et al., 2003), that ascend to RSC with a parallel but different organization (AD vs AV) and both appear to have a stronger relationship with gRSC compared to dRSC (Witter et al., 1990; Shibata, 1993a, 1994; Van Groen and Wyss, 1995).

4.2 Aims and Hypothesis

Given that theta propagation is thought to serve spatial mnemonic functions of the limbic system by optimizing synaptic plasticity and inter-regional communication (Hyman et al., 2003; Buzsáki, 2002, 2005; Buzsáki and Moser, 2013), here we used

theta as a marker for hippocampal coupling to determine whether gRSC and dRSC have distinct interactions with hippocampus. We hypothesized that theta-rhythmic firing would be stronger in gRSC compared to dRSC, reflecting a stronger interaction with the hippocampal navigational network. We then used retrograde tracing to see if the anterior thalamic inputs to the two RSC subregions could be differentiated. As we show here, we found that gRSC is more theta-modulated than dRSC, and with anatomical tracing we then found that it selectively receives a stronger input from dorsomedial AV (AVDM). These findings strengthen the evidence that gRSC is part of a subcircuit that connects with the hippocampal system, while dRSC is part of a parallel circuit that interacts more strongly with sensory cortices. We finish with some speculations about a possible role for RSC in linking these two systems.

4.3 Methods and Materials: Electrophysiology recording experiment

To address the aim set out by Experiment 1 reported in this Chapter, cells were recorded together with oscillatory LFP from gRSC and dRSC using multichannel extracellular techniques from four freely-moving rats, as reported in the General Methods. I analyzed data recorded by Dr. Ningyu Zhang and Dr. Pierre-Yves Jacob in Professor Kate Jeffery's Lab (UCL).

4.3.1 Animals and coordinates

For this study we used data from four male Lister Hooded rats (Charles River, UK) that were surgically implanted with tetrodes. Two of the rats (R602, R636) had participated in a previously published experiment (Jacob et al., 2017) and two were part of a new experiment (Zhang et al., 2021). We only included rats in which we could identify the electrode track in the histological section, and for which histology indicated that electrodes sampled both RSC subregions (electrodes advanced from dRSC into gRSC).

Surgery followed standard stereotaxic surgery techniques for chronic recording of extra-cellular activity in behaving animals (Szymusiak and Nitz, 2003). Implant coordinates were based on previous study of HD cells in the RSC of Jacob et al. (2017). These were as follows: AP, -5.5; -5.8; ML, ±1.0 - ±0.80; DV, 0.4 - 0.65 (in mm from Bregma). All rats were implanted in the left hemisphere. All experiments

were carried out in accordance with UK Animals (Scientific Procedures) Act, 1986 and EU directive (2010-63-EU), complying with ARRIVE guidelines for the care and use of laboratory animals.

4.3.2 Behavioural protocol and testing apparatus

Animals were screened daily for single unit activity. Screenings were made in an open field box within a cue-rich room. When a set of units was isolated, the animal was transferred to the experimental room and the recording session was conducted in a two-compartment box, which was configured to test a hypothesis (not addressed here) about directional encoding. Briefly, the apparatus comprised two identical rectangular compartments connected by a central doorway in the long wall that separated them (for details see Jacob et al., 2017). One short wall of each compartment was adorned with a large white cue card, and the compartments were differentially scented, one with lemon and one with vanilla. The apparatus was located within a curtained-off area. Each recording session consisted of five consecutive trials, with each trial involving a different box orientation. To promote exploratory behaviour throughout the recording, rice was randomly thrown in the box by the experimenter. For the purposes of the present analysis, only the first 10min-long baseline trial was considered.

4.3.3 Data Analysis

Data were analyzed using TINT (Axona, UK) and MATLAB R2018a (MathWorks, USA) with custom-made programs and functions. CircStat toolbox was used for analysis using circular statistics (Berens, 2009).

4.3.3.1 Spike sorting

Spike-sorting was performed using KlustaKwik (Kadir et al., 2014) followed by manual refinement using the TINT software package (Axona). To confirm that isolated clusters resulted from single unit activity, the following inclusion criteria were adopted: (1) an average waveform displaying the classical action potential shape, and (2) fewer than 10% of spikes occurring in the first 2ms of the autocorrelogram (action potential refractory period). Only cells meeting these criteria were accepted into further analysis.

4.3.3.2 Spectral Analysis

The LFP signal, recorded by low-pass filtering the raw neural signal, was analyzed using a fast Fourier transform (FFT). The power of each frequency component was defined as the square of the magnitude of the output of the FFT. To compare across animals, power measures within each trial were normalized to z-scores and then plotted and smoothed with a Gaussian kernel (bandwidth=2Hz; standard deviation=0.5Hz). The power of theta frequency was found as the maximum z-score within the movement-associated (Type-1) theta frequency range (6-12Hz). Average theta frequency was found as the frequency value associated to peak theta power.

4.3.3.3 Theta analysis

As already described in the General Methods, theta rhythmicity and spike-LFP coherence were assessed by computing an index of rhythmicity (IR) and an index of theta phase-coupling (IC), respectively. To recap, IR computes a value for each cell, reflecting the difference in the peak and trough of the autocorrelogram within the theta frequency range, divided by its sum. IC computes the mean vector length of the spikes-phases distribution. The index of theta phase-coupling (IC) was used to sort cells into theta-modulated vs not. See General Methods; Chapter 3.

4.3.3.4 Cell identification and inclusion criteria

HD and bidirectional cells were identified as described in Jacob et al. (2017), and removed from the current analysis, as they were previously included in Jacob et al. (2017), and they were not theta-modulated. Briefly, to analyze the directional firing characteristics of single units, the spike times and position samples of the rat's facing direction were sorted into bins of 6°. The mean firing rates per angular bin (Hz) were smoothed with a 5-bin (30°) smoothing kernel and polar-plotted. Finally, the angles were doubled and plotted modulo 360° in order to remove any bidirectionality that might be present in the tuning curves of bidirectionally tuned cells. Hence, to be considered for analysis, cells needed to have (1) a tuning curve that was not obviously unimodal/bidirectional from visual inspection; (2) Rayleigh vector length of the doubled HD angles <0.22, which is the original threshold used by Jacob et al. (2017) and (3) average firing rate>0.1Hz for the trial.

To provide a control for each cell against which to measure its theta-phase coupling we created a time-shifted distribution in which the entire sequence of spike times was circularly time-shifted by a random amount lying between 20s and the duration of the recording session minus 20s. This preserved the number of spikes and the temporal structure of the spiking sequence, but dissociated the time of spiking from the theta oscillations. This was repeated 1000 times for each cell, and the IC was computed for each repetition. All values were pooled together to derive a control distribution, representing the chance level for which the activity of each RSC cell was locked to theta. A cell was considered as significantly modulated at theta frequency if the IC was>99^{th} percentile of the control distribution for that neuron.

4.3.3.5 Cell-specific temporal firing characteristics

To investigate bursting properties of RSC neurons, inter-spike intervals (ISI) were plotted in a frequency histogram between 0-250ms with 2ms bins. The peak ISI of a cell was derived as the center of the bin with the highest frequency count. Cells with peak ISI <10ms, which defines a burst mode (Fanselow et al., 2001), were classified as bursting and the remainder as non-bursting. The burst index was calculated as the ratio of spikes with peak ISI <10ms to all the spikes in a trial (Mizuseki et al., 2012). Burst index values closer to 1 indicate the presence of intra-burst spikes, whereas smaller values indicate a prevalence of single spikes. Firing rate and waveforms parameters for each cell were quantified as described in the General Methods; Chapter 3.

4.3.3.6 Statistics

For gRSC-dRSC comparisons, if data were found to deviate significantly from a normal distribution (Matlab functions *kstest*), we used a non-parametric test (Wilcoxon Rank-sum test, WRS, Matlab function *ranksum*). Otherwise, we used parametric tests. To evaluate simultaneously the effect of two grouping variables (brain region and cell type) on waveform parameters, we used a two-way ANOVA. We also used the Chi-squared goodness-of-fit test (X^2) when testing observed numbers of theta-rhythmic cells in gRSC and dRSC against an expected equal proportion, and the number of interneurons against an expected equal proportion. To test the significance between two circular distributions, we employed the Watson-Williams multi-sample F-test for equal circular means (WW, Matlab function *circ_wwtest*, CircStat toolbox), in

addition to the Rayleigh test. All statistical tests are two-tailed. For all box plots, a line is marked at the sample median, boxes at the interquartile range, whiskers at the minimum and maximum value. Markers represent individual data points. In all figures and tables, p-value significance level: $*$=0.05, $**$=0.01, $***$=0.001

4.4 Methods and Materials: Retrograde tracing experiment

This Section describes the tracing techniques used in our anatomical study to investigate thalamocortical projections from AV to RSC. I analyzed data collected by Dr. Mathias Mathiasen in Professor John Aggleton's Lab (Cardiff University) and Dr. Han Yin Cheng in Professor Kate Jeffery's Lab (UCL).

4.4.1 Animals and tracers

Twenty-three male Lister hooded rats (Charles River, UK; Envigo, UK) weighing 291-614g at the time of surgery were used for the retrograde tracer experiments. Four retrograde tracers were employed for a total of 29 injections: (i) cholera toxin subunit B (CTB; Polysciences Inc, Eppelheim, Germany), (ii) fast blue (FB; Polysciences Inc, Eppelheim, Germany), (iii) biotinylated dextran amine tracer (BDA; 3 kD version; Life Technologies Ltd, Paisley, UK), and (iv) fluorogold (FG; Fluorochrome Inc., Denver, CO, USA). The CTB was used either unconjugated or conjugated with Alexa Fluor 594 (Ctb-AF594; Molecular Probes, Invitrogen Inc.) or with Alexa Fluor 488 (Ctb-AF488; Molecular Probes, Invitrogen Inc.). The single BDA case was also included in a previous study (Mathiasen et al., 2017), which provides full methodological procedures for this tracer. Six animals had dual injections while the others had single injections placed in either gRSC or dRSC.

4.4.2 Surgery

All injection surgeries took place under isoflurane anesthesia (isoflurane-oxygen mixture 1.5-2.5%) with the rat positioned in a stereotaxic frame (Kopf Instruments, Tujunga, CA). A dorsal craniotomy exposed the central sinus and adjacent tissue.

Lambda and bregma were set at the same depth coordinates, creating a flat skull. Tracers were injected either mechanically (all FB, FG, Ctb-AF594, Ctb-AF488 injections) via a 0.5µl, 0.66µl or 1.0µl Hamilton pipette (Hamilton, Bonaduz, Switzerland) or iontophoretically. See Appendices (Supplementary Table A.1) for injection coordinates. Mechanical tracer injections were infused with a flow of 10-20 nl/min. In all cases, the needle was left in place for a further 10min before being retracted. As a part of the analgesia regime, lidocaine was administered topically to the scalp (0.1ml of 20 mg/ml solution; B. Braun, Melsungen, Germany) and meloxicam was given subcutaneously (0.06ml of 5mg/ml solution, Boehringer Ingelheim Ltd, Berkshire, UK). After 6-8 days post-injection, each rat was perfused followed by histological analysis.

4.4.3 Histology and tracing

At the completion of all experiments, rats received an overdose of sodium pentobarbital (Euthatal, Merial, Harlow, United Kingdom) and were perfused transcardially with 0.1M phosphate-buffered saline (PBS) followed by paraformaldehyde (PFA) perfusion (4% paraformaldehyde solution in 0.1M PBS) or with saline (0.9% sodium chloride solution) followed by 10% formalin perfusion (10% formalin in 0.9% sodium chloride solution). The brains were removed, stored in 10% formalin or PFA, followed by 25-30% sucrose solution (25-30% in 0.1M PBS), and finally frozen with dry ice. Sections were cut coronally (30-50μm) with a freezing microtome or cryostat and were mounted on glass slides. Tetrode locations were histologically verified from cresyl violet stained brain sections. Digital images were acquired with an Olympus microscope (Olympus Keymed, Southend-on-Sea, U.K.)

In cases with unconjugated CTB tracer injections, sections were first washed for 3x10 min in 0.1M PBS, washed 3 x 10min in PBS-TX (0.2% Triton X-100 in 0.1M PBS) and incubated with the primary antibody rabbit anti-CTB overnight (1:3000) (Sigma-Aldrich, UK). Sections were washed for 3 x 10min (PBS-TX) and incubated with the secondary antibody goat anti-rabbit (1:200) (conjugated to DyLight 594; Vector Laboratories, CA) for two hours. After a further 3 x 10min wash (PBS), sections were mounted. Sections were then further dehydrated (ethanol), defatted (xylene), and coverslipped with DPX. All slides were mounted in DPX or Vectashield antifade mounting medium (Vectorlab, H-1000). Slides from animal 717 were mounted in Vectashield antifade mounting medium with propidium iodide (Vectorlab, H-1300) which stained the nucleus red, while slides from animal 878 were mounted in Vectashield antifade mounting medium with DAPI (Vectorlab, H-1200) which

stained the nucleus blue. Slides were analysed for retrograde cell labelling in the AV, using epi-fluorescence microscopy for CTB, FG and FB labelling and brightfield microscopy for the single case with BDA label. For visualization purposes, FG labelled images were pseudo-coloured in cyan, CTB and Ctb-AF594 in red, Ctb-AF488 in green, and FB in blue.

4.5 Results

4.5.1 RSC electrophysiological experiment

4.5.1.1 Histology

For the analysis we only included four rats for which histology indicated that electrodes sampled both RSC subregions (electrodes advanced from dRSC into gRSC). The cell locations were estimated based on the reconstruction of the electrode tract from histology and the record of screw turns that lowered the electrodes each day, starting from a known DV within the dRSC. Figure 4.1 illustrates examples of brain sections in which the electrode track is clearly visible. The electrodes tip is marked and represents the deepest recording site. For one animal (R887), the tract suggested that electrodes were implanted more laterally and were advanced through the white matter tract of the cingulum fibers (Cg; Figure 4.1; see also Supplementary Figure A.2). This could explain the under-sampling of cells from this animal (Table 4.1, first row).

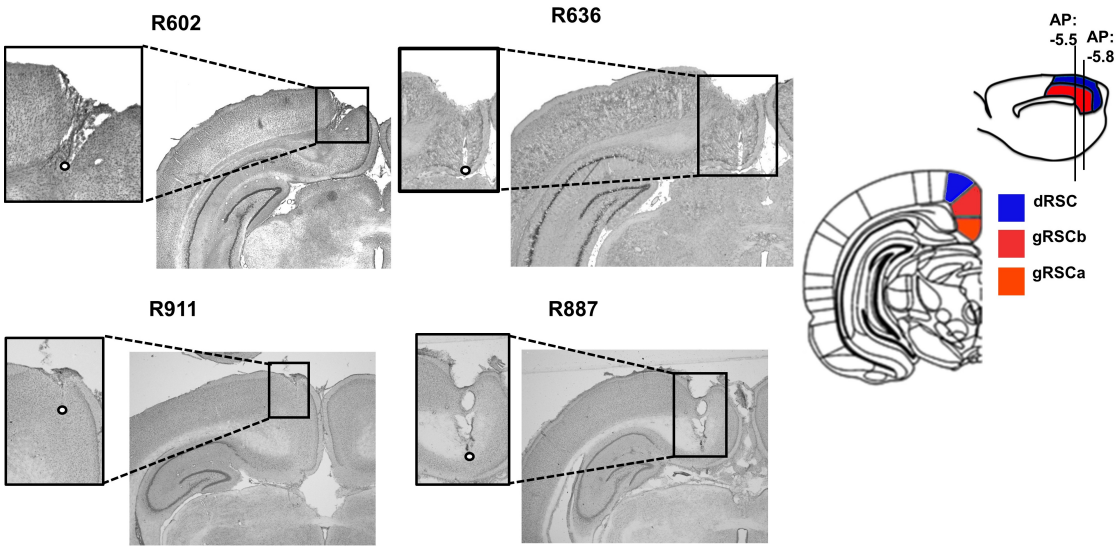


Figure 4.1: **Histology of RSC recordings.** . Left: Photomicrographs of the Nissl-stained coronal sections through the recording site, for each of the four rats implanted in RSC (left hemisphere). White dots depict the final electrode depth (location of electrodes tip on the day of perfusion). Top right: schematic of the AP-level (mm) of the recording sites within the RSC. R636 and R602, AP=-5.8; R911 and R887, AP=-5.5. AP-levels estimated based on the shape of cingulum fibers (Cg) and the width of the central sulcus (See Appendices, Section A.2). Middle right: schematic of the RSC subregions for a coronal AP level of -5.5, adapted from Paxinos and Watson (2007). Images for R602 and R636 were supplied by the authors of Jacob et al. (2017). See additional histology in Figure A.2.

4.5.1.2 The same LFP theta oscillations are recorded from gRSC and dRSC.

Consistent with previous work in freely moving animals, the LFP showed characteristic network patterns, including clear theta oscillations (Dillingham et al., 2019; Young and McNaughton, 2009; Borst et al., 1987; Talk et al., 2004). Theta oscillations from gRSC and dRSC did not differ in average peak Type 1 (movement-associated; Olvera-Cortés et al., 2002; Caplan et al., 2003) theta power and frequency (6-12Hz; Figure 4.2). Average peak theta power was 6.88±0.38 for gRSC recordings and 6.577±0.35 for dRSC recordings (WRS test, z=0.7, p=0.49). The associated average frequency was 8.73±0.14Hz for gRSC recordings and 8.63±0.16Hz for dRSC recordings (z=-0.84, p=0.40). The lack of differences between gRSC and dRSC LFP was maintained when the data were segregated according to animal (WRS test, all p>0.05).

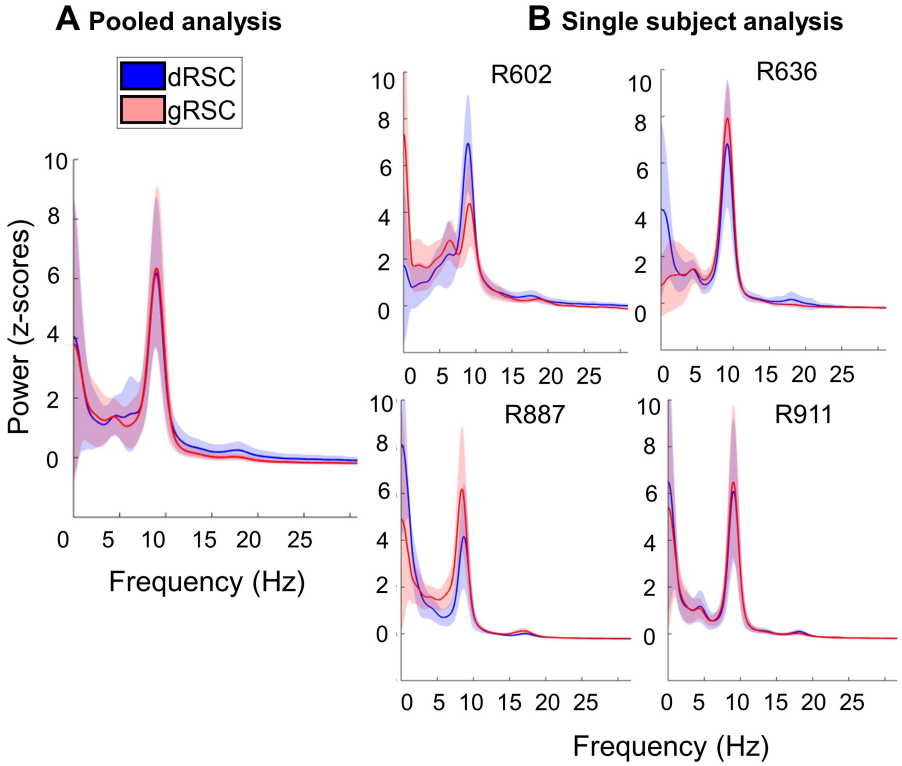


Figure 4.2: **Theta oscillations have the same power and frequency.** Theta oscillations have the same power and frequency. Average normalized power spectrum across all trials, **(A)** combined across all animals (n=4; pooled analysis), and **(B)** within each animal (single subject analysis). Shaded area is the standard deviation. X-axis, frequency (Hz); y-axis, power (z-scores). No difference in LFP theta oscillations were seen between gRSC and dRSC.

4.5.1.3 An anatomically organized theta-modulated cell population exists in the RSC.

We then looked at theta-band properties of spiking in single neurons. A total of 642 non-directional cells were analyzed from the four rats moving freely in the two-compartment box to determine whether there is differential coupling of gRSC and dRSC with the hippocampal navigational network, reflected in differential theta modulation. Single-cell results were obtained first after pooling cells across animals into a single distribution (pooled analysis), and second, from cells recorded for each animal individually (single subject analysis). Unless otherwise stated, the same results were observed in both analyses and between animals.

We first assessed whether cells were theta-modulated by determining their IC. Of the 642 non-directional cells identified, 292 cells came from gRSC and 350 from

dRSC. Of these cells, half (n=321/642, 50%) reached the criterion for significant theta modulation, based on the IC being greater than the 99^{th} percentile of the control distribution for that neuron. Table 4.1 reports a summary of recording locations and number of theta-phase-locked cells recorded in each RSC subregion for the four animals.

Despite the lack of LFP theta differences between gRSC and dRSC recordings discussed above, the distribution of theta-modulated cells varied considerably between RSC subregions, as indicated by the significance of a Chi-squared test for differences in proportions. Across all animals, 67.12% (196/292) of gRSC cells fired in phase with theta, compared to only 35.71% (125/350) of dRSC cells (χ^2=62.82; p<0.0001). Significant differences were confirmed when the data were segregated according to animals (all p<0.05), except for one animal (R887) for which differences did not reach significance (χ^2=0.12; p=0.73; Table 4.1). As already noted, for R887 there was under-sampling of gRSC cells (n=15 across 7 trials), possibly due to the tract trajectory passing through white matter tracts before reaching gRSC. We concluded that while the majority of gRSC non-directional cells were theta-modulated, the majority of non-directional cells in dRSC fired uncoupled from theta (see pie chart in Figure 4.6).

Table 4.1: **Distribution and electrophysiological properties of non-directional RSC neurons.**

Non-directional neurons						
	Area	R602	R636	R887	R911	All rats
No. of Trials		30	29	16	30	105
No. of non-directional theta-modulated cells	gRSC dRSC both	41/64 86/265 127/329	79/105 7/24 86/129	10/15 13/18 23/33	66/108 19/43 85/151	196/292 125/350 321/642
% of non-directional theta-modulated cells	gRSC dRSC	64%, 32%***	75%, 29%***	67%, 72%	61%, 44%*	67%, 36%***
Mean rate (Hz)	gRSC dRSC	4.08, 3.39**	4.91, 2.34***	5.88, 4.54**	4.52, 1.42***	4.63±0.5, 3.13±0.19**
Burst Index	gRSC dRSC	0.08, 0.04**	0.07, 0.03**	0.16, 0.04***	0.1, 0.02**	0.08±0.007, 0.04±0.003***
Index of phase coupling (IC)	gRSC dRSC	0.1, 0.06***	0.14, 0.06***	0.19, 0.07**	0.19, 0.08***	0.15 ±0.008, 0.06 ±0.003***
Index of Rhythmicity (IR)	gRSC dRSC	0.0001, -0.01	0.04, -0.01*	-0.01, -0.02	0.06, -0.05	0.04±0.27, -0.02±0.22***
Peak-to-Trough width (μs)	gRSC dRSC	258.13, 359.32***	318.29, 350	186.67, 377.78*	299.81, 373.95**	291.51±9.26, 361.43±7.39***

Table 4.1: Average for each animal and combined across animals, compared between gRSC and dRSC. For each rat, the following are reported: total number of trials, number of theta-modulated cells/ number of cells, electrophysiological properties. Significance of differences in proportions was tested using Chi-squared test for differences in expected proportions. Otherwise, multiple two-sample WRS tests were used. The level of significance of each test is indicated for each animal and across animals. The last column contains the results of the pooled analysis (average±SEM). The level of significance of each test is indicated for all within subjects and pooled comparisons.

Theta-strength (spike-LFP coupling) and rhythmicity (autocorrelograms) were assessed by computing IC and IR, respectively. At the single cell level, the average IC was significantly higher in gRSC compared to dRSC (IC: gRSC (292), 0.15±0.01; dRSC (350), 0.06±0.003; WRS test, z=-10.09, p<0.001). This reflects the overall larger proportion of theta-modulated neurons in gRSC (Figure 4.6), as well as the stronger theta modulation-depth within each of these neurons. In this respect, the firing of cells that reached the theta-modulation criterion in gRSC was considerably more phase-locked to theta compared to the same cells recorded in dRSC, which only displayed weak spike-LFP coherence (IC: gRSC (196), 0.2±0.01; dRSC (125), 0.1±0.01;

WRS test, z=7.17, p<0.0001; Figure 4.3). Significant IC differences were confirmed when the analysis was performed individually for each animal and no difference was observed between animals (Table 4.1; See Supplementary Figure A.3 for phase preference analysis of the theta-rhythmic neurons.

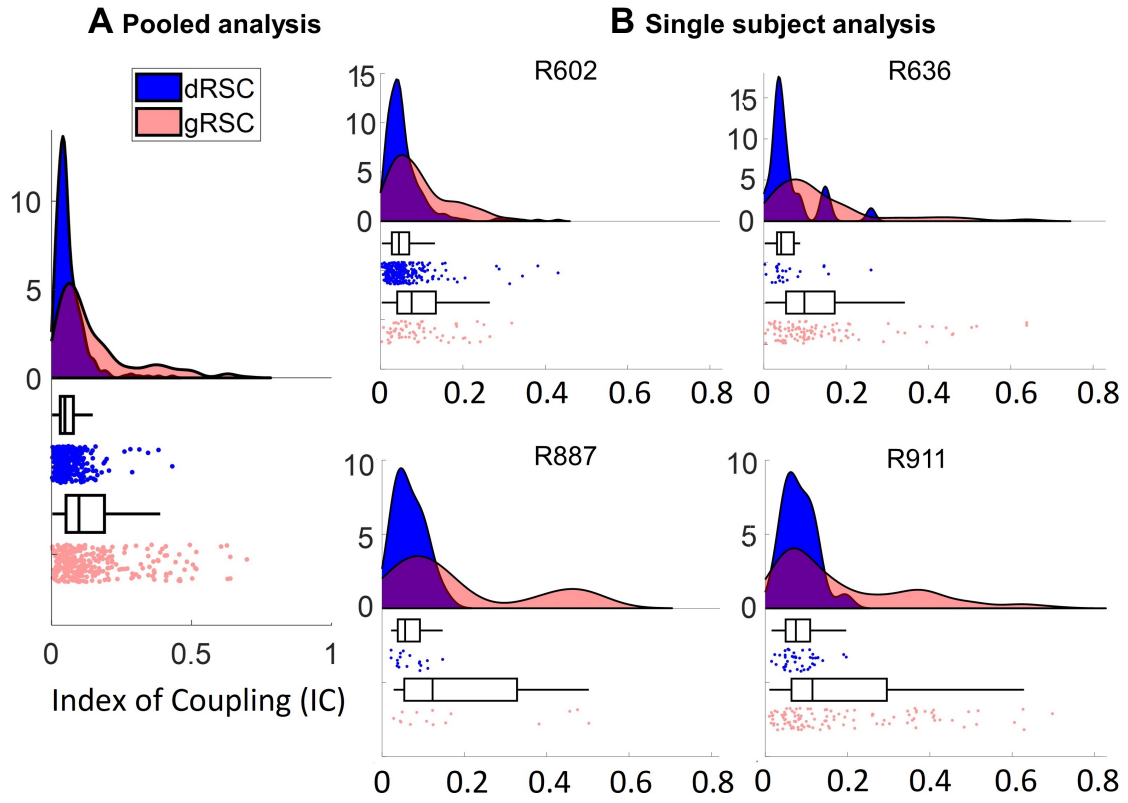


Figure 4.3: **Differences in theta-phase locking.** Distribution of ICs **(A)** for all cells and **(B)** within each animal. (C) Distribution of IC considering only cells with firing significantly coherent with theta (IC>99^{th} percentile shuffling). Data is shown as a split violin plot + raw jittered data point + boxplot. Split violin plots show the probability density function (PDF) of the observed data points. Each marker is a cell (dRSC, blue; gRSC, red). gRSC: the higher average IC reflects a larger proportion of neurons with firing locked to theta, as well as stronger theta-modulation depth within each neuron.

Average IR was significantly higher and more positive in gRSC compared to dRSC when all cells were pooled into a single distribution (IR: gRSC, 0.04±0.02; dRSC, -0.02±0.01; WRS test, z=-4.61, p<0.0001). In the single subject analysis, however, differences in IR did not reach a statistical significance in more than half of the experimental animals (3/4; only for R636; z=-2.09; p=0.04; Table 4.1), albeit in all cases averages were higher in gRSC compared to dRSC. This is because some neurons (total, 49.53%; gRSC, 42.86%; dRSC, 60%) with significant phase-locking

to theta did not show significant theta rhythmicity in their spike trains, suggesting spikes emitted at theta frequency for only brief periods of otherwise theta-unrelated spikes. This discrepancy, in which more cells fired phase-locked to theta than fired rhythmically, means that our classification criteria (based on IC) is sensitive to low amounts of locking, which can potentially occur in cells with non-rhythmical spiking, as previously reported for RSC (Eliav et al., 2018; Alexander et al., 2018, 2020a) and ATN neurons (Albo et al., 2003). Figure 4.4 displays examples of a theta phase-locked and rhythmic cell (high IC, IR>0.001), and a theta-locked but non-rhythmic cell (low/moderate IC, IR<=0.001). As can be seen, the main difference between the two cell types, aside from the autocorrelation differences (sinusoidal vs flat), is the degree of theta-modulation and height of the baseline firing (firing at low-excitability phases) that is visible in the spike-phase histograms (iii). Theta phase-locked and rhythmic cells exhibit strong locking to the theta cycle and low baseline firing outside of a narrow oscillatory range, whereas phase locked and non-rhythmic cells exhibit weaker, and sometimes virtually no locking to theta and a higher baseline firing.

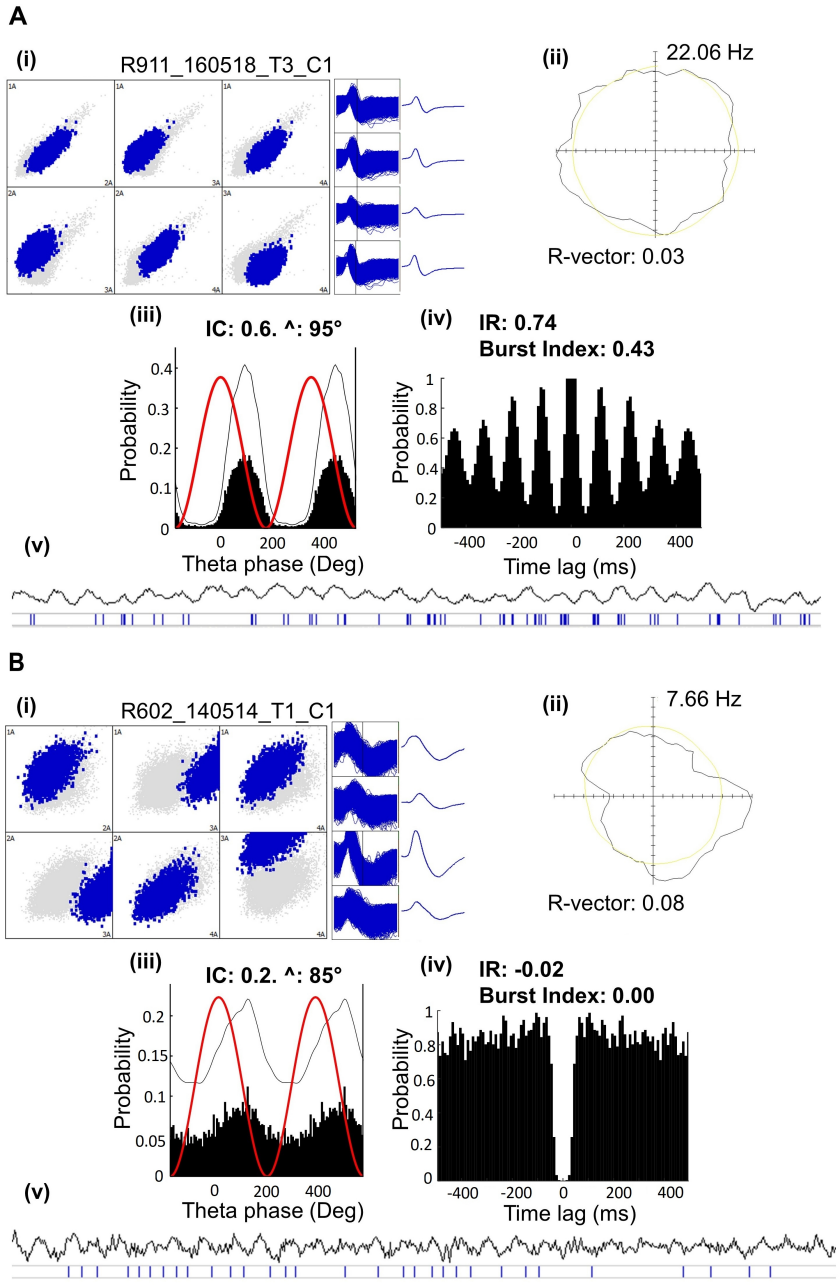


Figure 4.4: **Two types of theta cells: (A) theta coupled and rhythmic vs (B) theta coupled and non-rhythmic.** For each cell the following plots are shown: **(i)** Cluster space plots and associated tetrode spike waveforms. **(ii)** Polar plot of firing rate vs head direction, showing a uniform directional firing distribution (Hz). Peak firing rate is reported next to each plot. Thinner line circle indicates dwell time distribution (seconds). **(iii)** Double-plotted histogram of spike frequency relative to theta phases. The thin line is the corresponding smoothed density estimates (see Methods). The thicker line is the sine wave representing two theta cycles. For cell (B), the spike-phase histogram displays weak locking and elevated baseline firing. **(iv)** Spike time autocorrelogram showing theta-frequency rhythmicity for (A) but non-rhythmical

firing for (B). **(v)** Spike raster and corresponding unfiltered LFP signal recorded from the same tetrode. Each trace shows 3s of recordings. Cell (A) fires rhythmic spike trains, roughly corresponding to the frequency of LFP. In contrast, theta-modulation is not visually detectable in the LFP traces of (B), and here is based on IC>99^{th} percentile shuffling.

4.5.1.4 gRSC cells have higher firing rate and spike bursting propensity

In addition to differences in the intrinsic oscillation of single cells, gRSC and dRSC displayed a number of other interesting differences in their temporal firing properties. gRSC cells fired with significantly higher mean firing rates compared to dRSC (mean firing rate: gRSC, 4.63±8.61Hz; dRSC, 3.13±3.6Hz; WRS test, z=2.73, p<0.01). Furthermore, gRSC cells displayed a higher propensity to burst. In gRSC, 88/292 cells (30%) fired in bursts with peak ISI<10ms, compared to only 41/350 cells (11.7%) in dRSC (χ^2=33.65; p<0.0001). The prevalence of bursting units in gRSC was reflected in a significantly higher average burst index (burst index: gRSC, 0.08±0.01; dRSC, 0.04±0.01; WRS test, z=6.30, p<0.001).

Figure 4.5 shows examples of bursting and non-bursting cells. Among bursting cells, bursts were discharged rhythmically within theta frequencies in gRSC, but not dRSC where cells mostly burst at other frequencies (theta-bursting cells, gRSC, 76/88, 86.3%; dRSC, 17/41, 41.1%; χ^2=28.03; p<0.0001). Hence, theta-modulated cells were further subdivided into theta-modulated non-bursting units (gRSC, n=120 vs dRSC, n=108), and theta-bursting units (gRSC, n=76 vs dRSC, n=17). Theta-modulated units emitted compact spike trains at theta frequency, without bursts, as their ISI reached values>10ms. In contrast, theta-bursting units fired rhythmically at theta frequency with ISI <10ms. Differences in firing frequency and burst index were maintained when data were segregated according to animal, and again no difference was found between animals (all p<0.05; Table 4.1). Overall, these results confirm gRSC as a locus of theta-bursting neurons (Figure 4.6).

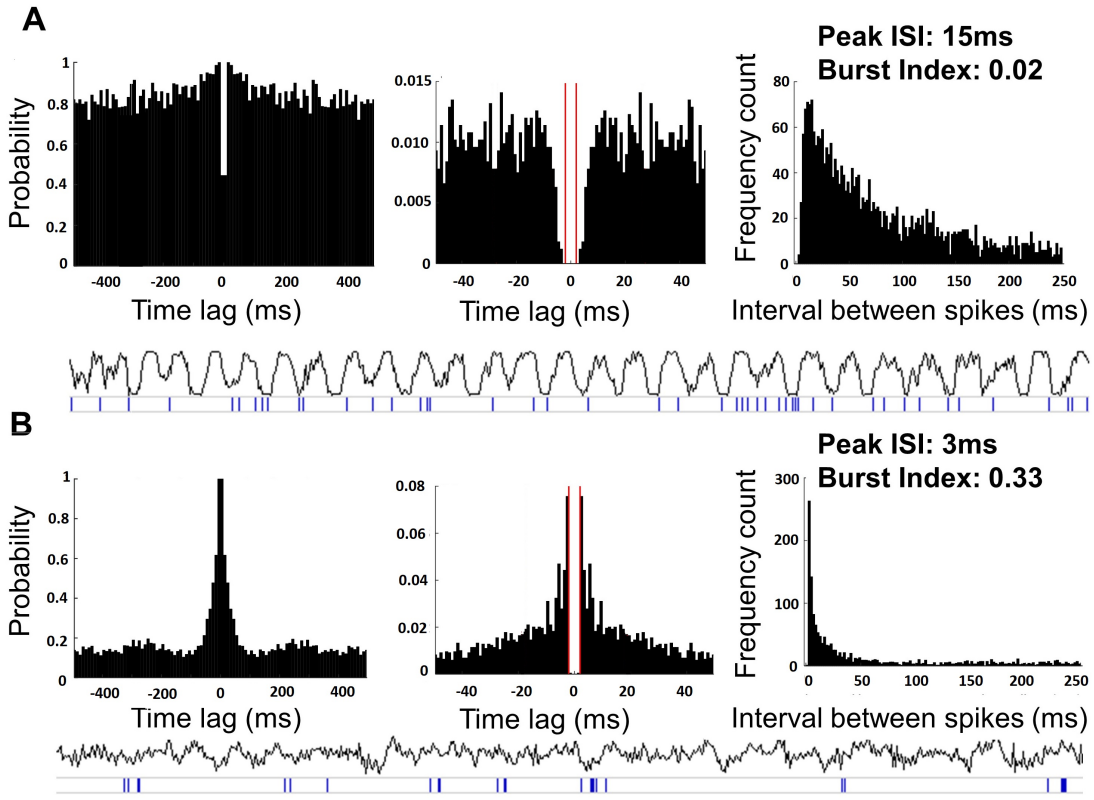


Figure 4.5: **Two types of temporal firing modes: (A) non-bursting vs (B) bursting.** Two examples of non-theta-modulated cells. The following plots are shown. From left to right: (1) Normalized spike time autocorrelogram implemented between ±500ms. (2) Temporal autocorrelogram implemented between ±50ms: gaps at intervals <2ms reflect the refractory period; (3) Inter-spike interval (ISI) histogram and (4) plots of spiking events (bottom) relative to the raw LFP trace (top). Non-bursting unit (A): fires single spikes (in groups of 1-2) and displays a prevalence of long ISI. Bursting unit (B): spikes are emitted in groups of 2-3 spikes separated by ISI <10ms, defined as a compact spike train. The prevalence of short ISI is reflected in a fast-decaying central peak of the ISI histogram and autocorrelogram, which can be contrasted to the less steep histogram peak in (A). Each spike train typically has a pause longer than 120ms before and after it, as firing is not aligned to theta.

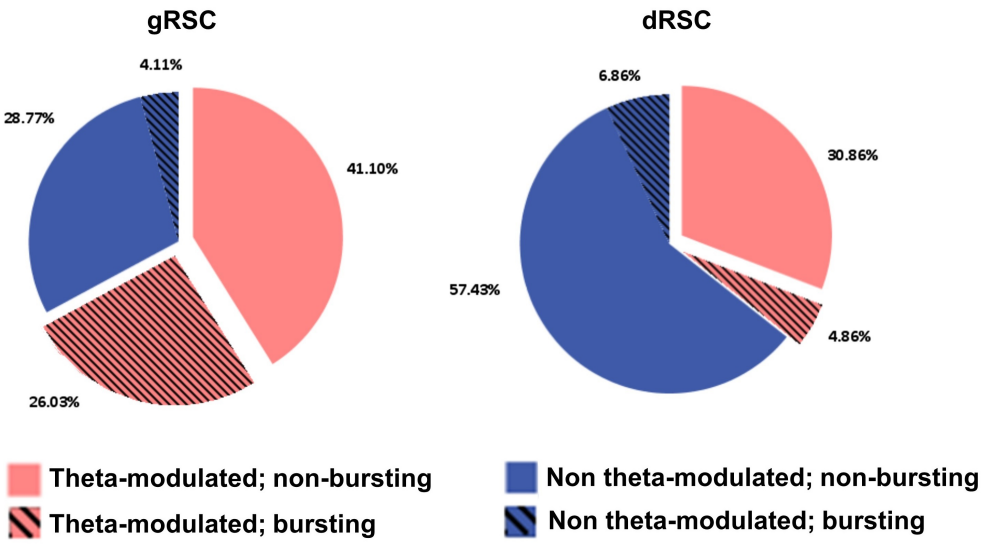


Figure 4.6: **Theta-modulated cells are concentrated in the granular subregion of the RSC (gRSC).** Theta-modulated and non-theta-modulated cells include bursting and non-bursting cells, divided based on peak ISI for the cell less than 10ms. gRSC: the majority of the cells fire coupled to the LFP theta, whereas most dysgranular RSC (dRSC) cells fire uncoupled from theta. gRSC also contains a higher proportion of bursting units, and the majority of these cells are theta-bursting. In contrast, dRSC contains only a marginal subpopulation of bursting cells, both theta and non-theta.

4.5.1.5 Waveform differences: theta phase-locked cells have narrower waveforms

Finally, we examined whether theta-modulated and non-theta modulated cells in RSC were also distinct in their waveforms. We first examined the distribution of peak-to-trough widths by fitting a two-Gaussian component, and two conservative cutoffs were identified on this model to separate cells into narrow, broad and in-between (see General Methods). We discarded 28 cases because spike waveforms did not reach time for repolarization. The analysis resulted in two modes (cell types): narrow spiking cells, 47.23%; broad spiking cells, 46.58%. A further 6.19% of cells were left unclassified based on values falling into the dip of the bimodal distribution (Figure 4.7). The calibrated Hartigan's Dip Test discarded the null hypothesis of unimodality (DIP=0.062; p<0.001). We then compared the firing characteristics of cells in the two groups identified by the model. Cells classified as the narrow spiking type displayed a higher proportion of theta-modulated cells (narrow, 196/290; broad, 99/286; χ^2=62.65, p<0.001; Figure 4.7) and significantly stronger theta phase locking (IC: narrow, 0.14±0.009; broad, 0.06±0.003; z=-6.80;p<0.001) compared to the broad type.

Cells were considered to be interneurons if the waveform peak-to-trough width was <250μs and mean firing rate was >5Hz (Henze et al., 2000; McCormick et al., 1985). We compared the proportion of interneurons between cell types and subregions. The proportion of interneurons was significantly higher among theta-modulated cells compared to non-theta modulated cells (theta-modulated: 63/321, 19.63%; non-rhythmic: 10/321, 3.12%; χ^2=43.42, p<0.001). As a result, this proportion was significantly higher in gRSC compared to dRSC, due to the higher concentration of theta cells (gRSC: 39/292, 13.36%; dRSC: 12/350, 3.53%; χ^2=21.45, p<0.001).

In agreement with the estimations based on comparisons of proportions, a two-way ANOVA conducted on waveform peak-to-trough widths found a main effect of cell type, F(1,1)=20.12, p<0.001, and brain region, F(1,1)=18.38, p<0.001, but no interaction, F(1,1)=3.57, p=0.06. According to these results, theta-modulated cells, predominantly found in gRSC, displayed considerably shorter waveform duration compared to non-theta modulated firing cells, predominantly found in dRSC (theta-modulated: 295.26±9.05μs; non-theta-modulated: 363.99±7.36μs; WRS test, z=-6.85, p<0.0001). Average peak-to-trough width for gRSC cells were as follows: theta-modulated (n=196), 266.02±11.54μs; non-theta-modulated (n=96), 343.54±14.08μs. Average peak-to-trough width for dRSC cells were as follows: theta-modulated (n=125), 341.12±13.66μs; non-theta-modulated (n=225), 372.71±8.58μs. Between-subjects analysis confirmed a narrower average waveform in gRSC compared to dRSC (gRSC, 291.51±9.26μs; dRSC, 361.43±7.39μs; WRS test, z=6.68, p<0.001). As seen in Table 4.1, this difference was repeated in the within-subject analysis, albeit in one animal it was not significant (R636; z=1.45; p=0.15). Results suggest that a higher number of theta-modulated cells are fast-spiking interneurons compared to cells that fire uncoupled from theta (Figure 4.7). Given that interneurons in RSC project to themselves and to pyramidal neurons within the limits of RSC (Brennan et al, 2020), theta-modulated cells likely project to local head direction cells and prime their firing for integrating inputs from other brain areas.

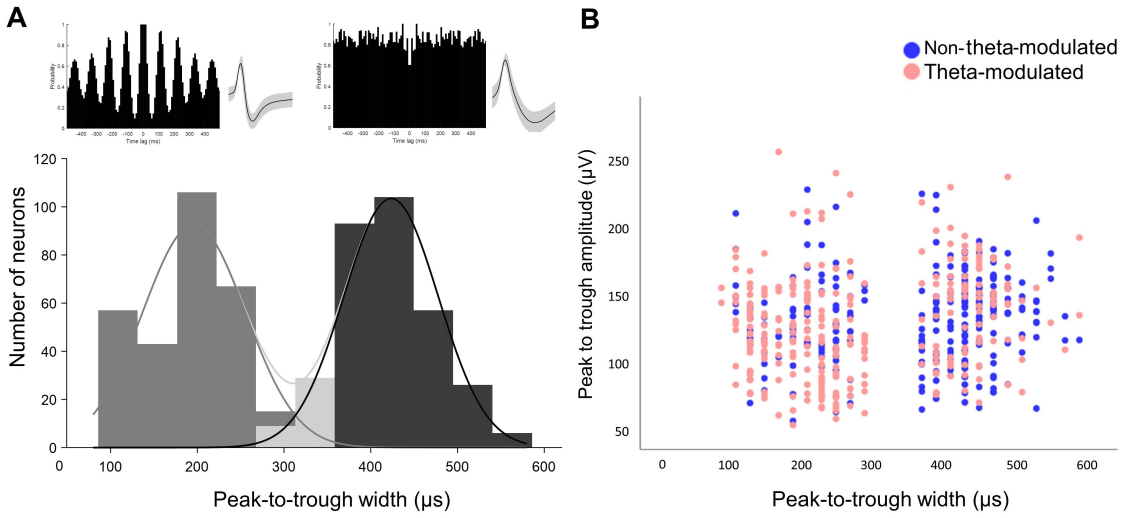


Figure 4.7: **Broad and narrow spiking cells display differences in theta-modulation strength.** **(A)** Distribution of the peak-to-trough width (μs) across all cells. Gaussian fits for the different modes (cell types) are displayed: broad (black), narrow (dark gray), and unclassified (light gray). Top, examples of autocorrelogram and averaged waveform for theta-modulated (left) and a non-theta-modulated (right) unit. Mean and standard deviation of the waveforms are shown. Theta-modulated cells tend to have spikes of shorter duration and a higher firing frequency than non-theta-modulated ones, suggestive of a higher prevalence of fast-spiking interneurons. **(B)** Waveform width of narrow and broad spiking cells in (A), plotted as a function of waveform amplitude (μV). A higher number of theta-modulated cells is found in the narrow group (n=196/290; 66.6%), whereas a higher number of non-theta-modulated cells is found in the broad group (n=187/286; 65.4%).

4.5.2 Retrograde tracing experiment results

We next compared, using retrograde tracers, the anteroventral thalamic projections to gRSC and dRSC to see if they might help to explain the RSC subregion electrophysiological differences. The initial analyses involved cortical tracer injections at or close to the AP levels (-5.5 and -5.8 from bregma) used in the electrophysiological studies. Next, we examined tracer injections appreciably more rostral or caudal within the RSC (see Table 4.2) with respect to the electrophysiological recording sites to determine the generality of any anatomical findings. The injections were made in two different laboratories (UCL, n=6 animals; Cardiff University, n=17 animals), providing an internal replication for our findings (see Supplementary Table A.1 for injection coordinates). All injections were made by Dr. Mathias Mathiasen (Cardiff University) and Dr. Han Yin Cheng (UCL).

When considering the location of each retrograde tracer, depth position was also noted, reflecting interest in the laminar termination of the anterior thalamic efferents to RSC and whether this feature might further distinguish some inputs. In some cases, especially those with CTB injections, the precise laminar position of the injection was difficult to determine precisely. This was particularly challenging for the superficial layers since these are thin and compressed in RSC. Therefore, when we designated injections as being either 'superficial' (s) or 'deep' (d), the criterion for 'deep' was that we could exclude involvement of layer I (leaving some uncertainty as to whether there might be limited involvement of layers II-IV in some cases).

Here, we first highlight the principal findings. We observed that AVVL was labelled after tracer deposits in both gRSC and dRSC, whereas dense cell label in AVDM only followed gRSC injections. This dense AVDM cell label was, however, only seen in a subset of the cases with gRSC injections. Further inspection revealed that AVDM label was strongly associated with obvious involvement of the most superficial gRSC layer by the tracer injection, consistent with a specific AVDM projection to superficial layer(s) of the gRSC. Meanwhile, AVVL projected more diffusely to both gRSC and dRSC. This pattern was repeated following injections positioned along different AP portions of the RSC; thereby, suggesting that these findings can be generalized to most, if not all, of the extent of the structure. In addition, repeated support was found for a previously described topography within AV, namely that ventral AV projects to more rostral RSC and dorsal AV projects to more caudal RSC (Shibata, 1993a).

Case No.	Injection site (electrode level))	Tracer	AV label	Laboratory Tracer
222#9	dRSC s+d	CTB	AVVL	Aggleton; Cardiff
222#10	dRSC s+d	CTB	AVVL	Aggleton; Cardiff
077941#13	gRSC (d)	CTB	AVVL	Aggleton; Cardiff
077942#14	gRSC d	CTB	AVVL	Aggleton; Cardiff
878	gRSC s (d)	Ctb-594	AVVL/AVDM	Jeffery; London
878	dRSC s+d	Ctb-488	AVVL	Jeffery; London
731	gRSC s+d	Ctb-594	AVVL/AVDM	Jeffery; London
731	dRSC s+d	FG	AVVL	Jeffery; London
730	gRSC s+d	FG	AVVL/AVDM	Jeffery; London
730	dRSC d	Ctb-594	(AVVL)	Jeffery; London
717	dRSC s+d; (M2)	FG	AVVL	Jeffery; London
729	dRSC s+d	FG	AVVL	Jeffery; London
682	gRSC s (d)	Ctb-594	AVVL/AVDM	Jeffery; London
Case No.	**Injection site (rostral/caudal)**	**Tracer**	**AV label**	**Laboratory Tracer**
187#9	gRSC d (s); (Rostral)	BDA	AVVL	Aggleton; Cardiff
64#3	dRSC s+d; (M2/V2); (Rostral + caudal)	FB	AVVL	Aggleton; Cardiff
172#27	dRSC s+d; (M2/V2); (Rostral + caudal)	FB	AVVL	Aggleton; Cardiff
172#28	dRSC s+d; (M2); (Rostral + caudal)	FB	AVVL	Aggleton; Cardiff
223#1	dRSC s+d; (Rostral)	CTB	AVVL	Aggleton; Cardiff
223#4	dRSC s+d/gRSC d; (Rostral)	CTB	AVVL	Aggleton; Cardiff
225#4	dRSC s+d; (Rostral)	CTB	AVVL	Aggleton; Cardiff
225#12	dRSC s+d/gRSC d; (Rostral)	CTB	AVVL	Aggleton; Cardiff
227#16	dRSC d; (Rostral)	CTB	AVVL	Aggleton; Cardiff

227#16	dRSC s+d/gRSC d; (Caudal)	FB	AVVL	Aggleton; Cardiff
227#22	dRSC s+d; (Rostral)	FB	AVVL	Aggleton; Cardiff
227#22	dRSC d; (Caudal)	CTB	AVVL	Aggleton; Cardiff
227#24	dRSC s+d; (Rostral)	FB	AVVL	Aggleton; Cardiff
227#24	gRSC d; (Caudal)	CTB	AVVL	Aggleton; Cardiff
227#202	gRSC s+d; (Caudal)	CTB	AVVL/AVDM	Aggleton; Cardiff
227#204	gRSC s+d; (Caudal)	CTB	AVVL/AVDM	Aggleton; Cardiff

Table 4.2: **List of all retrograde tracer injections (23 animals with a total of 29 injections).** Injection sites were made either at the electrode level (n=13) or at more rostral/caudal locations (n=16). Injection site indicates the center of the tracer deposit; s and d indicate "superficial" and "deep" layers of the granular retrosplenial cortex (gRSC) or dysgranular RSC (dRSC). The term "deep" is used here to indicate when layer I was not involved while "rostral" and "caudal" refer to the AP position with respect to the recording electrodes. Cases 64#3, 172#27, 172#28 had multiple injections, at both rostral and caudal dRSC locations. Those regions and layers in parenthesis indicate weak involvement in the injection site. The third column indicates the subfield of the anteroventral thalamic nucleus (AV) with densest cell label resulting from the injection. AVDM, dorsomedial subfield of the AV; AVVL, ventrolateral subfield of the AV. Tracers are as follows. FB, fast blue; CTB, cholera toxin subunit b; BDA, biotinylated dextran amine; FG, fluorogold.

4.5.2.1 Injections at the level of recording

Thirteen retrograde tracer injections (n=10 animals) targeted RSC at approximately the same AP levels as the recording sites (for representative injections see Figure 4.9; all injection sites reported in Table 4.2). In three cases (730, 731, 878), dual injections were made, one in dRSC (n=6) and the other in gRSC (n=7; Table 4.2). For dRSC, all injections included portions of both deep and superficial layers except a single injection (case 730) restricted to the deep layers.

In all cases, retrogradely labelled cells were present in the ipsilateral thalamus, with varying amounts of label in AD, AV, and the anteromedial nucleus (AM). Whereas both gRSC and dRSC injections consistently resulted in widespread AD labelling, the distribution of labelled cells within AV differed between the two injection sites.

In all cases with injections largely confined to dRSC, retrograde cell label was virtually restricted to the ventrolateral (AVVL) subfield of the AV nucleus (e.g.,

cases 222#9, 222#10). In contrast, in four of the six cases that targeted gRSC (cases 682, 730, 731, 878), retrograde cell label was observed in both AV subfields, i.e., AVVL and dorsomedial AV (AVDM). The two remaining gRSC cases (077941#13, 077942#14) contained label in both AVVL and AVDM, but the preponderance was in AVVL (Figure 4.9).

The overall pattern of differences (AVVL to dRSC; AVVL and AVDM to gRSC) can be observed in Figure 4.9, which provides a schematic depicting the AV area with the densest cell body labelling across the various injection cases (label in AD is not shown). In further support of this difference in AV innervation, Figure 4.10 shows photomicrographs of the two different patterns of AV labelling in a single case (878) that had injections in both dRSC and gRSC.

We then correlated the variations in labelling with variations in injection site. For gRSC, in the four cases with combined AVDM/AVVL label the injection site included both deep and superficial layers (cases 682, 730, 731, 878), whereas in two cases where the label was predominantly in AVVL, the gRSC injections were restricted to the deep layers (cases 077941#13, 077942#14; see Figures 4.8 D, E; 4.9). This difference implies that the AVDM projection preferentially terminates in more superficial gRSC.

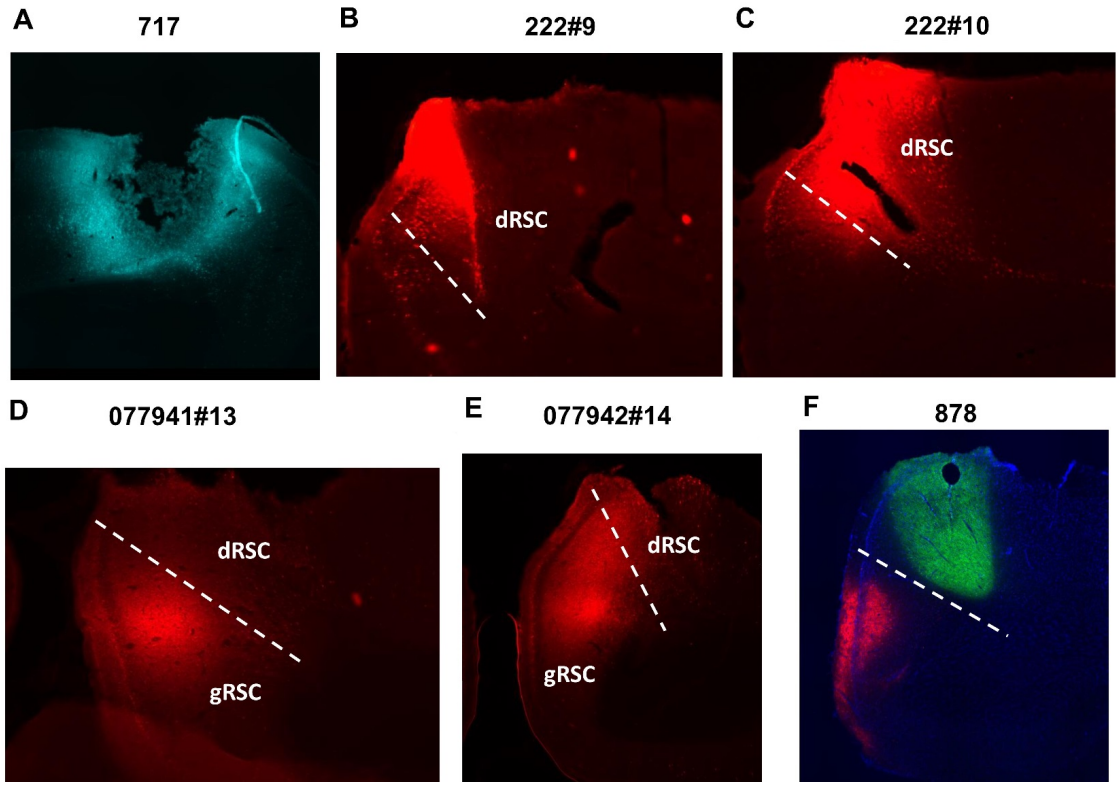


Figure 4.8: **Injections in retrosplenial cortex (RSC) made at the electrode recording levels.** Cholera toxin subunit b (CTB) and fluorogold (FG) injections in **(A-B-C)** dysgranular RSC (dRSC, both superficial and deep layers) and **(D-E)** granular RSC (gRSC, mainly deep layers). **(F)** Dual injection in granular (mainly superficial layers) and dysgranular (superficial and deep layers) RSC. AP level: -5.5mm. 30μm slides analyzed with epi-fluorescence microscopy. Scale bars 200µm.

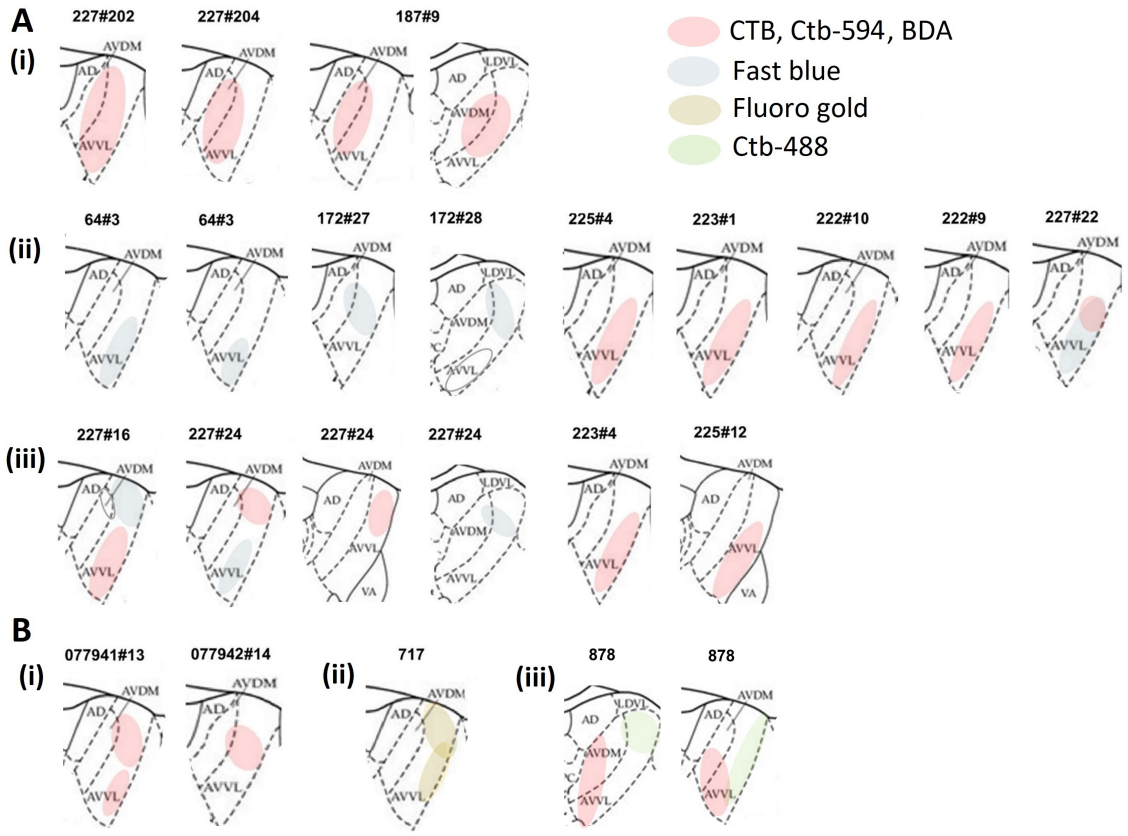


Figure 4.9: **Ventrolateral AV (AVVL) projects to both gRSC and dRSC, dorsomedial AV (AVDM) projections are more restricted to superficial layers of gRSC.** Schematics showing areas of retrograde cell labelling in AV. **(A)** Tracer injections rostral or caudal of electrode level; **(B)** injections at the electrode level. **(i)** AV label in cases of single tracer injection in gRSC. **(ii)** AV label in cases of single injection or multiple injections (64#3, 127#27, 127#28, 227#22) in dRSC. **(iii)** AV label in cases with combined gRSC and dRSC tracer injections. Cases 227#16, #24 and 878 have dual injections placed in dRSC and gRSC. Cases 223#4 and 225#12 had single injections involving both gRSC and dRSC. Areas of label are color coded according to tracer type (see legend). For cases 227#16 and 172#28 there was weak additional labelling in AVDM and AVVL respectively, resulting from FB injection in dRSC (empty circles). Abbreviations: AD, anterodorsal thalamic nucleus; AVVL and AVDM, ventrolateral and dorsomedial subfields of the anteroventral thalamic nucleus; VA, ventral anterior thalamic nucleus; LDVL, ventrolateral subfield of the laterodorsal thalamic nucleus.

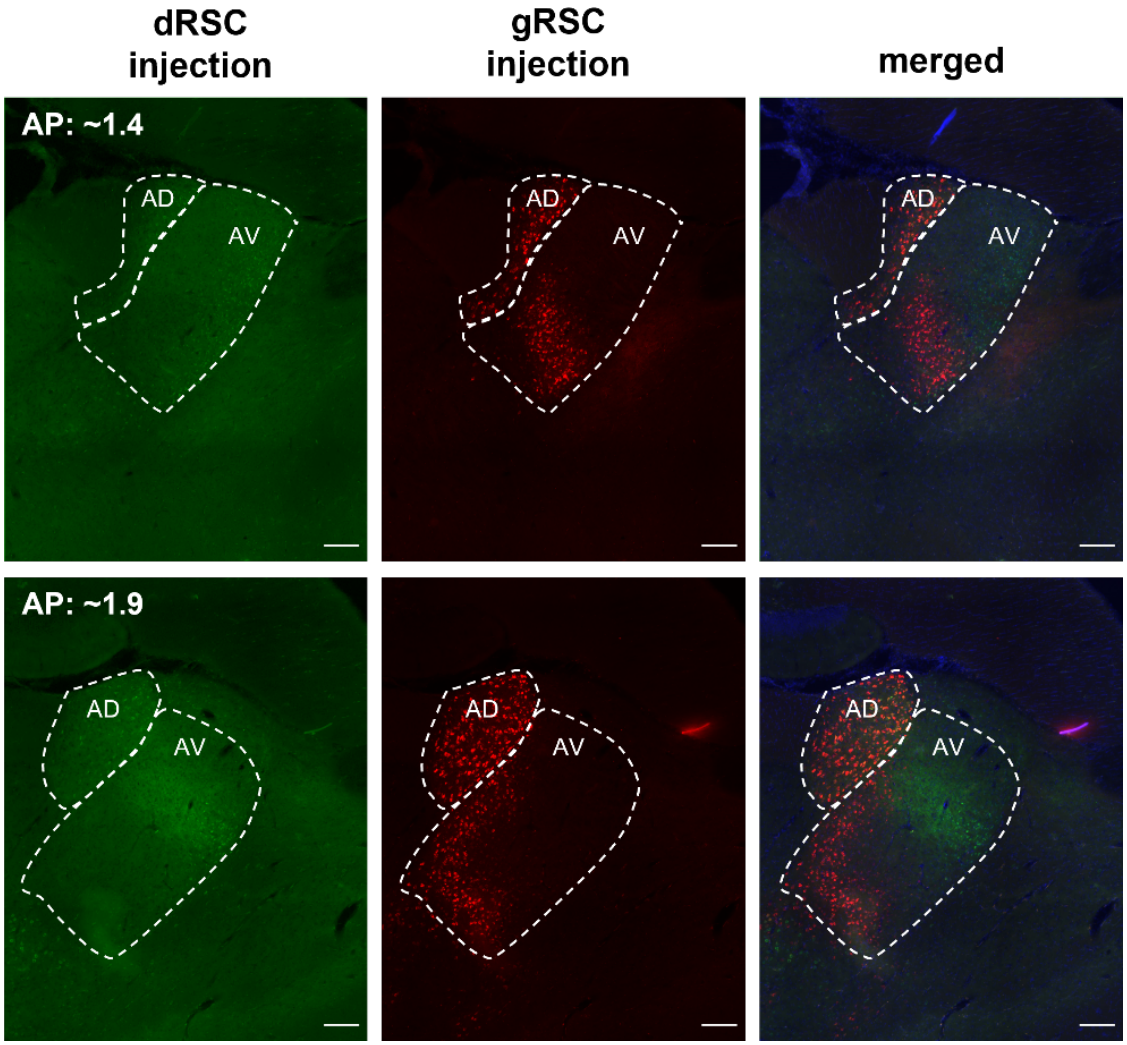


Figure 4.10: **Contrasting patterns of AV retrograde label from separate gRSC and dRSC injections.** Case 878 had dual tracer injections, one in dRSC (CTB-488 green) and one in gRSC (CTB-594 red). See injection sites in Figure 4.8. The photomicrographs show separate and combined images for two different AP levels within the same animal (borders of nuclei indicated by dashes). Cell bodies labelled with CTB-488 (green; dRSC) are concentrated in lateral AV, corresponding to AVVL (with fiber labelling more medial), whereas CTB-594 label (red, gRSC centered in superficial layers) is also present more medial, i.e., in both the AVVL and the AVDM subfields (see Figure 4.9 for schematic). Scale bars 200μm.

4.5.2.2 Injections at more rostral and caudal RSC locations.

In a further sixteen retrograde tracer injections (n=13 animals), we targeted portions of RSC>0.5mm rostral or caudal to the electrophysiology recording sites (Table 4.2; for representative injections see Supplementary Figures A.4-A.5). Of these, six injections

were from three cases with dual tracer injections at different AP levels (Supplementary Figure A.4). Nine tracer injections seemed restricted to the dRSC, four to the gRSC and three included both RSC subregions (Supplementary Figure A.5). These dRSC injections included both superficial and deep layers, except for two cases where the injections appeared restricted to deep dRSC (rostral 227#16, caudal 227#22). Irrespective of AP level, we observed consistent labelling differences after dRSC and gRSC injections (Supplementary Figure A.4) that closely matched those differences seen when the injections were placed at the level of the electrodes. Once again, dRSC injections were consistently associated with AV label in AVVL (only occasionally extending marginally into AVDM towards its dorsal border), while gRSC injections resulted in label in both AVVL and AVDM (Figure 4.9).

Further examples of these differential patterns of AV label can be see in Figure 4.11. This figure contrasts when a tracer injection involved both dRSC and gRSC, versus when it was located in just the dRSC subregion. An injection of CTB involving both RSC subregions resulted in extensive cell labelling across both AVDM and AVVL (case 227#202; Figure 4.11 A, B). Meanwhile in a separate case with dual injections (case 227#16) the rostral dRSC injection (CTB, red) resulted in ventral AVVL label, while the caudal fast blue injection (primarily dRSC but also deep gRSC) labelled dorsal AVVL (case 227#16; Figure 4.11 C, D). This same case highlighted the dorsal-ventral topography within AV (ventral to rostral RSC, dorsal to caudal RSC).

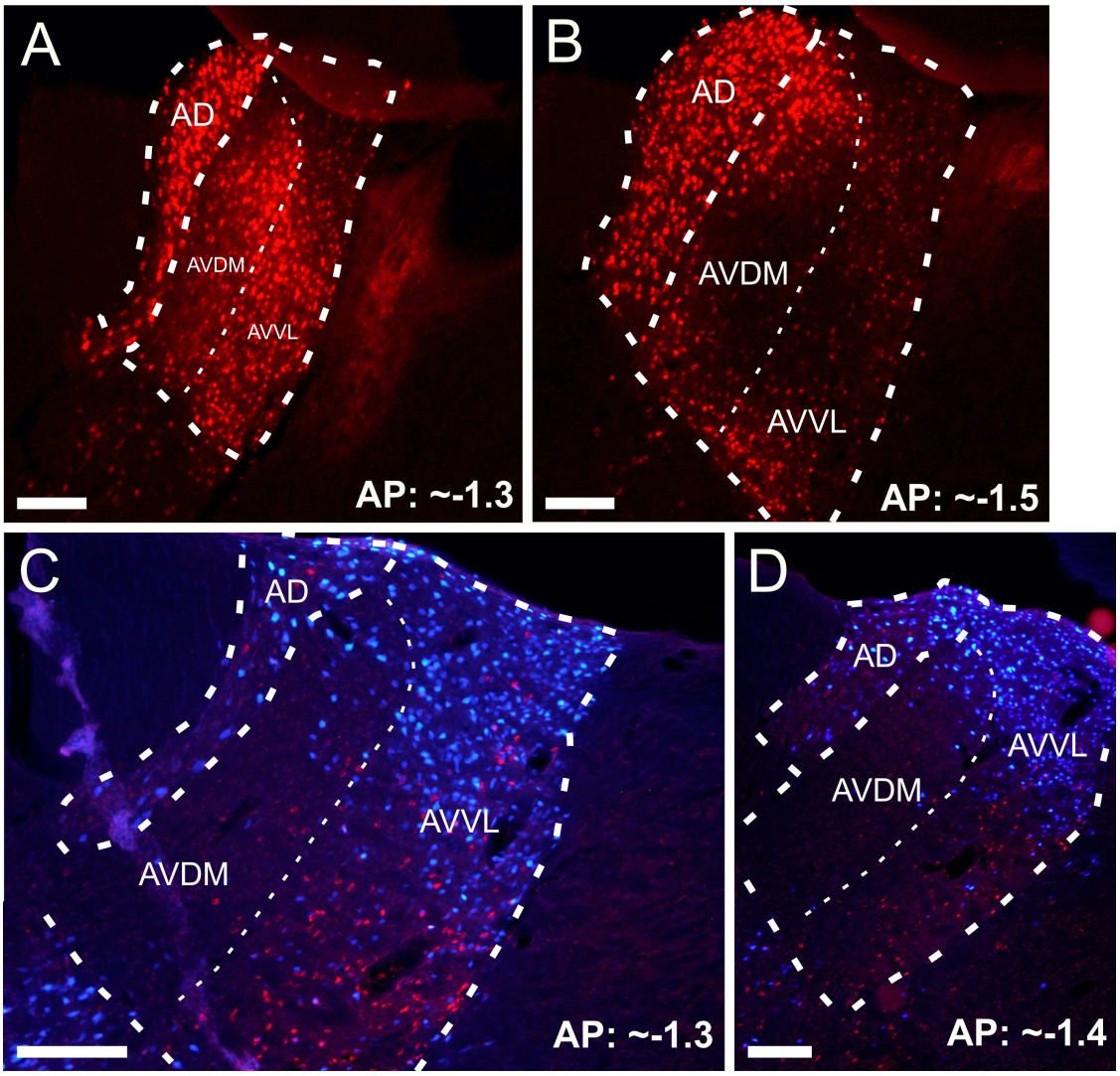


Figure 4.11: **Injections involving both gRSC and dRSC (upper) produce label across AVDM and AVVL, while dual dRSC injections (lower) leave label restricted to AVVL.** Photomicrographs of AV and AD depicting retrograde cell label after retrosplenial injections. **(A-B)** Cell label following a CTB injection in gRSC (case 227#202, superficial and deep layers). Retrograde labelled cells are seen in both AV subfields. See injection sites in Supplementary Figure A.5. **(C-D)** Retrograde labelled cells following dual injections in dRSC at rostral (CTB) and caudal (FB) portions (case 227#16). See injection sites in Supplementary Figure A.4. For both injections, cell labelling is predominantly present in the AVVL subfield, with more scattered cell label in the AVDM subfield (see Figure 4.9 for schematic). Two different APs are shown for the same animal. AD, anterodorsal thalamic nucleus; AVDM, dorsomedial subfield of AV; AVVL, ventrolateral subfield of AV; AV, anteroventral thalamic nucleus. Scale bars 200μm.

In case 227#24 (Figure 4.12) separate injections were placed in rostral dRSC (CTB, involving deep and superficial layers) and in caudal gRSC (fast blue, deep layers;

see also schematic Figure 4.9). This and other cases with dual injections positioned at rostral and caudal portions of the RSC (cases 227#22 and 227#24, 227#16; Figures 4.11-4.12) further supported the previously described topographical pattern (Shibata, 1993): namely, that ventral AV preferentially projects to the rostral RSC whereas dorsal AV targets caudal RSC (see Figure Figure 4.11 C, D). This topography appeared to be independent of the involvement of a specific RSC region (e.g., both injections are in dRSC in case 227#22).

This same gRSC injection (227#24) showed a clear preponderance of AVVL cell label (Figure 4.12), whereas three other cases with gRSC injections resulted in combined AVVL/AVDM cell label (cases 187#9, 227#202, 227#204; as also described above for the gRSC injections close to the AP of the recording sites see Figures 4.8-4.9). Further inspection revealed that the single case with restricted AVVL label (227#24) had a gRSC injection largely confined to its deep layers, whereas the three cases with further AVDM involvement had either obvious (case 227#204; 227#202) or likely (case 187#9; Supplementary Figure A.5) involvement of superficial layers in the injection sites. These observations support the earlier conclusion that it is particularly the superficial layers of gRSC that receive AVDM projections. In further agreement, the three remaining cases with combined gRSC/dRSC injections had cell label in AVVL (but not AVDM) and in these cases the gRSC portion of the injection sites seemed largely contained within the deep layers (cases 225#12, 225#4, 227#16). As none of our rostral gRSC injections clearly included the most superficial layers, some uncertainty remains as to whether AVDM targets gRSC at its most rostral portions.

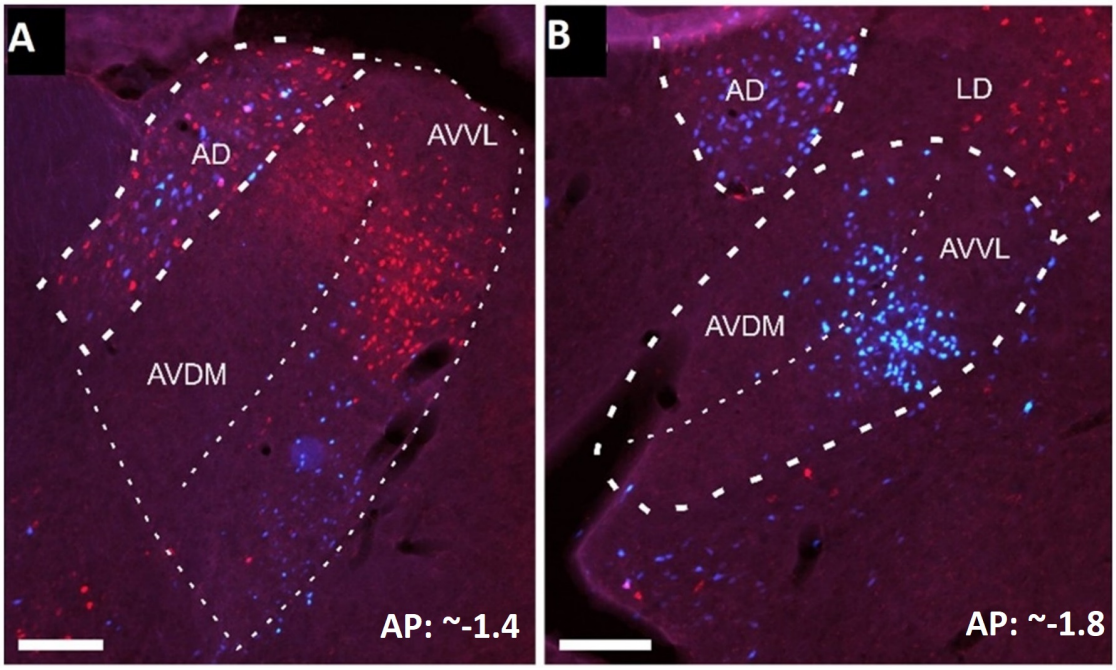


Figure 4.12: **Tracer injection confined to deep gRSC layers resulted in AVVL cell labelling, akin to dRSC injections.** Photomicrographs of AV label after combined injections in caudal gRSC (deep; cholera toxin-b) and rostral dRSC (superficial and deep; fast blue), at two different AP levels for case 227#24. See injection sites in Supplementary Figure A.4. AVDM and AVVL labeling is region-specific and layer-specific: unusually for a gRSC injection, the retrograde label (red) was largely confined to AVVL, potentially reflecting the deep location of the tracer injection. The conclusion is that superficial and deep gRSC layers receive segregated projections from AVDM and AVVL, respectively. Two different APs are shown for the same animal. Abbreviations: AD, anterodorsal thalamic nucleus; AVDM, dorsomedial subfield of AV; AVVL, ventrolateral subfield of AV; LD, laterodorsal thalamic nucleus; AV, anteroventral thalamic nucleus. Scale bars 200μm.

4.6 Discussion

As part of an ongoing attempt to understand the contribution of retrosplenial cortex to spatial memory processing, we investigated what distinguishes its two principal subregions, granular (gRSC) and dysgranular (dRSC). Recent findings of landmark-sensitive directional neurons restricted to the dysgranular region only (Jacob et al., 2017) have suggested that RSC may comprise two subcircuits, one (gRSC) more connected to hippocampus and the other (dRSC) more connected to sensory cortices (Aggleton et al., 2021). We thus investigated whether there are electrophysiological or anatomical differences that shed light on this dichotomy. With electrophysiology, we

compared the temporal firing characteristics, waveform characteristics and relation to the local LFP of non-directional cells recorded from gRSC and dRSC during free exploration in rats, finding greater coupling with theta oscillations in gRSC compared to dRSC. Anatomically, we used retrograde tracing to label gRSC and dRSC projections from one of the main inputs to RSC, the anteroventral thalamus, to see if there might be differential projections from this nucleus; we found that both dorsomedial (AVDM) and ventrolateral (AVVL) subfields of the AV project to gRSC. However, AVDM projects almost exclusively to gRSC and this projection mainly involved superficial layers. In contrast, the AVVL projection to gRSC involved deep layers, and AVVL additionally projects to dRSC, targeting both deep and superficial layers. Below, we examine these findings, and then conclude with some speculations about the possible functional role of these two thalamocortical subcircuits.

4.6.1 Increased theta coupling in gRSC

Comparison of the two subregions (in both pooled and single subject analysis) revealed that gRSC had a much higher mean IC (index of theta phase-coupling), firing frequency and spike-bursting propensity, and theta-modulated cells in this region exhibited considerably larger theta-modulation depth. However, we found no difference in LFP theta oscillations between the two subregions, highlighting a dissociation between theta rhythms in the LFP and oscillations present at the single cell level i.e., theta rhythms are not generated uniquely from local ensemble activity within gRSC, in line with prior results (Young and McNaughton, 2009; Borst et al., 1987; Talk et al., 2004). These observations raise two questions: what causes these differences and what, if any, are their functional implications?

One possibility is that these signals are a consequence of differential network connectivity between gRSC/dRSC and the medial septum, considered as the main hippocampal theta pacemaker. Septal GABAergic neurons expressing theta-rhythmic bursting innervate both CA1 and gRSC – but dRSC much less so – with a common projection pattern (Unal et al., 2015, 2018; Viney et al., 2018). They selectively target and inhibit GABAergic interneurons, resulting in a rhythmic disinhibition of the principal neurons, the activity of which thus becomes phase-locked to septo-hippocampal theta. Rhythmic disinhibition supplied by the medial septum has been demonstrated to pace the synchrony of hippocampal theta activity (Hangya et al., 2009) and could offer a similar explanation for the concentration of theta cells in

gRSC. Given the lack of septal input to dRSC, some dRSC neurons might become locked to theta indirectly via cell-to-cell projections from gRSC theta cells.

An alternative possibility is that theta is modulated by the strong anterior thalamic projection to RSC (both gRSC and, more moderately to, dRSC). Like cells in the medial septum, theta rhythmically discharging cells in the AV fire locked to the local and hippocampal theta oscillations, and these oscillations are strongly coherent (Albo et al., 2003; Vertes et al., 2001; Tsanov et al., 2011, 2010). The MMN distribute massively to the AV via the mammillothalamic tract (Seki and Zyo, 1984; Shibata, 1992), and projects to the AV a theta signal that combines tegmental, septal, and hippocampal theta activity (see reviews by Vertes et al., 2004; Vertes and Kocsis, 1997). A role of the mammillary bodies-AV axis in complementing the septo-hippocampal theta system (Zakowski et al., 2017; Ruan et al., 2017) may explain the occasional report of theta oscillations in gRSC that persist or are enhanced in the absence of hippocampal theta (during hippocampal large amplitude irregular activity, Young and McNaughton, 2009; or electrolytic septal lesions, Borst et al., 1987). A third possibility is that gRSC inherits theta rhythmicity via its stronger afferent connections with the dorsal hippocampus, both from CA1 (Haugland et al., 2019; Opalka et al., 2020; Unal et al., 2015) and subiculum, which is the major output of the hippocampus and sends a strong projection to gRSC, but not dRSC (Meibach and Siegel, 1977). We emphasize that these options are not mutually exclusive. Thus, the AV may exert an excitatory rhythmical influence on target cortical neurons receiving converging hippocampal or septal projections (Yamawaki et al., 2019), which may be crucial for allowing a subcortically-mediated regulation of coordinated hippocampus-RSC communication (Chambers et al., 2021).

The second major question arising from the differential theta coupling observed between gRSC and dRSC is what, if any, might be the functional consequences. Theta is widely thought to have the function of synchronizing the excitability of brain regions throughout the hippocampal formation (Korotkova et al., 2018), perhaps to facilitate information transfer or synaptic plasticity. Within hippocampus itself, each theta cycle contains a sequential activation of hippocampal neurons (usually manifesting as place cells) and may function to organize sequential information as part of a spatio-temporal memory system. It may be that gRSC with its greater hippocampal connectivity has the role of mediating between incoming sensory information and ongoing spatial computations, with theta facilitating the transfer and maintaining the spatio-temporal organization. We will return to this point later.

4.6.2 Differential AV projections to gRSC and dRSC

Our dataset of retrograde tracer injections adds to previous anatomical descriptions of anterior thalamic inputs to RSC. Overall, in agreement with previous studies, a topography emerged from our tracing studies such that ventral AV projects to rostral RSC while dorsal AV projects to caudal RSC (Shibata, 1993a). Within AV, we found a clear differentiation of AVDM and AVVL projections to the gRSC and dRSC, in line with previous anatomical evidence in rabbits (Shibata and Yoshiko, 2015). The AVVL subfield targeted both retrosplenial subregions, providing moderate fiber input to both superficial and deep layers (see also Van Groen and Wyss, 1990a, 1992, 2003; Shibata, 1993). In contrast, the AVDM subfield provided a selective projection to the gRSC; mainly to the superficial layers (Shibata, 1993a). Overall, the present results argue for the presence of two related but distinct AV-RSC subcircuits: AVVL to dRSC, AVVL and AVDM to gRSC.

Two anatomical facts are relevant for clarifying the observed variations in the electrophysiology data between gRSC and dRSC. First, the difference in the overall projection strength to the two RSC subregions should be noted, in addition to the topographical organization of AV projections from within AV to each of these subregions (Shibata, 1993a). In relation to the first point, our data demonstrate stronger AV projections to gRSC compared to dRSC (see also Van Groen and Wyss, 2003). Second, there are differences in the source of these projections from different AV subfields. Superficial gRSC layers receive a distinct projection from AVDM, which sends no or only moderate projections to dRSC. In contrast, dRSC only receives a portion of the widespread AVVL projections that target both retrosplenial regions, including their deep layers. Hence, observed differences in theta modulation across the RSC might not simply be an effect of variations in AV fiber density (stronger AV to gRSC) but may also be explained by considering anatomically distinct cell populations within the AV projecting to the two RSC subregions.

4.6.3 Two interacting thalamocortical subcircuits

Previous behavioural, connectivity and neuroanatomical evidence, together with our current findings, combine to indicate that the RSC is not a unitary structure (Aggleton et al., 2021). The gRSC is more strongly coupled with the hippocampal formation, as evidenced by both anatomical connectivity and theta-modulation: the latter of which accords with the fact that theta is a distinguishing feature of neurons

in brain regions that are linked to the hippocampal spatial system (Burgess et al., 2002; Buzsáki, 2002, 2005; Buzsáki and Moser, 2013; Hasselmo and Eichenbaum, 2005). By contrast, dRSC is dominated by visual interactions (Fischer et al., 2020; Powell et al., 2020; Keshavarzi et al., 2021b; Pothuizen et al., 2009; Cooper et al., 2001; van Groen and Wyss, 1990b,c,a). Our findings add to this picture by showing that the gRSC is part of a subcircuit that connects the AV (both AVDM and AVVL) to the septo-hippocampal network, with AVDM providing a selective contribution to this network, via gRSC. dRSC is part of a parallel subcircuit that connects AVVL with sensory cortices. This conclusion is bolstered by the recent findings of Jacob et al. (2017) and Alexander et al. (2020a), who demonstrated stronger visual responsiveness in dRSC directional signals and coding of egocentric information in dRSC, which suggested a partial uncoupling from the main head direction signal.

While these results suggest a functional differentiation within the AV-RSC circuit, an additional dichotomy may exist within gRSC (in deep vs superficial layers). This is consistent with findings that gRSC neurons can exhibit large-scale responses to visual cues (Vedder et al., 2017). Hence, the RSC (as a whole) could be seen as a site for integration of allothetic (visual) and idiothetic (mnemonic) information, and yet visual information may first gain entrance to the HD network via dRSC, from neocortical areas, given the lack of direct visual input to ATN (Seki and Zyo, 1984; Shibata, 1992). Regardless of how visual responses in RSC could arise, it is now clear that heterogeneity exists in respect to theta coding in RSC, and so the interaction of RSC with the hippocampal formation should not be considered as single unit but should be considered according to each subregion.

Based on this evidence, it can be predicted that there are differences in neural activity between AVDM and AVVL. This prediction may be partially supported by the finding of Gabriel (1993), who showed differential learning-related changes in firing between different subfields of the AV during instrumental discriminative avoidance in rabbits. Future work will need to determine the distinct physiological properties of AVDM neurons, and the consequence on gRSC processing of removing this projection. The question thus arises: why does the brain maintain these separable subsystems?

One possibility is that this separation allows for the comparison of two information streams that may agree or differ in their content, and thus allow for comparison and appropriate error correction. The streams in RSC comprise interoceptive signals arising from subcortical regions and exteroceptive signals coming in from the sensory periphery. A specific example of these converging information

streams is provided by the RSC head direction signal, which arises from convergence of self-motion inputs (primarily interoceptive cues such as vestibular signals, motor efference and proprioception) and static environmental information from the sensory cortices (Yoder and Taube, 2014). The findings of Jacob et al. (2017) that directionally tuned neurons in dRSC operate independently of this consensus head direction signal have suggested that RSC may be the site of weighted cue integration between the current estimate of head direction and incoming sensory information (Page and Jeffery, 2018). A similar principle may account for RSC processing more generally: that is, the gRSC input from AD may supply an estimate of a current state, the dRSC supplies current sensory input, and intrinsic connections between the two subregions could allow for integration and weighted cue combination. Thus, via granular-dysgranular interconnections (Shibata et al., 2009; Sugar et al., 2011), RSC can mediate exchange and integration of information between more mnemonic/internal (from hippocampus and AD) and more perceptual/external (from neorcortex) computations, with theta from AV providing a temporal reference for coordinating this interaction.

Finally, of note is our finding that interneurons in gRSC are theta-modulated, based on differences in spike width. This complements in vitro studies on the physiology of the mouse gRSC, showing that superficial granular layers contain fast-spiking inhibitory neurons providing feedforward inhibition to excitatory pyramidal cells that receive inputs from postsubicular head direction cells, highlighting a prominent role of inhibition in this circuit (Brennan et al., 2020). *In vivo* studies in awake rats probing differences in spike patterns between deep and superficial gRSC layers will advance our understanding of their differential contribution to navigation.

4.6.4 Summary and future directions

Our results detail differences in theta-related spiking between gRSC and dRSC along with the existence of two interdependent AV-RSC subnetworks, suggesting two distinct streams of information to the RSC. We propose that these conform to a more interoceptive stream that conveys the results of internal mnemonic processing and a more exteroceptive stream that conveys the state of the external world as assessed by the senses. The cognitive stream is characterized by close connectivity with the hippocampus, as well as a unique input from the AVDM. This convergence may represent a key aspect of RSC function, consistent with evidence from human neuroimaging studies showing a role for RSC in monitoring landmark stability (Auger

et al., 2012) and integrating across scenes and reference frames (Sherrill et al., 2013; Marchette et al., 2014; Bicanski and Burgess, 2016; Byrne et al., 2007). In the future, a complete understanding of the limbic system will necessarily need to consider the inter-related functions of these subnetworks, rather than the function of either AV or RSC as a whole.

For instance, single unit recordings from the two AV subfields that differentially project to gRSC and dRSC will be useful to determine whether the functional segregation of theta-modulated neurons within the RSC may also be present at the AV level, and shine light on what information are transmitted along AVDM-gRSC and AVVL-gRSC/dRSC pathways. With this motivation, we conducted AV recordings in Experiment 2, described in the next two Chapters.

4.6.5 Limitations

The main limitation of the electrophysiological work in this Chapter is the undersampling from one rat (R887), which contributed a relatively small number of cells to the sample (n=33). For this animal, no single units were recorded toward the end of recordings probably due to electrodes being in white matter tract, as seen from the histology. This weakened the statistical power of our analysis, as R887 was the only animal for which the proportion of theta-modulated units in gRSC and dRSC did not reach a significant difference. One way to overcome this issue would be to sub-sample the data across animals so that equal numbers of gRSC and dRSC units are included for each animal. However, this has the risk of underestimating the proportion of theta-modulated units in gRSC, given that the minimum number of cells recorded from one RSC subregion from a single animal was small (n=15 from the gRSC of R887, recorded across 7 trials). Despite this, differences in theta strength, firing frequency, burst index and spike waveform between gRSC and dRSC were always consistent when the data was segregated according to animals and no difference was found between animals. The observed phenomena are clearly not artifacts resulting from biased sampling in one animal.

5

Temporal firing properties of anteroventral thalamic neurons

5.1 Background and Rationale

Experiment 2 in this Chapter and the following one was directed toward two general aims: understanding what information is encoded in the firing of AV neurons, and determining the topographical organization of this information processing within the two AV subfields, AVDM and AVVL.

As described extensively in Chapter 2, different ATN nuclei present contrasting electrophysiological and anatomical properties, and can be functionally differentiated. Electrophysiologically, the majority of neurons recorded along the AD pathway are responsive to HD and AHV, or a combination of the two, and so this is known as the main HD system (Taube, 1995; Blair et al., 1998; Stackman and Taube, 1997, 1998; Sharp et al., 2001). In contrast, the AV pathway is characterized by a prevalence of cells having firing entrained by theta oscillations, and so this is part of a theta system (Tsanov et al., 2010, 2011; Vertes et al., 2001; Albo et al., 2003; Kocsis et al., 2001; Bassant and Poindessous-Jazat, 2001; Vann, 2009; Bland et al., 1995; Kirk et al., 1996). A remarkable feature of HD and theta systems is their ascending parallel organization comprising different components (more lateral vs more medial) of common structures, namely: tegmental nuclei of Gudden (dorsal vs ventral; DTN

vs VTN) → mammillary bodies (lateral vs medial; LMN vs MMN) → anterior thalamic nuclei (dorsal vs ventral; AD vs AV) → retrosplenial/subicular/entorhinal cortices → hippocampus (Jankowski et al., 2013; Witter et al., 1990; Shibata, 1993b; Van Groen and Wyss, 1995). Starting from the well accepted notion of parallel AD (HD) and AV (theta) circuits, ATN projections to RSC comprise a multifaceted, rather than uniform, neuronal circuit that mediates the flow of different information to hippocampus. An intriguing scenario suggested by our anatomical results from Experiment 1 (Chapter 4) is that a further functional division may exist within the AV-RSC (theta) circuit, given that AVDM and AVVL subfields differentially project to the two RSC subregions. In agreement with this notion, AVDM and AVVL also receive inputs from anatomically segregated populations of cells in dorsal and ventral MMN areas (Seki and Zyo, 1984; Shibata, 1992).

While the functional significance of AV in theta signalling is well established based on lesions (Zakowski et al., 2017; Ruan et al., 2017) and recording studies in freely moving and anesthetized rats (Tsanov et al., 2011, 2010; Welday et al., 2011; Vertes et al., 2001; Albo et al., 2003), less is known about what spatial information is encoded in AV and about the content of the information that is projected to RSC from each of the two AV subfields. Challenging the notion of AV as a pure theta relay, Tsanov et al. (2011) found cells with a significant directionality in the AVDM (69%). A subset of these HD cells (39%) is theta-modulated, discharging rhythmic spike trains at theta frequencies when the animal faces the PFD (Tsanov et al., 2011). This property suggests a mechanism by which different information streams (HD vs theta) converging at the single cell level within AV are also kept separate when transmitted to RSC, where no directionality was found for the theta-modulated neurons. Directional cells discarded from Experiment 1 were analyzed in Jacob et al., 2017 and showed no theta-modulation, providing the motivation for excluding these cells from our dataset. However, the specific AV contribution to downstream spatial signalling in cortex remains largely unclear. Moreover, previous AV investigations in foraging rats (Tsanov et al., 2010, 2011) only conducted recordings from AVDM, at the border with AD. As such, it remains unclear if directional cells are specific to AVDM or they are present throughout the entire AV extent. To shine light on these issues, and further characterize the functional properties of AV neurons, in Experiment 2 we recorded single units from the two AV subfields of rats during exploration.

5.2 Aims and Hypothesis

The specific aims of Experiment 2 can be summarized as:

1. Replicate previous finding by Tsanov et al. (2011) of cells with directional selectivity in AVDM, and extend upon this previous work by recording from the entire AV extent.
2. Present a wider and more detailed exploration and characterization of AV neural firing characteristics. Temporal firing properties and relationship to LFP theta are explored in this Chapter (Chapter 5). Spatial and motor firing properties are explored in the next one (Chapter 6).
3. Determine whether anatomically-segregated AV-RSC projections described in Experiment 1 (AVDM-gRSC; AVVL-dRSC/gRSC) also correspond to differences in electrophysiological properties between AVDM and AVVL. A functional specialization of theta processing within AV could help to explain differences in theta-modulation between the two RSC subregions. Based on Experiment 1 results, we hypothesized that theta-modulation would be stronger in AVDM compared to AVVL, reflecting a stronger interaction with gRSC.

5.3 Methods and Materials

To address the questions set out by Experiment 2, cells were recorded together with oscillatory LFP from AV of six freely-moving rats, using multichannel extracellular techniques described in the General Methods.

5.3.1 Animals and coordinates

For this study we used data from six male Lister Hooded rats (Charles River, UK) that were surgically implanted with tetrodes. For our recording sites, we targeted either lateral (AVVL subfield) or medial (AVDM) AV locations. AVDM implant coordinates (n=4) were: AP, -1.7; ML, ±1.4−1.5; DV, 3.6. AVVL implant coordinates (n=2) were: AP, -1.7; ML, ±1.8−1.7; DV, 3.4. Five rats were implanted in the left hemisphere and one in the right hemisphere. Coordinates were tested prior to implant surgeries. See Supplementary Figure A.1.

5.3.2 Behavioural protocol and testing apparatus

Screening and testing sessions took place inside a 90x90x60cm squared open field box with 60cm high walls, within a cue rich room (Figure 3.3). No surrounding curtains were present. Walls and floor of the box were covered with black vinyl sheets, and no cue card was attached to the walls. Screening sessions consisted of 5-10 min-long trials during which spikes were monitored and initial spike-sorting was performed (TINT software) to identify single units. Polar plots were also generated with spike-sorted data in TINT to determine whether single units were tuned to HD. If a single unit was detected in the screening sessions, the rat was removed from the arena and transferred back to its homecage in a separate room, and the arena's floor and walls were cleaned to remove uncontrolled nonvisual cues. The rat was then placed back in the arena and a 8 or 16 min-long experimental trial was conducted, during which the rat foraged for rice that was randomly tossed into the arena to encourage even sampling of all locations and directions. Variable inter-trial interval durations were used, ranging between 5-10 minutes.

5.3.3 Data Analysis

Data were analyzed using TINT (Axona, UK) and MATLAB R2018a (MathWorks, USA) with custom-made programs and functions. CircStat toolbox was used for analysis using circular statistics (Berens, 2009).

5.3.3.1 Spectral analysis

To calculate global theta characteristics, power spectral analysis was conducted using the FFT method, as described in the General Methods. In addition to the mean power and frequency of Type-1 theta oscillations (6-12Hz) , we examined the comparative dynamics of theta (6-12Hz) and delta (2-4Hz) oscillations. The theta-delta ratio represented the ratio of the relative spectral powers.

5.3.3.2 Theta relationship with running speed

To test the relationship between running speed and theta oscillations, we used similar methods to those described in Grieves et al. (2020). The LFP signal was bandpass

filtered at theta frequency range (6-12Hz) with a 4^{th} order Butterworth filter, and the Hilbert transform was applied to derive instantaneous theta frequency and amplitude that matched with running speed information recorded by the camera (downsampled from 250 to 50Hz sampling rate). Instantaneous running speed was calculated as the distance between two consecutive position data points, divided by the time between them.

To analyze the relationship between instantaneous theta power versus running speed, we binned speed data into 10cm/s bin, within a range of 0-50cm/s. Average theta power was computed for each speed bin, and a linear regression model was fitted to the data using the least-squares fitting approach. The slope of the regression line and Pearson's linear correlation coefficient (r) between speed bins and the corresponding power was derived. The same was done to analyze the relationship between instantaneous theta frequency and speed.

5.3.3.3 Analysis of phase precession

The approach used to investigate phase precession consisted of comparing the intrinsic oscillation of cells (the theta frequency in the temporal autocorrelogram) to the global theta oscillation frequency (the theta frequency in the LFP, computed with the FFT as described below). When cells phase precess, they fire progressively earlier with each successive theta cycle, so on average the theta frequency in their autocorrelogram is slightly faster than the global LFP theta frequency. Comparing intrinsic oscillation frequency to the global LFP frequency thus allows to derive a convenient count of precessing neurons in each cell category, and compare between them (Meer and Redish, 2011).

Autocorrelograms were constructed using 10ms bins between ±500ms, normalized to the maximum value between 100-150ms (corresponding to theta modulation peaks), and clipped within 0-1 range. A decomposing sine wave of frequency ω was then fitted to the autocorrelogram:

$$y(t) = a*(sin(2\pi*\omega*x+(\pi/2))+1)+b).*exp(\frac{-|x|}{t1})+(c*exp(\frac{-(x^2)}{t2^2})) \quad (5.1)$$

where t is the autocorrelogram time lag, and a-c, ω, and t12 were fit to the data using a non-linear least squares method (Matlab function *fit*). Parameters were restricted to the following values : ω to [6, 12], a-b to non-negative values [0 Inf], c to [0, 0.8], t2 to [0, 0.05]. Intrinsic theta frequency corresponds to the fit parameter ω (Royer et al., 2010).

5.3.3.4 Cell classification

As for Experiment 1, directionality of a cell was quantified by the mean vector length (R-vector) of the directional tuning curve. Theta-modulated cells were defined as cells that fired rhythmic spike trains at theta frequencies, based on both the Index of Coupling (IC) and Index of Rhythmicity (IR). This was in light of our Experiment 1 results that IC is sensitive to low levels of locking present in cells with non-rhythmical activity and the IR is a reliable theta estimator only for cells that are highly theta modulated (that pass the IC criteria). IC computes the mean vector length of the phase distribution for a cell. IR measures the frequency of the temporal modulation of the cell's autocorrelogram (see General Methods). Cell classification was done according to the spike-time series shuffling procedure (see Section 3.6.5.4), in addition to a number of other criteria reported below. In combination with these parameters we also manually refined the resulting cell classification in order to resolve false positives and negatives.

5.3.3.5 Classic HD

A classic HD cell is a cell with significant directionality that was not also theta-modulated. A cluster was classified as a classic HD if it satisfied the following criteria:

1. peak firing rate in the directional field >1Hz;
2. tuning curve R-vector >=cutoff threshold derived from 99.9^{th} percentile shuffling;
3. IC <cutoff threshold derived from 99.9^{th} percentile shuffling.

5.3.3.6 Theta-by-HD

A Theta-by-HD cell is a cell with significant directionality whose firing rate is also modulated at theta frequencies (6-12Hz). A cluster was classified as a Theta-by-HD if it satisfied the following criteria:

1. peak firing rate in the directional field >1Hz;
2. tuning curve R-vector >=99.9^{th} cutoff threshold;

3. IC >=99.9th cutoff threshold (theta phase-locked);
4. IR >=0.001 (rhythmic spiking). This cutoff was selected based on Tsanov et al., (2010; 2011).

In combination with these parameters, the resulting Theta-by-HD cell classification was verified by visual inspection to resolve false positives and negatives that can arise due to the variability in autocorrelogram shape for slow-spiking units, as demonstrated by Climer et al. (2015).

5.3.3.7 Intermediate HD

A cell with significant directionality that fired only occasionally at theta frequencies was termed intermediate HD cell. Intermediate HD cells passed the theta phase-locking criteria but did not show any intrinsic spike rhythmicity. Following from previous studies (Albo et al., 2003), a cluster was classified as an intermediate HD if it satisfied the following criteria:

1. peak firing rate in the directional field >1Hz;
2. R-vector >=99.9th cutoff threshold;
3. IC >=99.9th cutoff threshold (phase-locked);
4. IR <0.001 (no intrinsic spike rhythmicity).

As for Theta-by-HD cell classification, intermediate HD cells were confirmed by visual inspection to account for autocorrelogram variability. Intermediate neurons with only partially theta-related firing were previously found in all three ATN nuclei of anesthetized rats (Albo et al., 2003), and seem to constitute a general feature of limbic structures that contain theta in their LFP (Alexander et al., 2018; Eliav et al., 2018; Lomi et al., 2021).

5.3.3.8 Place cells

We defined a place cell as a cell with significant place-related firing whose firing rate was modulated at theta frequency (6-12Hz). A cluster was classified as a place cell if it satisfied the following criteria, based on Grieves et al. (2020):

1. mean firing rate >0.1Hz but <10Hz;
2. peak firing rate inside the place field >1Hz;
3. locational information content >0.8 bits/spike;
4. sparsity score <0.2;
5. IC >=99.9th cutoff threshold.

Arguably, these thresholds are more conservative than what is typical of analogous studies involving place cells (i.e., Grieves et al., 2020; see further discussion on our classification approach in the Limitations Section). However, being conservative is a sensible precaution and should ensure that the cells being classified as place cells in the AV would certainly be considered place cells had they been recorded from a different brain region – given that place cells have not been previously been reported in AV.

5.3.3.9 Theta-skipping analysis

Units that fire locked to theta oscillations can fire on every theta cycle, or on alternate ones. This phenomenon is known as theta cycle-skipping, and appears in the temporal autocorrelogram of a cell as the first side peak (125ms) being smaller than the second one (250ms). To determine whether theta-skipping occurs in AV, we derived a theta skip index (TS), taken from Brandon et al. (2013). A curve was fitted to the autocorrelogram implemented between±400ms with 10ms bins, using the equation:

$$y(x) = [a_1(cos(\omega x)+1)+a_2(cos(0.5\omega x)+1)+b]*exp(-|x|/\tau_1)+(c.*exp(-x^2/\tau_2^2))$$

with x=autocorrelogram bins, m=maximum autocorrelation value. Fit parameters were defined as: $a_1 = [0, m]$, $a_2 = [0, m]$, $b = [0, m]$, $c = [-m, m]$, ω=[10π,

18π], $\tau_1 = ([0,5])$ and $\tau_2 = ([0,0.05])$. TS index, bound between -1 and 1, quantifies how much the first peak is skipped from the theta-modulated signal. it was found as the height of the second peak of the fitted curve, minus the height of the first peak of the fitted curve, divided by the largest of the two:

$$\text{TS autocorrelation} = \frac{p_2 - p_1}{max(p_1, p_2)}$$

For the TS index analysis, we selected only cells that passed our theta phase-locking criterion (IC>99.9th percentile shuffling). Among these cells, a theta-skipping cell had to meet following criteria (Figure 5.1):

1. a satisfactory fit of the model parameters to the autocorrelogram, measured by the coefficient of determination (R2>0.7);
2. a baseline theta power component in the autocorrelogram (IR>0.001);
3. the first side peak of the autocorrelogram smaller than the second side peak (TS index>0.1, according to the cutoff used by Brandon et al. (2013));
4. all cells were confirmed by visual inspection of their autocorrelogram.

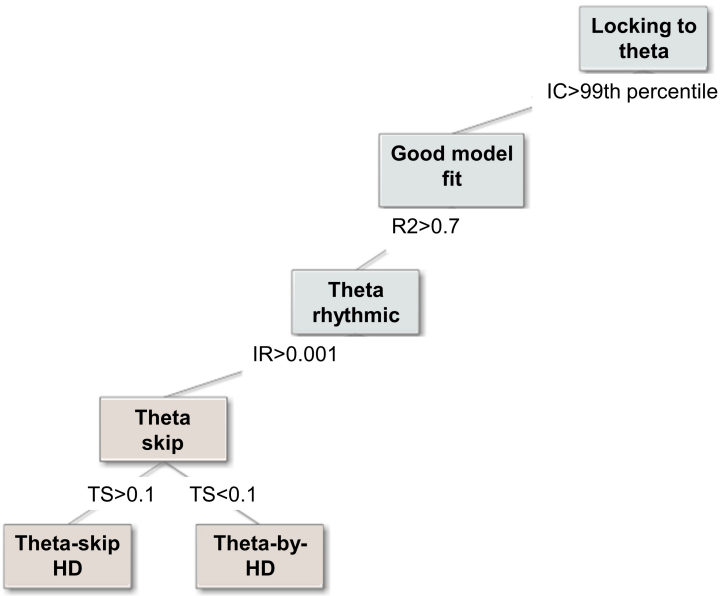


Figure 5.1: **Flowchart of theta-skipping cell identification.**

In trials in which two theta-skipping cells were co-recorded on the same tetrode (n=12 pairs), cross-correlation analysis was conducted to determine whether the two cells skipped the same or different theta cycles. We defined these cells as synchronous and anti-synchronous, respectively. Cross-correlations were plotted for each pair of cells and were fitted by a similar equation as above, without assuming a main center peak (c=0) nor symmetry of the signal around 0 lag:

$$y(x) = [a_1(cos(\omega x + \varphi) + 1) + a_2(cos(0.5\omega x + \varphi) + 1) + b] * exp(-\left|x + \varphi\omega^{-1}\right| / \tau_1)$$

with fit parameters a1=[0, m], a2=[-m, m], b=[0, m], ω=[$10\pi, 18\pi$],φ=phase offset parameter [-pi, pi], τ_1 = ([0,5]). The TS index in cross-correlogram was found as:

$$\text{TS cross-correlation} = \frac{p_{0,2} - p_1}{max(p_1, p_{0,2})}$$

where $p_{0,2}$ is the mean of the model values at the center (x=0) and second side ($x = 4\pi/\omega$) peaks, and p_1 is the model value at $x = 2\pi/\omega$, corresponding to the first and second side peaks. Synchronous cells skip the same alternating cycle and display the highest cross-correlation peak at 0ms (TSxcorr>0.1). Anti-synchronous cells skip opposite alternating cycles and display the highest peak at 125ms (TSxcorr<-0.1).

5.3.3.10 Cell-specific temporal firing characteristics

To investigate bursting firing properties, ISI histograms were created by binning all ISIs in the range 0-250ms with 2ms bins. Three measures were derived: (1) peak ISI, taken as the center of the histogram bin with the highest count; (2) burst index, defined as the ratio of spikes sharing ISI<6ms to all spikes emitted by the cell in a trial; (3) width at half-peak of the ISI histogram (ISIFW), indicating the time required for the exponential fit of the histogram ($y = a^{bx}$; Matlab Curve Fitting toolbox) to decay to half the peak value (Lozano et al., 2017).

5.3.3.11 Statistics

This section describes the statistical tests applied to the analysis of Experiment 2 presented in this Chapter and the following one. Prior to each statistical test, we checked the assumption of normality (Matlab function *ktest*) and equal variance (SPSS Version 26). If assumptions were met, we used parametric statistical tests for significance. Comparisons between two groups were conducted using independent-samples or paired-samples t-tests. For more than two groups, a one- or two-way

ANOVA were used, with cell type as the between-subject factor, and post-hoc tests compared population means (SPSS, Tukey's HSD for equal sample variance, or Games-Howell Test when equality of variance could not be assumed (Games et al., 1979), Bonferroni correction). For circular data, a Watson-Williams multi-sample F-test compared circular means between two or more groups.

Otherwise, we used non-parametric statistical tests. Comparisons between groups were conducted using the two-sample Wilcoxon Rank-sum tests and paired-sample Wilcoxon Signed rank tests. For more than two groups, a Kruskal-Wallis Test was conducted, followed by multiple pairwise comparison of group ranks (SPSS, Bonferroni correction). We also used the Chi-square goodness-of-fit test when testing differences in the observed number of cells between two groups against an expected equal proportion. For circular data, equality of the two distributions was tested using a Kuiper test (Fisher, 1993).

All statistical tests are two-tailed. In all figures and tables, *p*-value significance level: $* = 0.05$ significance level, $** = 0.01$, $*** = 0.001$. Table 5.1 provides a summary of the tests used and how they were conducted.

Table 5.1: **Summary of statistical tests, their abbreviations and software used.**

Parametric	Test	Abbreviation	Software
y	two-sample t-test	-	Matlab *ttest2*
y	paired-sample t-test	-	Matlab *ttest*
y	one/two-way ANOVA	-	SPSS
y	Watson-Williams	WW	Matlab *circ_wwtest*
n	Wilcoxon Rank-sum test	WRS	Matlab *ranksum*
n	Wilcoxon Signed rank test	WSR	Matlab *signrank*
n	Kruskal-Wallis	KW	SPSS
n	Kuiper test	-	Matlab *circ_kuipertest*
n	Chi-square test	χ^2	Matlab *chi2_perc_diff*

5.4 Results

5.4.1 Histology

Six animals were selected based on correct electrode placement in AV (n=2 implanted in AVVL; n=4 implanted in AVDM). For the two rats implanted in AVVL (R222 and R449) electrodes sampled only the AVVL, given the anatomical configuration of the two subfields. For one rat implanted in the AVDM (R762) electrodes sampled only the AVDM and were not lowered further into deeper AVVL regions. For the remaining three rats (R448, R651 and R652), electrodes were implanted in the AVDM and advanced through the entire AV extent, starting from AVDM into AVVL (Table 5.2 for details on the cells recorded for all animals and AV fields).

Table 5.2: **Summary of recording locations and cell distribution in AV for all animals.** (n=733 cells in six animals).

Recorded cells			
Rat number	Hemisphere	Region	Number of cells
R222	Left	AVDM	0
		AVVL	24
R448	Left	AVDM	106
		AVVL	76
R449	Left	AVDM	0
		AVVL	211
R651	Right	AVDM	31
		AVVL	66
R652	Left	AVDM	116
		AVVL	32
R762	Left	AVDM	71
		AVVL	0
All		AVDM	324
(n=6)		AVVL	409

In the last two experimental animals (R448, R449), we made a high-frequency current microlesion immediately prior to perfusion to mark the precise location of the tip (NanoZ device; Neuralinx, USA). In these animals, the lesion was induced on the same electrode that was recording a Theta-by-HD and a place cell, respectively, to confirm that these cells were being recorded from the AV. No damage to hippocampal and parahippocampal tissue was visible in the histological slides that contained the tract and the lesion was located well within the AV region (more details in Discussion, see Section 5.5.1.2).

To determine the location of each recorded unit, we marked the AVDM-AVVL border and our best estimate of the electrodes tip on the histological sections that contained the electrode tract for each animal. The location of each unit within AV was then estimated in respect to the tip, by combining information about the known electrodes length and the number of screw turns that advanced the electrodes each day. Figure 5.2 presents the histology for all animals, and the estimated location of all place cells identified for each animal.

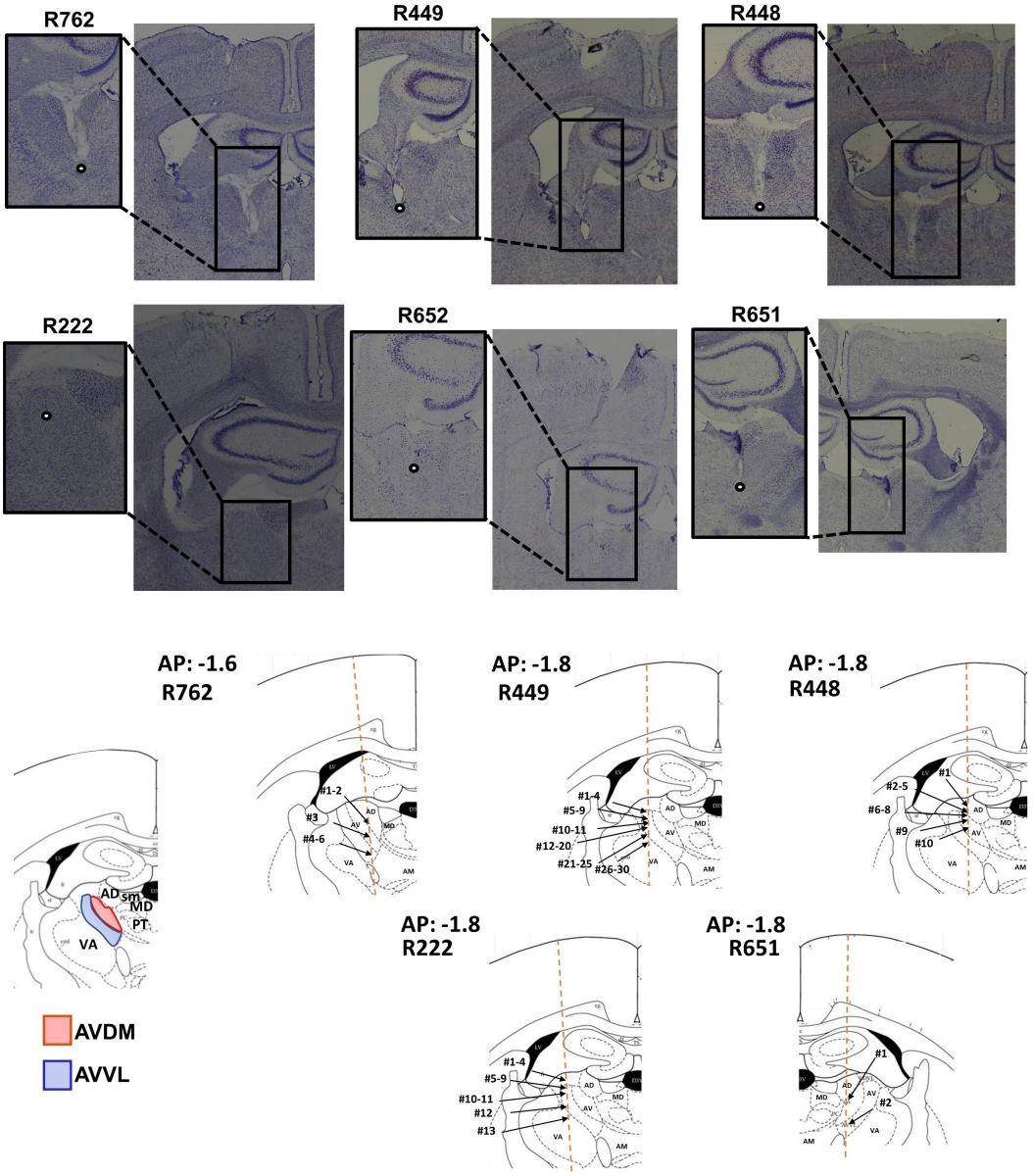


Figure 5.2: **Histology of anteroventral thalamic recordings.** Top, photomicrographs of the Nissl-stained coronal sections through the recording site, for each of the six implanted rats. Hollow dots in the insets is the final electrode depth. Recording

locations were estimated based on the schematic line drawing of AV subfields on the right, adapted from Paxinos and Watson (2007). R449 and R222 had AVVL only recordings; R762 had AVDM only recordings. R448, R651 and R652 had both AVDM and AVVL recordings. Bottom, location of place cells in the AV, shown for five rats for which place cells could be recorded (no place cell in R652). The location of each place cell is reconstructed on the atlas section and is indicated by numbers. Red line is the estimated direction of the tract. Anterior-posterior (AP) location of each atlas section is indicated (-1.6 or -1.8mm from bregma). Abbreviations: AD, anterodorsal thalamic nucleus; AM, anteromedial thalamic nucleus; AVVL and AVDM, ventrolateral and dorsomedial subfields of the anteroventral thalamic nucleus; MD, mediodorsal thalamic nucleus; VA, ventroanterior thalamic nucleus; sm, stria medullaris; PT, parataenial nucleus.

5.4.2 Local field potential signal

To demonstrate that theta rhythmicity was not restricted to individual neurons, we recorded the LFP signal from the same electrodes that were recording single units, given previous evidence that hippocampal and AV theta oscillations are coherent and phase-offset relative to each other (AV theta precedes hippocampus by 70-10ms; Tsanov et al., 2011). The local LFP signal contained oscillations in Type-1 theta frequency range (6-12Hz) and these oscillations were modulated by the animal's behaviour, similarly to other limbic system regions (McFarland et al., 1975; Richard et al., 2013; Belchior et al., 2014). The LFP theta power reached its peak at an average frequency of 8.79±0.64Hz, corresponding to theta frequency. The average spectral power of this frequency was 3.49±2.53 (Figure 5.3). Although in most trials the LFP signal contained a secondary delta oscillation (2-4Hz), the average theta-delta ratio, evaluated as an additional measure of theta oscillation strength, was greater than 0 (mean of 1.32±1.65). Theta power and frequency correlated with running speed: average correlation coefficient was 0.90±0.13 for Type-1 theta power-speed and 0.87±0.18 for Type-1 theta frequency-speed (Figure 5.3). Across all animals, the slope of the linear regression line was positive in 188/192 trials for both power and frequency.

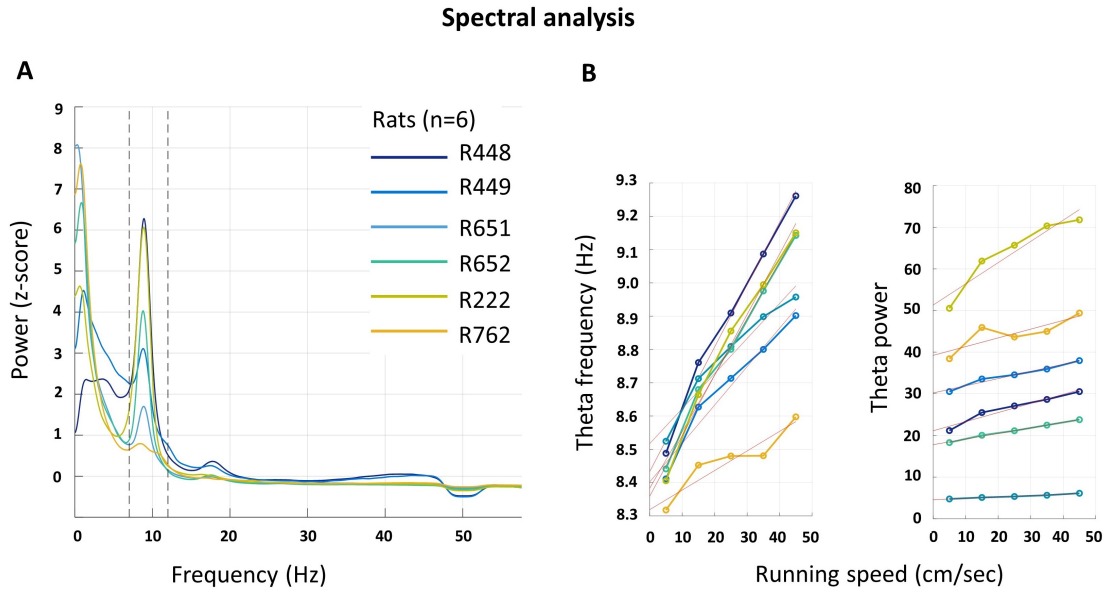


Figure 5.3: **Theta oscillations were modulated by running speed. (A)** Average normalized power spectrum across all trials, colour coded by rat. x-axis, frequency (Hz); y-axis, z-scores. In a typical trial, LFP oscillations contain Type-1 theta frequencies (6-12Hz) and weaker delta frequencies (2-4Hz). **(B)** Average speed-power and speed-frequency relationships across all trials for each rat, colour coded as in A. Red lines are linear regression lines to compute the slope and y-intercept for the animal.

5.4.3 Overview of the cell data set

A total of 733 cells were collected from the 6 animals (n=324 in AVDM, n=409 in AVVL). Of these cells, 341 had spatial correlates. The majority of these cells were directional cells, comprising Theta-by-HD cells (n=158), classic HD (n=96) and intermediate HD (n=26), identified based on the index of coupling (IC) and rhythmicity (IR). Theta-by-HD cells were phase-locked and rhythmic. Classic and intermediate HD cells fired non-rhythmically and uncoupled, or only partially coupled, to theta. Another group were place cells (n=61). A further 285 cells were classified as theta-modulated cells that did not exhibit any particular spatial properties. The remaining 107 cells were classified as unidentified cells that did not exhibit any temporal or spatial properties. Table 5.3 reports more details on the cell types recorded from the AV in each animal. In the table, classic and intermediate HD cells were combined into a single group of non-rhythmic HD cells.

Table 5.3: **Numbers and percentages of AV cell types recorded in each animal.**

		AV cell types				
Rat number	Tot.cell number	Non-rhythmic HD	Theta-by-HD	Place cells	Theta	Unidentified
R448	182	30 (17%)	31 (17%)	10 (6%)	88 (48%)	23 (13%)
R449	211	2 (1%)	53 (25%)	30 (14%)	81 (38%)	45 (21%)
R651	97	3 (3%)	37 (38%)	2 (2%)	34 (35%)	21 (22%)
R652	148	80 (54%)	19 (13%)	0	46 (31%)	3 (2%)
R222	24	0	3 (13%)	13 (54%)	8 (33%)	0
R762	71	7 (10%)	15 (24%)	6 (9%)	28 (39%)	15 (21%)
All	733	122 (17%)	158 (22%)	61 (8%)	285 (39%)	107 (15%)

5.4.3.1 Classic HD cells

Across all six animals, 96 cells met the inclusion criteria for classic HD cells, like the ones typically described in the AD and PoS/RSC (non-phase-locked, non-rhythmic; 13% of all recorded units, or 34% of the total HD cell population). Figure 5.4 shows typical single-unit activity. For each cell, the tuning curve (ii; blue curve) indicated that firing rates were clustered along a narrow range of directions, as for putative HD cells first documented by Taube et al. (1990), having a directional firing range of approximately 100° and background rate of approximately 0Hz. There was a uniform sampling of all directions (ii; gray curve) and spatial locations by the animal (iii; black line is the spatial sampling of the rat). There was a uniform distribution of spatial firing activity (iii-iv), suggesting no evidence of spatial selectivity. Cells fire non-rhythmically and unrelated from theta, reflected in a uniform phase distribution (vi) and flat autocorrelogram (v).

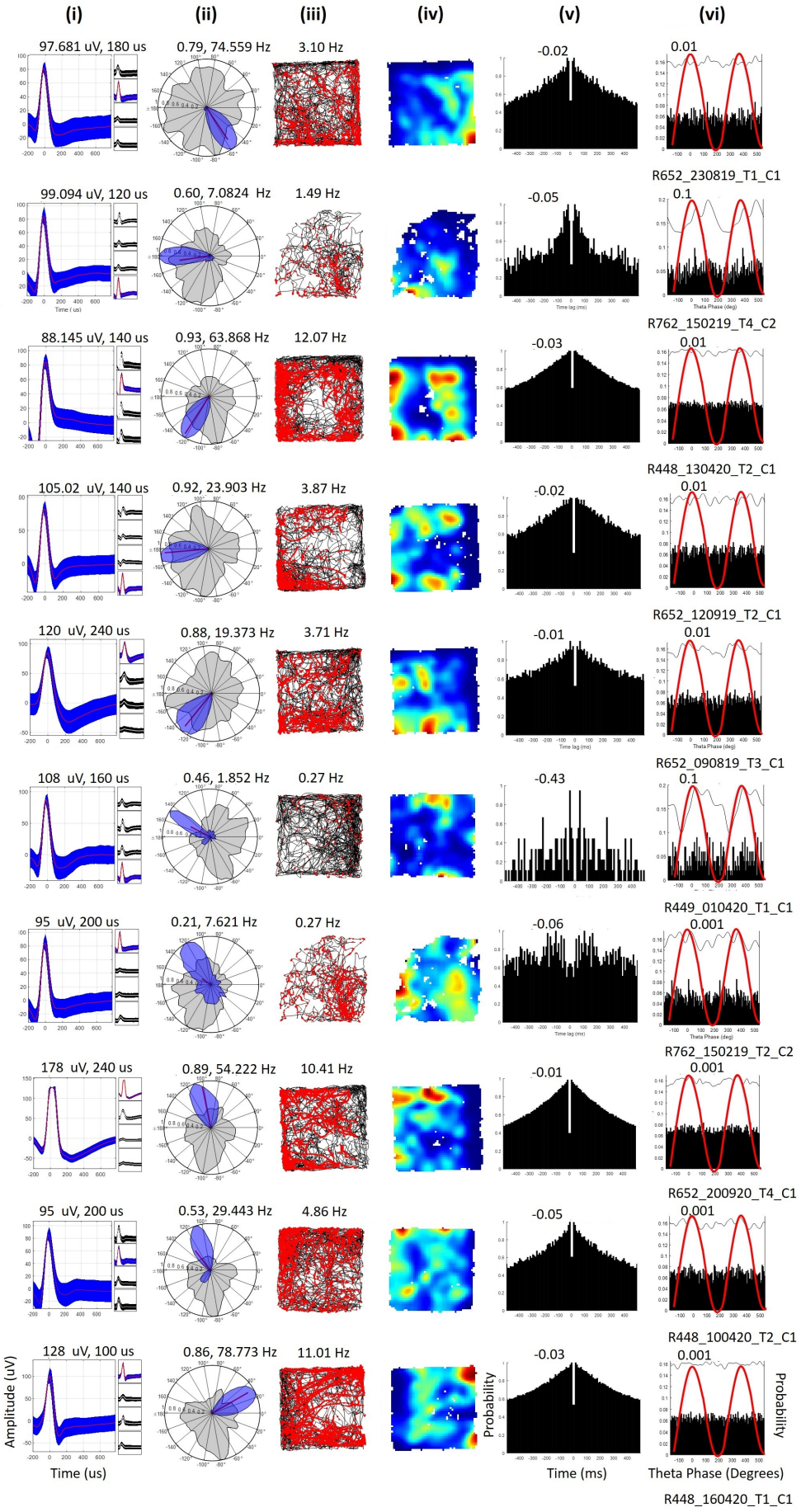

(i)
(ii)
(iii)
(iv)
(v)
(vi)
97.681 uV, 180 us
0.79, 74.559 Hz
3.10 Hz
-0.02
0.01
R652_230819_T1_C1
99.094 uV, 120 us
0.60, 7.0824 Hz
1.49 Hz
-0.05
0.1
R762_150219_T4_C2
88.145 uV, 140 us
0.93, 63.868 Hz
12.07 Hz
-0.03
0.01
R448_130420_T2_C1
105.02 uV, 140 us
0.92, 23.903 Hz
3.87 Hz
-0.02
0.01
R652_120919_T2_C1
120 uV, 240 us
0.88, 19.373 Hz
3.71 Hz
-0.01
0.01
R652_090819_T3_C1
108 uV, 160 us
0.46, 1.852 Hz
0.27 Hz
-0.43
0.1
R449_010420_T1_C1
95 uV, 200 us
0.21, 7.621 Hz
0.27 Hz
-0.06
0.001
R762_150219_T2_C2
178 uV, 240 us
0.89, 54.222 Hz
10.41 Hz
-0.01
0.001
R652_200920_T4_C1
95 uV, 200 us
0.53, 29.443 Hz
4.86 Hz
-0.05
0.001
R448_100420_T2_C1
128 uV, 100 us
0.86, 78.773 Hz
11.01 Hz
-0.03
0.001
Amplitude (uV)
Time (us)
Probability
Time (ms)
Theta Phase (Degrees)
Probability
R448_160420_T1_C1

Figure 5.4: **Basic characterization of classic head direction cells.** For each example cell, from left to right: **(i)** average spike waveform with peak-to-trough amplitude (μV) and width (μs); x-axis, μs; y-axis, μV; **(ii)** polar plot of the directional tuning curve (blue; firing rate vs head direction) and dwelltime curve (gray; dwelltime vs head direction). R-vector and peak rate are reported; tuning curves are unidirectional, suggesting direction-specific firing; **(iii)** spikemap; **(iv)** dwelltime-normalized ratemap, with mean firing rate (Hz), showing no locational specificity; **(v)** peak-normalized spike time autocorrelogram implemented between±500ms, with index of rhythmicity (IR), showing irregular spike discharge. x-axis, time lag (ms); y-axis, probability; **(vi)** spikes vs theta phases distribution, shown as raw histogram and as smooth density estimate, with index of coupling (IC). x-axis, degrees; y-axis, frequency count (right) or probability (left). Phases are double plotted between -180° and 540°, with 6° bin. Red sine wave is the theta cycle. For each cycle, 180° represents the trough, 0/360° the peak. Uniform phase distributions indicate that spike discharge was unrelated from theta. All axis labels are noted in the last row.

5.4.3.2 Theta-by-HD cells

A total of 158 units were classified as Theta-by-HD cells, as those originally reported by Tsanov et al. (2011) in AV (theta phase-locked, rhythmic; 22% of all recorded units, or 56% of the HD cell population). Figure 5.5 depicts typical patterns of Theta-by-HD cell activity. For each cell, the tuning curve (ii) portrayed a unidirectional firing pattern like for classic HD cells, although Theta-by-HD cell directional fields were more dispersed and asymmetric, suggesting less-robust directional encoding (see analysis of spatial properties in the next Chapter). Occasionally, Theta-by-HD cells could display broad patches of inhomogeneous firing in their ratemaps, as spikes were not completely uniform across the environment but accumulated at specific locations (iii-iv). Crucially however, Theta-by-HD cell firing fields were larger and less spatially compact compared to place cells, and none of our Theta-by-HD cells met our place cell inclusion criteria based on locational information and sparsity score (see Methods). Cells fire rhythmically and strongly coupled to descending theta phases, reflected in a unimodal phase distribution (between 0-180°) (vi) and a rhythmic autocorrelogram (v).

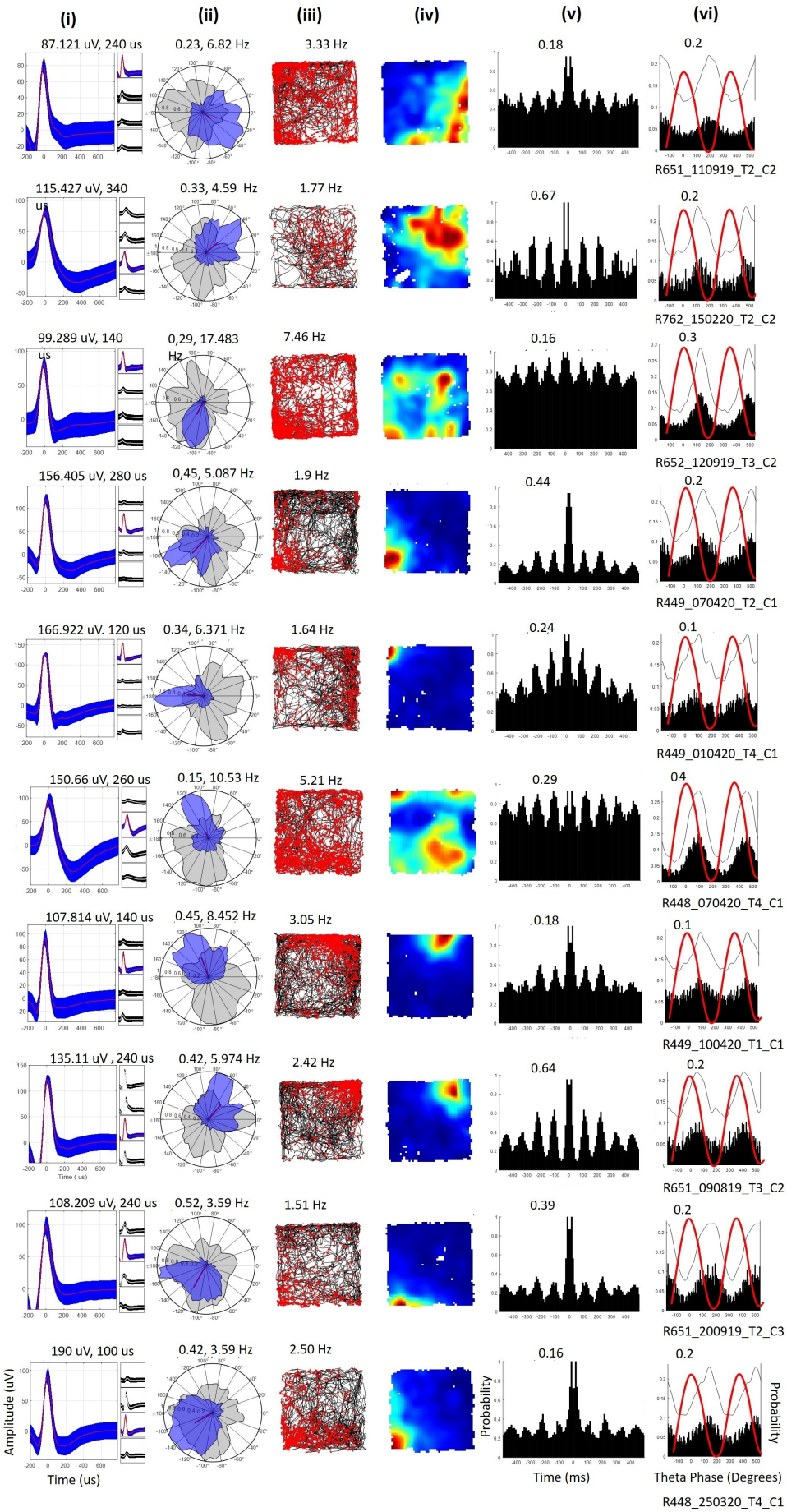

(i)
(ii)
(iii)
(iv)
(v)
(vi)
87.121 uV, 240 us
0.23, 6.82 Hz
3.33 Hz
0.18
0.2
R651_110919_T2_C2
115.427 uV, 340 us
0.33, 4.59 Hz
1.77 Hz
0.67
0.2
R762_150220_T2_C2
99.289 uV, 140 us
0,29, 17.483 Hz
7.46 Hz
0.16
0.3
R652_120919_T3_C2
156.405 uV, 280 us
0,45, 5.087 Hz
1.9 Hz
0.44
0.2
R449_070420_T2_C1
166.922 uV. 120 us
0.34, 6.371 Hz
1.64 Hz
0.24
0.1
R449_010420_T4_C1
150.66 uV, 260 us
0.15, 10.53 Hz
5.21 Hz
0.29
04
R448_070420_T4_C1
107.814 uV, 140 us
0.45, 8.452 Hz
3.05 Hz
0.18
0.1
R449_100420_T1_C1
135.11 uV , 240 us
0.42, 5.974 Hz
2.42 Hz
0.64
0.2
R651_090819_T3_C2
108.209 uV, 240 us
0.52, 3.59 Hz
1.51 Hz
0.39
0.2
R651_200919_T2_C3
190 uV, 100 us
0.42, 3.59 Hz
2.50 Hz
0.16
0.2
R448_250320_T4_C1
Amplitude (uV)
Time (us)
Probability
Time (ms)
Probability
Theta Phase (Degrees)

Figure 5.5: **Basic characterization of Theta-by-head direction cells. (i)** average spike waveform; **(ii)** polar plot showing unidirectional spike discharge; **(iii-iv)** spiekmap and ratemap showing the distribution of spatial firing. Occasionally (n=20/158 cells), cells show spatially inhomogeneous firing in the form of broad firing fields, which was however much weaker than in place cells. None of the Theta-by-HD cells have sparsity score<0.20 and average locational information content is lower than in place cells; **(v)** autocorrelogram indicates strong spike rhythmicity; **(vi)** spikes vs theta phases distribution showing phase-locking to the theta cycle (red line), with the highest spiking probability at descending theta phases.

5.4.3.3 Intermediate HD cells

Intermediate HD cells (n=26; 3% of the recorded units or 9% of the total HD cell population) were defined as HD cells that fired non-rhythmically (IR<0.001; range: -0.22, 0.0009) and only partially coupled to theta (IC>=99.9th percentile shuffling). See examples in Figure 5.6. Like classic HD cells, the tuning curve (ii) was tightly-tuned and unidirectional, and ratemap displayed a uniform distribution of spatial firing activity (iii-iv). Although cells passed the phase-locking criteria based on IC, theta was not clearly visible from the phase distribution (vi) and autocorrelogram (v), suggesting that cells alternated periods of irregular firing incoherent from theta to only short periods of locking to theta. Hence, while Theta-by-HD cells exhibited strong locking to theta and low firing outside of a narrow oscillatory range, intermediate HD cells exhibited weak, and sometimes virtually no locking, to theta and high baseline firing.

Intermediate HD cells were recorded from 3/6 implanted rats, and one rat contributed 85% of these cells (R652, n=22/26), suggesting that they may depend on AV anatomical location. In two of these animals, we recorded nine intermediate HD cells simultaneously on the same tetrode as one or two Theta-by-HD cells, and two of these cells were also co-recorded on the same tetrode with multiple classic HD cells.

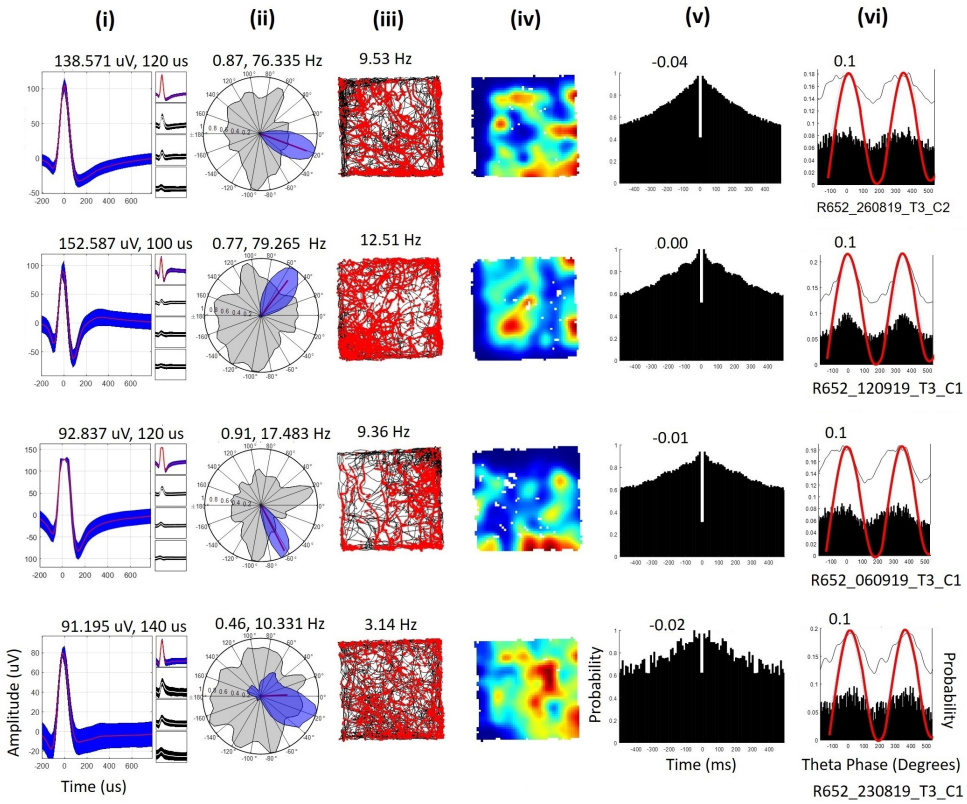


Figure 5.6: **Basic characterization of intermediate head direction cells. (i)** average spike waveform; **(ii-iii-iv)** cells display directionally-selective firing but no sign of locational modulation; **(v-vi)** the phase distribution is unimodal and clustered around theta peaks (360°), despite elevated background firing also at other phases, suggesting that cells only occasionally fire at theta frequency, reflected in a lack of intrinsic spike rhythmicity.

5.4.3.4 Place cells

While our primary aim was to record and further characterize neurons integrating HD and theta signals within AV, during recordings we made the unexpected discovery of cells with spatial and temporal firing correlates very similar to those of typical hippocampal pyramidal neurons, having firing entrained by theta oscillations and firing over a very restricted region of the recording box, with low background firing rates outside of this place field (O'Keefe and Dostrovsky, 1971). We will therefore refer to these newly identified AV cells as place cells. We recorded a total of 61 place cells from 5/6 animals (8% of the total recorded units). Locational information in bits/spike was derived to measure how well the animals spatial location in the box could be inferred from the cells firing rate. Locational information threshold for inclusion as a place cell was set to>0.8, and sparsity threshold was set to<0.20, as

it has been typically done for place cells (Jankowski et al., 2015; Hok et al., 2018; Jankowski and O'Mara, 2015; Grieves et al., 2020; Duvelle et al., 2019).

Figures 5.7 and 5.8 depict examples of typical place cell activity seen in AV, associated with high locational selectivity. Some units had a single discrete place field (Figure 5.7) while others had multiple fields (Figure 5.8). The fields of these latter units often appeared regularly spaced. For both groups, place fields were highly compact and often round in shape, which could be contrasted to the more irregularly-shaped fields typically described for hippocampal pyramidal neurons. See specific examples in Figure 5.7. Place fields were confirmed by presenting spikemaps alongside ratemaps (ii-iii), and by recording cells across trials. Very clear examples of stable spatial patterns are provided in next Chapter, Figure 6.2. All place cells showed rhythmic spike discharge at theta frequencies in their autocorrelograms (iv), and firing was strongly locked to descending theta phases (v). Phases were computed relative to the local LFP, although hippocampal and AV theta oscillations are coherent, displaying a small phase lag (7-10ms lag; Tsanov et al., 2011). As shown below, spike bursting was a property of the theta-rhythmic units, namely place cells and Theta-by-HD cells, reflected in a high central peak of the autocorrelogram (see examples in Figure 5.7 iv and Figure 5.5 v).

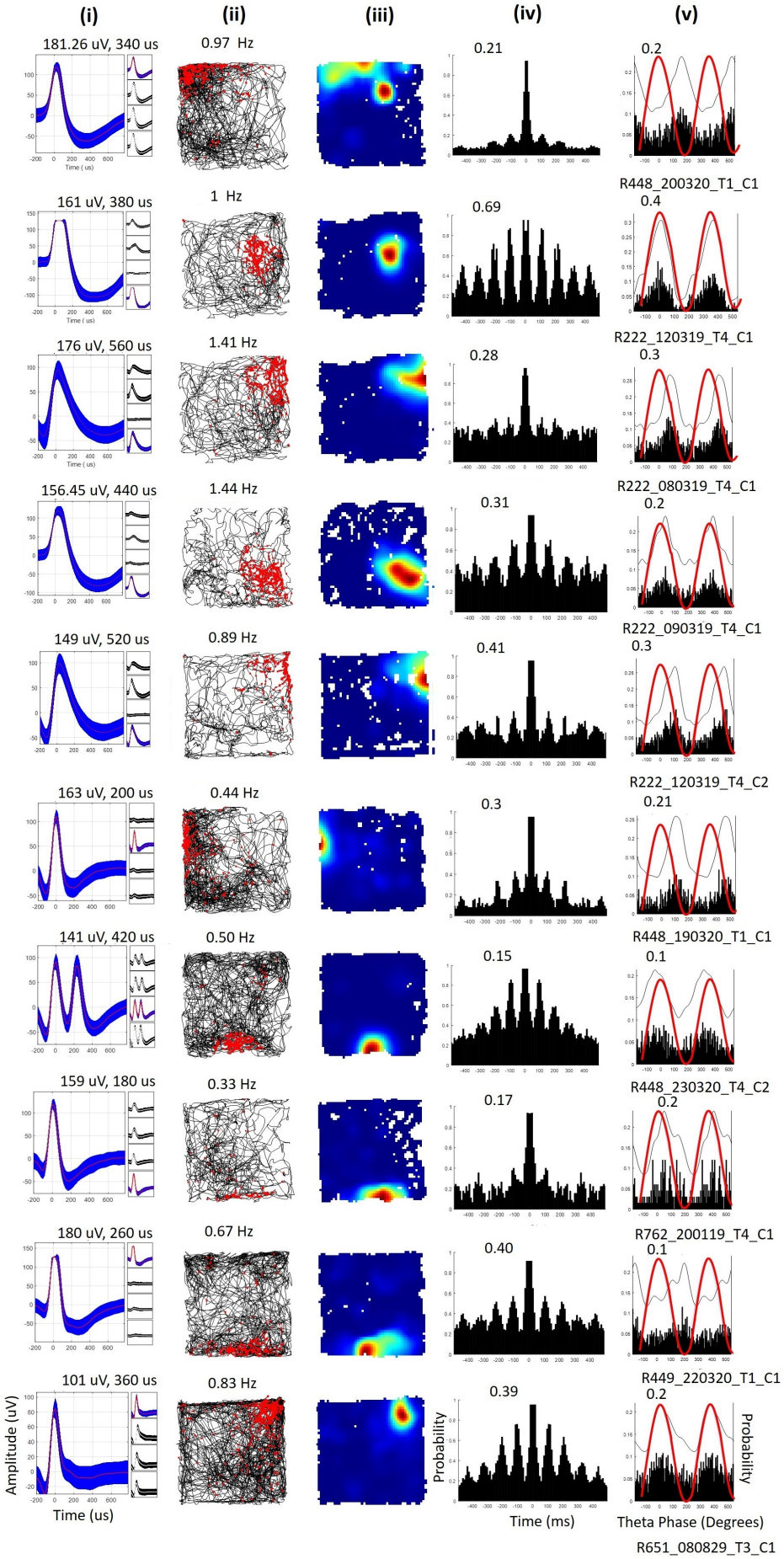

(i)
(ii)
(iii)
(iv)
(v)
181.26 uV, 340 us
0.97 Hz
0.21
0.2
R448_200320_T1_C1
161 uV, 380 us
1 Hz
0.69
0.4
R222_120319_T4_C1
176 uV, 560 us
1.41 Hz
0.28
0.3
R222_080319_T4_C1
156.45 uV, 440 us
1.44 Hz
0.31
0.2
R222_090319_T4_C1
149 uV, 520 us
0.89 Hz
0.41
0.3
R222_120319_T4_C2
163 uV, 200 us
0.44 Hz
0.3
0.21
R448_190320_T1_C1
141 uV, 420 us
0.50 Hz
0.15
0.1
R448_230320_T4_C2
159 uV, 180 us
0.33 Hz
0.17
0.2
R762_200119_T4_C1
180 uV, 260 us
0.67 Hz
0.40
0.1
R449_220320_T1_C1
101 uV, 360 us
0.83 Hz
0.39
0.2
Amplitude (uV)
Time (us)
Probability
Time (ms)
Probability
Theta Phase (Degrees)
R651_080829_T3_C1

Figure 5.7: **Basic characterization of place cells with a single firing field.** **(i)** average spike waveform with peak-to-trough amplitude (μV) and width (μs); **(ii)** spikemap; **(iii)** dwelltime-normalized ratemap showing highly compact, round firing fields; mean firing rate (Hz) is reported; **(iv)** peak-normalized autocorrelogram implemented between ±500ms, with IR, showing peaks at theta frequency range; **(v)** spikes vs theta phases distribution with IC. Red sine wave is the theta cycle. Phase distribution is unimodal and highly clustered on descending theta phases, indicating rhythmic spike discharge locked to theta.

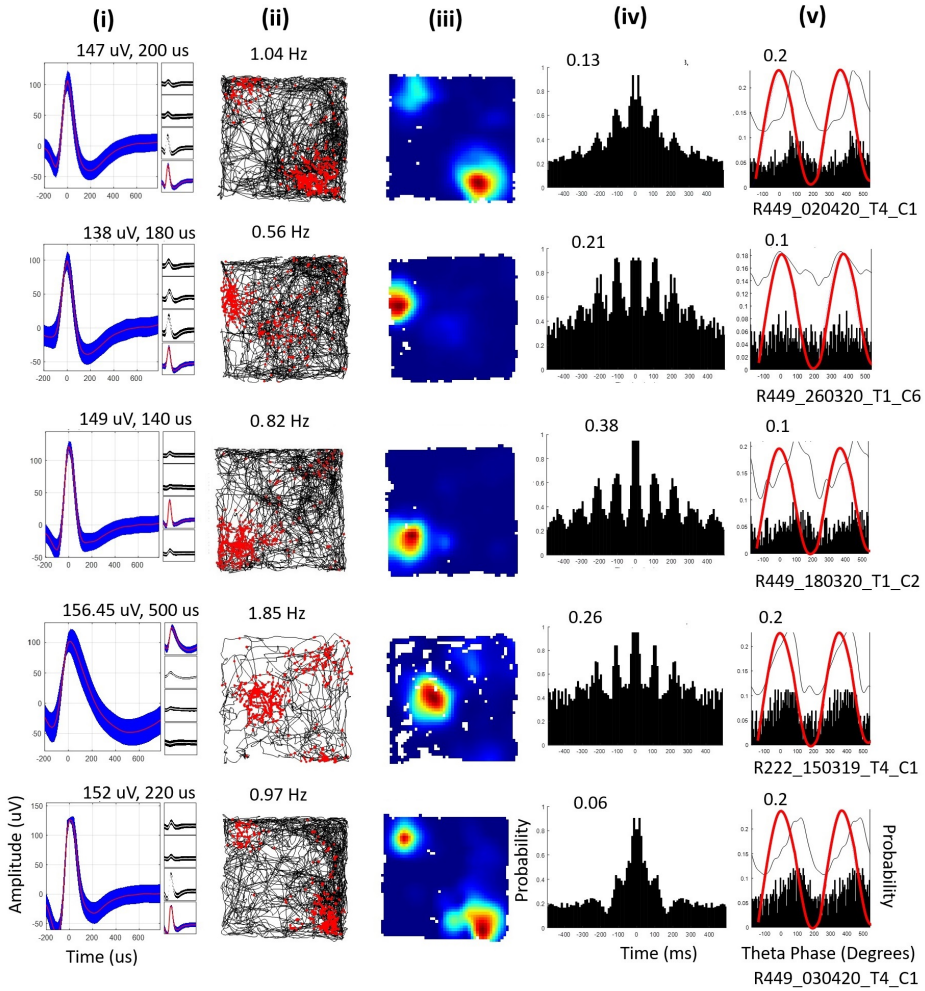


Figure 5.8: **Basic characterization of place cells with multiple firing fields.** Same caption as in Figure 5.7. Place fields were round and regularly-spaced place fields were observed. The visible grid-like pattern is discussed in the Limitations Section.

In two animals, we recorded seven place cells simultaneously on the same tetrode as one or two Theta-by-HD cell, across six different recording days. An example is provided by Figure 5.9, depicting one Theta-by-HD and two place cells co-recorded on the same tetrode (see also examples of Figures 6.7 and 6.8 in the next Chapter). As Theta-by-HD cells are not also present in hippocampal CA fields, evidence of co-recorded neurons suggests that place cells are part of the local AV circuit rather than being recorded from hippocampus.

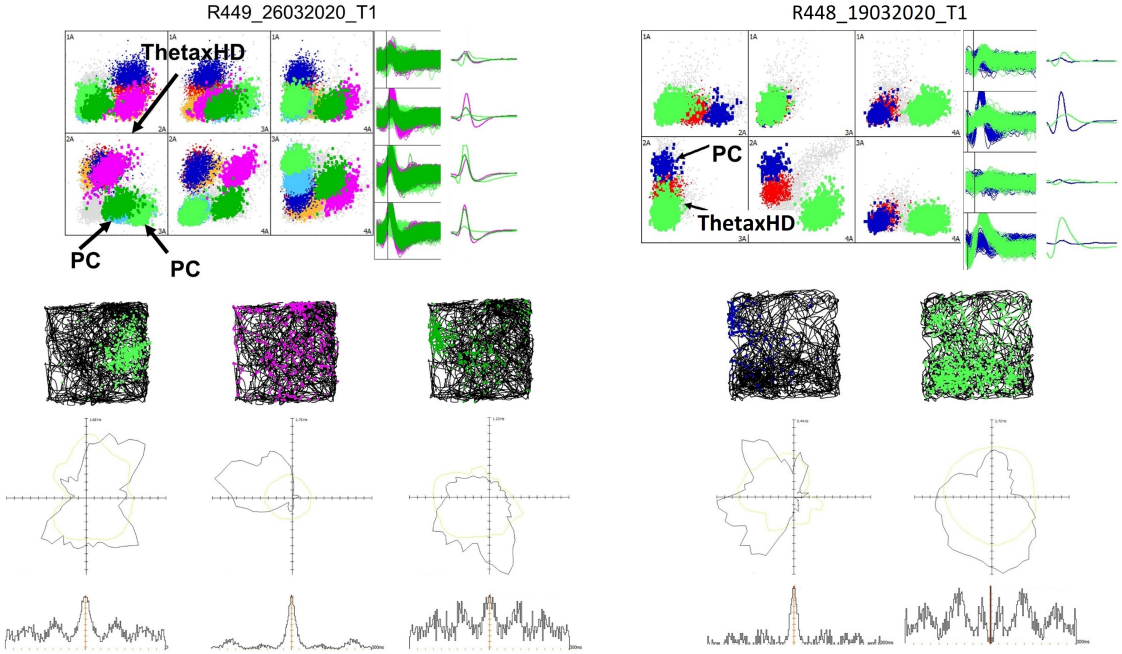


Figure 5.9: **Examples of place cells co-recorded on the same tetrode with an anteroventral thalamic cell.** Left, trial in which two place cells (light and dark green clusters) were co-recorded with a Theta-by-HD cell that showed theta-skipping (pink cluster). Right, trial in which a place cell (blue cluster) was being co-recorded with a Theta-by-HD cell (green cluster). For each cell, the following plots are shown: trial cluster space, average waveform for each cluster, spikemap, tuning curve showing firing rate (Hz) vs HD (degrees), autocorrelogram between±300ms; x-axis, time (ms); y-axis, probability.

5.4.4 Are there differences in theta-modulation among AV cells?

We have identified location and direction selective signals in AV that are differentially related to the local LFP theta oscillations. Classic HD cells showed no locking to theta and no autocorrelogram rhythmicity (Figure 5.4). Theta-by-HD and place cells showed high levels of locking, reflected in strong autocorrelogram rhythmicity

(Figure 5.5, Figure 5.7). Intermediate HD cells showed weak to virtually no locking to theta and no intrinsic spike rhythmicity (Figure 5.6). We now compare the temporal properties between cell groups.

Table 5.4: **Statistical analysis on the temporal properties and relation to LFP theta of AV cells with spatial profiles.**

Temporal firing properties						
	Place cells	Classic HD	Theta-by-HD	Int. HD	H-value***	Post-hoc tests
Index of coupling (IC)	0.15 ±0.01	0.05 ±0.004	0.17 ±0.008	0.08 ±0.007	132.135	1, 2***, 3***, 4***, 5, 6***
Index of rhythmicity (IR)	0.24 ±0.02	0.004 ±0.02	0.26 ±0.01	-0.03 ±0.008	165.469	1, 2***, 3***, 4***, 5, 6***
Bursting cell %	69%	0.07%	47%	0.08%	NA	1, 2***, 3*** 4***, 5**, 6***
Burst Index	0.18 ±0.01	0.07 ±0.009	0.11 ±0.008	0.12 ±0.02	75.763	1**, 2***, 3***, 4, 5***, 6
Peak ISI (ms)	5.75 ±0.22	27.71 ±3.93	10.24 ±1.19	19.77 ±0.43	122.109	1, 2***, 3***, 4*, 5*, 6***
ISIFW (ms)	14.02 ±0.07	30.05 ±2.99	22.12 ±1.75	20.39 ±2.411	52.697	1**, 2***, 3***, 4, 5***, 6
Peak-to-trough width (μs)	284.26 ±20.35	278.75 ±15.72	267.98 ±10.39	183.08 ±22.94	19.093	1***, 2, 3, 4***, 5, 6**
Mean rate (Hz)	1.1 ±0.1	3.71 ±0.45	2.55 ±0.18	8.07 ±0.72	79.065	1***, 2, 3***, 4***, 5***, 6***
Peak rate (Hz)	11.29 ±0.96	20.38 ±2.94	5.20 ±0.31	51.70 ±6.43	54.005	1***, 2***, 3, 4***, 5***, 6**

Table 5.4: For each measure, average, SEM and significant differences between groups are reported. Cell groups are place cells, classic head direction (HD), Theta-by-HD and intermediate HD (Int.HD). H-value, results of the KW tests that compared each measure. Proportions of bursting units were compared using multiple Chi-square tests. Post-hoc comparisons (Bonferroni correction): 1, HD vs intermediate HD; 2, HD vs Theta-by-HD; 3, HD vs place cell; 4, intermediate HD vs Theta-by-HD; 5, Theta-by-HD vs place cell; 6, intermediate HD vs place cell. The level of significance for each test is indicated. ISI, inter-spike interval; ISIFW, half-width of the inter-spike interval histogram.

Measures of theta phase-locking (IC) varied directly with measures of rhythmicity of the cells (IR). Two KW tests compared these measures and found that, although intermediate HD cells met the classification criteria based on IC, their theta-modulation did not differ significantly from classic HD cells that did not meet this criteria, suggesting predominantly theta-unrelated spiking. Average IC

and IR of classic HD and intermediate HD cells were the same. Both groups were considerably lower than Theta-by-HD and place cells, which were also the same (IC: H(3)=132.135, p<0.0001; HD vs int.HD, p=1; HD vs Theta-by-HD, p<0.0001; HD vs place cell, p<0.0001; int.HD vs Theta-by-HD, p<0.0001; Theta-by-HD vs place cell, p=1; int.HD vs place cells, p<0.0001; IR: H(3)=165.469, p<0.0001; HD vs int.HD, p=0.081; HD vs Theta-by-HD, p<0.0001; HD vs place cell, p<0.0001; int.HD vs Theta-by-HD, p<0.0001; Theta-by-HD vs place cell, p=1; int.HD vs place cells, p=0.009; Table 5.4). Average and SEM of IC and IR for each group are reported in Table 5.4 and their distribution is illustrated in Figure 5.10. Note three peaks for IC but two peaks for IR, which justifies our choice of cell classification. Hence, only Theta-by-HD and place cells were theta-modulated in both a phase-locked and a rhythmic manner. The described temporal patterns were confirmed by looking at the plots of spiking events relative to the raw LFP trace, as the ones presented in Figure 5.11. Even by eye, it is clear that only Theta-by-HD and place cells fired spike trains roughly corresponding to the frequency of LFP. These spikes were often emitted in groups of 2-3 spikes, or 4-5 for higher rate cells, matching the spike bursting property seen in the autocorrelogram. In contrast, theta-modulation was not visually detectable in the traces of classic HD and intermediate HD cells.

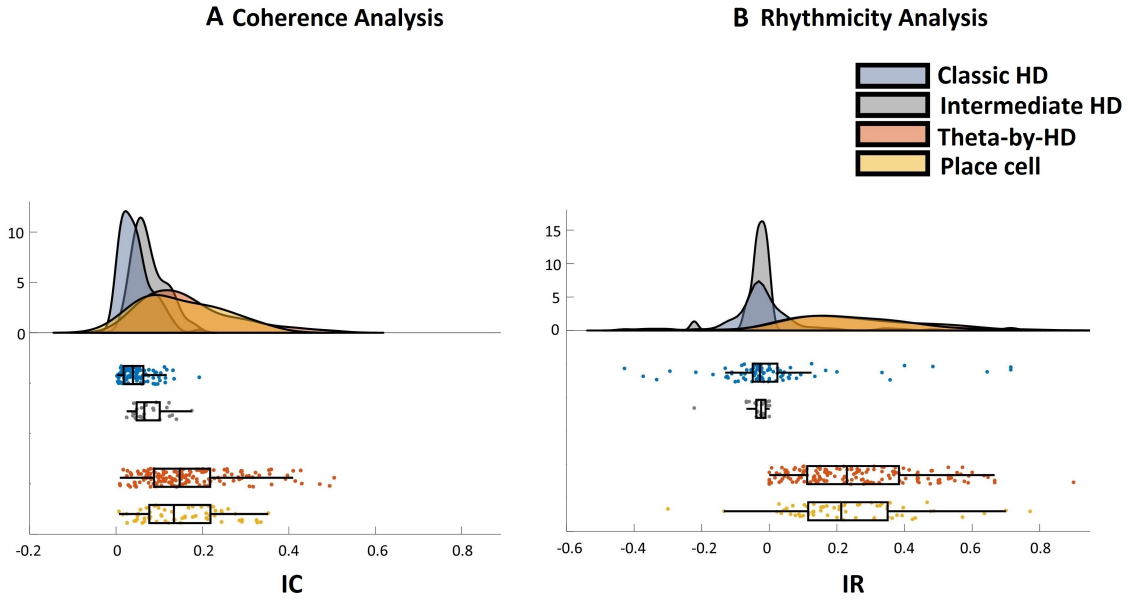


Figure 5.10: **Only Theta-by-HD cells and place cells showed rhythmic modulation of their firing rates at theta frequency.** Distribution of **(A)** index of phase-coupling (IC) and **(B)** index of rhythmicity (IR). Measures are shown as raw data + boxplot + split violin plot (y-axis is probability). Theta-by-HD (red) and place cells (PC; yellow) show the same levels of locking strength (IC) and intrinsic spike rhythmicity (IR),

both higher than classic HD cells (HD; blue) and intermediate HD (gray), which did not differ. Cell types are specified in the legend and the same colour coding will be used throughout this thesis. Intermediate HD cell distribution was in-between classic HD and Theta-by-HD cell for IC, as firing was not always coherent with theta during a trial, but not for IR.

5.4.5 Do different cell groups fire on the same or different theta phases?

We computed the preferred theta phase of each cell and plotted these values in circular histograms (Figure 5.11) to determine whether firing of different cell groups converged on the same or different theta phases. Phases were recorded relative to the local AV theta and not to a fixed hippocampal theta reference, but theta phase lag coordination between these structures is known (Tsanov et al., 2011).

Classic HD cells that did not fire on any specific phase at the single cell level showed a uniform phase distribution also at the population level. The R-vector of these angles was 0.17 and the mean theta phase for all cells was 64.12°. The Omnibus test failed to reject the null hypothesis of uniformity (m=35, p=0.125). Phase preference was consistent for all other cell types (Figure 5.11). For Theta-by-HD and place cells, phases were highly clustered on descending theta phases, around a mean of 124.02° for Theta-by-HD (R-vector=0.67; Rayleigh test, z=69.824; p<0.0001) and 76.02° for place cells (R-vector=0.59; Rayleigh test, z=21.653, p<0.0001). In contrast, for intermediate HD cells, phases were highly clustered on ascending theta phases close to theta peaks, around a mean of 338.86° (R-vector=0.78; Rayleigh test, z=15.948, p<0.0001). Mean preferred theta phases for all these groups differed significantly from each other (two-samples WW tests, place cell vs Theta-by-HD, F=31.4775; place cell vs Int.HD, F=31.478; Theta-by-HD vs Int.HD, F=135.062; all p<0.0001). Based on these results, signal from different cell groups maintained a constant phase-relationship to the theta cycle and to each other over time. Theta-by-HD and place cells showed sequential, phase-shifted activation on descending theta phases, with place cells firing slightly earlier closer to the peak, and Theta-by-HD firing later on, closer to the trough, while intermediate HD cells preferentially fired at the peak, or just before the peak of the theta cycle (see bottom schematics in Figure 5.11). Since theta was not measured from a fixed reference point across all trials, these differences could be due to differences in electrode placement, although this seems unlikely given that AV is a non-layered structure.

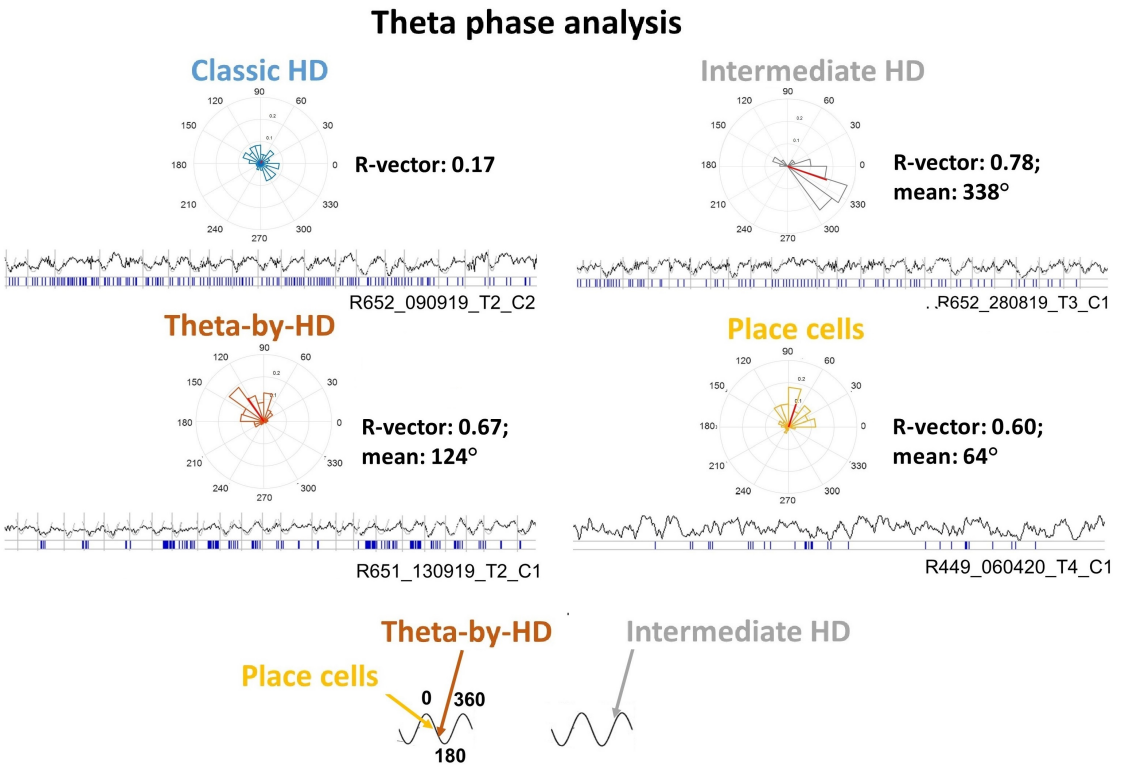


Figure 5.11: **All cell groups have different preferred theta phases from each other.** Top, Circular histogram of preferred theta phases for each cell group. The corresponding mean vector length (R-vector, red line) is reported next to each plot. When the R-vector is significant, the mean preferred phase is also reported (direction of the R-vector). Below each phase distribution, a spike raster plot depicts an example of unit recording paired with the raw LFP trace for each cell type. Each trace shows 3s of recordings. Theta-by-HD and place cells fired in theta-bursts, and bursting events aligned with descending theta phases. Classic and intermediate HD cell fired in a non-bursting manner (single spikes predictive of non-rhythmic cells). Single spikes occurred independently, or mostly independently, of theta. For intermediate HD cells, phase-locking was not visually detectable from the spike rasters and here it was based on index of coupling values (IC). Phase distribution was uniform for classic HD cells but unimodal for other cell types. As a population, place cells preferentially fired on the first half (76°) and Theta-by-HD cells fired on the second half (124°) of descending theta phases, while intermediate HD cells become preferentially active on ascending theta phases (338°). Bottom, schematic diagram of these results, showing that mean preferred theta phases different for all cell groups. A value of 180° was assigned to theta troughs and 0/360° to peaks.

5.4.6 Do cells show phase precession?

The earlier phase preference of place cells compared to Theta-by-HD cells could result from the precession of firing phases relative to theta (O'Keefe and Recce, 1993). If cells phase precessed, their intrinsic oscillation (the theta frequency in the temporal autocorrelogram) should be slightly faster than the global theta frequency (the theta frequency in the LFP), since spikes would occur progressively earlier on each successive cycle, thus resulting in an average earlier phase preference for the trial (Hafting et al., 2008; Bush et al., 2022).

Matching this prediction, on average place cells fired at a rate faster than the global theta frequency (mean intrinsic vs global frequency: 9.09 vs 8.54Hz; t-test, t(60)=-3.595, sd=1.198, p<0.0001), and 47/61 (77%) place cells phase precessed (Chi-square test of expected proportions, χ^2=35.705, p<0.0001). Theta-by-HD cells also fired at a rate faster than theta (intrinsic vs global frequency: 8.9 vs 8.63 Hz,; t(157)=-4.084, sd=0.815,p<0.0001), and 101/158 (64%) Theta-by-HD cells phase precessed (χ^2=24.506, p<0.0001). However, this proportion was lower than in place cells (χ^2=3.460 p=0.063) but the same as in non-rhythmic HD cells (χ^2=1.241, p=0.265), which showed no difference between global and intrinsic theta frequency (intrinsic vs global frequency: 8.81 vs 8.66 Hz; t(121)=-1.080, sd=1.578, p=0.282). 70/122 (57%) non-rhythmic HD cells phase precessed (χ^2=5.311, p=0.02). This proportion was lower than in place cells (χ^2=6.825 p<0.01).

Non-rhythmic HD cells here include both intermediate and classic HD cells. The reason for the large number of phase precessing neurons is that a good fit of the model (decaying sine wave) to the autocorrelogram is seen only for cells that are highly theta modulated (with a rhythmic autocorrelogram). Only for these cells, the autocorrelogram fit parameter ω provides a reliable estimate of theta frequency. Given that a lack of good model fit for non-rhythmic HD cells (R2<0.7) means that cells are not theta-modulated (weak or no significant spike time-theta phase relationship), calculation of precession relative to LFP phases is not meaningful, and is reported here only for completeness. In the future, one solution would be to discard from this analysis all cells with a non-rhythmic autocorrelogram (IR<0.001) or weight ω by the R2 of the model fit.

We concluded that place cell spikes more steeply precessed than other neurons. By looking at spike rasters, precession appears subtle on a spike-by-spike basis (Figure 5.12, bottom). However, this matches previous observations that phase

precession is typically weak for hippocampal place cells recorded in an open field box compared to a linear track (Cacucci et al., 2007; O'Keefe and Recce, 1993), and here is consistent with their narrow oscillatory range.

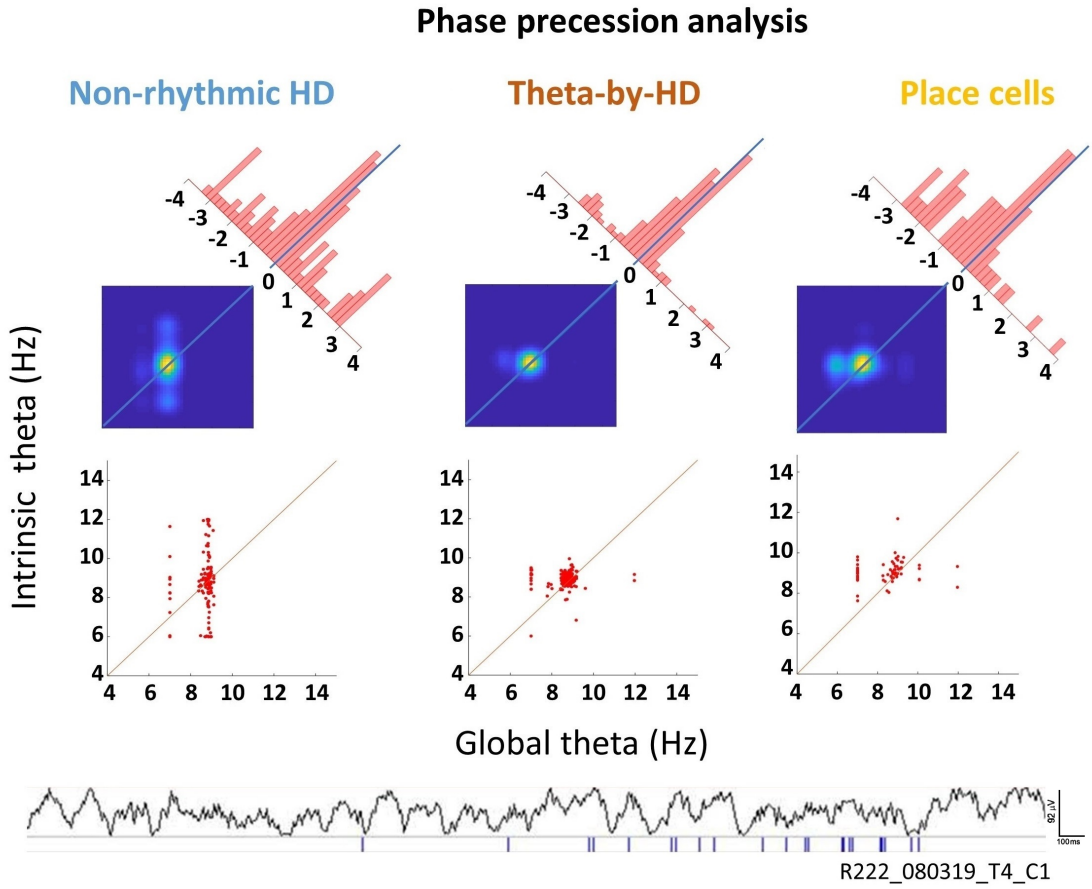


Figure 5.12: **Place cells phase precess relative to the local theta oscillations.** Intrinsic theta frequency (measured from the autocorrelogram, see Methods; x-axis) vs global theta frequency (from the LFP; y-axis), displayed as heatmaps and scatterplots. Red markers represent cells, if a marker is above the diagonal line then the cell was precessing. Corner histograms display the distance of each cell from the diagonal. A negative distance means that the cell falls above the diagonal, and hence is precessing. Classic and intermediate HD cells were combined into a single distribution of non-rhythmic HD cells. We do not expect precession for these cells, given their weak relationship to theta phases, and the lack of a good model fit to the autocorrelogram. A higher number of place cells precessed compared to the HD dataset. Bottom, example of place cell unit recording and raw LFP trace, for 3s of recording. The spike trace shows evidence of bursting (spikes grouped in 2-3 aligned with descending theta phases) and phase precession (spikes occurring slightly earlier with each successive cycle).

5.4.7 A subset of Theta-by-HD cells show theta cycle-skipping

A small subset of Theta-by-HD cells (n=46/158; 29.11%) showed evidence of theta cycle-skipping in their temporal autocorrelogram. These cells, named theta-skipping HD cells, mostly fired on alternating cycles, with only some spikes emitted at theta frequency (some cycles were not skipped), as indicated by the first autocorrelogram side-peak at 125ms being smaller than the second side-peak at 250ms. Note that our cell-type inclusion criteria for Theta-by-HD cells based on IC and IR did not allow to formally distinguish theta phase-locked units that were theta-rhythmic from phase-locked units that were rhythmic and skipping, given that they would display equal levels of locking and autocorrelogram rhythmicity. Hence, to classify theta-skipping HD cells, we derived a theta-skip index (TS) from the autocorrelogram that indicated how much the first side-peak was skipped by the firing activity. Only cells being both theta-modulated (based on IC) and rhythmic (based on IR) were considered for TS calculations.

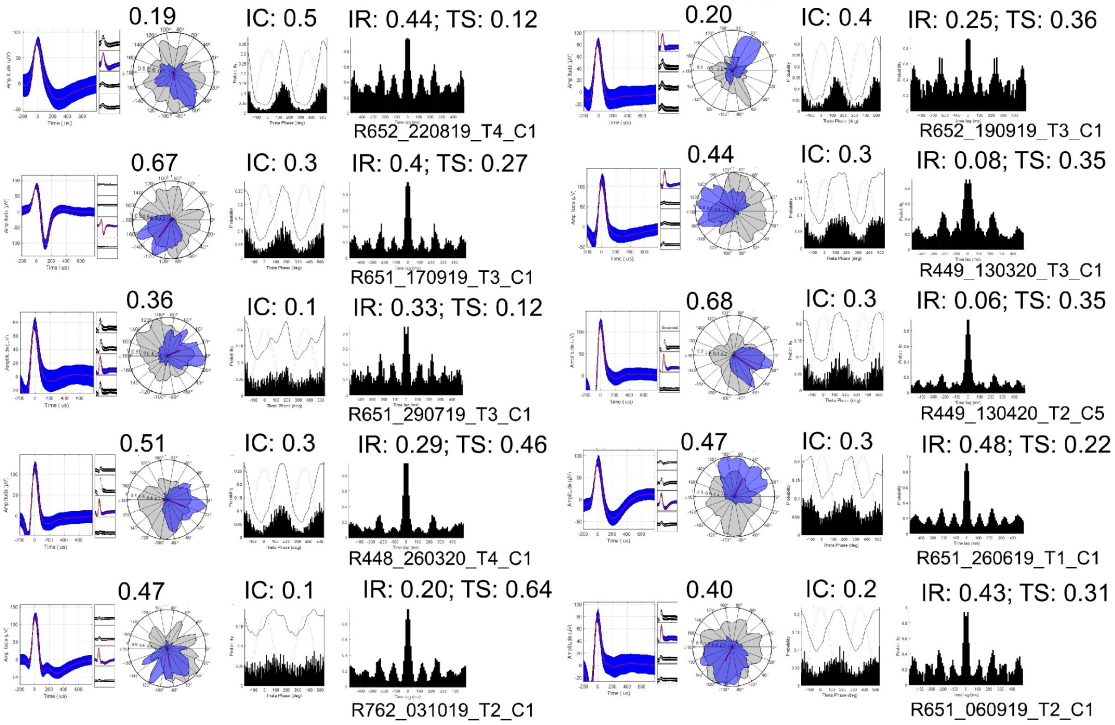


Figure 5.13: **Examples of Theta-by-HD cells showing theta cycle-skipping in the autocorrelogram**. 29% of Theta-by-HD cells were theta-skipping. From left to right: average spike waveform; x-axis, time (μs); y-axis, amplitude (μV); polar plot of directional tuning curve (blue) and dwelltime curve (gray), with R-vector; spikes vs theta phases histogram, shown as raw and as density estimate, with Index of Coupling (IC); x-axis, degrees; y-axis, frequency count (left) or probability (right). Spikes

preferentially occurred on descending theta phases; peak-normalized temporal autocorrelogram implemented between±500ms, with Index of Rhythmicity (IR) and theta-skip index (TS).

Among all 158 Theta-by-HD cells, 119 (75.3%) displayed a good autocorrelogram model fit (R2>0.7), and 47 of these cells (39.5%) exceeded the threshold for theta-skipping (TS>0.1). One cell was removed by visual inspection, leaving a total of 46 theta-skipping HD cells (29% of the Theta-by-HD cells, see examples in Figure 5.13). A total of 53/61(86.9%) place cells displayed a good model fit and seven of these cells (13.7%) exceeded the threshold for theta-skipping. Six of these cells were later removed by visual inspection (variable autocorrelogram shape due to small spike number), leaving only one theta-skipping place cell that was not analyzed further. None of the intermediate HD cells met the requirement for a baseline theta power component in the autocorrelogram and thus were not considered for TS calculations. We found no difference in preferred theta phase, spatial and temporal firing properties between Theta-by-HD cells that were rhythmic and Theta-by-HD cells that were rhythmic + skipping (not shown), except for differences in TS index magnitude (0.19±0.01 vs -0.01±0.01; WRS test, z=9.28, p<0.0001).

5.4.7.1 Theta-skipping was coordinated between co-recorded cells

When two theta-skipping HD cells were simultaneously recorded on the same tetrode (n=12 cell pairs), we conducted cross-correlation analysis to determine whether theta-skipping was coordinated across cells. We derived a TS index for the cross-correlogram, bound between -1 and 1, with positive values indicating cells that fired in synchrony (same alternating cycles), negative values cells that fired in anti-synchrony (opposite alternating cycles), and increasing magnitude of the TS index indicating more cycle skipping. The majority (n=10/12 cell pairs) showed evidence of coordinated activity in their cross-correlation, having an absolute TS index in the cross-correlation>0.1. Eight of these pairs fired in synchrony (TS index in the cross-correlation>0.1) and the remaining two pairs fired in anti-synchrony (TS index in the cross-correlation<-0.1). Examples of cross-correlations for synchronous and anti-synchronous cell pairs are provided in Figure 5.14.

Analysis was then conducted to compare PFDs between cells within each pair, to determine whether synchronous cells would have more overlapping tuning curves than anti-synchronous ones, whose firing is separated by one theta cycle, as previously reported by recordings of parahippocampal theta-skipping HD cells by

Brandon et al. (2013). Matching previous findings, average absolute angular separation between PFDs was 18.75°±6.56 for synchronous cells (n=8) and 102.69°±23.32 for anti-synchronous cells (n=2; two-sample WRS; ranksum=36, p=0.044) (Figure 5.14 D). Results, albeit preliminary and needing verification by recording from a larger dataset, are in line with a general role of theta oscillations in the functional and temporal segregation of neuronal activity (more details in the Discussion, Section 5.5.3).

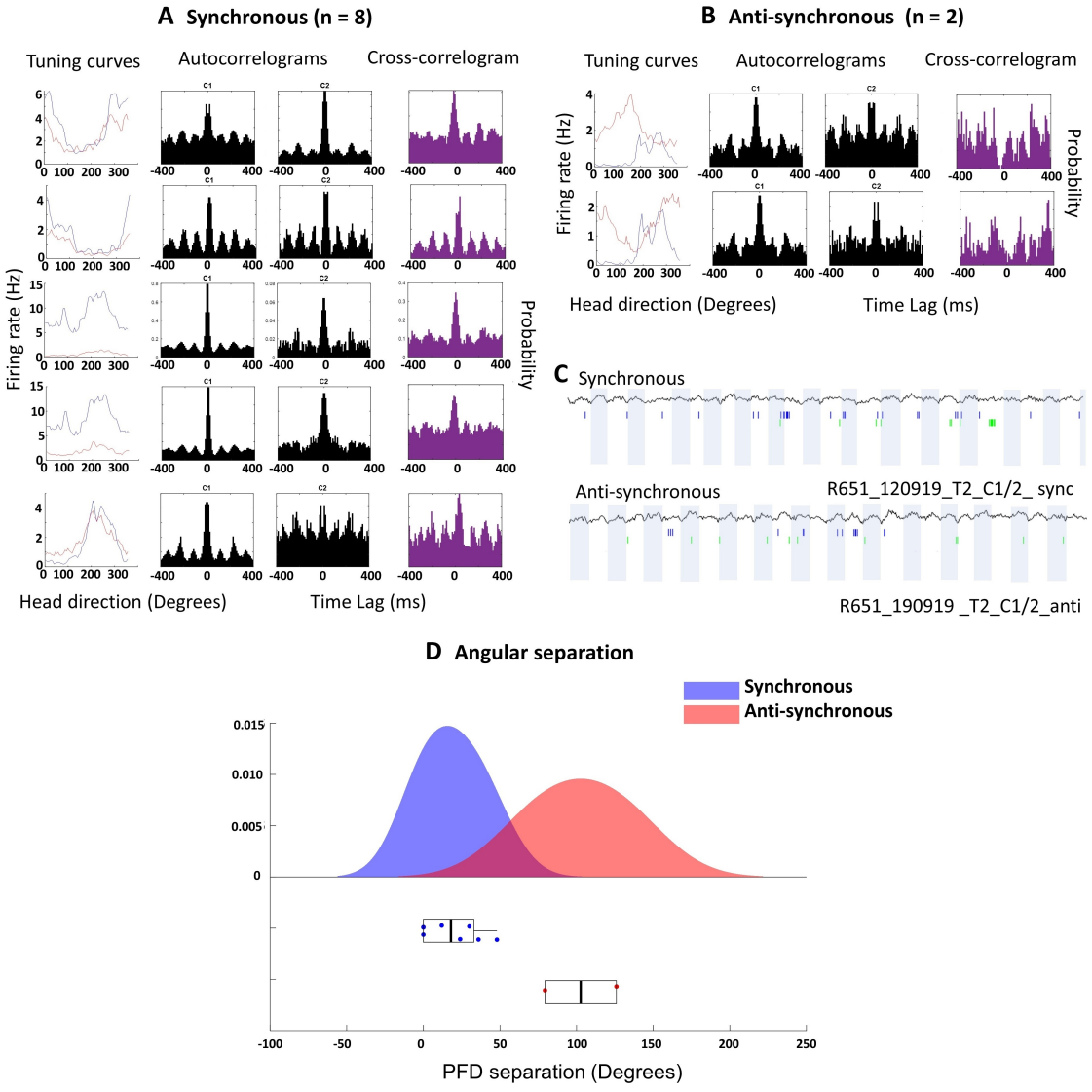


Figure 5.14: **Theta-skipping cells maintain fixed temporal relationships to the theta cycle over time.** Examples of co-recorded theta-skipping HD cells. **(A)** Synchronous and **(B)** anti-synchronous pairs have the same or opposite relationships to theta. Reflected in cross-correlogram peak at 0ms and 125ms, respectively. For each cell pair, from left to right: tuning curves of firing rate (Hz) vs HD (degrees); peak-normalized

temporal autocorrelogram (black); peak-normalized cross-correlogram of the two cells (purple). x-axis, ms; y-axis, probability. **(C)** Spike rasters for synchronous and anti-synchronous cells. Spiking events are displayed relative to the raw LFP trace. Odd theta cycles are highlighted in gray, even cycles in white. Synchronous cells: both skip the even cycles. Anti-synchronous cells: cell 1 (blue) skips the even, cell 2 (green) skips the odd cycles. **(D)** Angular separation between the preferred firing directions (PFD) of synchronous vs anti-synchronous pairs, shown as raw data + boxplot + split violin plot. x-axis, degrees; y-axis, probability.

5.4.8 Are there differences in firing mode?

5.4.8.1 Place cells contain the highest proportion of bursting neurons

A spike burst was defined as a train of 2+ spikes, separated by ISIs<6ms. A complex spike burst was defined as a burst of spikes with decreasing amplitude. We derived the peak ISI to distinguish cells with bursting (peak ISI<6ms) and non-bursting (peak ISI>6ms) firing mode, and examined the proportion of bursting units within each cell group. Results of this analysis are reported in Table 5.4. Place cells contained the highest proportion of bursting units (42/61, 69%) compared to the HD dataset (Chi-square test, place cell vs HD: χ^2=65.84; place cell vs Theta-by-HD: χ^2=8.565; place cell vs int.HD: χ^2=27.28; all p<0.01), matching the pattern of complex spike bursting visible in the raster plots (Figures 5.11 - 5.12). Within the HD dataset, Theta-by-HD cells contained equal proportions of bursting and non-bursting units (74/158, 47%), and the proportion of bursting units was larger than both classic HD and intermediate HD (Theta-by-HD vs HD: χ^2=42.99; Theta-by-HD vs int.HD: χ^2=14.11; all p<0.001). Classic HD and intermediate HD contained only a very marginal subset of bursting units (7/96, 0.07% and 2/26, 0.08%) and these proportions were the same (HD vs int.HD: χ^2=0.005; p=0.945).

In agreement with the estimations based on comparisons of bursting cell proportions, on average place cells exhibited shorter peak ISIs compared to the HD dataset (Table 5.4). Within the HD dataset, classic HD and intermediate HD had the same peak ISI, both being longer than peak ISI of Theta-by-HD cells. Theta-by-HD values were intermediate between place cells and the two groups of non-rhythmic HD cells (ISI: H(3)=122.109, p<0.0001; HD vs int.HD, p=0.178; HD vs Theta-by-HD, p<0.001; HD vs place cell, p<0.001; int.HD vs Theta-by-HD, p=0.011; Theta-by-HD vs place cell, p=0.011; int.HD vs place cells, p<0.001). Differences in burstiness were not perfectly repeated when looking at burst index (H(3)=75.763,

p<0.001) and ISIFW (H(3)=52.697, p<0.0001), which instead resulted in more highly overlapping distributions. The mean burst index of place cells was higher than that of Theta-by-HD and classic HD cells, but not significantly different from that of intermediate HD cells. Similarly, values for intermediate HD cells were higher than classic HD cells but not significantly different from Theta-by-HD cells (burst index: HD vs int.HD, p=0.001; HD vs Theta-by-HD, p<0.001; HD vs place cell, p<0.001; int.HD vs Theta-by-HD, p=1; Theta-by-HD vs place cell, p<0.001; intHD vs place cell, p=0.118). These differences were repeated for ISIFW (ISIFW: HD vs int.HD, p=0.024; HD vs Theta-by-HD, p<0.001; HD vs place cell, p<0.001; int.HD vs Theta-by-HD, p=1; Theta-by-HD vs place cell, p=0.015; int.HD vs place cell, p=0.196). See Table 5.4. We concluded that only rhythmic units, namely Theta-by-HD and place cells, could fire either in a bursting or non-bursting mode, while non-rhythmic units, namely classic HD and intermediate HD cells, fired single spikes predominantly uncoupled from theta (Figure 5.11). Further qualitative observations on cell firing mode are reported in Section 5.4.10.

5.4.8.2 Does burstiness reflect theta strength or cell type?

We have found that classic HD and intermediate HD cells display the same degree of theta-modulation strength and bursting propensity, both considerably lower than the other groups considered here. We asked whether burstiness of a cell correlates with its theta strength, as such correlation could introduce spurious differences in bursting propensity, because of our cell-type classification criteria based on theta strength. To examine this possibility, we used generalized linear models (GLM, Matlab function *fitglme*) to model burstiness (burst index) of a cell as a function of two predictors, theta strength (IC) vs cell type, as a normally distributed variable. Cell types (classic HD, Theta-by-HD, place cells and intermediate HD) were dummy coded into categories A,B,C,D respectively. Methods and model's notation were taken from Ebbesen et al. (2016).

There was a non-significant dependence of burstiness on theta strength (GLM1, burst index~1 + IC; ANOVA, p_{theta}=0.715), but a significant dependence on cell type (GLM2, burst index~1 + type; ANOVA, p_{type}<0.0001). When modeled as a function of both predictors, using a model that allowed for interactions between cell type and theta strength, dependence on type but not dependence on theta strength remained significant (GLM3, burst index~1 + IC + type + IC * type ; ANOVA, p_{theta}=0.05; p_{type}=0.015). The interaction was also moderately significant

(ANOVA, $p_{theta*type}$=0.029). To determine which model better explained the data, we calculated the Akaike information criterion (AIC; Akaike, 1974). GLM2 and GLM3 had similar Akaike information criterion, both considerably more negative that GLM1 (GLM1, -595.58; GLM2, -639.12; GLM3, -646.42). Hence, adding cell type as a predictor in addition to IC explained the data better than IC alone, suggesting that differences in burstiness more reliably reflect the type than the theta strength of a neuron.

5.4.9 Do cells have different waveform properties?

5.4.9.1 Spike waveform shape is variable among AV neurons

Next, we undertook analysis to determine whether cells could be distinguished based on their spike waveform width, as this can be informative of cell typology. In previous efforts to record from AV, half of AV cells had peak-to-trough width<250μs and there was no difference in average width (174.2±6.5μs vs 189.5±22.6μs) and average firing rate (31.5±1.55Hz vs 33.5±1.66Hz) between classic HD and Theta-by-HD cells (Tsanov et al., 2010, 2011). We observed waveform properties comparable to those previously reported in AV. Approximately half of our cells had peak-to-trough width<250μs (193/341, 56.6%), with the following proportions for each group: classic HD, 51%; Theta-by-HD, 54%; place cell, 56%; int.HD, 85%. As expected from these proportions, average peak-to-trough width for intermediate HD cells was smaller than that of all other groups, whose values did not differ from each other (H(3)=19.093, p<0.001; HD vs int.HD, p<0.001; HD vs Theta-by-HD, p=1; HD vs place cell, p=1; int.HD vs Theta-by-HD, p<0.001; Theta-by-HD vs place cell,p=1; int.HD vs place cell, p=0.001). See results in Table 5.4.

The fact that all the cell groups have the same waveform width and contain the same proportion of narrow and broad spikes (except for intermediate HD cells, which are overall narrower) could be used as an argument against place cells being axon spikes. The existence of wider spikes is also seen when plotting the distribution of waveforms for all the cells and for place cells alone. The two distributions show the same bimodal pattern (Figure 5.17). Recordings from different AV subfields, referred to as parvicellular and magnocellular in the literature based on differences in cell body size (Shibata and Yoshiko, 2015; Gabriel, 1993), may be a contributing factor for the variable waveform shapes reported. We found differences in average waveform width between AVDM and AVVL (shown below).

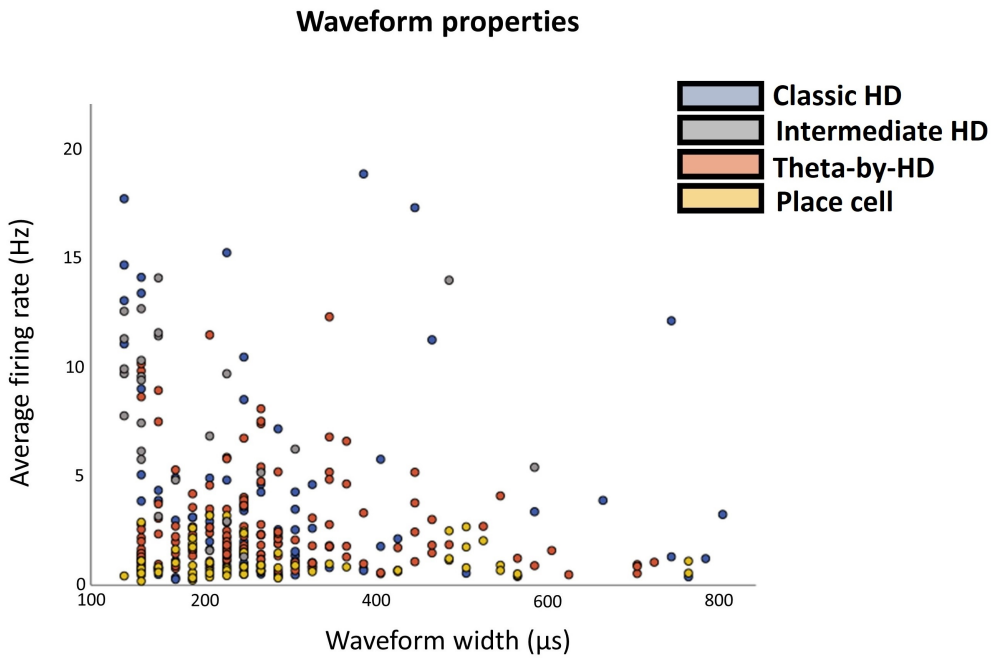


Figure 5.15: **Cells have a variable extracellular waveform duration.** Each marker is a cell, mean firing rate (Hz) is plotted against peak-to-trough width (μs). Classic HD (blue); Theta-by-HD (red); intermediate HD (gray); place cell (yellow). Intermediate HD cells are clustered at the top left while other cell types have more variable waveforms. Place cells have low firing rates that cover the full range of waveform widths, while in hippocampus widths are expected to be clustered at high values>500μs.

Intermediate HD cells also fired at higher mean rate compared to other groups (Figure 5.15). There was no difference between mean rate of classic HD and Theta-by-HD, and both were higher than place cell rates, firing at the lowest mean rate compared to other groups (Table 5.4; H(3)=79.065, p<0.001; HD vs int.HD, p<0.001; HD vs Theta-by-HD, p=1; HD vs place cell, p<0.001; int.HD vs Theta-by-HD, p<0.001; Theta-by-HD vs place cell, p<0.001; int.HD vs place cell, p<0.001). See results in Table 5.4. Hence, there was a weak, but significant, negative correlation between peak-to-trough width and mean firing rate (Pearson's r=-0.16; p=0.0042). The result that narrow and broad spiking cells have the same firing rate is consistent with a lack of putative interneurons in the rodent ATN (Arcelli et al., 1997; Jones, 1985; Henze et al., 2000).

5.4.9.2 Are there differences in the firing properties of narrow and broad spiking cells?

We plotted the distribution of peak-to-trough widths for all the cells and fitted a two-Gaussian component (Figure 5.17 A). Two conservative cutoffs were identified on this model to separate waveforms into narrow, broad and unclassified/in-between (see General Methods, Section 3.6.2). Few cases (n=11) were discarded because spike waveforms did not reach time for repolarization. Cells were classified as follows: narrow spiking, 77.6% (n=256); broad spiking, 12.7% (n=42); 9.7% unclassified (n=32). We compared spatial and theta properties between the two groups identified by the model. The odds of finding a cell with a significant place or theta component in the broad spiking group were 2.8× and 4.3× higher, respectively, than in the narrow group (Fisher exact test; all $p<0.0001$; n=298). In contrast, cells with a significant direction, linear speed and AHV component were no more likely to be found in the broad group than in the narrow one (all $p>0.05$; n=298). See further analysis in Appendices (Figure A.7, Section A.4.2). Hippocampus-related spiking patterns, namely theta- and place-modulation, were more likely to co-occur in broad spiking cells than in narrow ones, independently from HD- and velocity-modulation. These properties could be derived by AV neurons from a common hippocampal source, via the Sub, whereas HD and velocity signals could be derived from brainstem pathways originating outside of hippocampus, via MMN or mediated by descending RSC projections.

From the above results, it was particularly striking that some place cells have a broad waveform, resembling that of hippocampal pyramidal neurons, whereas others have a much narrower width, resembling that of place cells that have been found in other subcortical structures outside of hippocampal formation (Jankowski and O'Mara, 2015; Jankowski et al., 2015). Since a narrow width of waveform could result from axonal recordings, we applied the two-Gaussian model to the distribution of peak-to-trough widths for place cells to determine whether there were two peaks or whether the distribution was continuous (Figure 5.17 B). Few cases (n=2) were discarded based on waveform not reaching repolarization. The analysis resulted in two modes, albeit in very different proportions: narrow spiking, 79.7% (n=47); broad spiking, 20.3% (n=12). No cells were left unclassified based on values falling into the dip of the bimodal distribution. The calibrated Hartigan's Dip Test discarded the null hypothesis of unimodality (DIP=0.059; $p<0.01$). These values match those derived from fitting the two-Gaussian model to the whole AV cell population (shown above), in which place cells formed 44/256 (17.9%) of the narrow cells and 12/42 (28.6%) of the broad cells (although n=3 place cells were left unclassified by this analysis).

Place cells classified as broad displayed stronger theta-modulation compared to narrow ones (IC: 0.24±0.02 vs 0.13±0.01; two-sample WRS test, z=3.399, p<0.001; Figure 5.17). There was no differences between the two groups in any of the other firing properties tested (all p>0.0.5), namely locational information content (1.51±0.12 vs 1.33±0.07), directional information content (0.41±0.09 vs 0.39±0.05), modulation by linear speed (speed score: 0.52±0.06 vs 0.56±0.04) and AHV (AHV score: 0.26±0.04 vs 0.33±0.02), mean firing rate (1.27±0.22Hz vs 1.06±0.11Hz), peak firing rate (3.91±0.43Hz vs 3.15±0.33Hz), and spike bursting propensity (burst index, 0.18±0.02 vs 0.17±0.01). No correlation was found between peak-to-trough width and all the above measures, except for theta-modulation strength (IC: Pearson's r=0.28; p=0.03). Correlations were as follows: locational info: r=0.08; directional info: r=0.05; speed score: r=-0.03; AHV score: r=0.13; mean rate: r=0.03; peak rate: r=0.027; burst index: r=0.12 (all p>0.1).

The result that many AV neurons, including (but not only) place cells, have a short spike waveform duration, and in place cells this is not correlated with locational information content, suggests that our place cells are different from hippocampal ones and are not the result of axonal recordings from hippocampus. Furthermore, although place cell waveforms are narrower than hippocampal ones, they are actually broader than other AV cells, based on the odds ratio, although this difference does not reach statistical significance based on the Kruskal-Wallis test (Table 5.4).

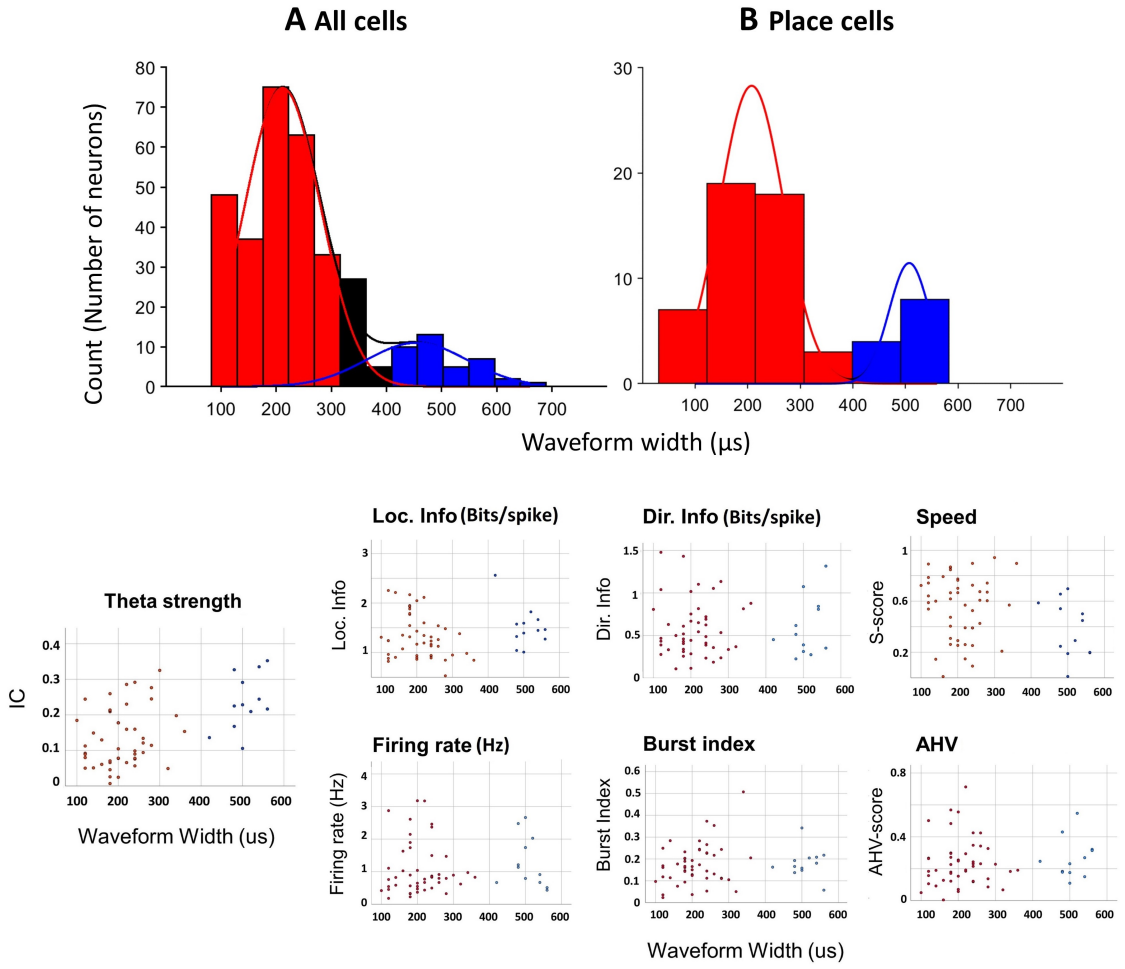


Figure 5.17: **Differences between broad- and narrow-spiking place cells.** Frequency distribution of peak-to-trough width for **(A)** all cells, **(B)** place cells. x-axis, μs; y-axis, frequency count. Gaussian fits for the different modes (cell types) are displayed: broad (blue), narrow (red), unclassified (gray). Bottom, for the place cells delineated in B, peak-to-trough width (μs) is plotted against different firing properties, colour coded by waveform type (broad vs narrow). From them all, only theta-strength (measured by the Index of Coupling, IC) between narrow and broad types reached a significant difference (p<0.0001).

5.4.10 Qualitative observations on firing mode

To summarize the findings of the temporal analysis presented in this Chapter, we now report qualitative observations on cell firing mode: theta-modulated vs non-theta-modulated (based on IC), rhythmic vs non-rhythmic (based on IR), bursting vs non-bursting (based on peak ISI). Observations were from visual inspection of ISI

scatterplots (Figure 5.18). Each point is a spike. X-axis indicates the interval before, y-axis indicates the interval after each spike. Points falling below the red horizontal line are intra-burst spikes (pre-ISI<6ms), and the proportion of these spikes to total spikes was quantified by the burst index. For each cell, the corresponding ISI histogram is shown, alongside measures of peak ISI and burst index. Clearly distinct patterns of temporal firing emerged, summarized as:

1. Classic and intermediate HD cells (i): ISI profiles are characterized by one main ISI cluster with variable pre- and post-ISI ranges, suggesting no preference for a specific interval. Very few intra-burst spikes with pre-ISI<6ms.

2. Theta-by-HD and place cells (ii; iv-vi): two additional ISI clusters are visible in the higher pre- and post-ISI range (around 120ms), respectively, formed by the first and last spike of rhythmically-grouped spike trains emitted at theta (6-12Hz) frequencies. We refer to these spikes as a train rather than a burst, because not all spikes have pre-ISI<6ms. In some cases, a fourth cluster is visible in the high pre- and post- ISI range (top right), formed by single spikes (not part of a train) emitted at theta frequencies, with pause of approximately 120ms both before and after each spike. The main difference between the two ISI profiles was the size of this fourth cluster, which tends to be smaller for place cells, in line with their shorter ISIs.

3. Intermediate HD cells (iii): ISI profiles are similar to those of classic HD cells (i), being characterized by one main ISI cluster and limited number of intra-burst spikes. The two additional clusters are much smaller than for the theta-modulated cells, in line with spikes emitted only occasionally at theta frequencies.

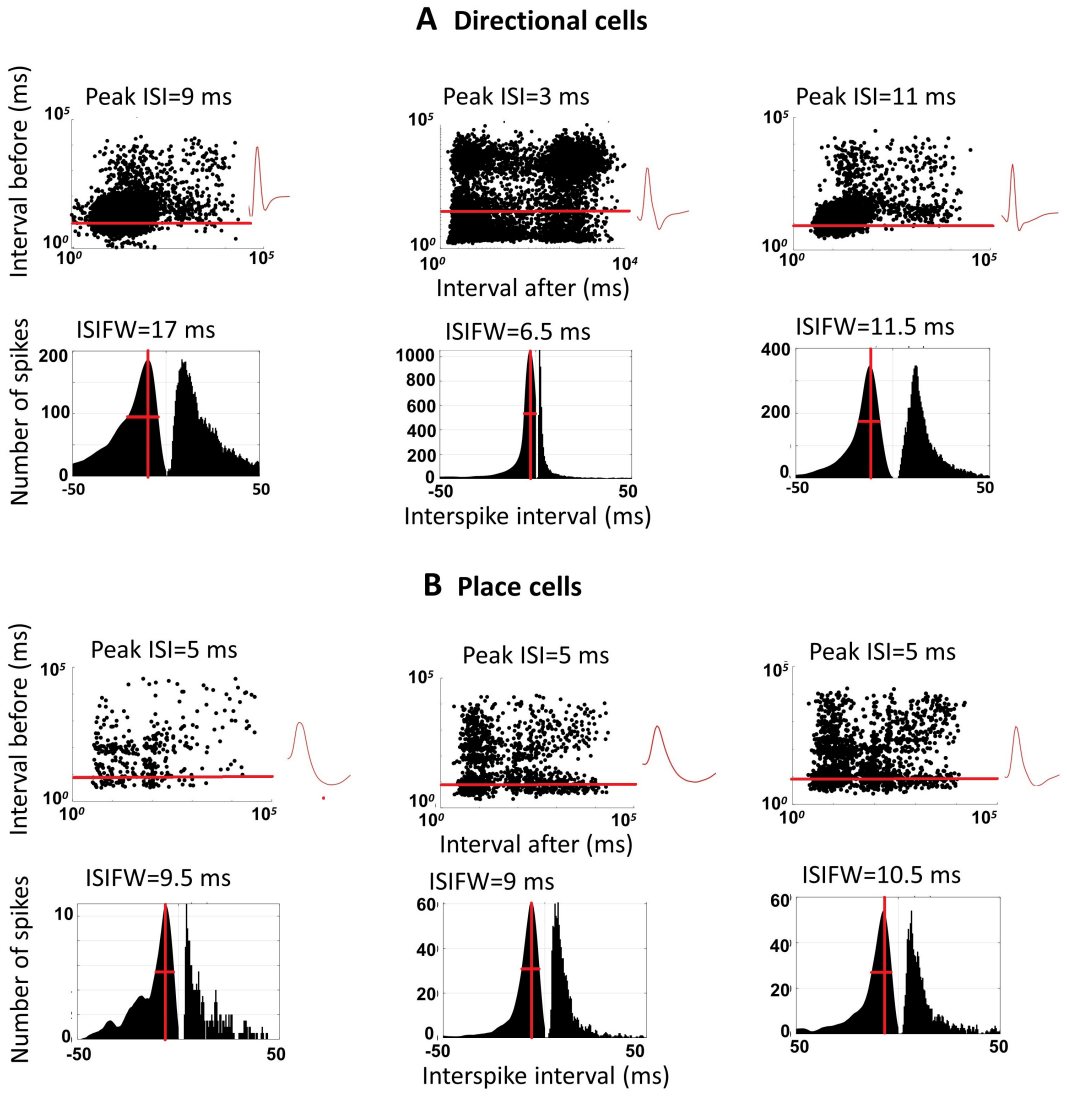


Figure 5.18: **Specific temporal firing profiles can be visualized by inter-spike interval scatterplots.** **(A)** Examples of directional neurons, in order from left to right are: classic HD, Theta-by-HD and intermediate HD. Only Theta-by-HD cells display bursting firing mode. **(B)** Examples of place cells, all showing bursting firing mode. For each cell in A-B, the following plots are presented. Top, log-scale scatterplot of inter-spike intervals (ISI); x-axis, interval to the previous spike (ms); y-axis, interval to the next one (ms). Each marker is a spike. Red line marks the 6ms pre-ISI that defines a burst. The more spikes reach this threshold, the more the ISI histogram will display a fast-decaying peak, indicating a prevalence of short intervals. Bottom, ISI histogram shown as raw and as smooth density estimate. x-axis, ISI in 2ms-time bins (ms); y-axis, frequency counts. Peak ISI and ISI half-width (ISIFW) are marked in red and reported for each cell. Average spike waveform is depicted in red next to each cell.

5.4.11 Are there differences between AV subfields?

Since theta activity differed between the two RSC subregions, being more present in gRSC (Lomi et al., 2021), we compared theta modulation between the two AV subfields, AVDM and AVVL, to determine whether AV efferents could explain RSC results. It was surprising to see no theta difference between the two AV subfields (two-sample WRS test, IC: 0.17 vs 0.14, z=0.21, p=0.834). Instead, we found a more subtle difference in the anatomical distributions of cell types between AVDM and AVVL. For simpler comparisons, classic HD (96/122) and intermediate HD cells (26/122) were pooled into a single population of 122 non-rhythmic HD cells, as both cell types fired non-rhythmically, with the same mean IC and IR. A larger proportion of non-rhythmic HD cells and theta cells with no spatial correlates were recorded in the AVDM subfield, projecting almost exclusively to gRSC. In contrast, a larger proportion of Theta-by-HD and place cells were recorded in the AVVL subfield, projecting more heavily to dRSC. There was no difference in the anatomical location of the un-classified units with no spatial/temporal correlates (proportions are reported in Figure 5.19). Results of the Chi-square test for differences in cell proportions between AVDM and AVVL were as follows: non-rhythmic HD cells, χ^2=9.059, p=0.0026; Theta-by-HD cells, χ^2=9.276, p=0.0023; place cells, χ^2=7.197, p=0.0073; theta cells, χ^2=9.334, p=0.0022; un-classified cells, χ^2=3.054, p=0.081.

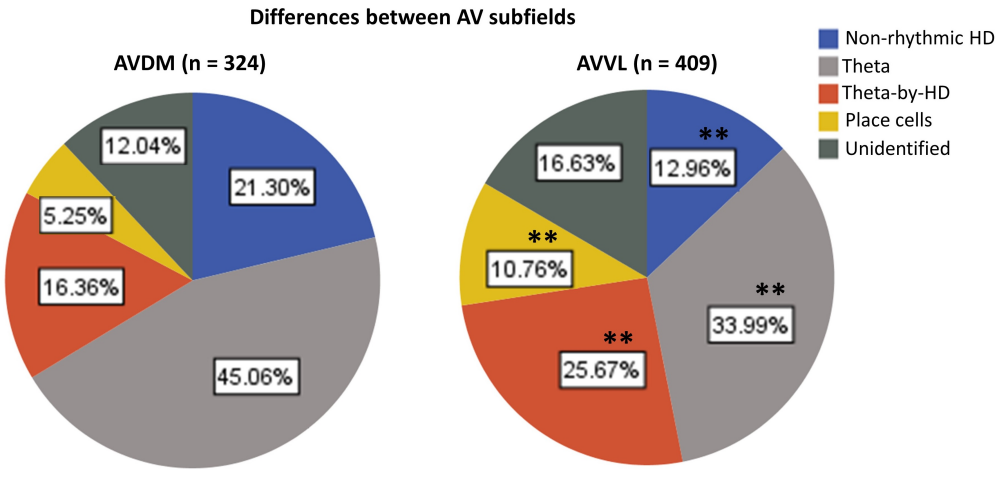


Figure 5.19: **Different anatomical distribution of neurons within AV.** Proportion of cells in two AV subfields, dorsomedial (AVDM) and ventrolateral (AVVL). AVDM contains a larger proportion of non-rhythmic HD and theta cells with no spatial correlates. Non-rhythmic HD cells here include intermediate and classic HD cells (both non-rhythmic and non/only partially phase locked). AVVL contains a larger

proportion of Theta-by-HD and place cells (both rhythmic and strongly phase locked). Unidentified cells were equally distributed in AVDM and AVVL. Proportions were as follows (AVDM vs AVVL): non-rhythmic HD (classic HD+intermediate HD cells), 21% vs 12%; Theta-by-HD, 16% vs 26%; place cell, 5% vs 11%; Theta, 45% vs 34%; Unidentified, 12% vs 17%. In the figure, **=0.01 significance, Chi-squared test.

Consistent with the larger concentration of place cells in AVVL, place modulation (locational information content: 0.26 vs 0.37 bits/spike, z=-3.32, p<0.001) and spike bursting propensity (burst index: 0.08 vs 0.09; z=-2.874; p=0.0041) were significantly higher in AVVL compared to AVDM. Peak-to-trough waveform width was larger among AVDM neurons compared to AVVL ones (330.24μs vs 284.83μs; z=4.262; p<0.0001), as expected from their respective magnocellular and parvicellular morphology (Shibata and Yoshiko, 2015; Gabriel, 1993). We found no difference in other properties tested, namely HD modulation (directional information content: 0.33 vs 0.32 bits/spike, z=-0.449, p=0.653; Rayleigh vector: 0.25 vs 0.26, z=-1.45, p=0.146), mean firing rate (3.62Hz vs 3.32Hz; z=-2.874, p=0.68) and theta-skipping strength (TS index: -0.004 vs -0.007, z=0.05, p=0.960).

5.5 Discussion

In this Chapter, we have examined the activity of spatial neurons recorded from the AV of freely-moving rats, with the aim to further characterize temporal firing characteristics and relationship to the local LFP theta of this relatively unknown thalamic nucleus. We have reported a number of expected, as well as unexpected findings, which indicate that AV is not only a subcortical relay of theta signals to the hippocampal formation, as commonly thought, but also plays a role in processing elements of space, including heading direction and spatial location. Unexpectedly, apart from directional neurons, we described a small group of spatial neurons (n=61) with strong locational selectivity that had not been reported before under anesthetized or free exploration conditions in AV. These cells were termed here place cells based on their similarities with hippocampal spatial neurons.

We compared temporal firing properties and found that the spatial cell population in AV can be divided into two broad categories based on differences in theta phase-locking (IC) and spike rhythmicity (IR): (1) classic HD and intermediate HD cells (IR<=0.001; low or moderate IC); (2) Theta-by-HD and place cells (IR>0.001; high IC). Average IC and IR was the same for classic and intermediate HD cells, both

being non-rhythmic and mostly non-theta-modulated, and it was the same for Theta-by-HD and place cells, both being theta-modulated in a rhythmic, phase-locked and phase-precessing manner (although precession was stronger for place cells). Theta-by-HD cells were modulated either at theta (6-12Hz) or half the theta frequencies (4-6Hz; 29% were theta-skipping). Theta-modulated cells, namely Theta-by-HD and place cells, could be either theta-bursting or theta-modulated non-bursting, whereas non-theta cells mostly fired single spikes uncoupled form theta. The relationship between these directional and locational correlates and theta is summarized in Figure 5.20. These spatial characteristics are analyzed in the next Chapter. In the last section of the results, we described differences in cell types between the two AV subfields. Against our primary hypothesis, we found no difference in theta-modulation between AVDM and AVVL. Instead, we found a more complex relationship between the spatial phenotype recorded and AV location. Implications of this finding will be discussed in the General Discussion (Section 8.3).

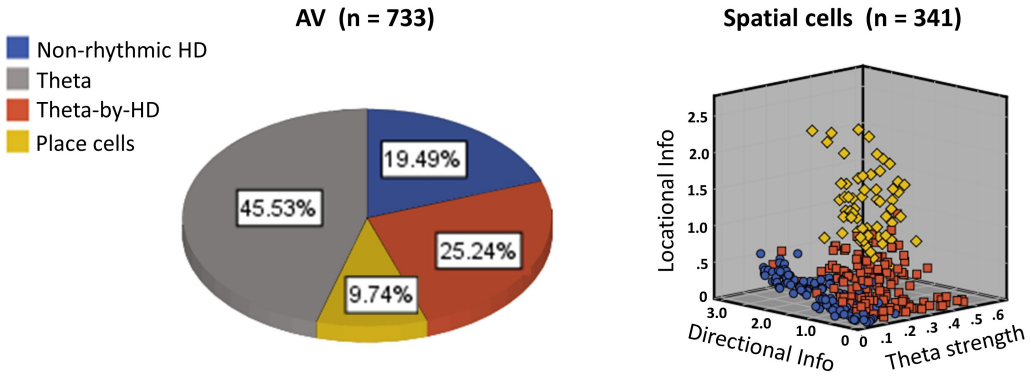


Figure 5.20: **Spatial cells in AV are well segregated in a 3D-scatter plot.** Left, proportions of cell types, excluding unidentified cells. Cell numbers are as follow: non-rhythmic HD (classic HD + intermediate HD), 122 (blue); Theta-by-HD, 138 (red); place cells, 61 (yellow); Theta, 258 (gray); Unidentified, 107 (not shown). Right, the three groups of spatial cells (n=341; shown on the left) were plotted in a scatterplot along three independent parameters. x-axis, directional information (bits/spike); y-axis, locational information (bits/spike); z-axis, theta-strength (IC). Ranges and means for each group: locational information, place cell, 0.61-2.50, mean of 1.51; non-rhythmic HD, 0.01-1.02, mean of 0.29; Theta-by-HD, 0.02-1.30, mean of 0.4; directional information, place cell, 0.11-1.48, mean of 0.58; non-rhythmic HD, 0.05-2.51, mean of 1.12; Theta-by-HD, 0.09-2.46, mean of 0.48; IC, place cell,0.01-0.35, mean of 0.15; non-rhythmic HD, 0.00-0.19, mean of 0.05; Theta-by-HD, 0.01-0.50, mean of 0.17.

5.5.1 Place cells exist in the AV

We provided the first evidence that spike discharge of AV neurons can be highly location-specific, as it is often seen for pyramidal neurons across cortical regions of the hippocampal formation, having critical implications for understanding how the brain encodes spatial signals. The extensive direct (from the Sub) and indirect (via RSC, PoS, MEC) hippocampal-AV interconnections support the notion that place cells could be found in AV. However, since axons of cortical cells may be recorded by AV tetrodes, and since our result was somewhat unexpected, we had to consider questions on whether alternative explanations could account for our place cell recordings. This Section summarizes the measures that were taken during recordings and subsequent analysis to rule out these alternative explanations and confirm the validity of our result. This is followed by considerations on whether place cells recorded from the hippocampal and anterior thalamic region can be differentiated based on any of their electrophysiological properties, to shine light on whether separate spatial codes could exist. Finally, we discuss what the functional relationship between these codes might be and suggest that AV place cells may drive subicular, but not hippocampal, spatial firing.

5.5.1.1 No sign of explanted hippocampal tissue

First, to ensure we recorded the place cells from the AV, we conducted a careful inspection of histological sections to make sure that explanted hippocampal tissue (especially from dorsal CA3 area, given the electrode tract trajectory) did not explain the observed spatial phenotypes. In all six animals, we used thin electrode wires (25μm) and the electrode tract visibly penetrated the AV, with the final tip positioned well within this region (Figure 5.2). In all cases, the inferior part of hippocampal/parahippocampal tissue remained intact, and was not dragged down by the electrodes. In two animals (R448; R449) we made an electrolytic microlesion prior to perfusion, and in R449 the lesion was induced on the same electrode that was recording a place cell on that day, allowing to verify the exact location of the cell on that day. In both rat, we saw a clear lesion in the ventral AV area, with undamaged tissue all around. Even after excluding dragged tissue with proper histology, we acknowledge that our setup was not designed to solve all possible histological issues. Arguably, it would still be possible for individual place cells to get stuck to the electrodes as they passed through hippocampus, as this may not necessarily result in tissue damage visible in the final histological slides (see next).

5.5.1.2 Place cells were co-recorded with AV cells and were stable across trials

To address this possibility, we made the following observations. Large numbers of theta-modulated cells, both directional and not, were typically recorded from the very first day of recordings and provided a reference during recordings for correct electrode placement within AV, given that theta cells are seen is only very small proportions in AD (12%) and AM (6%) (Vertes et al., 2001; Albo et al., 2003). It was possible for the same tetrode to simultaneously record a place cell and a Theta-by-HD cell (see examples in Figure 5.9). This observation constitutes a strong indication that place cells were part of the local AV circuit rather than being cells dragged from hippocampus, since only a very limited number of directionally-selective neurons was reported in CA1 (n=6), and these units were not also theta-modulated (Leutgeb et al., 2000), and were seemingly absent from CA3 (Royer et al., 2010).

The firing of a single place cell was highly stable across consecutive trials and days if electrodes were not lowered (Chapter 7). It is most likely that this stability would not be present in neurons dragged from their original neural circuits because it would be unlikely that they could still express their proper physiology — although this remains an open question. Similarly, stable locational representations would not be observed if cells resulted from axonal recordings of projections from surrounding brain regions that express place coding (Sharp, 1999; Sharp and Green, 1994; Cacucci et al., 2004). Moreover, a pure place code has not been observed in these regions, given that PoS place cells display conjunctive directional properties (Cacucci et al., 2004) and Sub place cells form broader place fields than the kind seen in hippocampus (Sharp, 1999; Quirk et al., 1992). Moreover, evidence suggests that ATN projections are required to establish this broad spatial selectivity, and not the other way around (Frost et al., 2022). Fully addressing the issue of axonal recordings requires analysis of spike waveforms, as well as muscimol inactivation of hippocampal/parahippocampal regions coupled with AV recordings, to determine whether it is possible for place cells to be independently recorded at the thalamic level.

5.5.1.3 Changes in cluster space

During recordings, electrodes were lowered into the brain in small, slow steps, which meant that the same place cell could sometimes be reliably recorded across consecutive days if electrodes were not lowered or if the screw turn was small. In this case, despite cell stability, we observed changes in the amplitude and polarity of the

cell waveform, which were accompanied by cluster-space changes (change in the relative position of the place cell cluster; Figure 5.21 A). Such changes arguably reflect electrodes moving first toward and then away from the cell that was being steadily recorded. In other instances, following a single screw turn, we noticed a change in cluster space that coincided with the appearance of a new place cell, as the place cell that was being recorded before advancing the electrodes disappeared (Figure 5.21 B).

In no instance was a place cell recorded during the very first day of recordings and the place cell number did not decrease with the progression of recordings, sugesting that repeated sampling of the same tissue rarely occurred and cells could not have been stuck to the electrodes across multiple days. Overall then, we could rule out the possibility that single cells were dragged down from hippocampus into the AV regions.

Ultimately, evidence of synchronous firing in the spike cross-correlation between co-recorded place cell and Theta-by-HD cells would provide final indication that cells are monosynatically connected. Although we did not find any evidence of such correlated activity, it is noteworthy that, even if place cells were part of the AV neuronal circuit rather than outsiders, chances of finding a place cell-non place cell pair that were co-recorded and also shared one synapse would be considerably low.

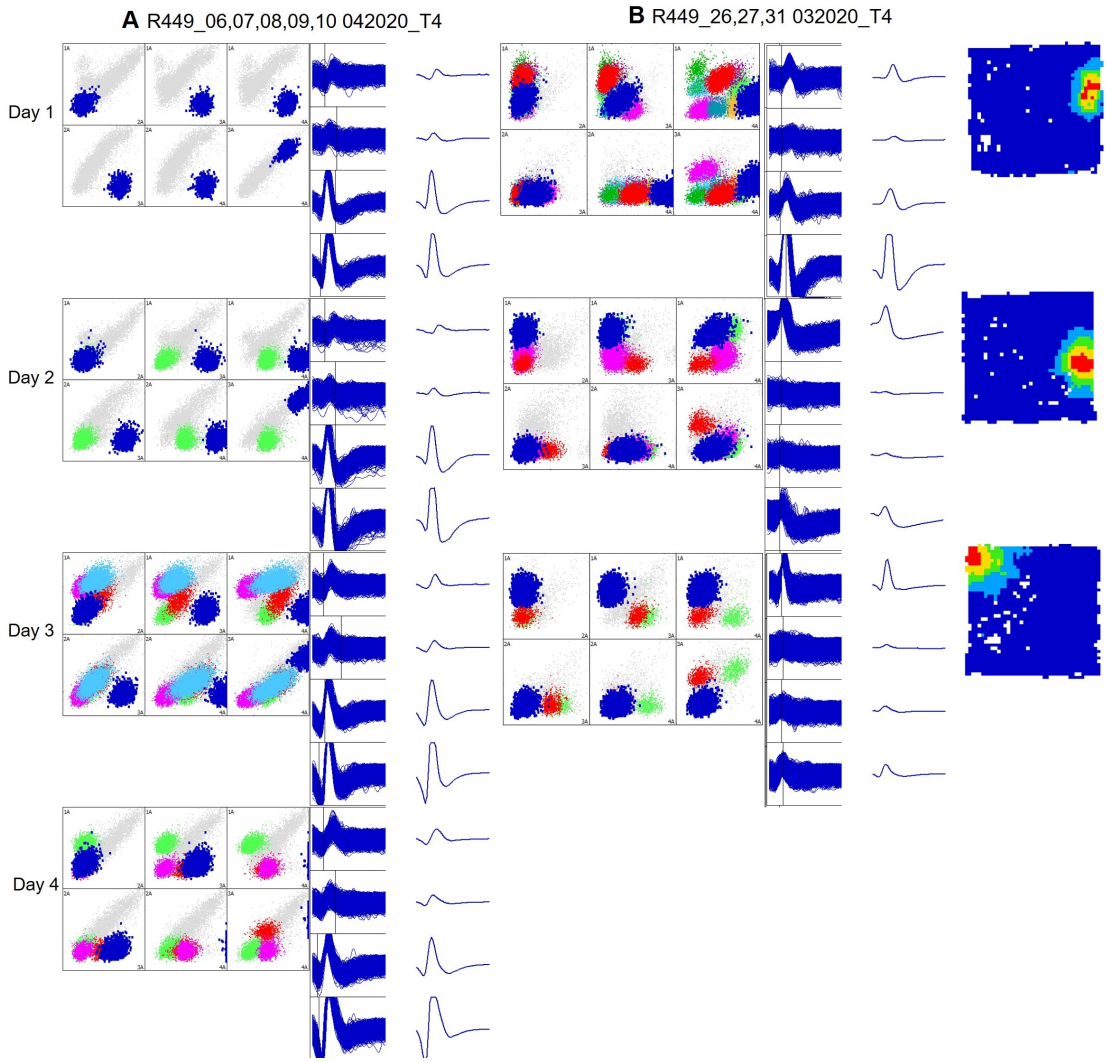


Figure 5.21: **Changes in cluster space and spike waveform of place cells over consecutive days recording.** Electrodes were lowered by 25-50 μm each day. For each day, six panels on the left show scatterplots of spike amplitudes on six pairs of tetrode channels (top left is electrode one vs two; bottom right: three vs four). Spikes from each place cell are highlighted in blue. For each day, panels on the right show all spikes recorded during the trial, while panels on the far-right show the average waveform on each electrode. **(A)** One place cell recorded by the same tetrode across four consecutive days. As electrodes moved past the cell, waveform amplitude changes and polarity reversed on Day 4. Cluster position also shifted (see electrode three vs four at the far bottom right, blue cluster). **(B)** Three different place cells recorded by the same tetrode across three consecutive days. At each screw turn, a new cluster appeared in the scatter plots, corresponding to a new place cell. The ratemap for each cell (blue cluster) is in the rightmost column. This rules out electrode-dragging issues.

5.5.1.4 Evidence of place cells in other non-hippocampal related structures

Then, if place cells existed in AV, why have they not been found before? Prior to this thesis, there has been only limited electrophysiological exploration of AV spatial correlates in behaving rats (Tsanov et al., 2011). This signal may not have been detected either because of a restricted scope of the analysis or due to a bias in sampling only the most medial part of AV (AVDM). Furthermore, rats may not have explored sufficiently all of the recorded surface arena for proper coverage necessary for place field data analysis.

Despite the new discovery of AV place cells, previous electrophysiological work has demonstrated that it is indeed possible for place cells to be recorded outside the hippocampal formation (O'Keefe and Dostrovsky, 1971), and in particular in other thalamic nuclei — thus strengthening the prior of finding these cells also in AV. These include the AM, parataenial nucleus and NRe (Jankowski et al., 2015). Another subcortical region that contains place cells in rats is the anterior claustrum (Jankowski and O'Mara, 2015). This finding is especially significant as electrodes would not have passed through the hippocampus and can therefore serve as a control measure for the existence of subcortical neurons with location-specific firing in structures away from hippocampus. More controversial evidence relates to place cells in dLGN (Hok et al., 2018) and somatosensory cortex (Long and Zhang, 2021). Further histology and control experiments to rule out the possibly of a sensory input causing the place response is needed.

Extra-hippocampal/parahippocampal place cells are similar in many ways to their hippocampal counterpart, being stable across trials and in darkness, present from the first exposure to the recording environment, and controlled by visual landmarks. Nevertheless, claustral and dLGN place cells can be distinguishable from hippocampal place cells by weaker spike-theta phase relationships (Jankowski and O'Mara, 2015; Hok et al., 2018), and absence of remapping in the presence of proximal objects (Jankowski and O'Mara, 2015). Another difference from hippocampal place cells pertains to spike waveform shape. In the hippocampal formation, spike width is typically used to delineate pyramidal and GABAergic interneurons. Place cells are pyramidal neurons with spike width>500, while inhibitory interneurons have shorter waveforms and do not display high locational specificity (Wilent and Nitz, 2007; Grieves et al., 2020; Mizuseki et al., 2012; Mizuseki and Buzsáki, 2013). On average, thalamic and claustral place cells have a waveform duration<250μs (Hok et al., 2018; Jankowski and O'Mara, 2015; Jankowski et al., 2015), despite having

highly spatially-selective firing fields. Waveform differences likely result from a combination of cellular sources, namely shorter axons, smaller cell bodies, a more irregular architecture, as well as a different distribution on ion channels and neurotransmitter content. Together, evidence points to the existence of two distinct neuronal networks specialized in the processing of information related to spatial location, one intrinsic to the hippocampal formation (CA1, CA3, Sub) and a more widespread extra-hippocampal/parahippocampal one, that includes thalamic areas. In our study, we may have uncovered an additional sub-component of such system.

5.5.2 Functional properties of hippocampal and AV place cells

A useful approach to demonstrate that place cells can be recorded from AV consists in looking for unique electrophysiological signatures that would not also be expected from hippocampal recordings — and particularly from dorsal CA3, given the electrode tract trajectory. Place cells identified here are similar to those reported in hippocampus with respect to many of their temporal and spatial firing characteristics, reviewed here.

5.5.2.1 Place cells show similar, but different, firing characteristics

Hippocampal place cells fire complex spikes when the rat enters a certain location within the environment, with peak firing rates between 1-40Hz and mean rates between 0.1-10Hz (Grieves et al., 2020; Royer et al., 2010). They form a single place field in small environments like the present one, but can develop multiple irregularly-spaced fields in larger environments (Fenton et al., 2008; Harland et al., 2021). In agreement, our place cells formed single or multiple fields, both spatially compact and highly stable, and exhibited complex spike bursting (seen in the autocorrelogram and spike raster plots). Peak ISI (5.75±0.22ms) and mean firing rate (1.1±0.1Hz) matched values reported for dorsal CA3 pyramidal neurons (peak ISI, 4.29±1.12ms; mean rate, 0.50±0.78Hz; Mizuseki et al., 2012). Previous recordings of hippocampal complex spiking neurons reported opposite theta phase preferences between areas CA3/CA4 (locked to descending phases after theta peaks) and area CA1 (locked to ascending phases before theta peaks) (O'Keefe and Recce, 1993; Dragoi and Buzsáki, 2006; Csicsvari et al., 1999; Cacucci et al., 2004; Fox et al., 1986). Place cells here discharged rhythmic spike trains at theta frequencies locked to descending phases of the local cycle. Despite a consistent phase preference across cells, firing phases

of each cell were not fixed but slightly precessed in time relative to theta. Phase precession is a key feature of the rodent hippocampal pyramidal neurons, being faster in dorsal compared to ventral CA3 (Royer et al., 2010). However, it is not a purely hippocampal phenomenon, as non-spatial neurons in MEC (Jones and Wilson, 2005) and ventral striatum (Meer and Redish, 2011), as well as MEC grid cells (Hafting et al., 2008), also phase precess. Entorhinal phase precession is not passively inherited from hippocampus given that it was not impaired by hippocampal inactivation (Hafting et al., 2008).

We have described very similar temporal and spatial phenotypes for hippocampal and AV place cells, and yet their architecture and cell types are very different. In cortical regions of the hippocampal formation, principal cells (pyramidal) have large and neatly organized cell bodies within a single cell layer. Their firing is highly location-specific and thus are considered as place cells, while interneurons are not signal spatial location, and thus they are not considered as place cells, being more correlated with running speed instead (Csicsvari et al., 1999; O'Keefe, 1976; Wilent and Nitz, 2007; Grieves et al., 2020; Mizuseki et al., 2012; Mizuseki and Buzsáki, 2013; McNaughton et al., 1983). Within the AV, cells are smaller and more irregularly arranged, especially in the parvicellular subfield. In agreement, a key feature of hippocampal place cells, namely their broad pyramidal-like spike waveform (>500μs in duration), was not consistently observed in our dataset. Instead, AV cells, including place cells, seemed to come in two flavours, broad vs narrow spiking. The fact that place cells could have both broad or narrow waveforms (average waveform width: 284.26μs), and this was not correlated with their spatial information, strongly argues against the possibility of hippocampal recordings as well as axonal recordings from the Sub. A similar spatial profile in spite of highly contradistinctive thalamic and hippocampal cell typology could be achieved by having strong cell-to-cell hippocampal inputs to AV, via the Sub, which would enable cells in this nucleus to inherit hippocampal spatial selectivity.

A particularly curious pattern emerged, whereby the two kinds of place cells (broad vs narrow spiking) differentially expressed theta in their firing, but did not differ in terms of locational and directional information, velocity modulation, bursting mode and frequency. The same firing rate and bursting propensity for narrow and broad spiking cells indicates that they are unlikely to be interneurons dragged from hippocampus, given that hippocampal interneurons are known to have higher mean firing rate (usually>15Hz) and considerably lower locational specificity, and lack complex spiking (Wilent and Nitz, 2007). Furthermore, a narrow waveform

is consistent with previous place cells recordings from subcortical structures outside of hippocampus, namely dLGN (≈150μs), AM (≈133μs), NRe (≈109μs) and anterior claustrum (≈161μs) (Hok et al., 2018; Jankowski and O'Mara, 2015; Jankowski et al., 2015).

Note that we cannot use width of spike to delineate interneurons and pyramidal neurons, given that imunohistochemistry studies have demonstrated a lack of putative interneurons in the rodent ATN, where all neurons are projecting thalamocortical neurons (Paré et al., 1991; Steriade, 1997; Arcelli et al., 1997; Jones, 1985; Henze et al., 2000). Although a very small number of GABAergic neurons have been described in the ATN of rats (Gonzalo-Ruiz et al., 1996) and guinea pigs (De Biasi et al., 1994), these studies have not differentiated interneurons from relay neurons.

5.5.2.2 Origin of the AV place signal

The notion that AV contains place cell should not be completely inconceivable, given its strong connections with limbic regions that signal spatial location. In this respect, there are dense reciprocal connections between AV and AM, both containing place cells (Jankowski et al., 2013), and the Sub (van Strien et al., 2009; Jankowski et al., 2013; Shibata, 1993a; Christiansen et al., 2016), where place cells exhibit broad firing fields (Sharp, 1999; Sharp and Green, 1994; Lever et al., 2009; Frost et al., 2021; Poulter et al., 2021). Projections from the Sub to ATN are bilateral to AVVL and AM, while AVDM receives only ipsilateral projections (Seki and Zyo, 1984). This is consistent with our result of weaker locational specificity in AVDM compared to AVVL. Back projections from AM target the ventral Sub, while AV projections target the dorsal Sub (Christiansen et al., 2016). There are no direct AD-Sub connections, consistent with a lack of AD place cells (Shibata, 1993a).

All three ATN nuclei also have reciprocal connections with parahippocampal areas, including MEC, PoS and RSC, where place cells tend to express more complex firing profiles i.e., PoS theta-by-place-by-direction cells (Cacucci et al., 2004); RSC place-by-direction (Cho and Sharp, 2001); MEC theta-by-grid-by-direction (Boccara et al., 2010). An exception is represented by the discovery of place cells recorded from superficial dRSC layers of head fixed mice running on a treadmill (Mao et al., 2017, 2018). It is possible that head fixation or the linear structure of the environment could have masked the more complex spatial properties typically seen during unrestrained navigation in rats. A location-specific component, if directly received by AV from

parahippocampal pathways, may already be integrated with other sources of spatial input before reaching the AV. Alternatively, parahippocampal place cells may arise from the conjunction of more elemental theta-modulated location and direction elements from AV. In support of this notion, dRSC place cells were only partially impaired by bilateral, but not unilateral, dorsal CA1 lesions (Mao et al., 2018). Residual place activity in bilaterally-lesioned animals indicates that RSC place fields could in part be generated by mechanisms independent of hippocampus, possibly via the AV (AVVL-dRSC pathway).

Clearly, further causal experiments are required to test the source of AV locational firing. When addressing this question, it is important to consider recent experimental data in rats indicating that Sub place cells are not principally driven by their CA1 inputs, but depend on the ATN. Specifically, ATN lesions, both permanent and temporary, were found to impair spatial alternation performance in rats (Frost et al., 2021) and led to a loss of spatial activities in Sub, including place, HD and grid cells, while sparing CA1 place cells (Frost et al., 2021). Likewise, place cells could still be recorded in CA1 after excitotoxic lesions confined to AD and/or PoS, despite a decrease in locational information and increase in directionality (Calton et al., 2003). This driving ATN action could be mediated by direct place cell discharge from AV and AM to Sub (Jankowski et al., 2013), in addition to a more indirect HD influence from AD. The present discussion opens questions on the relationship between anterior thalamic and hippocampal place cells, and whether they are part of interdependent or subordinate systems.

5.5.3 Significance and mechanisms of theta-modulation of AV spatial signals

The presence of theta in AV is important because entorhinal-hippocampal networks involved in spatial learning and containing place cells in rats are strongly entrained by theta oscillations. Theta can integrate functionally the AV into this system, and coordinate the processing and transfer of spatial information, namely representations of perceived head position and orientation, both being already represented upstream of hippocampus.

Theta-modulation was analyzed in relation to two temporal aspects: (1) intrinsic spike rhythmicity, measured by the IR and (2) phase-locking to the local LFP theta, measured by the IC. These two aspects were tightly coupled. Cells that

fired rhythmically also maintained a consistent relationship to theta (Theta-by-HD and place cells), whereas cells that fired non-rhythmically had no relationship to theta (classic HD), or only a weak/partial relationship such that it was not always seen during the trial (intermediate HD; firing only occasionally locked to theta). Phase relationships differed between all cells: Theta-by-HD and place cell spikes were strongly coupled to descending theta phases, with a small, yet significant, offset between the two groups, which could be attributed to the steeper place cell phase precession. In contrast, intermediate HD cell showed only weak coupling to, or just before, theta peaks, although most of the spikes were not emitted at theta frequencies, reflected in an overall non-rhythmic spike discharge for the trial. It should be noted that intermediate HD cells were recorded only in trials of high average theta power (qualitative observation), which excludes the possibility of an artefactual phase-locking resulting from a low power theta signal recorded by the LFP electrode due to ground wire problems.

Two additional relationships between spike discharge and theta became evident by looking at the frequency of the temporal modulation of autocorrelograms. First, comparing average theta frequency in the autocorrelogram with average LFP theta frequency revealed a phase precession phenomenon, whereby Theta-by-HD and place cell spikes occurred progressively earlier during the trial. This caused average intrinsic theta frequency to be slightly faster than global theta, despite a fixed average firing phase relative to theta at the population level. Phase precession was much weaker for Theta-by-HD compared to place cells, while non-rhythmic HD cells did not fire at a rate faster than theta. Since Theta-by-HD cells phase precessed in time but not relative to HD (see Appendices, Section A.4.1), phase coding of a different spatial dimension might occur. For example, spatial location for Theta-by-HD cells with broad firing fields. In the future, exploring whether cells might use phase coding of location will require recordings from AV in a linear track, to quantify the relationship between firing phases and the animal's location as it traverses the place field.

Second, not all Theta-by-HD cells exhibited the same frequency of the temporal modulation of their spike rhythmicity. While the majority fired at theta frequencies (6-12Hz), 29% fired at approximately half the theta frequencies (4-6Hz), termed theta-skipping HD cells. We did not observe theta-skipping among place cells. Co-recorded theta-skipping HD cells often displayed coordinated activity and were divided into two groups: anti-synchronous cells that fired in alternation on opposite cycles, and synchronous cells that fired on the same alternating cycles. Preliminary observations from a small number of cells revealed functional differences between

these two groups, in that synchronous cells shared more similar PFDs compared to anti-synchronous cells, whose PFDs were separated by a minimum of 79.37°. Similar results have been reported among parahippocampal Theta-by-HD cells (Brandon et al., 2013). Given that Theta-by-HD cells do not show phase coding of direction (Appendices Section A.4.1), theta-skipping rather than precession may provide the mechanism for temporal coordination of functionally-related HD cells, in line with previous evidence (Kay et al., 2020; Brandon et al., 2013). Theta-by-HD cells that fire together at a longer timescale (at the same PFD) are also co-active at a shorter timescale (on the same theta cycle and phase), allowing these cells to simultaneously reach their common RSC targets and, as a result, coordinate the formation of thalamocortical cell assemblies.

Prior to this thesis, Theta-by-HD cells (both theta-skipping and non) have been reported before in MEC/PaS (Brandon et al., 2013), both being interconnected with AV (van Groen and Wyss, 1990b; Van Groen and Wyss, 1995, 2003; Wright et al., 2010; Shibata, 1993a). In these regions, inactivation of the medial septum using muscimol disrupted grid cells and theta-skipping of directional units without affecting their directionality and theta rhythmicity (Brandon et al., 2013). The interpretation is that GABAergic septal inputs may drive theta-skipping, but not rhythmicity, of MEC/PaS cells, which instead is inherited from other subcortical pathways. In turn, MEC/PaS could provide a source of theta-skipping inputs to AV, accounting for our recordings. Alternatively, theta-skipping may be explained by the interference of theta and slower delta oscillations. AV cell firing threshold would be surpassed at the peaks of the resulting interference pattern, causing the membrane potential oscillation to be slower than the theta frequency.

The theta-skipping phenomenon has been most commonly observed among grid cells in MEC, more common in ventral than dorsal, and CA3 place cells, again, more common in ventral than dorsal (Deshmukh et al., 2010; Royer et al., 2010). Theta-skipping neurons with no spatial properties also exist at the subcortical level, in the NRe of the thalamus (Jankowski et al., 2014). Here, we provide the first demonstration that theta coordinates the timing of directional processing also upstream of cortex, which may influence spatial computations in connected cortical regions, like grid cell formation (Brandon et al., 2013).

5.5.4 Summary

The main finding of this Chapter is the observation that AV contains theta and HD signals, which are mostly kept more separate in AVDM but get combined to a higher extent (Theta-by-HD cells) in AVVL. Unexpectedly, there are place cells in AV, predominantly found in AVVL, adding to the evidence that a pure place code exists in subcortical regions outside of hippocampal formation. However, only in AV, but not in these other regions, we find an intermingled localization of place and HD cells, both operating at theta frequencies and converging on the same descending phase of the local and hippocampal theta cycle (based on Tsanov et al., 2011). This suggests a unique relevance of AV in coordinating cortical and subcortical networks.

In regards to the temporal characteristics analyzed here, only Theta-by-HD and place cells were deeply theta-modulated, and displayed stronger phase locking (IC) and theta rhythmicity (IR) compared to classic HD and intermediate HD cells, which displayed the same average IC and IR. Place cells showed the highest spike bursting propensity, followed by Theta-by-HD cells and then classic HD and intermediate HD cells, both being non-bursting. Average peak-to-trough spike width was the same for place cells, classic HD and Theta-by-HD cells, while intermediate HD cells on average fired spikes of shorter duration. Intermediate HD cells also fired at the highest mean rate, while place cells fired at the lowest rate. The next Chapter will focus on the analysis of the spatial and motor correlates of these cells.

5.5.5 Limitations

Locational information threshold was set relatively high for place cell inclusion (>0.8). In previous studies of hippocampal and subcortical place cells the threshold was generally set to lower values (i.e,>0.5 Jankowski et al., 2015; Hok et al., 2018; Jankowski and O'Mara, 2015; Grieves et al., 2020; Duvelle et al., 2019). Setting the threshold high, and also considering a sparsity threshold of 0.2 for the place cell sample, did mean that some cells which showed some spatial selectivity in their firing did not make it into the sample.

Although our place cell criterion is more conservative than what is typical of analogous studies in other brain regions, it seems to fit the data well: it excluded cells which certainly were not place cells, while the majority of cells exhibiting clear place fields were included in the sample. Notably, among all AV neurons with a sparsity

score<0.2, the minimum locational information recorded was 0.842 bits/spike, which is above our pre-defined place cell threshold. While it may have been useful to use a shuffle-based criterion for information content, it should be noted that this would most likely have increased the place cell count since thresholds are tailored for each individual neuron. Hence, our criterion was chosen intentionally to set a lower bound for the proportions of place cells in the AV, and ensure that only units with high spatial selectivity were included in the sample.

It can still be argued that, by categorizing data according to a set of pre-defined criteria, it is possible that at least some units fit into any one category by chance alone. While this is theoretically possible, it contradicts empirical evidence, in that a percentage of cells in the AD would also have been classified as place cells by previous studies. Having said this, while the percentage of recorded place cells is relatively small (61/733, 8%) compared to CA1 (about 80%; Grieves et al., 2020), this value is actually larger than previous published evidence of subcortical place cells in AM (6.2%), NRe (2%; Jankowski et al., 2015), and anterior claustrum (4.3%; Jankowski and O'Mara, 2015). This may be due to a more prominent role of these regions in coordinating cortical and subcortical spatial systems, rather than being mostly involved in place coding alone. Crucially, our criterion allowed to obtain a solid set of results, as indicated by the fact that place correlates were maintained across trials in the light and in darkness across all animals, suggesting that the phenomenon is unlikely to be an artifact resulting from classifying cells by chance (see Chapters 6 - 7).

Finally, we noted that AV cells with locational selectivity displayed place fields that were highly spatially localized and round. In cases of multiple place fields, firing peaks seemed regularly arranged. A limitation of the task design is the small size of our testing box (90x90cm), which makes it possible to miss-classify grid cells as place cells, as we would only be able to detect small grid scales. To illustrate this issue, Savelli et al. (2008) demonstrated that MEC cells that resembled classic hippocampal place cells in a 59x59cm box were grid cells in a larger box. However, issues linked to using a larger arena are the longer trial time necessary to ensure adequate sampling and the need for a larger room. It should be noted that grid cells have not been reported at the subcortical level before, although few (if any) studies have also recorded from these structures in awake animals in larger arenas.

6

Spatial firing properties of anteroventral thalamic neurons

6.1 Background and Rationale

We have identified a variety of functionally- and anatomically-distinct spatial cells in AV of rats. We recorded non-rhythmic HD, Theta-by-HD and place cells. In the previous Chapter, we showed that these neurons have clearly distinct temporal firing properties. The present Chapter focuses on the analysis of the spatial and movement correlates of these cells, namely (1) directional heading, (2) spatial location, (3) linear and angular head motion.

6.2 Data Analysis

Data were analyzed using TINT (Axona, UK) and MATLAB R2018a (MathWorks, USA) with custom-made programs and functions. CircStat toolbox was used for analysis using circular statistics (Berens, 2009).

6.2.1 Maximum-likelihood method to examine multiple independent spatial influences

Directional and locational firing rate maps were constructed and analyzed in the same way as is usually done for HD and place cells (see General Methods). When building these plots however, we did not take into account the sampling bias of the animal as he moves inside the arena and that can generate dependencies between spatial correlates (Burgess et al., 2005). If a cell is locational, its firing will be spatially inhomogeneous because not all orientations can be equally sampled by the animal at every spatial location. Spikes will tend to accumulate at the direction more often faced by the animal while approaching the place field, and so uncorrected calculations of tuning curve will result in an apparent directional preference toward that direction, despite the cell not having any true directionality. Hence, if we recorded cells with conjunctive directional and locational correlates, it was necessary to determine whether this effect was true or due to spurious behavioural couplings between spatial correlates.

6.2.1.1 Position times direction correction

Among the analytical solutions available to correct for sampling artifacts (Muller et al., 1994; Peyrache et al., 2017; Burgess et al., 2005; Lever et al., 2009; Rubin et al., 2014; Cacucci et al., 2004), we chose to rely on the *position times direction* (*pxd*) correction method, proposed by Burgess et al. (2005) , and first utilized by Cacucci et al. (2004). We used the original code, published online by these authors. Using a maximum-likelihood method (MLM), the *pxd* method allows to estimate the independent contribution of position (p) and direction (d) to the firing rates of a cell. Briefly, for each cell, the expected number of spikes n_{ij} in every locational (i) and directional (j) bin at time t can be modeled as the product of the two independent functions of time, p_i and d_j:

$$E(n_{ij}) = p_i d_j t_{ij}$$

Under the assumption of Poisson firing, the likelihood $p(n_{ij})$ of observing n spikes in every locational and directional bin at time t is:

$$p(n_{ij} \,|\, p_i, d_j, t_{ij}) = (\lambda_{ij})^{n_{ij}} \, exp(-\lambda_{ij}/n_{ij})$$

where $\lambda_{ij} = p_i d_j t_{ij}$. From this equation, it is possible to derive the overall likelihood of the observed data (L). p_i and d_j are the parameters that maximize L:

$$p_i = \frac{(\sum_{j=1}^{n} n_{ij})}{(\sum_{j=1}^{n} d_j t_{ij})}; d_j = \frac{(\sum_{i=1}^{n} n_{ij})}{(\sum_{i=1}^{n} p_i t_{ij})}$$

In other words, p and d are the multiplicative factors for which the observed number of spikes in each locational or directional bin differs significantly from the expected number of spikes in that bin, predicted based on directional or locational firing alone, respectively. p and d were converted to firing rate and displayed independently as corrected firing rate plots, showing the uncoupled effect of direction and location on a cell's firing rates. Firing rates were normalized to match the total number of spikes of the original trial. Similar number of bins were applied to locations and directions, unlike in other analyses of this thesis. There were 60 6° directional bins and 64 locational bins. No smoothing was applied. This provides better convergence of the *pxd* algorithm, and ensures that direction and location were given equal weight in finding the solution. This method was applied to all cells (1 HD cell for which the *pxd* correction algorithm did not converge upon a solution was discarded). Corrected firing rate plots were compared to uncorrected ones using cross-correlation procedures. Corrected and uncorrected measures of locational and directional information in bits/spike were calculated according to the formula in Skaggs et al. (1992).

6.2.2 Analysis of anticipatory firing

Anticipatory firing analysis was conducted to determine the temporal relationship between HD and Theta-by-HD cells within the AV, as well as infer the positioning of the AV within the broader HD pathway. This is because, in each region along this circuitry, anticipatory firing is thought to vary according to the direction in which vestibular information is propagated and becomes progressively integrated with visual inputs. Specifically, HD cells in cortical regions tend to display a less anticipatory firing compared to cells located at lower levels of the circuitry that are more dependent on vestibular, rather than visual, information (Stackman and Taube, 1998; Sharp et al., 2001). Hence, comparing anticipatory time intervals (ATI; Blair and Sharp, 1995; Blair et al., 1997; Taube and Muller, 1998) between cell types and brain regions can be informative of the direction of the flow of HD information.

For instance, whether the signal follows a descending projection from RSC to AV, or whether AV leads RSC HD signaling instead (like the AD).

Using the same analytical approach as in the present thesis (see below), Lozano et al. (2017) showed that HD cells in RSC anticipate the animal's future head direction by an average of approximately 48ms. If the AV HD signal is inherited from RSC via descending corticothalamic pathways, then AV HD cells should anticipate the future direction by a smaller interval than RSC ones. If, on the other hand, subcortical pathways transmit HD signals to AV, then AV HD cells should have a larger and more positive average ATI than RSC.

Here, the ATI of a cell was quantified using two different methods, described below. Before explaining each of these methods, it is important to understand the basic principles that allow a HD cell to anticipate the future heading direction. For HD cells with a positive ATI, for example of 48ms as for RSC neurons, firing rates correlate best with the animal's heading direction some time (48ms) into the future, rather than with the current direction (Blair and Sharp, 1995). As the animal approaches the cell's PFD from the left with positive AHV (clockwise turn; CW), firing is maximal 48ms before the rat reaches the PFD. At this time, the head is still to the left of the PFD, resulting in a CW directional tuning function shifted leftward. In contrast, as the animal approaches the PFD from the right (counterclockwise turn; CCW), firing is maximal when the head is still to the right of the PFD, causing the CCW tuning function to be shifted rightward. This introduces an angular separation between CW and CCW tuning curves, and this offset is what allows HD cells to anticipate the heading direction i.e., the more a cell is anticipatory, the larger its angular separation.

6.2.2.1 Decomposition of standard tuning function into CW and CCW

In the first method used here, the ATI of a cell was estimated based on cross-correlating decomposed CCW-CW tuning functions, as in Blair and Sharp (1995). Briefly, for each cell, CW and CCW spikes were identified according to the AHV at which the head was turning when a spike occurred. CW spikes occurred at AHV>60°/s, CCW spikes occurred at AHV<-60°/s. Spikes emitted at times in which the head was not turning (absolute AHV value<60°/s) were removed. CW and CCW spikes were time-shifted in steps of 20ms, from 20 to 160ms. 20ms steps coincide with the frames of the camera (50Hz sampling frequency). At each step, CW and CCW tuning curves were plotted, normalized to 1Hz and circularly cross-correlated by rotating

one relative to the other in steps of 6°. The rotation angle that produced the maximal cross-correlation (Pearson's r) between the two curves was derived. Angles were plotted as a function of the corresponding time shift, and a linear regression model was fitted to this plot using the least squares fitting method.

The ATI is the x-intercept of the line, corresponding to the amount of time shift required to align CW and CCW tuning functions (maximal cross-correlation should occur at 0° for nonanticipatory firing). The difference angle in degrees was defined as the rotation angle that yields the maximal cross-correlation between CCW and CW tuning functions for a time shift of 0ms. Cells for which this cross-correlation was less than 0.7 were not included in the analysis. Using this criterion, 10 cells were removed from the HD group, and 30 from the Theta-by-HD group.

6.2.2.2 Optimal-time shift analysis

According to the second method, the cell's ATI was derived based on optimal time-shift calculations for the standard tuning function, as in Blair and Sharp (1995). A cell's optimal shift corresponds to the amount of time shifts required to optimize its tuning curve parameters. By the above definition, the ATI of a cell corresponds to the amount of time shift required to align CW and CCW tuning functions. Then, if the standard tuning function is time-shifted by an amount equivalent to the ATI, the tuning width should be narrower than the un-shifted one.

Based on this prediction, optimal shifts were computed by shifting the entire spikes-time series (CW and CCW spikes combined) forward and backward in time in steps of 20ms, between 20 and 160ms, and between -20 and -160ms, and plotting the tuning curve at each step. The ATI is the amount of time shift that minimizes the width and maximizes the peak firing rate in the tuning curve.

6.2.3 Analysis of directional signal instability

Here, we describe the analysis performed to investigate changes in PFD over time. We begin with a description of the circular-linear regression approach used to quantify this drift (linear drift analysis). This is followed by a reflection on the statistical considerations that need to be kept in mind when comparing between the two cell groups, non-rhythmic HD and Theta-by-HD cells. From a statistical standpoint, we explain why we chose particular statistical tests and how we tested their distributional

assumptions prior to conducting them. Finally, we introduce a new method used here to determine whether PFD shifts were bidirectional rather than due to a gradual drift in one direction (non-linear drift analysis) and provide a justification of the choice of this method.

6.2.3.1 Linear drift analysis

We used the circular-linear regression method from Kempter et al. (2012) to quantify the average intra-trial drift rate of a cell's PFD in °/min. This method was originally designed to investigate hippocampal phase precession: applying a circular-linear regression model to the firing phase vs time relationship revealed a negative slope of the regression line, suggesting theta phase precession across time. Here, it was chosen because it does not presuppose a linear relationship between the HD and the time of spikes, representing a case of circular-linear associations instead.

For each cell in a trial, a scattergram of HD ϕ vs time x for each spike i was constructed and fitted by the following linear model:

$$\phi_i = 2\pi a * x_i + \phi_0;$$

The slope of the drift rate, bound between -180 and 180°/min, was found as the slope a that minimizes the angular distance (d) between observed HD (ϕ_i) and predicted HD ($\widetilde{\phi_i}$):

$$d(\phi_i, \widetilde{\phi_i}) = 2[1 - cos(\phi_i - \widetilde{\Phi}_i)];$$

This method is equivalent to finding the slope value that maximizes the mean vector length (R-vector) of the distribution of mean resultant vectors of these angles (d):

$$R = \sqrt{[\frac{1}{n}\sum_{i=1}^{n} cos(\phi_i - 2\pi a x_i)]^2 + [\frac{1}{n}\sum_{i=1}^{n} sin(\phi_i - 2\pi a x_i)]^2}$$

Only cells for which this mean vector length was greater than 0.2, suggesting a good fit of the regression model, were analyzed. The slope of the circular-linear

regression line a provides a measure of drift rate magnitude and direction. The circular-linear correlation coefficient (rho) and the statistical significance of this correlation (p-value) were also computed and compared between cell groups. A cell was considered as drifting if the significance level of the correlation was below 0.01.

6.2.3.2 Statistical considerations

After quantifying the slope and the direction of the drift rate, we wanted to determine if changes in direction over time were concentrated at a specific direction or they were random, and compare between cell groups. Directional drift data represents circular data and so it needs to be analyzed with circular statistics. For each cell group, to determine the probability of drift rates being uniformly distributed against the alternative hypothesis of unimodality, we used separate Rayleigh tests with an unspecified mean direction, or V-tests for an expected mean direction of 0°/min (Fischer et al., 2020). To derive a valid p-value, we verified that the assumption of unimodality was met before conducting these tests by displaying circular data along with descriptive statistics, including the mean vector length (R) and mean direction of the drift rate distribution.

However, when comparing two or more groups whose values are unimodally distributed around the same mean direction of 0°/min, but with different variances (concentration parameter k), both Rayleigh and V-tests will yield significant p-values. Conducting independent Rayleigh or V-tests is not a valid procedure to assess differences in the amount of PFD changes between groups, as these tests only assess departure from uniformity within one group. To draw such inference, circular data needs to be compared between groups. For this comparison, the parametric Watson-William F-test (Taube et al., 2013) can be used to test for a common mean direction, assuming a Von Mises distribution and a common concentration parameter, $k>1$ (Zar, 2010).

Testing for unimodality and for a common mean direction with the Watson-William F-test would not detect differences that are reflected in the variance of two distributions and which may result from greater PFD instability over time. In this case, the assumption of the Watson-William F-test are violated, and the test will fail to reject the null hypothesis, leading to the incorrect conclusion that no difference is present in the amount of PFD changes between the two groups. A circular mean of 0°/min will arise from circular data that are tightly clustered around this mean,

as well as from circular data that are dispersed in both the positive [0°, 180°] and the negative [0°, -180°] direction, as positive and negative values cancel each other out. Testing for a common concentration parameter k is a more meaningful measure for detecting this difference between groups. Alternatively, a non-parametric Kuiper two-sample test can be used to test whether two samples differ significantly, where the difference could be in any property of the distribution, including mean direction as well as concentration parameter (Fisher, 1993).

To illustrate this issue with an example, we consider a published study that has analyzed PFD changes over time in HD cells of rats. Yoder et al. (2015) recorded LMN HD cells following PoS lesions. The amount of direction shift for a cell was computed as the angle difference between the tuning curves from the first and last 2 minutes of the recording trial. The magnitude of drift rate was found by fitting a straight line to the HD vs time scatterplot and taking the absolute value of the slope. For trials in the light, V-tests conducted independently in control and PoS-lesioned animals revealed that both measures were significantly concentrated around a mean of zero for both groups. However, circular scatterplots for both measures revealed a greater amount of variability for the PoS-lesioned group compared to controls (Figure 6.1). To quantify this difference, authors could not test for a common mean direction between the two groups, as they were both clustered around the same mean. Instead, conducting k-tests for a common concentration parameter showed that PoS lesions resulted in a greater variability compared to controls, for both measures. Despite this, the average absolute drift rate did not not differ between the two groups. It was concluded that PoS lesions had a mild effect on the stability of LMN HD cells in the light, reflected in the sample variance but not in the mean of the population. Interestingly, tuning curves of PoS-lesioned animals also displayed a greater mean directional firing range compared to controls, likely due to the effect of lesions on intra-trial PFD stability.

Following from Yoder et al. (2015), in this thesis we compared PFD stability between different classes of directional neurons by plotting drift rate for each cell and (1) testing for differences in concentration parameters (matlab functions *circ_ktest* and *circ_kuipertest*), and (2) testing for differences in mean absolute drift rate (two-sample WRS test). We additionally compared directional firing ranges of cells at small time intervals, during the first 2 minutes of the recording trial. If drifting over time had an effect on a cell's directional specificity, then at short intervals, when drifting is small, average tuning width should also be small.

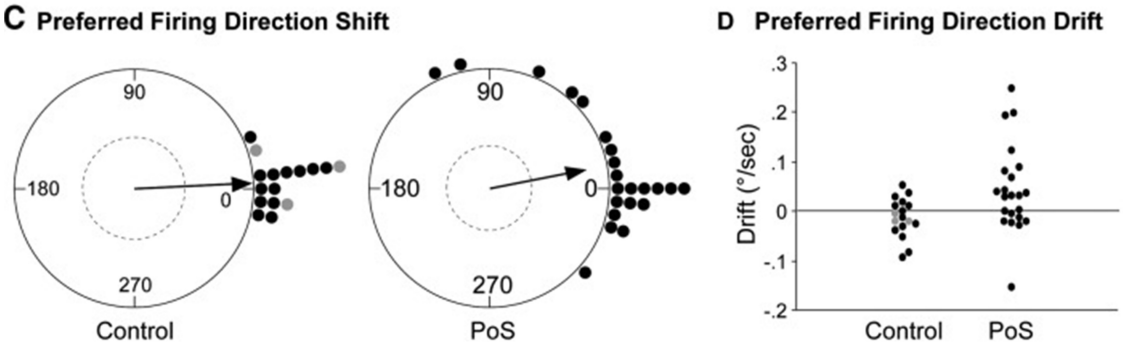


Figure 6.1: Example of analysis comparing intra-trial direction shifts. Each marker is a HD cell from LMN, compared between control and PoS-lesioned rats. Gray markers are from rats with lesions in other areas of cortex. There was a nonsignificant difference in mean shift **(C)** and mean absolute drift rate **(D)** between the two groups, but the lesion group displayed higher variability compared to controls. Taken from Yoder et al. (2015).

6.2.3.3 Non-linear shifts analysis

The above circular-linear regression method used to quantify the slope of the drift rate has the limitation of presupposing a constant rate (magnitude) and direction of drift during the trial, so it cannot successfully identify cells whose firing drifted at a constant rate but in different directions (non-linear shifts in PFD). This instance would result in a small overall slope of the drift rate for the entire trial, leading to the misleading conclusion than the signal was stable across time. We thus designed a separate method to quantify the magnitude of non-linear shifts in the PFD of a cell during a trial.

All episodes in which the rat's head made a full head sweep through the cell's PFD were selected from the 8- or 16 minute-long trial. To do this, we plotted the whole trial as a smoothed firing rate vs time histogram using 20ms bins, and then identified peaks in this curve, corresponding to times when the cell fired>50% of its intra-trial peak firing rate. At these times, the animal's head was crossing through the cell's PFD. We then extracted the HD value at each peak, and took all the spikes before and after it up to an angular distance of +/- 50°, corresponding to spikes emitted during full head sweeps through the PFD. A selection of spikes based on each individual sweep rather than on a reference frame from the whole dataset (the mean

PFD of the cell for the trial) meant that we did not need the PFD prior, which would bias our sampling of spikes in case of PFD shifting over time.

We computed the circular kernel density estimate (KDE) for all selected HD data for each sweep (Silverman, 1986; Bowman and Azzalini, 1997), using an automatically selected bandwidth parameter k, according to Taylor (2008). Probability distributions for all the sweeps in a trial were plotted together on the same graph (Figure 6.12). We used KDEs to avoid arbitrary decisions on binning and because distributional properties could be more easily assessed. For each peak, we computed the width at half-height and absolute direction of peak location. These measures were subjected to inferential statistics and compared between the cell groups using two-sample T-tests. This allowed us to test two different, but non-mutually exclusive, hypotheses to explain broader tuning curves of Theta-by-HD cells. If broader tuning is due to greater PFD shifting over time, KDE peaks in a trial should have a small mean width but larger jitter in peak location. If broader tuning is an intrinsic property of the cells (due to the directional firing range actually being larger), KDE peaks in a trial should have a large mean width but smaller variability in peak location.

Since the reliability of the density estimate depends on the number of data points (Fisher, 1993), only sweeps containing at least 5 spikes were considered for this analysis. Only cells with more than one full head sweep for the trial were included, allowing us to estimate the SEM. In the future, applying the circular KDE method will be useful to gain insights into whether HD signal instability or a true increase in directional firing range accounts for tuning curve changes reported by previous studies at different levels of the HD circuit (Giocomo et al., 2014), as well as after lesioning cortical HD cell components that impair landmark anchoring (Clark et al., 2010).

6.2.4 Analysis of motor correlates

We quantified the relationship between instantaneous firing rates and linear and angular speed of the head using a speed score (s-score) and an angular head velocity score (AHV-score), respectively. Each of these methods is described.

6.2.4.1 Running speed calculations

We derived instantaneous running speed as the total distance traveled between two consecutive position data points, divided by the time between them. For a cell, we derived instantaneous firing rate from the smoothed spike-time histogram, obtained using 20ms bins, coinciding with the frames of the camera (50Hz sampling rate), and smoothed with a 250ms-wide Gaussian filter. Dividing the spike count per bin by 0.02 converts counts to firing rate, allowing to derive a measure of instantaneous firing for each position data point (for each camera frame).

6.2.4.2 Speed-rate relationship

The relationship between linear speed and instantaneous firing rate of a cell was obtained following methods in Kropff et al. (2015). We binned instantaneous firing rate by running speed at a bin width of 2cm/s, within a range of 2 and 50cm/s, and fitted a linear regression model using the least-squares fitting method. Running speeds below 2cm/s were excluded from running speed analysis, as the animal was not moving. This bin width was selected because using larger bins has the risk, at low speeds, to include episodes of both immobility and very slow movements. The s-score is the Pearson's linear correlation coefficient between instantaneous firing rate and speed bins. As in Kropff et al. (2015), we identified speed-responsive cells based on absolute s-score>0.3.

6.2.4.3 Angular head velocity calculations

We measured instantaneous AHV by taking the angular difference between two successive HD data points, divided by the time between them (Blair and Sharp, 1995). This meant that measurements of AHV and HD were sampled 180° out of phase with each another. To correct for this phase offset, HD measurements were interpolated between consecutive samples, to bring them into temporal alignment with AHV measurements, and provide an estimate of the animal's HD at each AHV point. Each spike was then associated to the most recently interpolated HD value, and the most recently recorded AHV value.

6.2.4.4 Angular head velocity-rate relationship

A 2°/s bin width was used to bin instantaneous firing rate by AHV. A range of -100 and 100°/s was used. A scattergram of firing rate vs AHV was plotted, and linear regression lines were fitted to AHV values between -2 and -100°/s, and between 2 and 100°/s (least-squares fitting method). Values between -2°/s and 2°/s were discarded, as periods in which the head was not turning.

CW and CCW AHV scores are the Pearson's correlation between instantaneous firing rate and AHV bins for CW and CCW turns. To quantify modulation of rates by AHV irrespective of the head-turning direction, we considered the absolute value of CW and CCW AHV scores. AHV-responsive cells had absolute AHV score>0.3 for both CW and CCW turns. Taking the absolute values was necessary because previous studies from other brain regions found that HD cells can both increase and decrease firing rates with AHV in different turning directions (Bassett and Taube, 2001; Lozano et al., 2017; Stackman and Taube, 1998). Cells with symmetric AHV-rate profiles have slopes that are positive in one direction but negative in the other, which would cancel if raw values were taken. A small number of HD cells with asymmetric AHV-rate profiles were also reported in LMN (Stackman and Taube, 1998). These cells increase firing rates with AHV in one direction but decrease in the other, resulting in consistent CW and CCW slope values (both positive or both negative). We considered CW and CCW AHV-scores separately to classify cells as symmetric or asymmetric.

6.3 Results

6.3.1 Qualitative observations on signal stability

Qualitatively, spatial firing was verified by recording cells across three consecutive trials on the same day (T1-T2-T3; T3 was in darkness) and plotting the distribution of spatial firing rates for each trial (Figure 6.2). Quantification of this stability of the spatial pattern is discussed in the next Chapter. Among the directional neurons, a stable, unidirectional tuning curve peak indicates that directionality did not result from a biased sampling of different directions within a single trial. This is because, since tuning curves were constructed from binned data, firing rate in a given angular bin could be affected by the time that the animal spent facing that direction in a trial (see also Appendices, Figure A.9). Among the place cells, constructing the spikemap

for each trial provided very convincing evidence of place field stability both within and across trials, which did not result from heterogeneity in the animals position sampling within a single trial, nor from binning procedures applied when constructing the ratemap (Burgess et al., 2005). Note that, to avoid misleading classifications of single units as either HD or place, we had already adopted a selection criteria based on a minimum peak firing rate, and encouraged homogeneous spatial sampling by randomly throwing rice inside the open field box during recordings.

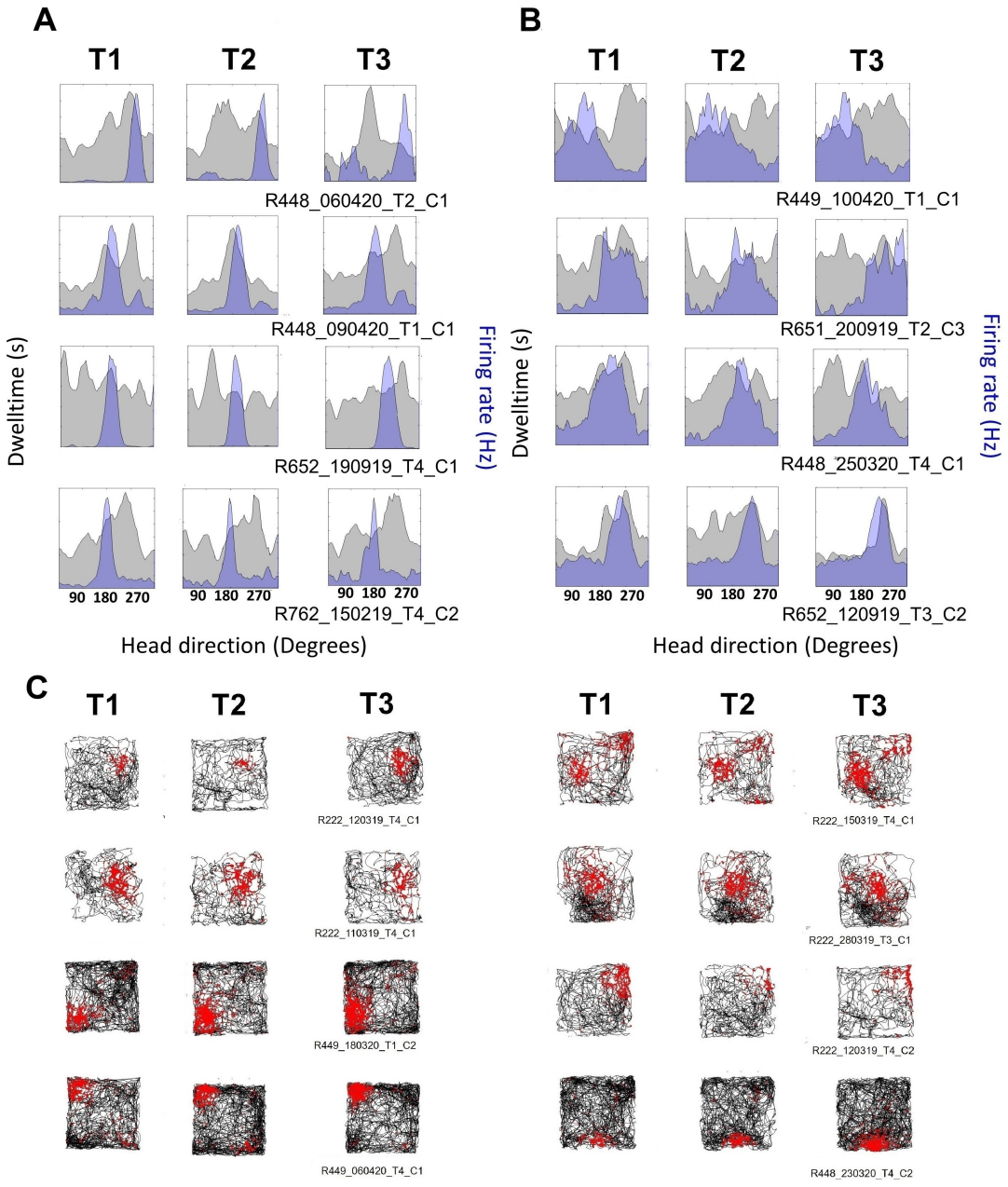


Figure 6.2: **Directional and locational fields verified by recording across trials.** Distribution of spatial firing for **(A)** classic HD, **(B)** Theta-by-HD and **(C)** place cells.

Each cell recorded across three consecutive trials (T1-2-3). Each trial is 8 or 16-minute long recorded in the same squared arena (T1 and T2 in the light; T3 in darkness). Tuning curves (blue) and dwelltime curves, showing firing rate (Hz) and dwelltime (s) for each 6° directional bin, respectively, are displayed as smoothed firing rate histograms, peak-normalized; y-axis range is always from 0 to 1, and x-axis range is 0-360°. Note that Theta-by-HD cells have broader directional tuning curves, classic HD cells are much more finely tuned.

6.3.2 Are there differences in directional tuning curve properties?

We performed statistical analysis on tuning curve parameters to compare between the different groups of directional neurons identified in Experiment 2. Four parameters were considered: R-vector, tuning width (degrees), concentration parameter (k) and peak rate (Hz). Average and SEM of these values are reported in Table 6.1. Multiple KW tests with cell-type as the between-subject variable were run and found a main effect of cell type on all tuning parameters. According to post-hoc comparisons, R-vector and concentration parameter were significantly smaller for Theta-by-HD cells compared to classic HD and intermediate HD cells, whose values were the same (R-vector: $H(2)=95.980$, $p<0.0001$; HD vs int.HD, $p=0.898$; HD vs Theta-by-HD, $p<0.0001$; int.HD vs Theta-by-HD, $p<0.0001$; k: $H(2)=95.980$, $p<0.0001$; HD vs int.HD, $p=0.898$; HD vs Theta-by-HD, $p<0.0001$; int.HD vs Theta-by-HD, $p<0.0001$). Again, tuning width was significantly larger for Theta-by-HD cells compared to classic HD and intermediate HD cells, whose values were the same (width: $H(2)=96.008$, $p<0.0001$; HD vs int.HD, $p=0.899$; HD vs Theta-by-HD, $p<0.0001$; int.HD vs Theta-by-HD, $p<0.0001$). Peak firing rates differed between all groups: intermediate HD cells exhibited the highest peak rate, Theta-by-HD cells the lowest, and classic HD between the two (peak rate: $H(2)=60.234$, $p<0.0001$; HD vs int.HD, $p<0.0001$; HD vs Theta-by-HD, $p<0.0001$; int.HD vs Theta-by-HD, $p<0.0001$). The significance of these differences between groups is displayed by the bar graphs of Figure 6.3 A.

Theta-by-HD cells exhibited a wider range of directional firing and smaller peak rates inside of this range, as compared to directional neurons with non-rhythmic spike discharge. The tuning width of these neurons is plotted and compared in the frequency histogram of Figure 6.3 B. Among the non-rhythmic HD sample, classic HD and intermediate HD firing followed an equivalent directional pattern except for differences in peak rate, being higher for intermediate HD cells. Despite the less-direction specific firing of Theta-by-HD cells, peak rate was at least 50% higher than the mean rate for 121/122 non-rhythmic HD cells and 151/158 Theta-by-HD

cells, indicating a clear directional tendency of spikes for both groups, as confirmed by the *pxd* analysis below (see Section 6.3.4).

Table 6.1: **Summary statistics for the three groups of AV neurons expressing directional properties.**

Directional tuning curve properties					
	Classic HD	Theta-by-HD	Intermediate HD	H-value***	Post-hoc tests
Tuning width	97.11 ±3.29	132.30 ±1.15	82.72 ±6.90	96.008	1, 2***, 3***
R-vector	0.60 ±0.02	0.33 ±0.02	0.69 ±0.05	95.980	1, 2***, 3***
Concentration parameter k	2.34 ±0.21	0.72 ±0.03	3.25 ±0.44	95.980	1, 2***, 3***
Peak rate (Hz)	20.38 ±2.94	5.20 ±0.03	51.70 ±6.43	60.234	1***, 2***, 3***

Table 6.1: For each directional measure, average, SEM and significant differences between groups are reported. H-value, KW tests results. Post-hoc comparisons (Bonferroni correction): 1, HD vs Intermediate HD ; 2, HD vs Theta-by-HD; 3, intermediate HD vs Theta-by-HD. Cell numbers are: HD, n=96; Int.HD, n=26; Theta-by-HD, n=158.

As predicted from the above results, we found a positive correlation between a cell's tuning width and its theta-modulation depth, measured by the Index of Coupling (IC; Spearman's r=0.43), as well as between a cell's tuning width and its intrinsic spike rhythmicity, measured by the Index of Rhythmicity (IR; Spearman's r=0.38, all p<0.0001). These relationships are visible in the scatterplots of Figure 6.3 C. To ensure that relationships between tuning width and theta were not a byproduct of other factors, the width parameter was also tested against average firing rate (r=-0.14), spike bursting propensity (burst index, r=-0.12; peak ISI, r=-0.19) and waveform peak-to-trough width (r=0.16). There was no significant relationship between these factors (all p>0.01) except for a negative correlation with peak ISI (p=0.002). It can be concluded that, for a directional neuron, the more the spike discharge was theta phase-specific (theta-modulated), the less it was HD-specific.

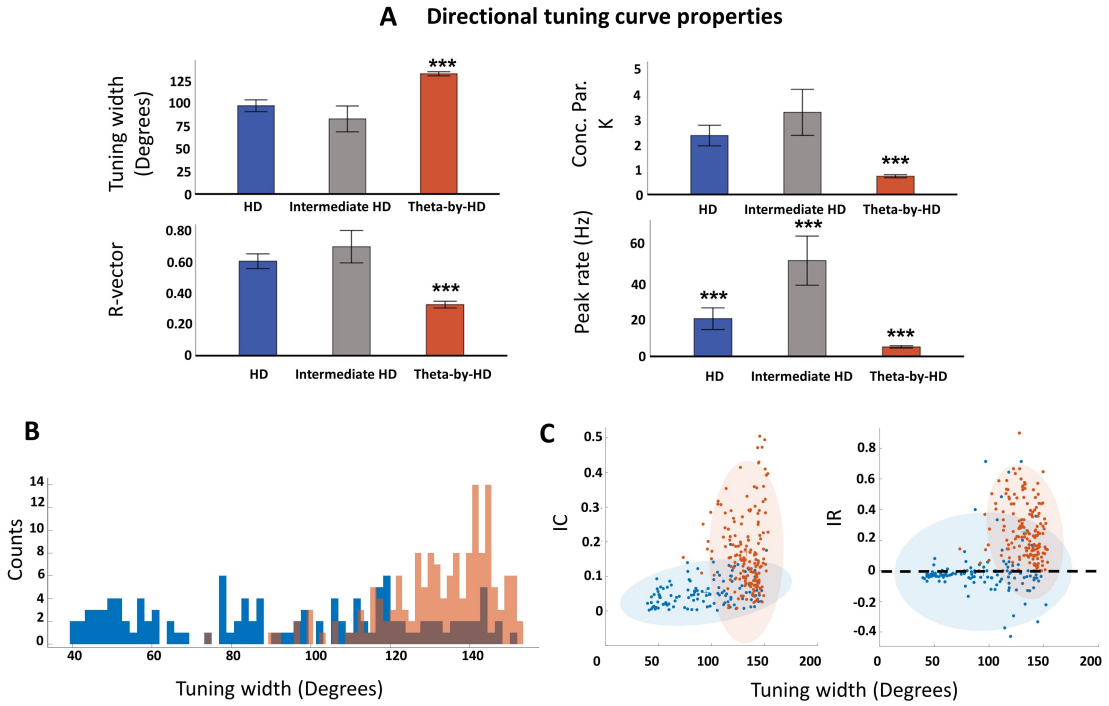


Figure 6.3: **Theta-by-HD cells have broader directional correlates.** **(A)** Mean with 95% confidence intervals bar graphs of tuning parameters: width (degrees), R-vector, concentration parameter *k*, peak firing rate (Hz). Cell groups are: classic HD (blue), Theta-by-HD (red), intermediate HD (gray). Theta-by-HD cells are broader than non-rhythmic HD cells, comprising classic HD and intermediate HD cells, whose firing follow an equivalent directional pattern. There is however a significant difference in peak rate between all groups (***=0.001 significance). **(B)** Frequency distribution (50 bins) of the tuning width parameter, compared between Theta-by-HD (red) and non-rhythmic HD cells (blue; combined classic HD and intermediate HD cells, given that they do not differ). **(C)** The width parameter of these cells positively correlates with Index of Coupling (IC) and Rhythmicity (IR). Each marker is a cell, colour coded as in (B). Shaded area, 95% percentile confidence ellipse. Horizontal line, IR=0.001; directional units had to reach this cutoff to be classified as Theta-by-HD.

6.3.3 Are there differences in the strength of spatial influences?

We have compared tuning parameters between directional neurons. We now attempt to compare the strength of the spatial influences on all AV cells using measures of information content for location and direction (bits/spike). Mean and SEM of these measures for each cell group, and results of the statistical analysis that compares between them are summarized in Table 6.2 below.

6.3.3.1 Some Theta-by-HD cells met the place cell threshold based on locational information

In order to be classified as a place cell, a cell had to achieve a locational information>0.8 bits/spike and sparsity score<0.2 (see General Methods). The mean locational information for place cells (n=61) was 1.51±0.06. Within the combined HD dataset (n=280) a small subset of Theta-by-HD cells (n=20/158) had locational information above the 0.8 threshold, the highest value being 1.30 (see values in Table 6.2). Mean locational information for the combined HD dataset cells was 0.35±0.02. However, none of the HD cells also had a sparsity score that satisfied the 0.2 threshold used for place cell classification. Even so, despite not reaching place cell criteria, Theta-by-HD cells occasionally displayed broad patches of spatially-inhomogeneous firing in their ratemap, suggesting some degree of locational signaling. See examples of Theta-by-HD cells in Figure 5.5.

We therefore conducted KW tests to compare location information and sparsity score and found a main effect of cell type on both measures (Table 6.2, "Before *pxd* correction"). As expected from our classification criteria, place cells had much higher location information in comparison to the HD dataset, whose locational information was markedly reduced and was the same for all groups (locational info: $H(3)=151.125$, $p<0.0001$; HD vs int.HD, $p=0.570$; HD vs Theta-by-HD, $p=0.140$; HD vs place cell, $p<0.001$; int.HD vs Theta-by-HD, $p=1$; Theta-by-HD vs place cell, $p<0.001$; int.HD vs place cell, $p<0.001$). Logically, place cells also displayed a significantly lower sparsity score in comparison to the HD dataset. Within the HD dataset, sparsity of classic HD cells was higher than that of Theta-by-HD cells, but not significantly different from that of intermediate HD cells. Similarly, sparsity of Theta-by-HD cells was not significantly different from that of intermediate HD cells (sparsity: $H(3)=156.241$, $p<0.0001$; HD vs int.HD, $p=1$; HD vs Theta-by-HD, $p=0.023$; HD vs place cell, $p<0.0001$; int.HD vs Theta-by-HD, $p=1$; Theta-by-HD vs place cell, $p<0.0001$; int.HD vs place cell, $p<0.001$). Comparisons were repeated using *pxd*-corrected measures of locational information (see Section 6.3.4 below). When corrected, place cells continued to display significantly higher locational information than the HD dataset. Within the HD dataset, corrected information for Theta-by-HD cells became higher than that of classic HD and intermediate HD cells, whose values did not differ (corrected locational info: $H(3)=204.640$, $p<0.0001$; HD vs int.HD, $p=1$; HD vs Theta-by-HD, $p<0.0001$; HD vs place cell, $p<0.0001$; int.HD vs Theta-by-HD, $p<0.0001$; Theta-by-HD vs place cell, $p<0.0001$; int.HD vs

place cell, $p<0.0001$). Results are reported in Table 6.2 under "After *pxd* correction". Overall then, occasionally Theta-by-HD cells showed some locational signaling when compared with non-rhythmic HD cells, although this was overall much weaker than in place cells (Figure 6.4). These results will be confirmed by the *pxd* analysis below.

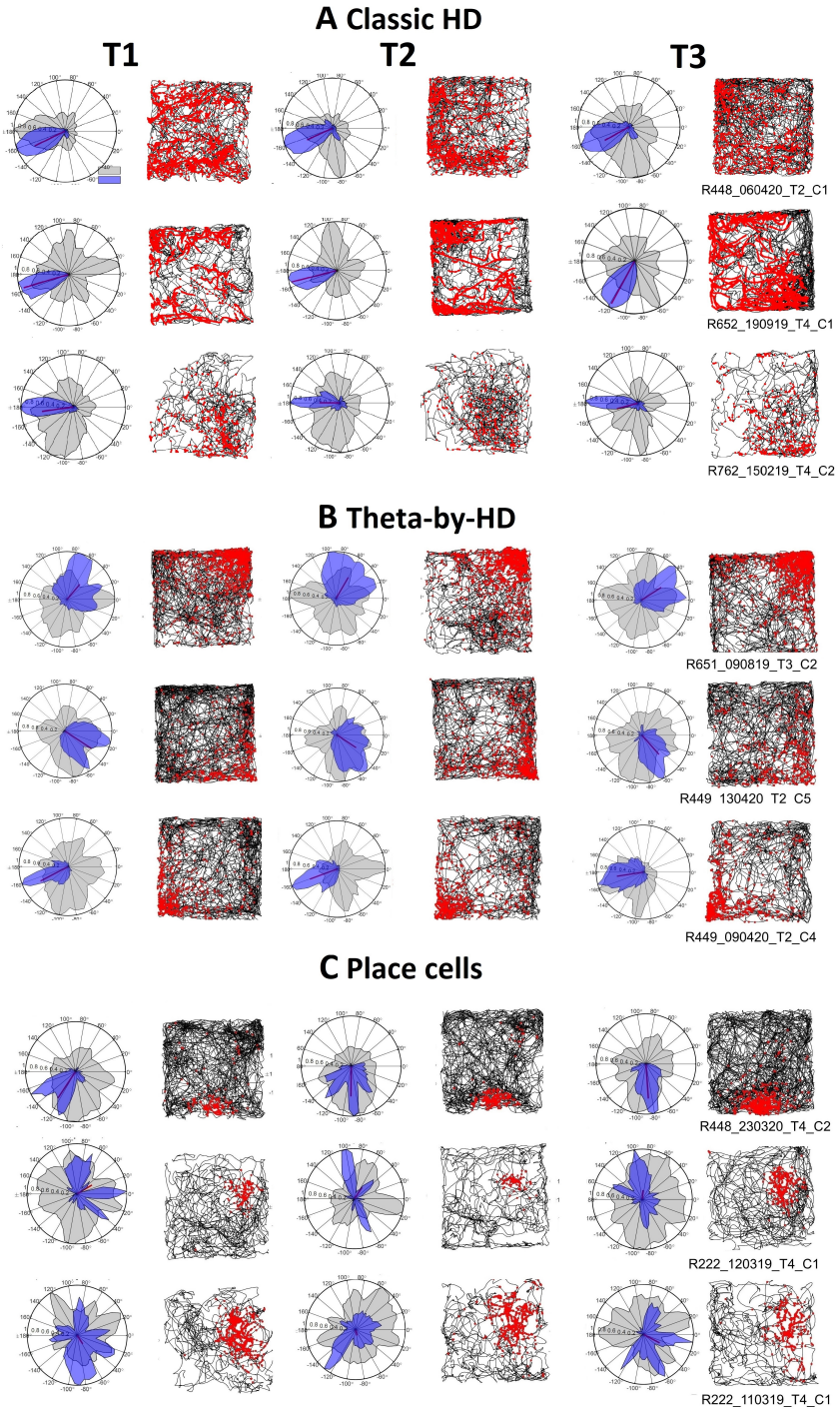


Figure 6.4: **A subset of Theta-by-HD cells formed larger place fields.** Examples of **(A)** classic HD, **(B)** Theta-by-HD and and **(C)** place cells. Each cell recorded across

three trials. Polar plots and spikemaps are presented for each trial. In the polar plots, the blue curve shows firing rate (Hz) for each 6° directional bin; the gray curve shows dwelltime (s) for each bin. For some Theta-by-HD cells (n=20), but not for the other directional neurons, spikes were not completely uniform but accumulated at specific locations within the box, as shown in the Figure. These cells met the locational information threshold>0.8 bits/spikes, but only place cells also met the sparsity threshold<0.2. Place fields of Theta-by-HD cells (B) were less spatially-compact than the place cell ones (C).

6.3.3.2 Some place cells met the head direction threshold based on the tuning curve R-vector

Of the 61 place cells recorded, about half (35/61) met our classification for a significant directionality, based on the tuning curve R-vector (see General Methods). Among place cells meeting this criteria however, only 13/35 cells had directional information content>0.8, compared to 96/280 cells in the HD dataset. A KW test found a main effect of cell type on directional information (Table 6.2, "Before *pxd* correction"). Classic HD and intermediate HD cells had the same directional information, both being higher than Theta-by-HD cells and place cells, whose values did not differ significantly from each other (directional info: $H(3)=71.228$, $p<0.0001$; HD vs int.HD, $p=1$; HD vs Theta-by-HD, $p<0.0001$; HD vs place cell, $p=0.003$; int.HD vs Theta-by-HD, $p<0.0001$; Theta-by-HD vs place cell, $p=0.075$; int.HD vs place cell, $p=0.001$). Results did not change when comparisons were conducted using *pxd*-corrected measures of directional information (corrected directional info: $H(3)=105.801$, $p<0.0001$; HD vs int.HD, $p=1$; HD vs Theta-by-HD, $p<0.0001$; HD vs place cell, $p<0.0001$; int.HD vs Theta-by-HD, $p<0.0001$; Theta-by-HD vs place cell, $p=0.603$; int.HD vs place cell, $p<0.001$). These results are reported in Table 6.2 under "After *pxd* correction". The low directional information of Theta-by-HD cells is consistent with their reduced directional tuning as compared to the non-rhythmic HD cell population, shown above. Directional signalling was overall much weaker for Theta-by-HD cells compared to non-rhythmic HD cells, to the point that it was not reflected in a high average directional information content. Although results suggest the possibility that place cells might carry some amount of directionality to their firing, the *pxd* analysis below demonstrates that this effect was a byproduct of their locational signaling, coupled with a biased sampling of orientations.

Table 6.2: **Summary statistics of spatial properties for AV cells with spatial profiles.**

	Spatial properties					
	Place cells	Classic HD	Theta-by-HD	Intermediate HD	H-value***	Post-hoc tests
Before *pxd* correction						
Directional Information	0.58 ±0.04	1.03 ±0.07	0.48 ±0.03	1.39 ±0.15	71.228	1, 2***, 3**, 4***, 5, 6**
Locational Information	1.51 ±0.06	0.27 ±0.02	0.4 ±0.02	0.37 ±0.04	151.125	1, 2, 3***, 4, 5***, 6***
Sparsity score	0.15 ±0.01	0.56 ±0.01	0.49 ±0.01	0.54 ±0.02	156.241	1, 2*, 3***, 4, 5***, 6***
After *pxd* correction						
Directional Information	0.40 ±0.04	1.03 ±0.07	0.32 ±0.02	1.34 ±0.15	105.801	1, 2***, 3***, 4***, 5, 6***
Locational Information	1.37 ±0.06	0.09 ±0.01	0.31 ±0.02	0.05 ±0.03	204.640	1, 2***, 3***, 4***, 5***, 6***

Table 6.2: For each spatial measure, average, SEM and significant differences between groups are reported. Cell groups are place cells, classic head direction (HD), Theta-by-HD and intermediate HD (Int. HD). H-value, results of the KW tests that compared each measure. Post-hoc comparisons (Bonferroni correction): 1, HD vs Intermediate HD; 2, HD vs Theta-by-HD; 3, HD vs place cell; 4, intermediate HD vs Theta-by-HD; 5, Theta-by-HD vs place cell; 6, intermediate HD vs place cell. Cell numbers: HD, n=96; Int.HD, n=26; Theta-by-HD, n=158; place cell, n=61. Information content is in bits/spike. Sparsity score is the proportion of the arena's surface area over which the cell fired. Information content for location and direction are reported before and after applying the place time direction (*pxd*) correction algorithm.

As no difference was observed regarding the locational and directional firing characteristics between classic HD (n=96) and intermediate HD (n=26), apart from peak directional firing rate of the tuning curve (shown above), we pooled the data into a single distribution of HD cells with non-rhythmical firing. Analysis henceforth was done considering only three groups of neurons for simpler comparisons: non-rhythmic HD cells (n=122; combined classic HD and intermediate HD), Theta-by-HD (n=158) and place cells (n=61).

6.3.4 Directional and locational influences on cell firing rate, corrected for the sampling bias

The above analysis suggested that locational and directional influences may not always be mutually exclusive, but may coexist in the same neuron for Theta-by-HD and place cells. In this Section we perform *pxd* corrections to determine the independent contribution of each of these influences on cell firing rates, with the aim to determine whether conjunctive coding was true or due to behavioural couplings. Answering this question is particularly important given extensive AV connections with cortical regions known to exhibit conjunctive locational-directional profiles (based on *pxd* correction), namely PoS, PaS, MEC (Sargolini et al., 2006; Cacucci et al., 2004; Boccara et al., 2010) and RSC (Cho and Sharp, 2001). In this Section, we will demonstrate that some Theta-by-HD cells (n=20) show a true but weak effect of both direction and location, in the form of broad directional and locational fields (Figure 6.4 B). In contrast, place cells show a true (and strong) effect of location and virtually no effect of direction (Figure 6.4 A).

6.3.4.1 Effects of the *pxd* correction: only Theta-by-HD cells show true conjunctive coding

Figure 6.5 illustrates the spatial distribution of directional activity for four place cells, with either direction-independent firing (A) or passing the directionality criteria based on R-vector (B, C, D). Directions are colour coded as in the polar plot at the top. Among the subset of place cells (35/61) meeting our directional criteria, all but two cells (33/35) had firing fields located near a boundary and a tuning curve oriented outward toward that boundary, as it would be expected from a sampling artefact (cell D in Figure 6.5). We did not find any case of clear dissociation between directional and locational preferences i.e., a tuning curve pointing to the opposite direction of the place field. The sampling bias is most acute near boundaries, as they can only be approached by the animal from a specific direction. A place cell with firing fields at these locations can therefore develop an apparent preference for the direction most often faced by the animal while entering the place field. Only two place cells (2/35) had fields in the arena's centre, whose directionality would not be easily explained by a tendency of the animal to approach the field from a specific direction (cells B-C in Figure 6.5). Hence, a more formal analysis was needed to determine whether conjunctive coding was true or artefactual. For purpose of clarity, the same four place cells as in Figure 6.5 will be used as examples in all other figures throughout this Section.

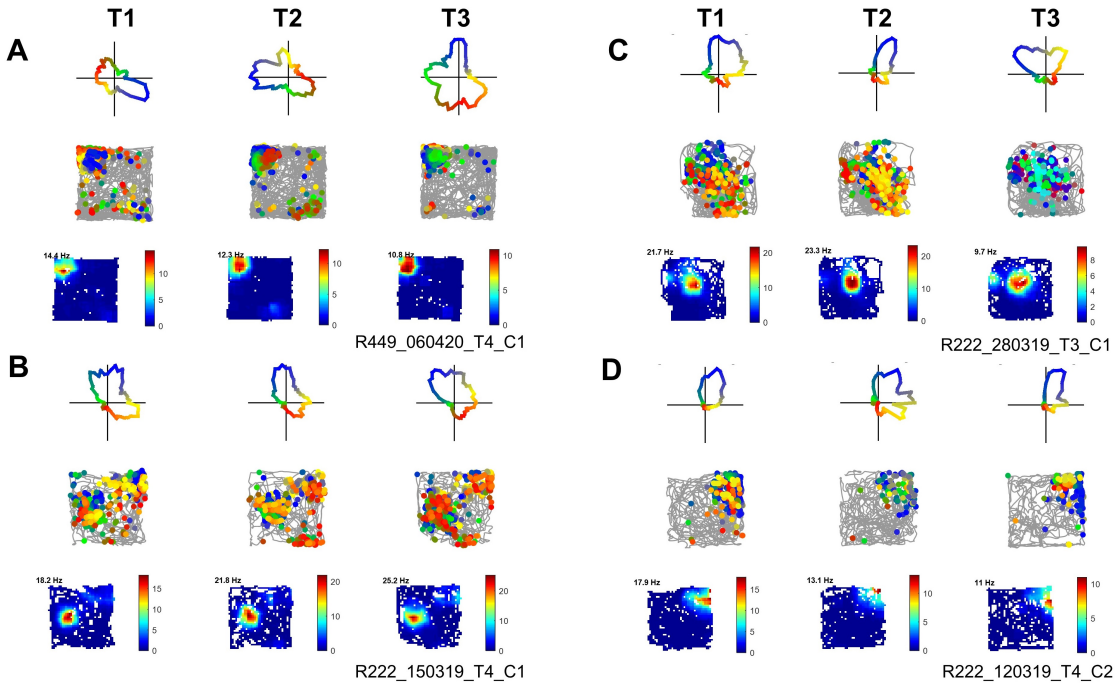


Figure 6.5: **Examples of place cells met the directionality threshold.** The figure shows **(A)** a place cell with no directionality; **(B-C-D)** three place cells that met the directionality threshold. Each cell was recorded across three trials. The following plots are shown. Top, directionally colour coded polar plot. The direction of the peak firing rate is blue, and the other directions follow a colour gradient changing every 90°. Middle, directionally colour coded spikemap. Each spike is coloured according to the associated direction at which the spike occurred and overlayed on the path of the rat (highly smoothed in 20ms bins). Bottom, spatial ratemap. Number is the locational peak rate for the trial. For cell A, place field spikes are not associated with a specific colour, while for the other cells there is a prevalence of spikes associated with the peak of the polar plot (blue).

Applying the *pxd* analysis revealed that place cells carried no significant amount of directionality to their firing. Figure 6.6 illustrates the effects of applying the *pxd* algorithm on the same four place cells as in Figure 6.5. Original firing rate plots are denoted as "pd" and corrected plots are denoted as "*pxd*". Correlation values between pd and *pxd*-corrected maps are reported for the first trial. When applying the algorithm, directional tuning curves were disrupted and were not consistently seen across trials (see for example cell A, T3), suggesting that directionality was a byproduct of the place field. In contrast, place cell ratemaps were always almost perfectly reconstructed by the algorithm. For place cells, directional information was reduced by 34.5% on average, ranging between -79% and 9.4%. Average reduction of locational information was 7% (range: -25% and 13%). Corrected and uncorrected values are reported in Table 6.2.

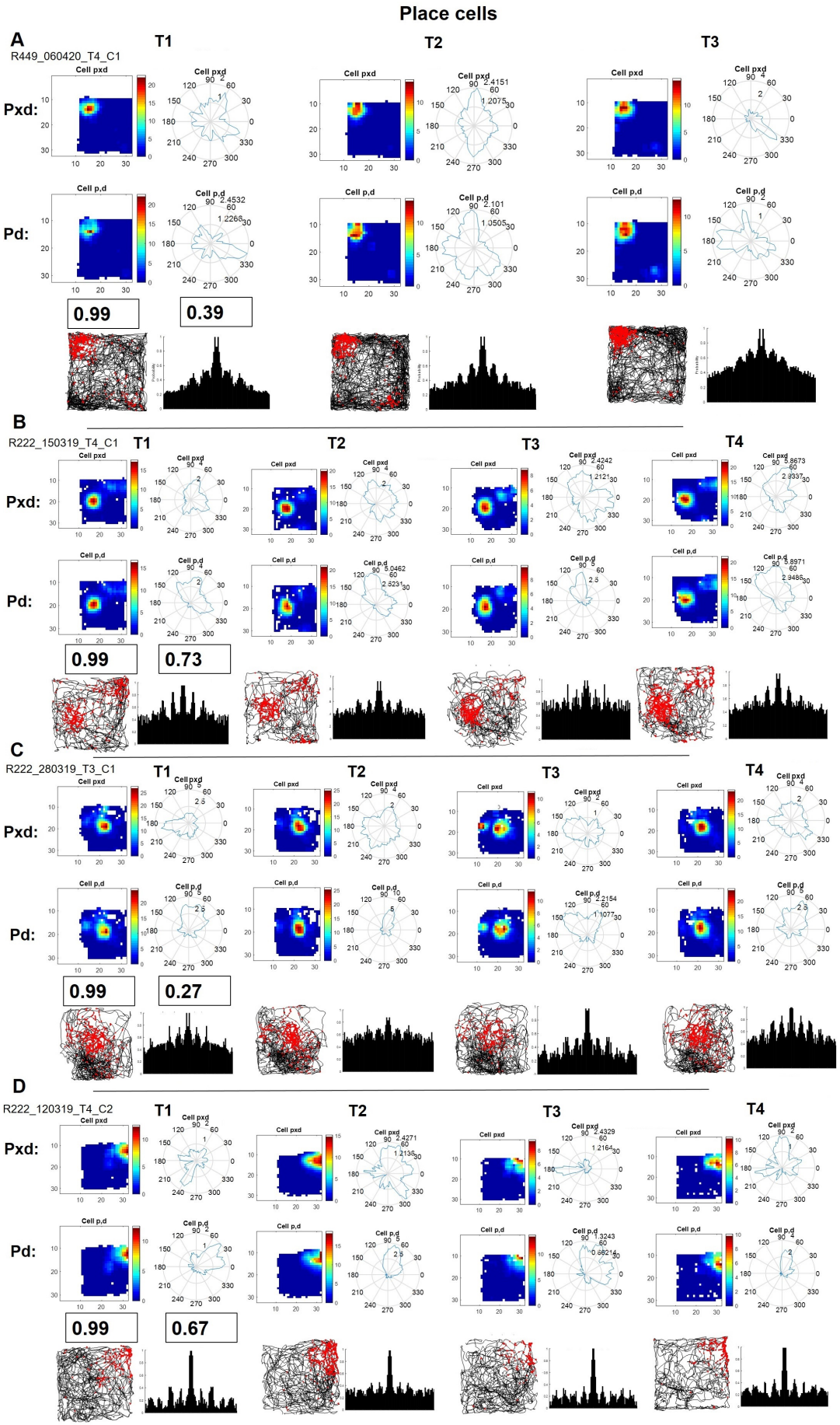

Place cells
A
R449_060420_T4_C1
T1
T2
T3
Pxd:
Pd:
0.99
0.39
B
R222_150319_T4_C1
T1
T2
T3
T4
Pxd:
Pd:
0.99
0.73
C
R222_280319_T3_C1
T1
T2
T3
T4
Pxd:
Pd:
0.99
0.27
D
R222_120319_T4_C2
T1
T2
T3
T4
Pxd:
Pd:
0.99
0.67

Figure 6.6: **The *pxd* correction disrupts directional correlates of all the place cells.** The figure shows the effects of applying the *pxd* correction on the same four place cells as in Figure 6.5. Each cell was recorded across multiple trials (four trials for A; three trials for B-C-D). Trial number is at the top. For each cell, the following plots are shown. First row (pxd), *pxd*-corrected firing rate maps for location and direction. Second row (pd), original firing rate maps. Third row, spikemap and temporal autocorrelogram. x-axis, time lag (ms); y-axis, probability. Numbers in box refer to correlation between pd and *pxd* maps for Trial 1. In some trials, cells B, C and D displayed an apparent directionality in the pd polar plots, which was however notably reduced by the algorithm.

In contrast, HD neurons carried a significant amount of directionality to their firing and a small subset of 20 Theta-by-HD cells also carried a a weak amount of spatiality to their firing, reproducible across trials, albeit much weaker than in place cells. Figures 6.7 and 6.8 illustrate the effects of applying the *pxd* algorithm on two pairs of Theta-by-HD and place cells, simultaneously recorded on the same tetrode. A good match was consistently observed between original and *pxd*-corrected tuning curves, whereas the effect on the ratemaps was less predictable. By applying the algorithm, directional information was reduced on average by 2.4% (range: -47% and 21%) for non-rhythmic HD and 2.9% (range: -68% and 57%) for Theta-by-HD cells, suggesting a true effect of direction. Locational information was reduced by an average of 68.2% (range: -96% and 15%) for non-rhythmic HD and 23.2% (range: -84% and 47%) for Theta-by-HD cells. For Theta-by-HD cells, the small average reduction in both directional and locational information is consistent with conjunctive coding, although note the large range values — the specific effect of *pxd* correction on a given Theta-by-HD cell was highly variable.

Pearson's correlation coefficients were used as a measure of similarity between original (pd) and corrected (*pxd*) maps. At the population level, average correlations for direction were: place cell, 0.77; non-rhythmic HD, 0.99; Theta-by-HD, 0.93. Average correlation coefficients for location were as follow: place cell, 0.997; non-rhythmic HD, 0.88; Theta-by-HD, 0.99. Correlations compared using Fishers r-to-z transformation were all statistically different from each other (all $p<0.0001$), and Theta-by-HD cells were in-between HD and place cells for both location and direction correlations. Correlations for place cell and non-rhythmic HD cells appeared strikingly similar to those reported for place cells in hippocampal CA1 (direction, 0.74; location, 0.96) and HD cells in PoS (direction, 0.99; location, 0.48), obtained using the same *pxd* approach as the present thesis (Cacucci et al., 2004). Overall then, place cells have stronger locational signaling, and almost no directional signaling, while non-rhythmic HD cell carry high directional and almost no locational

information. Theta-by-HD cells exhibit some degree of conjunctive locational and directional signaling, suggesting limited spatial influence from the place cell signal.

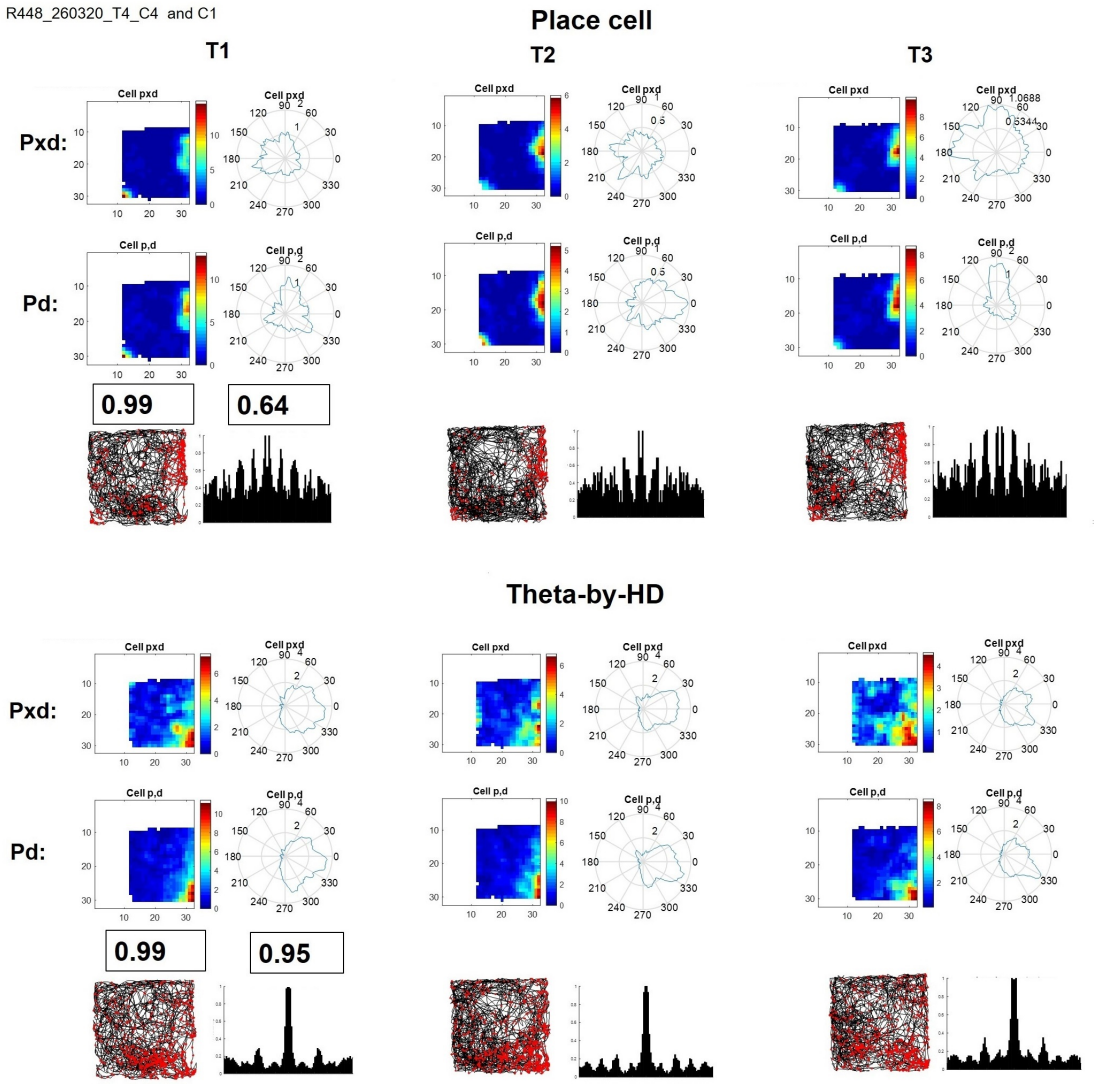


Figure 6.7: **The *pxd* correction does not alter Theta-by-HD cell directional correlates: example of conjunctive Theta-by-HD cell.** Effects of *pxd* corrections compared between a place cell (top) and a Theta-by-HD cell (bottom), co-recorded on the same tetrode across three trials. For each cell, the following plots are shown. First row (pxd), *pxd*-corrected firing rate maps for location and direction. Second row (pd), original firing rate maps. Third row, spikemap and autocorrelogram implemented between±500ms. x-axis, time lag (ms); y-axis, probability. A subset of Theta-by-HD cells displays conjunctive coding for place and direction, as in this example. For these cells, correction produced comparable directional and locational information content. For place cells, correction always produced comparable locational, but not directional, information content.

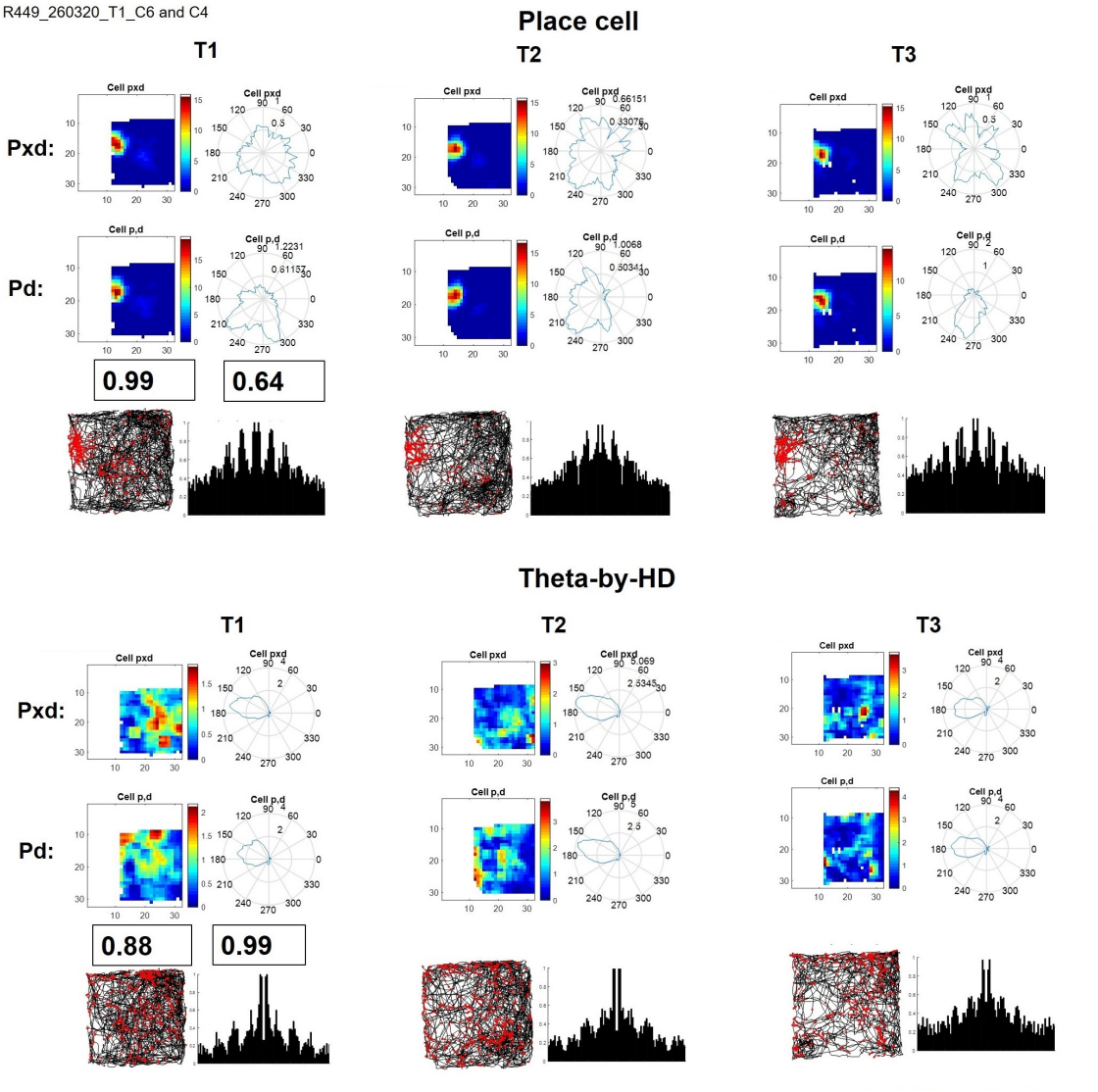


Figure 6.8: **The *pxd* correction does not alter Theta-by-HD cell directional correlates: example of non-conjunctive Theta-by-HD cell.** See caption in previous Figure. For Theta-by-HD cells, the effects of the correction were more variable compared to other cell types, as cells could be either conjunctive (as shown in the previous figure) or only encode direction. For non-conjunctive cells, as the one shown here, the correction produced comparable directional, but not locational, information content.

6.3.5 Do cells anticipate the animal's heading direction?

We have shown that Theta-by-HD cells exhibit reduced directional specificity and broader tuning curves compared to the non-rhythmic HD cells. We conducted analysis to determine whether this property of Theta-by-HD cells might reflect (1) a greater anticipatory firing, (2) a less stable directional signal (3) a true change in the cell intrinsic characteristics, due to firing range actually being larger. This Section will explore the anticipatory firing hypothesis.

First, we will derive the ATI and difference angle for each cell using two different approaches, based on correlations of CW-CCW tuning functions and optimal-time shifts for the standard tuning function, respectively. Second, we will determine whether non-rhythmic HD (combined classic and intermediate HD cells) and Theta-by-HD cells exhibited anticipatory firing and compared between the two groups. We will show that non-rhythmic HD cells anticipated the animals heading direction by a greater amount than Theta-by-HD cells. Finally, we will show that parameters of a cell's tuning curve, namely width (degrees) and peak rate (Hz), were not affected by the animals turning behaviour, suggesting that broader tuning curves of Theta-by-HD cells did not result from shifting in opposite directions during CW and CCW head turns, as it would be expected for cells with longer ATI values.

6.3.5.1 Theta-by-HD cell firing is less anticipatory

Decomposed CW and CCW tuning functions for a cell were derived based on the AHV value at the time of each spike. We plotted decomposed functions on the same graph alongside the standard function, built using all spikes, including those emitted during immobility (Figure 6.9). Doing so revealed a lower degree of overlap between decomposed tuning functions for non-rhythmic HD cells compared to Theta-by-HD cells, suggestive of greater anticipatory firing. Another useful way to visualize differences in anticipatory firing between these cells consists in plotting tuning curves as a function of AHV. Representative examples of each cell group are reported in Figure 6.10 A. For the non-rhythmic HD cell, but not for the Theta-by-HD cell, the tuning curve shifted linearly as a function of AHV in opposite directions for CW and CCW turns, and the left-to-right gradient is suggestive of anticipatory firing. For the Theta-by-HD cell, a smaller gradient suggests firing correlated with more present heading directions. This may imply that Theta-by-HD cells depend on the output of the HD network.

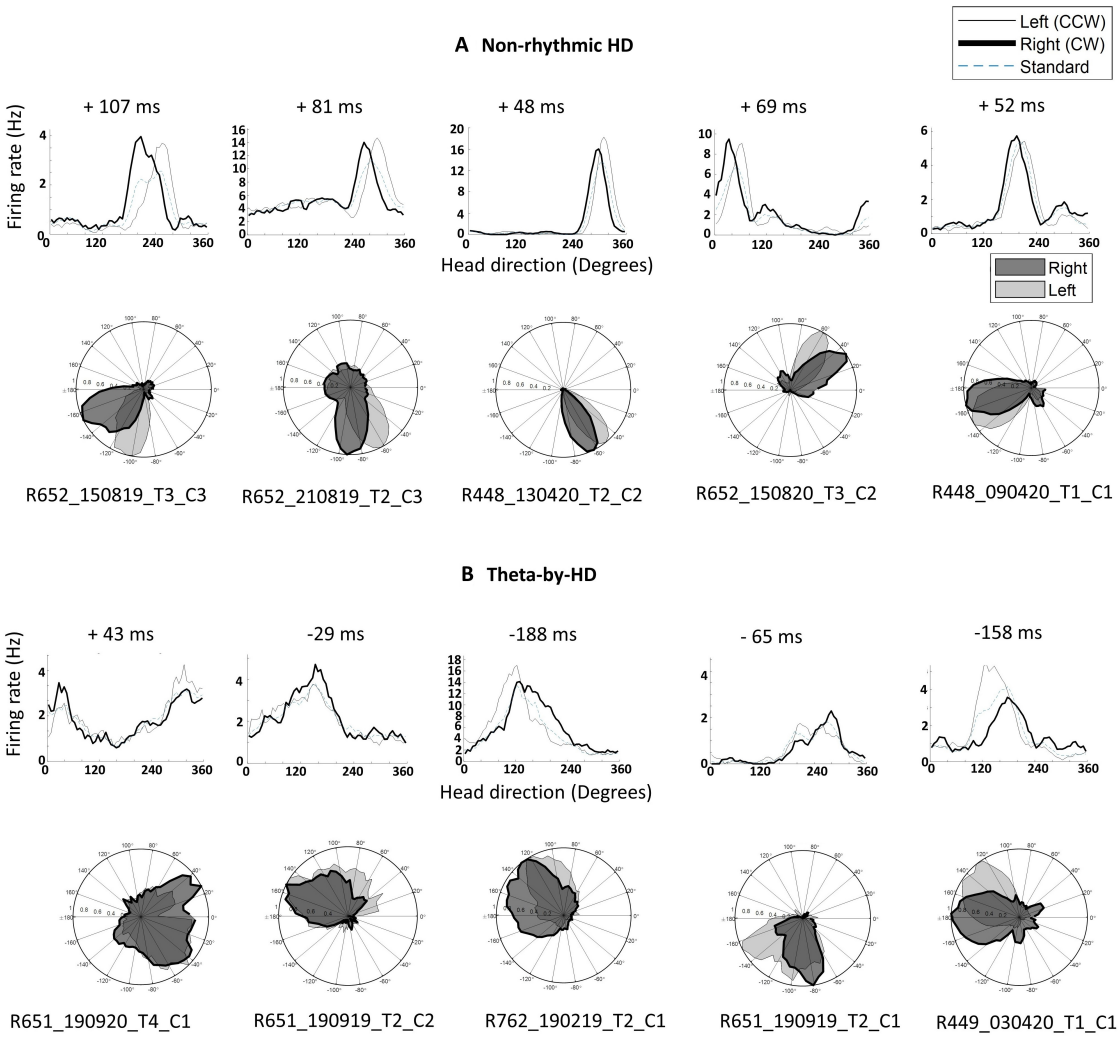


Figure 6.9: **Angular head velocity has a significant effect on the direction but not on the actual shape of the tuning curves.** Examples of tuning curve decomposition based on the AHV of each spike. **(A)** Non-rhythmic HD cells; **(B)** Theta-by-HD cells. Tuning curves of firing rate (Hz) vs HD (degrees) are shown at the top as smoothed histograms, and at the bottom as polar plots normalized to 1Hz. Clockwise (CW; black) and counterclockwise (CCW; gray) tuning curves were constructed using spikes with AHV>60°/s and <-60°/s, respectively. The standard tuning curve (blue dashed line in the firing rate histograms) incorporates all spikes, including those emitted when the head was not turning. Anticipatory time interval (ATI) of each cell is reported. Anticipatory firing is achieved by shifting the tuning curve in opposite directions during CW and CCW head turns. Theta-by-HD cell: decompoased tuning curves are broader and display a larger degree of overlap.

We considered 122 non-rhythmic HD and 128 Theta-by-HD cells based on having a CCW-CW correlation above 0.7. While non-rhythmic HD cells anticipated the heading direction by an average ATI of 41.7±2.56ms, Theta-by-HD cells lagged the heading direction by an average ATI of -17.3±6.64ms, and these were significantly different from each other (WRS test, z=7.048, p<0.0001). Thus, non-rhythmic HD cell firing preceded the firing of Theta-by-HD cells. Accordingly, the average CCW-CW difference angle was positive for non-rhythmic HD cells (9.71±1.32) but it was negative for Theta-by-HD cells (-9.54±1.54), and these were significantly different from each other (Kuiper two-sample test, k=9312, p= 0.001; Figure 6.9). Non-rhythmic HD cell values, but not Theta-by-HD cell values, differed significantly from zero (one-sample WSR test; HD, z=8.849, p<0.0001; Theta-by-HD, z=-1.819, p=0.069).

We then plotted measurements of ATI and difference angle in a frequency histogram (Figure 6.10 B). For both measures, Theta-by-HD cell distribution appeared more dispersed and centered around zero, with some cells lagging and others anticipating the actual heading direction, whereas non-rhythmic HD cell distribution appeared more skewed to the right and tightly clustered around its mean value (range of ATIs: non-rhythmic HD, -70, 130ms; Theta-by-HD, -280, 130ms). Theta-by-HD cells displayed greater ATI variability, being positive for 96% of non-rhythmic HD cells (107/112) but for only 56% of Theta-by-HD cells (59/128). As expected, there was a strong positive correlation between ATI and difference angle values (Pearson's r=0.63, p<0.0001; Figure 6.10 C). We concluded that, on average, non-rhythmic HD cells more consistently anticipated the animal's heading direction by the same positive amount.

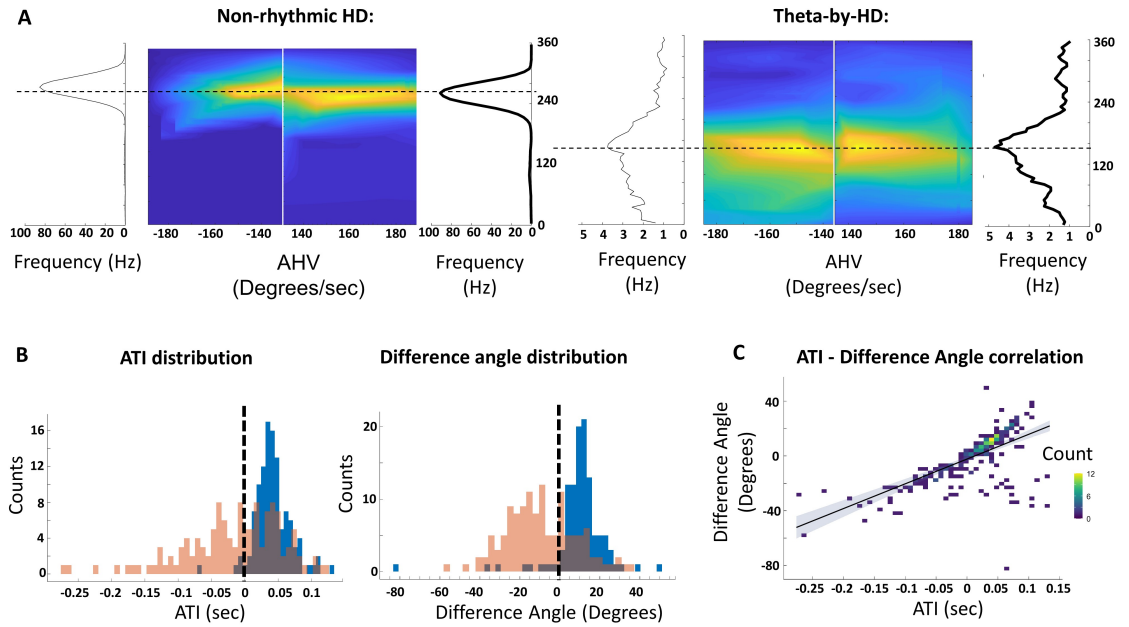


Figure 6.10: **Theta-by-HD cells are less anticipatory.** **(A)** Firing rate modulation by HD and AHV, for one non-rhythmic HD and one Theta-by-HD cell. Heat plots show HD (y-axis, degrees) vs AHV (x-axis, °/s)/. Heat colours denote the firing rate (yellow=peak rate). Horizontal dashed line is the preferred firing direction (PFD). Tuning curves collapsed across all velocities for clockwise (CW; thick line) and counterclockwise (CCW; thin line) turns are shown to each side. For non-rhythmic HD cell, the left-to-right gradient suggests anticipatory firing. Peak firing rate shifts linearly in positive directions during CCW head turns, and in the opposite direction during CW turns. For Theta-by-HD cell, the lower gradient suggests firing correlated with more present directions. Theta-by-HD cell maintain a larger range of peak firing across all velocities. **(B)** Frequency histograms of ATIs (s) and difference angles (degrees) for non-rhythmic HD (blue) and Theta-by-HD cells (red). For both measures, Theta-by-cells exhibit greater variability. **(C)** Positive correlation between ATI (s) and difference angle (degrees). Markers represent cells, heat colours denote marker density. Linear regression fit line, with 95% CI, is displayed.

6.3.5.2 Optimal time-shift method

The wider spread of ATIs across the Theta-by-HD cell population is consistent with the wider range of directions across which individual Theta-by-HD cells fire. It could be argued that cross-correlations of decomposed tuning functions cannot provide a robust ATI estimate for cells with tuning curves that are not perfectly symmetric, such as those that have a higher dispersion and multiple peaks, as those seen for Theta-by-HD cells here. For this reason, we then used the optimal time-shift method to derive ATI values, as this method relies on the standard tuning function alone.

However, this analysis produced ATI values that closely matched those estimated from the cross-correlation of decomposed tuning functions reported above (Figure 6.11). Mean optimal time-shifts for non-rhythmic HD cells were as follows: width, 40.33±5.70ms; peak rate, 35.40±3.40ms. Mean optimal time-shifts for Theta-by-HD cells were as follows: width, -10.51±6.42ms; peak rate, -7.6±7.10ms. As we have demonstrated with the previous method, on average optimal shifts for non-rhythmic HD cells were longer and more positive than Theta-by-HD cell values (WRS tests; peak rate, z=4.616; width, z=5.746, all $p<0.0001$). The majority of non-rhythmic HD cells had positive optimal shifts (87% for peak rate, 79% for width), whereas values for Theta-by-HD cells exhibited a greater variability and were overall more clustered around zero (40% for peak rate, 43% for width).

Based on these results, it is possible that the highly different ATI values for Theta-by-HD cells indicate variation in the balance of HD cell inputs received by individual Theta-by-HD cells in AV (from collateral projections from HD cells within AV or from descending corticothalamic projections). This may vary with location within AV, with some cells receiving stronger (or more direct) input from HD networks. Potentially Theta-by-HD cells in AVVL could receive more input from HD cells within AV, as compared to those in AVDM, based on differences in cell distribution. Nevertheless, the correlation between implant location and average ATI values did not reach significance (Pearson's r=-0.013, $p=0.87$), and there was no difference in the proportion of Theta-by-HD cells with a negative ATI between the two subfields, AVDM and AVVL (Chi-square test for differences in proportion; $\chi^2=0.239$, $p=0.625$). However, the depth of the cell within AV may be a contributing factor.

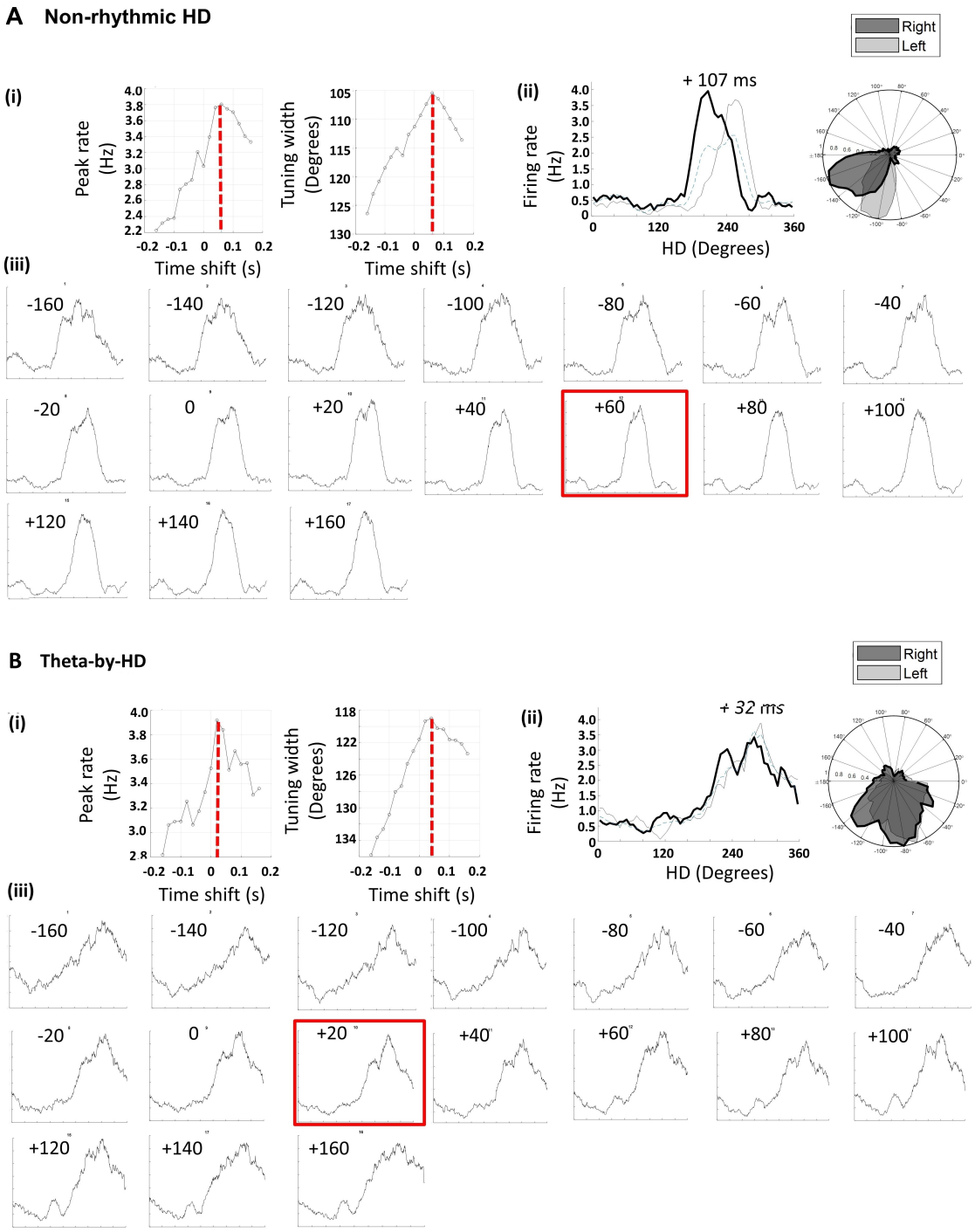


Figure 6.11: **Illustration of the optimal time shift method.** **(A)** shows a non-rhythmic head direction (HD) cell and **(B)** a Theta-by-HD cell. For each cell, the following plots are shown. **(i)** Optimal shift functions for peak rate and tuning width. Left: peak rate (Hz) vs time shift (s); Right: tuning width (degrees) vs time shift (s). The red line denotes the optimal time shift for each of the two parameters. For the non-rhythmic HD cell, optimal shift was 60ms for both peak rate and width. For the Theta-by-HD cell (B), optimal shift was 20ms for peak rate and 40ms for width. Width is plotted on a

reversed y-axis. **(ii)** Standard and decomposed tuning curves showing firing rate (Hz) vs HD (degrees). Curves are displayed as smoothed histograms and as polar plots normalized to 1Hz. The cell's ATI is reported at the top. See caption of Figure 6.9 for more details. **(iii)** Set of time-shifted tuning curves in 20ms steps, between±160ms. x-axis, HD (degrees); y-axis, firing rate (Hz). Numbers are the amount of time shift in ms. The tuning curve at 0ms represents spikes paired with current HD. Non-rhythmic HD cells: pairing spikes with directions 60ms into the future produced the maximal peak rate and minimal tuning width (highlighted in red). Theta-by-HD cells: peak rate was optimized by a 20ms shift (in red) and width by a 40ms shift.

6.3.5.3 Tuning curve shape is not affected by the animal's turning behaviour

While previous recordings from AD, LMN and PoS showed that HD cells with longer ATI values also have broader directional firing ranges (Stackman and Taube, 1998; Taube and Muller, 1998; Blair and Sharp, 1995), in AV we found only a weak negative correlation between a cell's tuning width and its ATI (Spearman's's r=-0.16, p=0.01), and no correlation between a cell's peak firing rate and its ATI (r=0.12, all p=0.049). If broadening of the tuning curve occurs because the CW-CCW angular separation is large, then this should disappear when the tuning curve is decomposed into CW and CCW (Figure 6.9). To address this prediction, we compared tuning parameters between standard and decomposed tuning functions by means of two-way ANOVAs, and showed that tuning width and peak rate did not change with AHV (Table 6.3). Cell type (F(1,1)=431.693, p<0.0001), but not turning direction (F(1,1)=0.346, p=0.708) nor their interaction (F(1,2)=0.153, p=0.858) had a significant effect on tuning width. Similarly, cell type (two-way ANOVA, F(1,1)=177.175, p<0.0001), but not turning direction (F(1,2)=0.251, p=0.778) nor their interaction (F(1,2)=0.077, p=0.926) had a significant effect on peak rate. The conclusion was that broader tuning of Theta-by-HD cells was not an artefactual consequence of larger CW-CCW angular separation (Blair and Sharp, 1995).

The above results show a lack of peak rate differences when the head was turning CW or CCW. All cells (non-rhythmic HD, n=112; Theta-by-HD, n=128) increased firing rates by the same amount during CW and CCW turns compared to standard (no turning bias). A total of 52 (46%) non-rhythmic HD cells and 61 (48%) Theta-by-HD cells fired more during CCW than CW head turns, with peak rates 17.57% and 18.24% higher than standard, respectively. In the same way, 60 (54%) non-rhythmic HD and 67 (52%) Theta-by-HD cells fired more during CW than CCW turns, with peak rates 14.98% and 20.25% higher than standard, respectively. This

matches results of the AHV analysis below, showing that firing rate modulation by AHV is bidirectional (both CW and CCW) and symmetric (with no difference between turning condition), with prevalence of positive responses (Section 6.4.2). Although a marginal subset of negative firing rate responses to AHV were reported, in all cases decomposed turning functions were higher than standard (which includes spikes emitted also at low velocities between -60 and 60°/sec). This discrepancy is likely due to the specific AHV threshold used here to classify CW and CCW spikes.

Table 6.3: **Analysis of tuning curve shape for right and left turns, and standard.**

Directional tuning curve properties during AHV			
	CCW	CW	Standard
Tuning width (degrees)			
Non-rhythmic HD	93.29 ±3.03	95.10 ±2.99	92.08 ±3.08
Theta-by-HD	131.53 ±1.32	131.5 ±1.23	130.81 ±1.29
Peak rate (Hz)			
Non-rhythmic HD	28.22 ±3.05	28.57 ±3.15	26.49 ±2.91
Theta-by-HD	5.81 ±0.38	5.96 ±0.40	5.34 ±0.35

6.3.6 Are Theta-by-HD cells more directionally unstable?

The following analysis will show that the reduced directional tuning of Theta-by-HD cells resulted from greater PFD shifting over time rather than an actual increase in directional firing range.

6.3.6.1 Linear drift analysis

To quantify PFD shifting for each cell in a trial, we applied a circular-linear regression model to the HD vs time scattergram. We used the slope of the regression line as a measure of linear drift rate. This analysis revealed that the PFD was relatively stable for both non-rhythmic HD (n=119) and Theta-by-HD cells (n=127), and drift rates were clustered around the same mean of zero (V-tests, all p<0.0001). This was confirmed by comparing proportions of drifting cells in the two groups, defined as cells with a significant p-value of the circular-linear correlation coefficient (HD=41/119, 34.44%

vs Theta-by-HD=46/127, 36.22%; χ^2=0.084, p=0.772). Similarly, comparing the circular-linear correlation coefficients (rho values) and drift rate (slope) revealed a non-significant difference (WRS test, rho, z=0.663, p=0.507; slope, z=0.794, p=0.427). PFD shifts over time did not show any trend for a specific direction. The same number of cells exhibited CW (positive slope of the drift rate) or CCW (negative slope) drift for both non-rhythmic HD (59 vs 60, χ^2=0.0167) and Theta-by-HD cells (58 vs 69, χ^2=1.905; all p>0.01).

Despite the weak association between spike time and HD for both groups, indicating overall slow drift rates, plotting the distribution of drift rates revealed a greater amount of variability for Theta-by-HD cells (Figure 6.12 A). Theta-by-HD cells had lower concentration parameter than non-rhythmic HD cells (k-test, f=4.20, p<0.0001). Eight Theta-by-HD cells drifted>8°/min, and drifts ranged from -17.3 to 13.32°/min, compared with only one non-rhythmic HD, whose drift values ranged from -13.89 to 7.88°/min. These proportions were statistically different from each other (χ^2= 5.194, p=0.023). Given that drift rates of Theta-by-HD cells were more spread out in both positive and negative directions, we then considered their absolute values, 0.88±0.15°/min for non-rhythmic HD and 2.52±0.26°/min for Theta-by-HD cells. Values were different from zero (one-sample WSR test; HD, z=9.4670; Theta-by-HD, z=9.7787, all p<0.0001) and differed significantly from each other (two-sample WRS test, z=-7.62, p<0.001). However, tuning curves constructed for the first 2 minutes of the recording trial (Figure 6.12 B) continued to be broader for Theta-by-HD compared to non-rhythmic HD cells, despite the short interval considered (average tuning width: non-rhythmic HD, 97.43°±2.80; Theta-by-HD, 133.09°±1.33; two-sample WRS test, z=-9.561,p<0.0001), consistent with the small slopes of the drift rate (Figure 6.12 C).

We concluded that a higher number of Theta-by-HD cells drifted at a faster rate compared to non-rhythmic HD cells, although this effect was only subtle in the light. We additionally hypothesized that more rapid, non-linear PFD fluctuations may have occurred at a shorter timescale than the linear drift rate for the whole trial. In favour of this hypothesis, visually first- and last-2 minute tuning curves for Theta-by-HD cells appeared somewhat less smooth, with multiple peaks, compared to non-rhythmic HD (Figure 6.12 B). However, non-linear PFD fluctuations would not be captured by the circular-linear regression approach above, given that a drift occurring at a constant rate but in different directions during a trial would result in a small overall slope of the drift rate for the trial. See next.

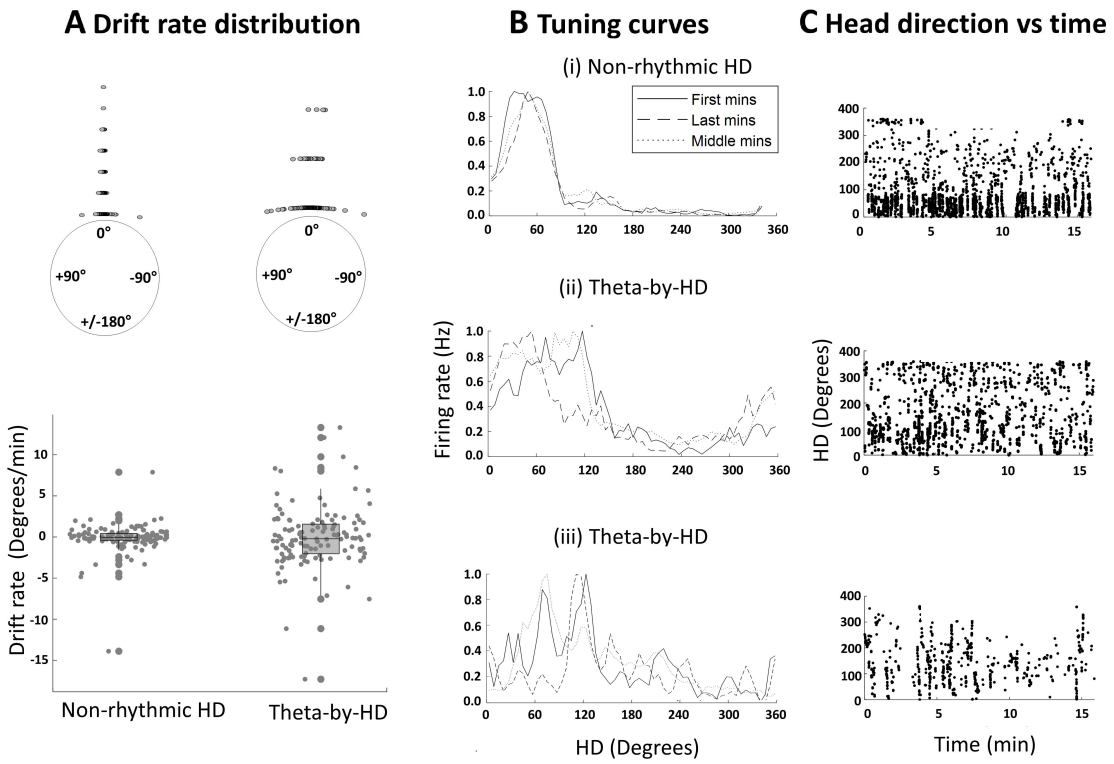


Figure 6.12: **Cells are relatively stable but a higher number of Theta-by-HD cells have fast drift rates compared to non-rhythmic HD cells**. **(A)** distribution of intra-trial drift rates in degrees/minute for the non-rhythmic HD and Theta-by-HD cell sample, presented as raw data in polar plots (top) and raw data + boxplot (bottom). Each marker is the average drift rate for a cell. Larger markers are outliers. Both cell groups have a population mean around 0. However, compared to Theta-by-HD cells, there were relatively fewer non-rhythmic HD cells with values higher or lower than the population mean. Examining the variability of the two distributions revealed a higher number of Theta-by-HD cells with fast drift rates, in both directions. **(B)** Peak-normalized tuning curves for the first and last 2 minutes of a 16-min recording trial. x-axis, HD (degrees); y-axis, rate (Hz). **(C)** Head direction vs time scatterplots for the cells in B. x-axis, time (min); y-axis, HD (degrees). Slope values were taken as a measure of rate and direction of drift for a trial. Absolute rate values were used for statistical analysis.

6.3.6.2 Non-linear shifts analysis

To probe this effect, we quantified the amount of variability in the firing direction of a cell when it fired >50% of its peak firing rate for the trial. We took all spikes emitted at these times, plus spikes emitted before and after it up to an angular distance of +/-50°, defining a full sweep of the head through the cell's PFD (Figure 6.13).

For each full-sweep event, we computed the KDE of the HD data, and derived the absolute direction and width at half-height of the KDE peaks. We considered 114 HD and 140 Theta-by-HD cells.

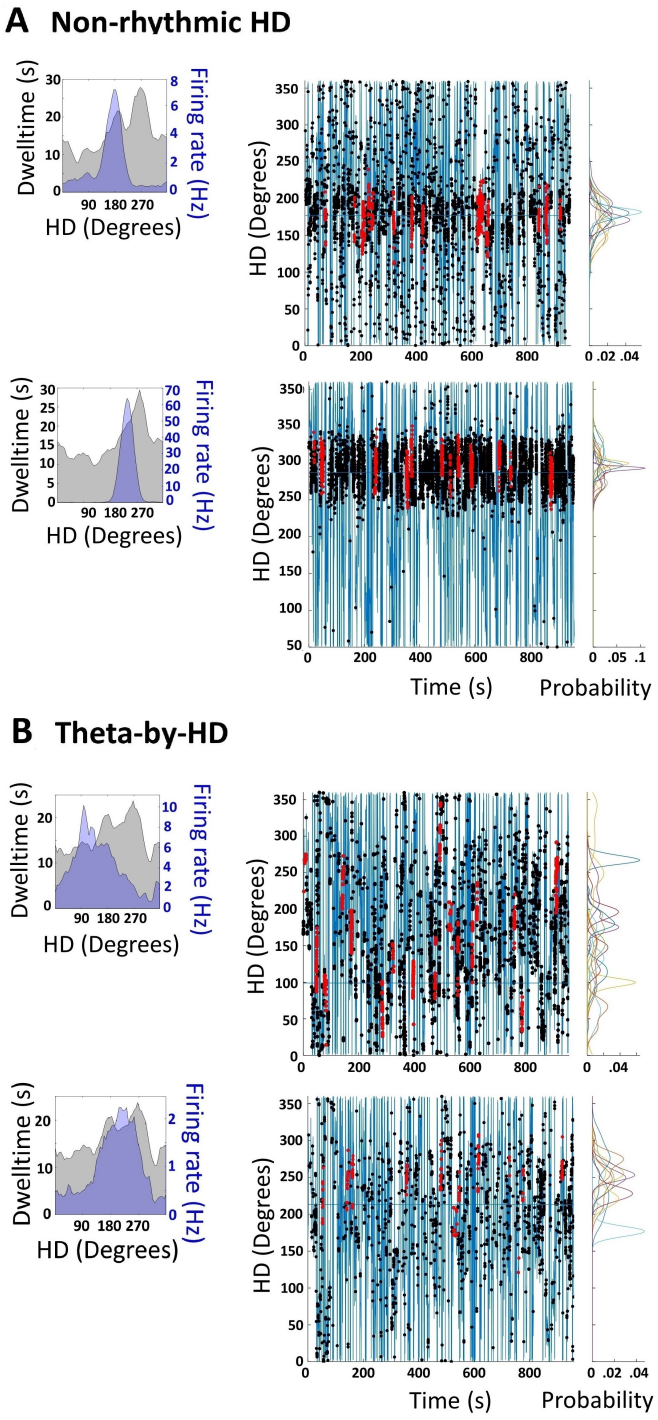


Figure 6.13: **Theta-by-HD cell tuning curves shifted more but were not inherently broader.** Examples of non-linear drift analysis for **(A)** two non-rhythmic HD cells

and **(B)** two Theta-by-HD cells. For each cell, the following plots are shown. Left, histogram of firing rate (blue; Hz) and dwelltime (gray; s) as a function of head direction (degrees). Center, spatial plots generated by plotting the un-smoothed directional heading of the rat (degree) as a function of time (s), and overlaid at the appropriate times and directions with the spikes (black markers). Red markers are spikes emitted when the cell fired >50% of its peak firing rate, plus spikes within +/-50° angular distance. Right, kernel density estimate plots (KDEs) of the HD data. Horizontal axis, probability; vertical axis, HD (degrees). Theta-by-HD cell spike trains occurred over a narrow range of directions but these directions were more variable in both positive and negative directions.

This analysis revealed a significantly larger variability in the absolute direction of the KDE peaks for Theta-by-HD compared to non-rhythmic HD cells (SEM of peak location: non-rhythmic HD, 13.66±0.60; Theta-by-HD, 16.59±0.67; two-sample T-test, t (244)=-3.161, sd=7.212, p=0.0018). KDE peaks for Theta-by-HD and non-rhythmic HD cell had an equivalent mean width, suggesting that directional firing range of the two groups was actually the same (mean width at half-height: non-rhythmic HD, 33.9±0.75; Theta-by-HD, 35.59±0.68; t(252)=-1.673, sd=8.016, p=0.096). SEM of peak width was also the same between the two groups (non-rhythmic HD, 4.52±0.22; Theta-by-HD, 5.22±0.28; t(244)=-1.916, sd=2.865, p=0.057).

Results corroborate our hypothesis that PFD shifted more for Theta-by-HD cells than non-rhythmic HD cells in light over time, which could have led to a broader tuning curve when collapsed across the whole trial (Figure 6.13). Note that Theta-by-HD cells could fire low-frequency ("noise") spikes at all directions — reflected in a higher background rate of the tuning curve.

6.3.7 Do cells represent information about head movements?

In addition to spatial influences, we now investigate whether firing rates are under multiple influences from other behavioural variables, and whether there are differences in the way different cell groups encode information about linear and angular head movements.

6.3.7.1 Linear and angular speed modulate cell firing rates

The majority of our spatial cells (n=269/341; 78.89%) met the criterion for linear speed tuning (Góis and Tort, 2018). Speed tuning was more prominent than AHV activation

(n=44/341; 12.90%). Equal proportions of speed-tuned units were observed in each cell group (Chi-squared tests; all p>0.1; Figure 6.15 C). Proportions were as follows: non-rhythmic HD, 98/122 (80%); Theta-by-HD, 121/158 (77%); place cell, 50/61 (82%). The strength of speed tuning was the same for all groups. Average absolute speed scores (s-scores) were as follows: non-rhythmic HD, 0.56±0.02; Theta-by-HD, 0.52±0.02; place cell, 0.55±0.03. All groups were significantly different from zero (one-sample WSR test; HD, z=9.585; Theta-by-HD, z=10.903; place cell, z=6.791, all p<0.0001) and did not differ between each other (KW test; H(2)=1.771, p=0.412). There was no correlation between linear speed modulation and theta-modulation strength of each cell, measured by the Index of Coupling (Spearman's r=-0.13, p=0.02).

Equal proportions of AHV-tuned units were observed in each group (Chi-squared tests; all p>0.1; Figure 6.15 C). Proportions were as follows: non-rhythmic HD, 11/122 (9%); Theta-by-HD, 24/158 (15%); place cell, 9/61 (15%). Average absolute AHV-scores were as follows: non-rhythmic HD, 0.22±0.01; Theta-by-HD, 0.24±0.01; place cell, 0.25±0.02. Although means were small, values were unlikely to have arisen from a population with an expected median of zero (one-sample WSR test; HD, z=9.5851; Theta-by-HD, z=10.9029; place cell, z=6.791, all p<0.0001) and did not differ from each other (KW test; H(2)=2.311, p=0.315), suggesting weak, yet significant, AHV activation. Most angular-tuned neurons were simultaneously sensitive to linear speed (n=39/44 of the AHV-tuned neurons; 88.64%; Figure 6.15 C). Proportions were as follows: non-rhythmic HD, 10/11 (90.91%); Theta-by-HD, 21/24 (87.50%); place cell, 8/9 (88.89%). For conjunctive cells, we always found the same direction of speed and AHV activation. That is, firing rates increased (n=30/39) or decreased (n=9/39) linearly as the animal ran faster, and also its head turned faster in both turning directions. Examples of how firing rates changed during linear and angular head movements for three conjunctive neurons are illustrated in Figure 6.14.

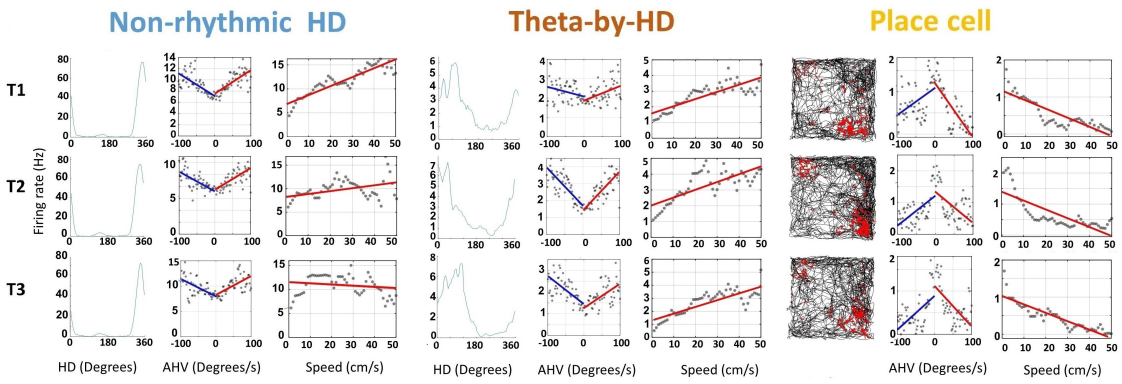


Figure 6.14: **Spatial cells modulated by linear and angular head movements.** Examples of non-rhythmic HD, Theta-by-HD and place cell showing conjunctive modulation by running speed and AHV. Each cell shown across three trials. For each cell, from left to right: tuning curve of firing rate (Hz) vs HD (degrees) or spikemap; scatterplot of instantaneous firing rate (Hz) vs AHV in 2°/s bins; scatterplot of instantaneous firing rate vs running speed in 2cm/s bins. Linear regression lines fitted to derive the slope and the y-intercept of the rate-AHV (CW, red; CCW, blue) and rate-running speed relationships.

6.3.7.2 Angular speed modulation is symmetric and does not depend on the turning direction

We then asked whether AHV-tuned units showed a differential response as the animal turned its head in different directions. To do this, we derived separate AHV-scores for CW and CCW movements. Almost all the AHV-tuned cells (n=42/44; 95.45%) exhibited a symmetric activation, with firing rates either increasing or decreasing in both turning directions with AHV. Asymmetric responses to AHV were also observed, although only in a marginal sub-population of two cells (one non-rhythmic HD and one place cell). A paired-sample WSR test comparing absolute CW and CCW AHV-scores for each cell found no effect of head-turning direction (z=2.057, p=0.04). Overall, there was no strong turning direction bias, both at the single cell level and at the population level.

Among the HD dataset, we further investigated the turning bias by plotting decomposed tuning curves and computing differences between their peak rates (Stackman and Taube, 1998). CCW-CW differences>0Hz indicated a CCW tuning curve higher than the CW one, differences<0Hz indicated a higher CW tuning curve, while differences=0Hz indicate no turning direction bias (Figure 6.15 B). Only directional neurons with CW-CCW correlation>0.7 were considered for this analysis (HD cells, n=112, Theta-by-HD cells, n=128). We found an equal number of cells with positive and negative differences: 52 (46%) non-rhythmic HD cells and 61 (48%) Theta-by-HD cells had a CCW (left) turning bias; 60 (54%) non-rhythmic HD and 67 (52%) Theta-by-HD cells had a CW (right) bias. This was not due to differences between brain hemispheres, given that five of the six animals were implanted in the left hemisphere. Peak rate differences for these neurons were plotted in a frequency distribution (Figure 6.15 B). The average difference for non-rhythmic HD and Theta-by-HD cells in the right and left sides of the histogram were as follows: right, 1.93 and 0.91Hz; left, 1.39 and 0.71Hz. Neither differences were significantly different

from zero (one-sample WSR test; non-rhythmic HD, z=-0.9232; Theta-by-HD , z=-0.956; all p>0.1), suggesting no tendency for peak rates during CW turns to be any different from CCW turns. Data is consistent with the ATI analysis above, in which tuning curves shifted but retained the same shape (height and width) as the head was turning CW, CCW or it was still (Section 6.3.5.3).

Firing rate correlations with running speed were positive for most non-rhythmic HD (79/98; 80.61%) and Theta-by-HD cells (91/121; 75.21%) cells, while only a minority (19.39% and 24.79%) had negative correlations. In contrast, equal proportions of place cells had positive and negative firing rate correlations with speed (24/50, 48.00% vs 26/50, 52.00%). See histogram of s-scores in Figure 6.15 A. Correlations with AHV were also positive for all non-rhythmic HD cells (10/10, 100%) and for most Theta-by-HD cells (18/24, 75.00%), while there were equal numbers of place cells (4/8, 50.00%) firing at lower or higher rates with faster AHV. For negatively-tuned place cells, firing rapidly declined as soon as the head started to move (see example of Figure 6.14). These place cells might code for position during immobility. In agreement, average firing rate at the lowest running speed (y-intercept) was 1.08±0.1Hz for place cells, implying that some significant locational signalling was present when the animal stopped.

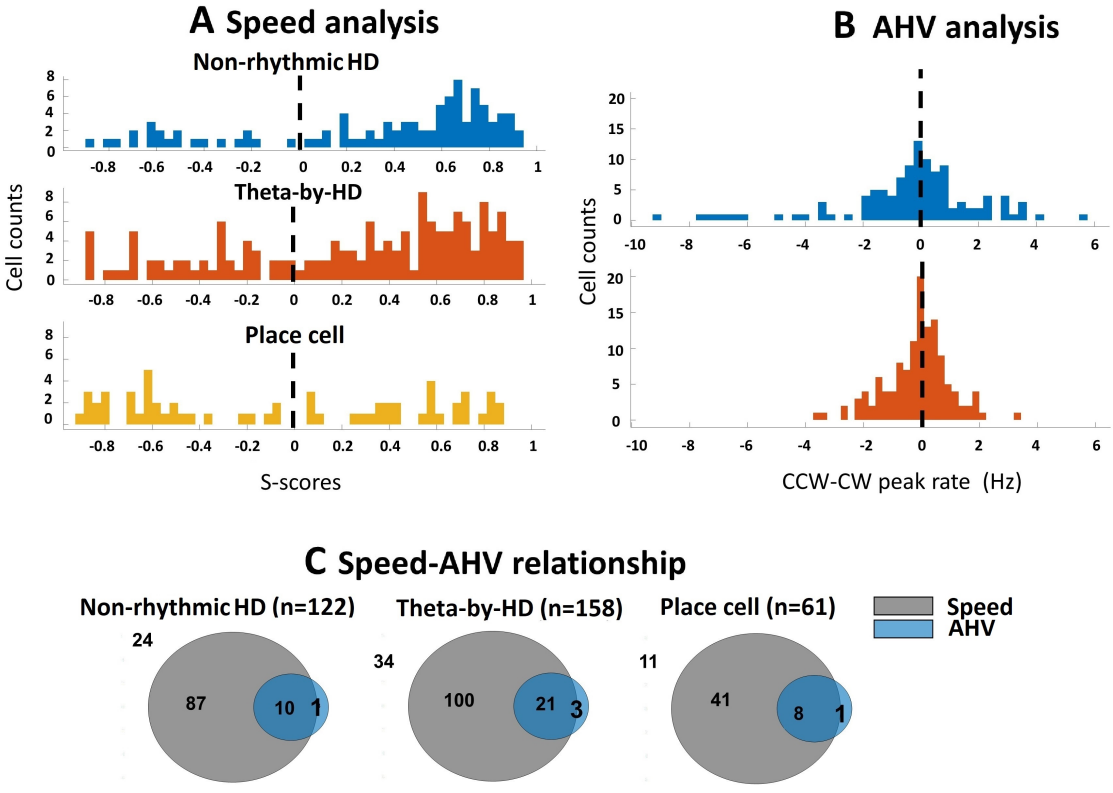


Figure 6.15: **Analysis of motor correlates and dependency on turning direction.** **(A)** Frequency distribution of speed-scores (s-scores). Non-rhythmic HD and Theta-by-HD distributions are skewed to the right, whereas place cells show equal proportions of positive and negative correlations. **(B)** Frequency distribution of differences between CCW-CW peak rate (Hz) for non-rhythmic HD and Theta-by-HD cells. Both are centered around a difference of 0Hz, with no difference between left and right sides, indicating no preference at the population level for either turning direction. Note however, that twelve HD cells (10.71%) have absolute CCW-CW differences>4Hz. For these cells, firing rates depend more heavily on the turning direction. **(C)** Summary of neurons with spatial, linear speed and angular head velocity (AHV) correlates. Cell numbers are in black. Most spatial neurons are tuned to speed, a minority is tuned to AHV. AHV activation often occurs in conjunction with speed.

6.4 Discussion

In this Chapter, we have explored the spatial and motor correlates of the cell types identified in AV, namely non-rhythmic HD, Theta-by-HD and place cells. Each of these groups had distinct locational and directional properties. Place cells showed strong locational signaling but carried virtually no amount of directional information to their firing. None of the non-rhythmic HD cells showed any substantial preference for locational signaling but carried high directional information. Theta-by-HD cells showed both directional and locational signaling, albeit this was generally weak — cells formed broader directional and locational fields compared to non-rhythmic HD and place cells, respectively. Additionally, we have found strong modulation of firing rates by linear speed (≈79%), and a weaker, yet significant, modulation by AHV (≈13%) for all cell groups, with no difference in modulation strength between groups. However, while for most of the directional neurons the relationship between rate and self-motion was positive, place cells displayed equal proportions of positive and negative responses. For all cells, the code for AHV was symmetric and bidirectional, meaning that responses were the same during CW and CCW head turns, with no apparent preference for either turning direction.

6.4.1 Theta-by-HD cells have broader directional correlates due to intra-trial directional instability

Comparing directional tuning profiles of the two types of directional neurons, Theta-by-HD and non-rhythmic HD, we have revealed clear differences in directional

properties. Theta-by-HD cells carried considerably less directional information and showed reduced directional tuning compared to non-rhythmic HD cells, which were much more finely-tuned and resembled cells typically seen along the main HD circuit (Taube et al., 1990a). We characterized this lower directional specificity of Theta-by-HD cells and identified its source, which was a greater shift in their PFDs over time.

To provide an estimate of how much directions shifted in a trial, we first computed the linear drift rate (°/seconds) as the slope of the HD vs time relationship for a cell. The drift magnitude was evaluated by the significance of this relationship. Findings indicated that drifting was relatively slow for both non-rhythmic HD and Theta-by-HD cells, the same proportion of cells in the two groups showed a significant rate of drift and tuning curves of Theta-by-HD cells were broader since the start of the trial (when drifting was small). However, Theta-by-HD cells exhibited higher variability of linear drift rates, in that faster rates occurred more frequently compared to non-rhythmic HD cells. In agreement, Theta-by-HD cells also displayed a higher amount of variability in their PFDs, which could have led to a broader tuning curve when collapsed across the trial. Whether Theta-by-HD cell instability was due to poor landmark control or impaired spatial updating mechanisms when integrating idiothetic information will be further investigated in the next Chapter by recording cells in the absence of visual input.

The tuning curve shape may additionally be influenced by the time interval by which cells anticipated the animals heading direction. Anticipatory firing is accomplished by the integration of the current heading direction and information about the velocity at which the head is turning (Blair et al., 1997; Taube and Muller, 1998), such that HD cells closer to vestibular inputs (i.e., LMN) tend to display greater firing anticipation and broader tuning curves (Blair and Sharp, 1995; Blair et al., 1997; Taube and Muller, 1998) compared to cortical regions receiving converging vestibular and visual inputs (Stackman and Taube, 1998; Sharp et al., 2001). We hypothesized that, if broader tuning curves resulted from shifting of the tuning curve when the head was turning in opposite directions, then Theta-by-HD cells should show more anticipatory ATIs and a greater angular separation between CW and CCW tuning curves (Stackman and Taube, 1998). Contrary to our prediction, on average non-rhythmic HD cells were much more anticipatory than Theta-by-HD cells, whose firing was only slightly lagging the heading direction, and much more centred around a mean of zero. Tuning curves retained the same width and height regardless of whether the head was turning or it was still, implying that broader tuning curves for Theta-by-HD cells were not a byproduct of greater anticipatory firing.

It did not appear that all Theta-by-HD cells displayed the same interval i.e., Theta-by-HD cells could either anticipate or lag the heading direction by a small amount. We have discussed how this variability could be due to a variation in the strength of inputs received by Theta-by-HD from non-rhythmic HD cells. This is also consistent with a weaker or more indirect influence of heading direction on Theta-by-HD cell firing. These cells may inherit directionality from non-rhythmic HD cells within AV via synaptic inputs (i.e., from collateral of thalamocortical projections), although direct cellcell transfer via gap-junctions could also occur. We briefly note here that another explanation for the wider range of ATIs for Theta-by-HD cells could be the greater amount of intra-trial directional instability, since this would mean that cells cannot maintain a fixed temporal relationship between spike times and the animal's heading direction during a trial, thus introducing a degree of errors in ATI calculations. Having established the temporal relationship between non-rhythmic HD and Theta-by-HD cell spike discharge, subsequent discussion should be centered on evaluating their functional relationship to explain how these cells may arise and how AV mediates vestibular signals. We will return to this point in the General Discussion (Section 8.2).

6.4.2 Spatial cells are conjunctively modulated by linear and angular head movements

The majority of AV cells displayed strong running speed correlates, similar to putative HD and place cells recorded from other brain regions (Lozano et al., 2017; Cho and Sharp, 2001; Stackman and Taube, 1998; McNaughton et al., 1983; O'Keefe et al., 1998). Only a minority additionally represented the velocity, but not the direction, of angular head movements, given that AHV responses were bidirectional and identical for both directions.

Several previous studies have shown that linear speed is widely encoded by hippocampal/parahippocampal neurons in conjunction with HD and/or locational information or as a pure self-motion code (McNaughton et al., 1983; Góis and Tort, 2018; Hinman et al., 2016; Kropff et al., 2015; Sargolini et al., 2006). Differently from linear speed, AHV information does not seem to be represented by neurons in the hippocampus of rats, despite the presence of neurons coding rotational and translational whole-body motion in macaque monkeys (O'Mara et al., 1994). Coding of AHV has been typically seen along the HD circuit in conjunction with HD or as a pure self-motion code i.e., DTN (Bassett and Taube, 2001; Sharp et al., 2001), LMN:

(Stackman and Taube, 1998); AD: (Blair and Sharp, 1995; Taube et al., 1990a; Taube, 1995; Stackman and Taube, 1997), PoS (Stackman and Taube, 1998; Taube and Muller, 1998; Lozano et al., 2017), RSC (Chen et al., 1994a; Lozano et al., 2017). Here, we provide evidence that AHV is not restricted to HD cells, but can also be expressed by place cells with no obvious directional correlates, in a region outside of the main HD circuit. This AHV sensitivity constitutes an additional argument against place cells being axon recordings. Preliminary evidence consistent with this finding comes from recordings of conjunctive HD-by-grid cells modulated by a combination of running speed and AHV in MEC/PaS (Spalla et al., 2021). Unlike in our recordings, about 50% of these AHV-tuned neurons were turn-specific, since responses were observed for only one turning direction, either CW or CCW, suggesting that AV provides a code for movement velocity only, which may become integrated with information about movement direction in higher parahippocampal areas.

Interestingly, we found evidence for a decoupling between speed- and theta-modulation at the single cell level, despite strong positive correlation between speed and theta in the LFP (see LFP analysis, Section 5.4.2). Speed-modulation was not restricted to the theta-modulated neurons, given that strong linear responses to speed were also seen among classic HD cells that fired non-coherently with LFP theta. There was no apparent relationship between the strength of speed- and theta-modulation at the single cell level. Notably, a sizable proportion of place cells actually exhibited strong negative responses to speed despite being theta-modulated in both a phase-locked and a phase-precessing manner. These observations suggest that speed-related activation of AV neurons is not directly associated to the LFP theta, arguing for a genuine rate code for speed, rather than an oscillatory code. Rate coding for speed makes use of an increase in the number of spikes per unit of time (i.e., per theta cycle) during higher running speed, resulting in higher firing rates regardless of the LFP theta frequency (Hinman et al., 2016). Oscillatory coding makes use of increased LFP theta frequency during higher running speed, which leads to higher firing rates and intrinsic oscillatory frequency for cells that fire locked to this frequency, despite keeping a constant number of spikes per theta cycle (Zhou et al., 1999; Hinman et al., 2016; Góis and Tort, 2018). Both coding types have been observed among entorhinal-hippocampal speed cells with no spatial correlates. However, we need to conduct further autocorrelation analysis to establish whether AV cells could carry an additional speed signal in the frequency of their spiking rhythmicity i.e., autocorrelogram frequency becomes faster at higher running speeds.

6.4.3 Summary

The analysis of this Chapter revealed key differences in the quality of the two directional signals that co-exists in AV — a broader one operating at theta frequency and carrying less direction-specific information locked to theta troughs (Theta-by-HD cells), and a more narrow and precise one operating independently of theta and carrying considerably higher directional content. Although occasionally Theta-by-HD cells yielded clear and reproducible locational firing, in general locational information was much lower than in place cells, and directional information was much lower than in non-rhythmic HD cells. Having established a functional relationship between spatial coding and the LFP theta, in the next Chapter we will examine stability of these spatial representations across trials and in darkness.

6.4.4 Limitations

In the analysis of motor correlates presented in the last Section of the Results, we found that almost all angular tuned neurons were simultaneously sensitive to linear speed (n=39/42), with the same direction of linear and angular activation. Although this result may point to an additive relationship between motor correlates, we cannot eliminate the possibility of behavioural couplings since high-speed translational and angular movements tend to co-occur during locomotion. To resolve this issue, we will need to apply the *pxd* correction approach to decouple the combined effects of linear and angular motion on cell firing rates, as well as the more complex relationship that may arise between motor and spatial influences i.e., for a cell with positive responses to linear speed, if the animal happened to accelerate as it was traveling in a specific direction, then the cell could develop an apparent preference for that direction.

7

Stability of anteroventral thalamic representation across trials and in darkness

7.1 Background and rationale

The rationale for Experiment 3 was to test the stability of AV spatial representations.

Spatial properties of HD and place cells are determined by a complex interaction between external and idiothetic information. Cells encode space primarily by integrating idiothetic vestibular and self-motion cues Stackman et al., 2002, 2003 , a process known as path integration, while external information (i.e., visual) is not necessary, given that cells maintain constant receptive fields after removal of visual landmarks (Taube et al., 1990b; Goodridge and Taube, 1995), in darkness after exposure to the environment in the light (Mizumori and Williams, 1993; Jeffery et al., 1997; Zhang et al., 2014), during blindfolding (Goodridge et al., 1998; Save et al., 1998; Hill and Best, 1981) and in novel environments (O'Keefe and Conway, 1978; Taube and Burton, 1995). However, path integration provides a less stable substrate for encoding spatial information, given that firing fields are more unstable when visual information is not available (Goodridge et al., 1998; Mizumori and Williams, 1993; Taube et al., 1990b; Goodridge and Taube, 1995; Save et al., 2000; Etienne and Jeffery, 2004).

Ensemble HD cell activity remains coherent during ongoing drift in the absence of visual landmark stabilization, and during landmark rotations that cause similar shifts of HD cell firing fields (Taube et al., 1990b; Taube and Burton, 1995; Peyrache et al., 2015; Yoganarasimha et al., 2006; Peyrache et al., 2015; Knierim et al., 1998; Hargreaves et al., 2007; Goodridge et al., 1998; Zugaro et al., 2001). Internal coherence between PFDs demonstrate the underlying HD network connectivity — continuous attractor network (Skaggs et al., 1995; Zhang, 1996). Interestingly however, there have been reports of HD cells in dRSC (Jacob et al., 2017), PaS/ MEC (Kornienko et al., 2018) and POR (LaChance and Taube, 2022) that react incoherently to visual landmark manipulations, suggesting that attractor dynamics may not be required for HD cells outside of the main HD generative circuit (DTN-LMN-AD-RSC/PoS based on the presence of "pure" HD cells that are hierarchically organized; See Introduction). This may be due to their greater links with visual and parietal regions as compared to the subcortical HD attractor.

Experiment 3 was designed to address the following questions. (1) Are AV spatially representations stable across trials and in darkness? (2) Are there differences in visual responsiveness between theta and non-theta HD cells? (3) Are these cells part of a continuous network attractor? To answer these questions, AV cells identified in Experiment 2 were recorded in two additional trials conducted in the same squared box. Spatial firing was monitored across trials in the light and after switching off all the lights.

7.2 Aims and Hypothesis

To address these questions, three main sets of hypotheses were formulated and tested by Experiment 3, categorized as:

1. Cross-trial stability of spatial patterns; all cells should maintain similar firing directions/locations across trials in both light and dark conditions by integrating idiothetic information available in both conditions (path integration).

2. Increased drifting in darkness; despite similar firing fields across trials, we expect neurons to drift more in the absence of vision, due to cumulative path integration errors. In Experiment 2 we showed that, during the course of a single trial in the light, both Theta-by-HD and non-rhythmic HD cells reliably encoded

a single direction, but Theta-by-HD cells drifted at a faster rate. Recording in darkness allowed to examine the cause of such instability. If this was due to incomplete integration of vestibular signal during path integration, Theta-by-HD cells should be more impaired in darkness compared to non-rhythmic HD cells. If this was due to poor updating of idiothetic cues by visual landmarks, cells should display an equivalent amount of PFD drift in darkness, when the system has to rely on path integration.

3. Rotational coherence; the result that Theta-by-HD cells were more directionally impaired than non-rhythmic HD cells, even in the light, suggests that these cells may not be able to form stable firing associations with one another (do not behave like a continuous attractor), given that a key prediction of an attractor architecture is that cells should maintain fixed angular differences between their PFDs at all times during a trial. To confirm whether Theta-by-HD cells formed a separate attractor ring, or no attractor at all, we recorded simultaneously non-rhythmic HD and Theta-by-HD cells and tested whether they maintained global rotational coherence between their PFDs during drifting in darkness.

7.3 Methods and Materials

To test these three hypotheses, cells were recorded from AV using multichannel extracellular techniques, as reported in the General Methods. Cells recorded in the squared open field box of Experiment 2 ("Light 1" trial) were recorded in two additional trials. In the first of these trials ("Light 2" trial), all cells from the six rats used in Experiment 2 were recorded during re-exposure to the same squared box, to assess cross-trial stability of spatial firing. In the second of these trials ("Dark" trial), cells from four of the six implanted rats were recorded in the same squared box after switching off the room lights and switching on an infrared light, to assess the impact that removing visual input has on spatial patterns.

7.3.1 Behavioural protocol and testing apparatus

All the three trials lasted a period of 8 or 16 minutes. During each inter-trial interval, the rat was removed from the arena and transferred back to its homecage in a separate

room, and the arena was cleaned to remove uncontrolled intra-maze non-visual cues. Variable inter-trial intervals were used, ranging between 5-10 minutes. The rat was then transferred back to the experimental room and the next trial was initiated via remote control after placing the rat inside the arena with a pseudo-random location and orientation. Light 1 trial was the baseline trial; Light 2 and Dark trials took place after Light 1. For the Dark trial, the animal was transported inside the experimental room only after lights were extinguished and the room was illuminated with infra-led LED lights, and the experimenter wore a red coat (Neitz and Jacobs, 1986). Noise from threshold-triggered spikes listed through loud speakers was not extinguished during the trial and animals were never disoriented prior to being placed in the arena, like in previous studies (Clark and Taube, 2011; Goodridge et al., 1998; Clark et al., 2009, 2010). This is because the goal was not to disrupt the spatial activity but to purely determine the influence of vision. In this way, we did not disrupt internal sources of spatial information (Dudchenko et al., 1997) and the only difference between Light and Dark trials was the availability of vision. Note that auditory cues from the loud speakers situated east of the arena did not represent a salient anchoring cue for the animal, since PFDs were uniformly distributed across the AV population (Figure 7.1). This matches previous results from cue rotation studies that HD cells do not follow the rotation of distal auditory cues, even in the absence of a visual reference Goodridge et al. (1998).

7.3.2 Data Analysis

Data were analyzed using TINT (Axona, UK) and MATLAB R2018a (MathWorks, USA) with custom-made programs and functions. CircStat toolbox was used for analysis using circular statistics (Berens, 2009).

7.3.2.1 Cross-trial stability

To address the cross-trial stability hypothesis and verify that cells were stably recorded across trials in both light and darkness, we used a standard cross-correlation approach (Taube and Burton, 1995). Directional and locational cross-correlations were computed for each of the following conditions:

Light-Light. Baseline Light and Second Light trials were correlated; performed on 115 HD cells, 144 Theta-by-HD cells and 56 place cells.

Light-Dark. Baseline Light and Dark trials were correlated; performed on 107 HD cells, 119 Theta-by-HD cells and 34 place cells.

7.3.2.2 Directional cross-correlation

To assess stability of directional cells, a circular cross-correlation analysis was applied to the smoothed tuning curves obtained in each pair of trials. Tuning curves were rotated relative to each other in 6° increments, and the Pearson's correlation (r) was computed at each step. The correlation at 0° rotation was used as a measure of directional similarity across the two trials. The distribution of all correlations was plotted and compared to the distribution of correlations derived from cross-correlating tuning curves in the Baseline Light trial with shuffled tuning curves in either the Second Light or Dark trial.

The distribution of shuffled correlations was obtained and represents the probability that a HD cell could have the same PFD by chance. The 95^{th} percentile value from the distribution was taken as a threshold value against which to test the similarity of directional representations. Cells with r>threshold have similar tuning curves while r≤threshold indicate PFD shifts.

Shuffled tuning curves were derived by shifting the entire spike-time series of a cell relative to the HD data 10'000 times by an amount randomly selected between 20s and the trial duration minus 20s, and then wrapped around to the beginning so that the number of spikes for each shift remained constant. This method was used instead of randomly shuffling spike times, because it allows to re-arrange spike times while maintaining the same temporal relationships between adjacent spikes, that is the same spike intervals and burst events occurring in the original spike-time series. Two-tailed two-sample Kolmogorov-Smirnov test was used to test the significance between the cumulative distribution functions for the correlations of different cell types, and between control and original distributions.

7.3.2.3 Locational cross-correlation

To assess place field stability, a bin-by-bin cross-correlation analysis was applied to the smoothed ratemaps obtained in each pair of trials. Bins with 0Hz firing rate in both trials were discarded. The Pearson's correlation (r) was used as a measure of similarity of the locational representations in our two conditions. The distribution of

all correlations was plotted and compared to the distribution of correlations derived from cross-correlating random cells.

A control distribution of correlations was obtained and represents the chance level for which a place field was at the same exact location by chance. The 95^{th} percentile value from the distribution was used as threshold value to identify cells with similar spatial representations in each condition (r >threshold).

Control distributions were built by pooling all ratemaps from each condition together (Light-Light, Light-Dark). Cell pairs were randomly selected 10'000 times with replacement from this pool (cell identity shuffles) and their ratemaps were correlated. Two-sample Kolmogorov-Smirnov test was used to compare distribution of the original correlations with the distribution of correlations derived from correlating random cells.

7.3.2.4 Increased drifting in darkness

To assess the hypothesis that directional cells increase drifting in darkness, given the absence of a visual reset signal, we applied the circular-linear correlation approach described in Chapter 6 (see details about methods in Section 6.2.3.1). This approach allows to quantify the magnitude and direction of a cell's linear drift rate. Absolute rate values were used for statistical analysis. Comparisons between cell groups were made using two-sample Wilcoxon Rank-sum tests (WRS). Comparisons between Light 1 and Dark trials using paired-sample Wilcoxon Signed rank (WSR) tests. For this analysis, we considered only non-rhythmic HD and Theta-by-HD cells that were recorded in both Light-Light and Light-Dark conditions, with a good linear-regression model fit in both conditions ($R2 > 0.7$).

7.3.2.5 Rotational coherence of the PFDs

To confirm whether a fixed internal network organization exists for non-rhythmic HD and Theta-by-HD cells, we asked whether PFD differences between co-recorded non-rhythmic HD and co-recorded Theta-by-HD cell pairs were kept constant during ongoing drift in darkness, or whether cell pairs modified their PFD differences. We used methods described in Kornienko et al. (2018) and Bassett et al. (2018). We identified pairs of simultaneously-recorded non-rhythmic HD and Theta-by-HD cells that were recorded in Condition 2 (Light-Dark). For each pair, the difference

in PFD within each trial was calculated. Cell pair-specific PFD differences from the two trials were then correlated with each other (Pearson's r). If co-recorded cells drifted in the Dark trial by a similar angle, then angular differences in their PFDs should be maintained across trials, and so correlations should be high. If co-recorded cells drifted by different angles correlations should be small. Correlation values were compared between the two cell groups using Fisher r-to-z transformation.

7.4 Results

The three classes of spatial neurons identified in AV, namely non-rhythmic HD, Theta-by-HD and place cells, were recorded across three consecutive trials, in order: Baseline Light, Second Light and Dark trial. The spatial pattern of all cells was highly stable across trials, with no sign of abrupt shifts in firing direction/location.

7.4.1 Are cells controlled by room cues?

As recordings were conducted in a cue-rich environment, before assessing cross-trial stability, it was first necessary to make sure that PFDs were not controlled by specific background room cues but were uniformly distributed across all directions. A uniform distribution would be expected from putative HD cells (i.e., from AD), but this may not be the case for cells that are more visually driven. For these cells, PFDs might tend to represent the local orientation of room cues rather than the global sense of direction of the animal (LaChance and Taube, 2022).

Independent Omnibus-tests were applied to test for non-uniformity of PFD distributions across all cells in the Baseline Light trial and failed to reject the null hypothesis of a uniform distribution for both non-rhythmic HD (m=45, p=0.07) and Theta-by-HD cells (m=65, p=0.297; Figure 7.1). Non-significant p-values were also obtained when tests were run within each animal (not shown). The same results were found when PFDs were considered in Second Light and Dark trials (all p>0.05). To confirm that the distribution of PFDs from Baseline Light and Dark trials remained consistent, a Kuiper test was applied and found no differences between PFDs distributions, for both cell groups (all p>0.05). These results agree with the lack of any specific salient landmarks in our recording room that could serve as an anchoring cue for HD cells and confirm a uniform sampling of all directions.

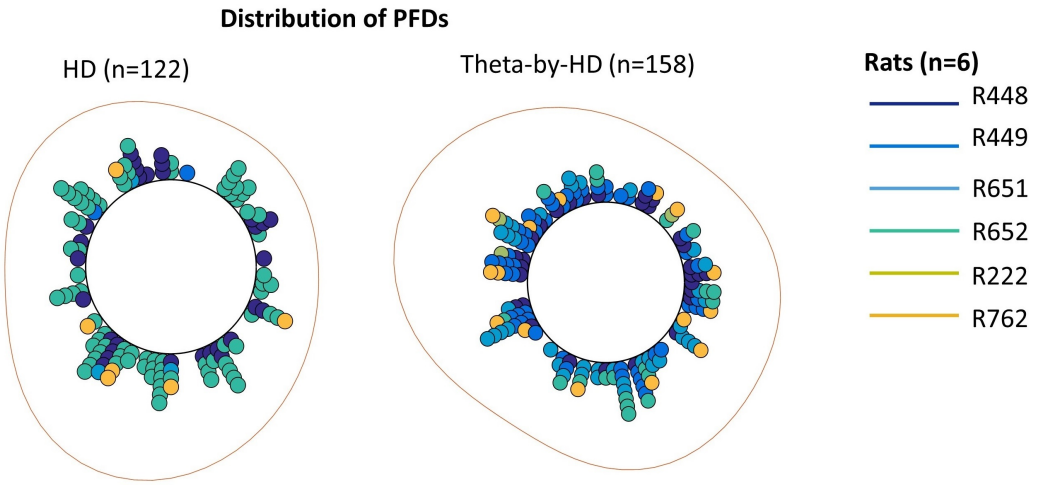


Figure 7.1: **No influence of uncontrolled room cues during the Baseline trial in the Light.** Each marker is the preferred firing directions (PFDs) of a cell, with the associated kernel density estimate (KDE; bandwidth=50), colour coded by rat (n=6). **(A)** Non-rhythmic HD cells; **(B)** Theta-by-HD cells. For both groups, the distribution was uniform and did not differ from the distribution obtained in the Dark trial, suggesting no anchoring to a specific room cue that could help animals to maintain their sense of direction in darkness.

7.4.2 Are directional cells stable across trials and in darkness?

7.4.2.1 Similarity of directional firing

We investigated the stability of directional neurons by computing the correlation between tuning curves for each pair of trials. In Condition 1 (Light-Light), tuning curve correlations were as follows: non-rhythmic HD, 0.89±0.19; Theta-by-HD, 0.81±0.01. In Condition 2 (Light-Dark), correlations were as follows: non-rhythmic HD, 0.89±0.02; Theta-by-HD, 0.79±0.02. The stability of directional firing was not affected by light manipulations, as tuning curves were equally correlated in the two trial pairs (two-sample Kolmogorov-Smirnov test; non-rhythmic HD, ks-stat=0.068 ; Theta-by-HD, ks-stat=0.098; all p>0.5; Figure 7.2 A-B).

When we compared correlations between Condition 1 and Condition 2, one main cluster is apparent in the top-right quadrant, with high correlations in both conditions (Figure 7.2 C). The majority of cells had correlations above the 95^{th} percentile threshold of the distribution derived from shuffling the tuning curves. The number of cells with similar directional representation (more likely than chance to

have the same direction) in Condition 1 was: non-rhythmic HD, 109/115; Theta-by-HD, 142/144. In Condition 2, this number was: non-rhythmic HD, 101/107; Theta-by-HD, 116/119. Distributions of observed and shuffled correlations differed significantly from each other for both non-rhythmic HD (two-sample Kolmogorov-Smirnov test, Condition 1, ks-stat=0.939; Condition 2, ks-stat=0.944; all p<0.0001) and Theta-by-HD cells (Condition 1, ks-stat=0.972; Condition 2, ks-stat=0.95; all p<0.0001). Overall, similarity of the directional firing was above chance. Despite directional constancy for both non-rhythmic HD and Theta-by-HD cells, tuning curve correlations differed between the two groups, being higher for non-rhythmic HD compared to Theta-by-HD cells (two-sample Kolmogorov-Smirnov test; Condition 1, ks-stat=0.576; Condition 2, ks-stat=0.587; all p<0.0001).

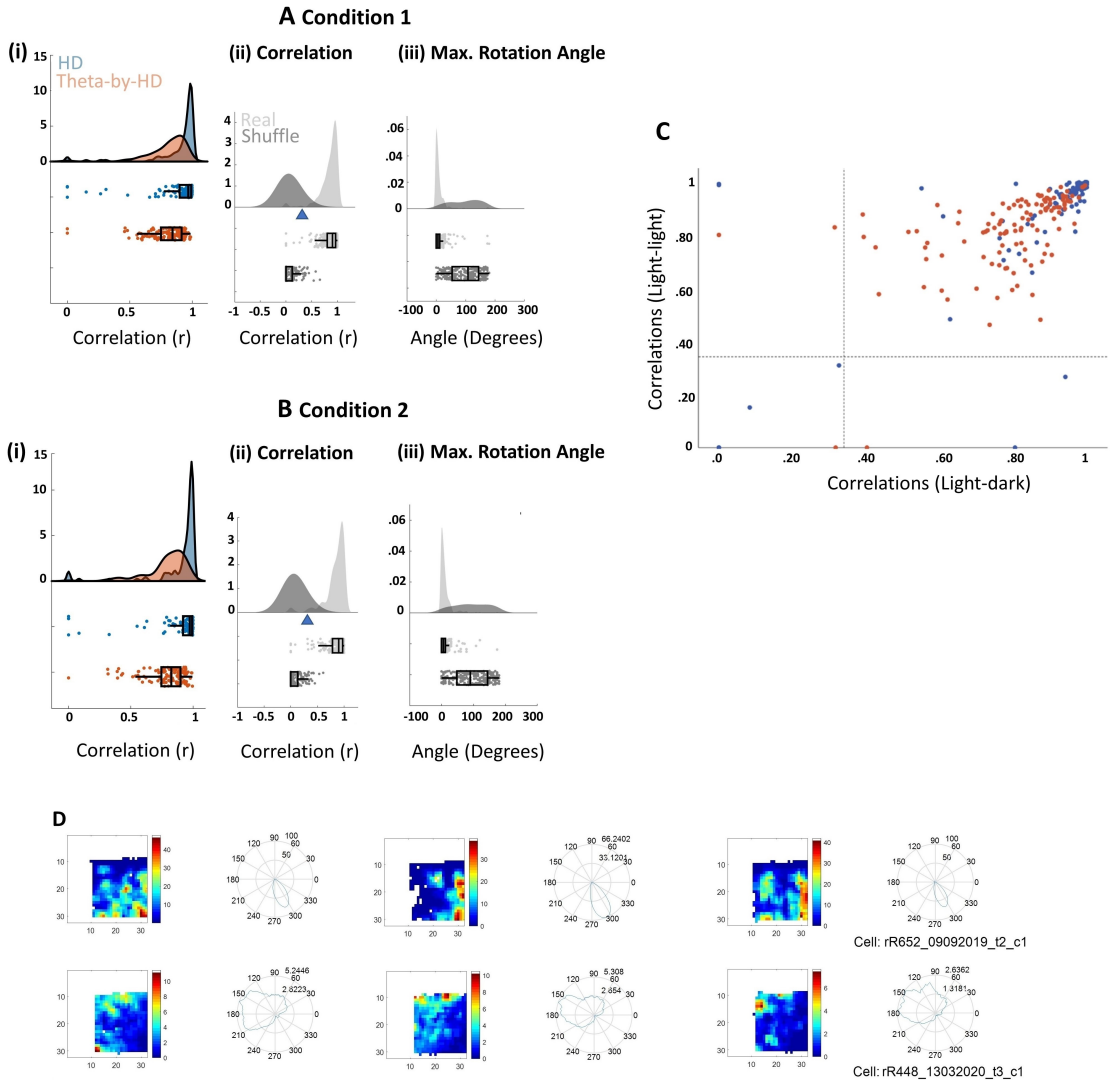


Figure 7.2: **Similar directional firing across Light-Light and Light-Dark conditions.** **(A)** Condition 1 (Light-Light); **(B)** Condition 2 (Light-Dark). For each condition, the

following plots are shown: (i) distribution of tuning curve correlations compared between non-rhythmic HD (blue) and Theta-by-HD (red) cells. (ii-iii) Distribution of correlation coefficients and angles of maximal correlation for all cells, compared to the shuffle distribution. The 95^{th} percentile (blue triangles) informs us of the probability of cells having the same direction for each trial pair (using correlation values). No difference between Condition 1 and Condition 2: both cell groups are stable in both light and darkness. **(C)** Relationships between condition-specific correlations for non-rhythmic HD (n=107) and Theta-by-HD (n=119), colour coded as in (A). Each marker is the correlation for a trial pair. x-axis, Condition 1 . y-axis, Condition 2. Dashed lines are the 95^{th} percentile threshold as determined by the shuffle distribution for each condition. For both trial pairs, correlations are higher for non-rhythmic HD compared to Theta-by-HD cells, but both are higher than chance. **(D)** Example of non-rhythmic HD (first line) and Theta-by-HD cell (second line) recorded across the three trials, in order: Baseline Light, Second Light, Dark. For each trial, the distribution of spatial firing is presented (ratemap and polar plot).

7.4.3 Do cells drift in darkness?

We hypothesized that the amount of PFD drift should increase in darkness due to the lack of a visual reset signal. We limited the following analysis to the directional neurons recorded in Condition 2 (Light-Dark), with a good linear-regression model fit in both trials (R2 >0.7; non-rhythmic HD, n=104/107; Theta-by-HD, n=91/119).

The mean drift rate in the Baseline Light trial was -0.18°/min for non-rhythmic HD and 0.40°/min for Theta-by-HD cells. The mean drift rate in the Dark trial was 0.49°/min for non-rhythmic HD and -1.18°/min for Theta-by-HD cells. Both cell groups were concentrated around a mean of 0°/min (Figure 7.3 A). This was true both for the Baseline Light trial (V-test, non-rhythmic HD, v=103.958; Theta-by-HD, v=90.872; all p<0.0001) and for the Dark trial (non-rhythmic HD, v=103.864; Theta-by-HD, v=90.259; all p<0.0001), indicating reliable directional coding even in darkness. However, on average, drift rate distributions showed a greater amount of variability in the Dark compared to Baseline Light trial (k-test for equal concentration parameters, f=5.174, p<0.0001). The range of drift rates was 58.51° in the Dark, compared to a range of 27.21° in the Light (with n=11 vs 5 cells drifting faster than 8°/min) and these proportions reached a significant difference (χ^2=2.3, p=0.12). To determine whether drift rate distributions from the two trials remained consistent, a circular Kuiper test was applied. There was a significant difference between distributions from the two trials (k=19305; p=0.001). These results indicate mildly reduced directional stability in the dark for both cell groups, without any abrupt PFD shift (Figure 7.3 B).

We now consider each cell group individually. Absolute drift rate values increased in the Dark compared to Light for both non-rhythmic HD (1.09±0.27°/min vs 0.72 ±0.14°/min) and Theta-by-HD cells (4.09±0.65°/min vs 2.08±0.23°/min). However, differences between the two trials reached statistical significance only for Theta-by-HD cells, as indicated by a paired-sample WSR test conducted on absolute drift rate values (HD, z=-1.589, p=0.112; Theta-by-HD, z=-3.131, p =0.0017). For both groups, the variability of drift rates increased in the Dark compared to Light, as indicated by the significance of circular k-tests for equal concentration parameters (non-rhythmic HD, f=3.217; Theta-by-HD, f=5.758; all p<0.0001). Absolute drift rates were faster for Theta-by-HD compared to non-rhythmic HD cells during both Light and Dark, as indicated by two-sample WRS tests (Baseline Light, z=-7.062; Dark, z=-6.721, all p<0.0001). In summary, although many of the drift rate values clustered around 0°/min in both Light and Dark recordings, indicating reliable directional coding, Theta-by-HD cells were more impaired than non-rhythmic HD cells.

The absence of vision did not disrupt firing properties of these cells. There was no alteration in directional information (bits per spike; WSR test, non-rhythmic HD, z=-0.4631; Theta-by-HD, z=-0.2254; all p>0.1) nor were there any significant changes in the global mean firing rate (non-rhythmic HD, z=1.6597; Theta-by-HD, z=2.4025; all p>0.01) between Baseline Light and Dark trials for both cell groups.

7.4.4 Is there evidence of coherence of PFD drifting in cell pairs?

We have shown that both non-rhythmic HD and Theta-by-HD cells maintained a similar PFD across trials, despite some ongoing drift in darkness. To shine light on their internal network organization, we now investigate whether this PFD drift was coherent between simultaneously-recorded cells.

We identified pairs of simultaneously-recorded non-rhythmic HD (n=43) and Theta-by-HD cells (n=35) recorded in Condition 2, and conducted statistical analysis to compare their PFD differences between Baseline Light and Dark trials. Scatterplot of these differences (Figure 7.3 C) revealed that non-rhythmic HD cells mostly fell on the diagonal line (correlation=1): PFD differences in the Light were almost always perfectly maintained in the Dark, as indicated by a significant Pearson's correlation between the two trials (cells stayed stable together or drifted together; r=0.98; p<0.0001; Figure 7.3 C). By contrast, Theta-by-HD cells reorganized their PFD differences between the two trials, as indicated by a lack of significant correlation

(cells drifted by different angles; r=0.21; p=0.238; Figure 7.3 C). These observations were confirmed by a significant comparison of correlations between non-rhythmic HD and Theta-by-HD cells (Fisher r-to-z transformation, z-score=9.250, p<0.0001). Ten Theta-by-HD cell pairs (28.57%) drifted in opposite directions during darkness, while there was not a single instance among non-rhythmic HD cells.

To test whether the degree of spatial coupling was significantly higher than chance, we compared the obtained correlations to those derived from a shuffle distribution, computed by shuffling cell pair identity 10'000 times (non-rhythmic HD, r=0.05, p=0.75; Theta-by-HD, r=-0.15, p=0.39). Correlations were higher than chance for non-rhythmic HD (z-score=-7.60, p<0.0001) but not for Theta-by-HD cells (z-score=-0.63, p=0.53). We concluded that only non-rhythmic HD cells displayed stable spatial couplings between cells, even during drifting in darkness.

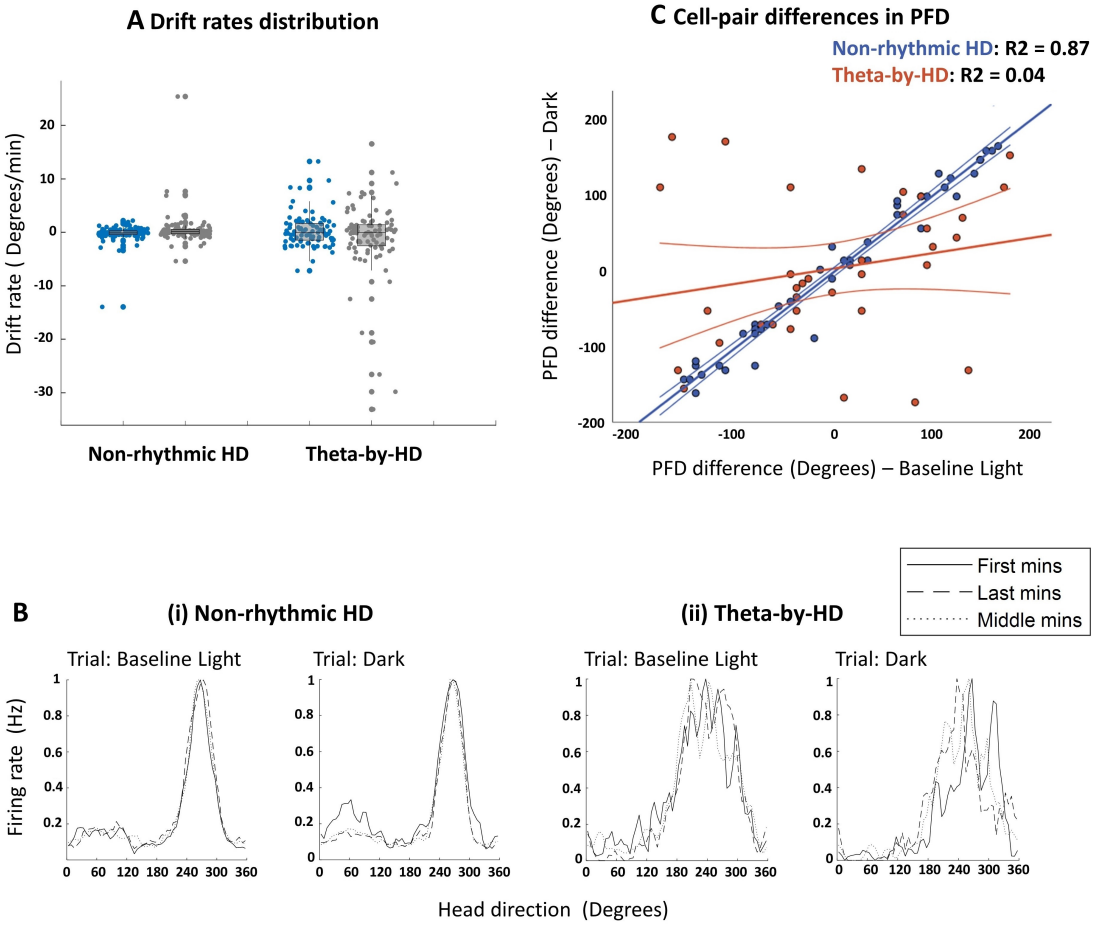


Figure 7.3: **Theta-by-HD cells are more impaired in integrating movement cues.** **(A)** Distribution of trial-specific drift rates for non-rhythmic HD and Theta-by-HD

cells, shown as raw data + boxplot. Each marker is the drift rate of a cell in the Baseline Light trial (blue) and in the Dark trial (gray). Larger markers are outliers. Both cell groups show reliable directional coding (mean drift rate around 0°/min), but distributions of Theta-by-HD cells were more dispersed compared to non-rhythmic HD cells (higher number of Theta-by-HD cells with fast drift rates). Both cell groups showed a greater variability of drift rates in the dark compared to light (drifting by a larger amount). **(B)** Tuning curves of (i) non-rhythmic HD and (ii) Theta-by-HD cell, constructed for the first and last 2 minutes of the Baseline Light trial and subsequent Dark trial. No evidence of abrupt PFD shift, suggesting a gradual drift instead. **(C)** Evidence of uncoupling of simultaneously recorded Theta-by-HD cell pairs. Each marker is a cell-pair specific difference between preferred firing directions (PFDs). x-axis, differences in Baseline Light trial. y-axis, differences in the Dark trial. The diagonal line indicates a correlation=1 between these differences. Line of best fit with 95% CI is displayed. R2s measure how close data points are to this linear fit. Pairs of non-rhythmic HD cells (blue), but not Theta-by-HD cells (red), demonstrated significantly correlated differences between PFDs.

7.4.5 Are place cells stable across trials and in darkness?

7.4.5.1 Similarity of locational firing

We investigated place cell stability by computing ratemaps correlations for each pair of trials. The obtained correlations were compared to the 95^{th} percentile threshold determined by a control distribution derived from shuffling the cell identify, and only ratemap pairs with a value above this threshold were deemed stable (more likely than chance to have the same place field; Figure 7.4 A-B). Ratemap correlations were 0.9±0.01 in Condition 1 (Light-Light) and 0.87 ±0.03 in Condition 2 (Light-Dark). The stability of location firing was not altered by light manipulations, as ratemaps were equally correlated in the two trial pairs (two-sample Kolmogorov-Smirnov test; ks-stat=0.144, p=0.74; Figure 7.4 A-B) and a low number had values below the 95^{th} percentile threshold from the shuffle distribution (Figure 7.4 C; Condition 1: 45/56 cells; Condition 2: 31/34 cells; cells in upper right quadrant). Observed and control distribution of correlation coefficients differed significantly from each other, suggesting that similarity of the locational firing was above chance for both trial pairs, and that remapping rarely occurred (two-sample Kolmogorov-Smirnov test, Condition 1, ks-stat=0.86; Condition 2, ks-stat=0.853; all p<0.0001; Figure 7.4 A-B).

While place fields were highly stable and there were no significant changes in the global mean firing rate between Baseline Light and Dark trials (z=-0.958, p>0.1), the locational information carried by place cells was reduced in the dark

(bits per spike; paired-sample WSR test, z=4.160, p<0.0001). Thus, it is possible that a small, but significant, place field drift occurred. Given the short intra-trial intervals and their variable durations (between 5-10 minutes), it is possible that greater field reorganization would occur at longer intervals (see Limitations).

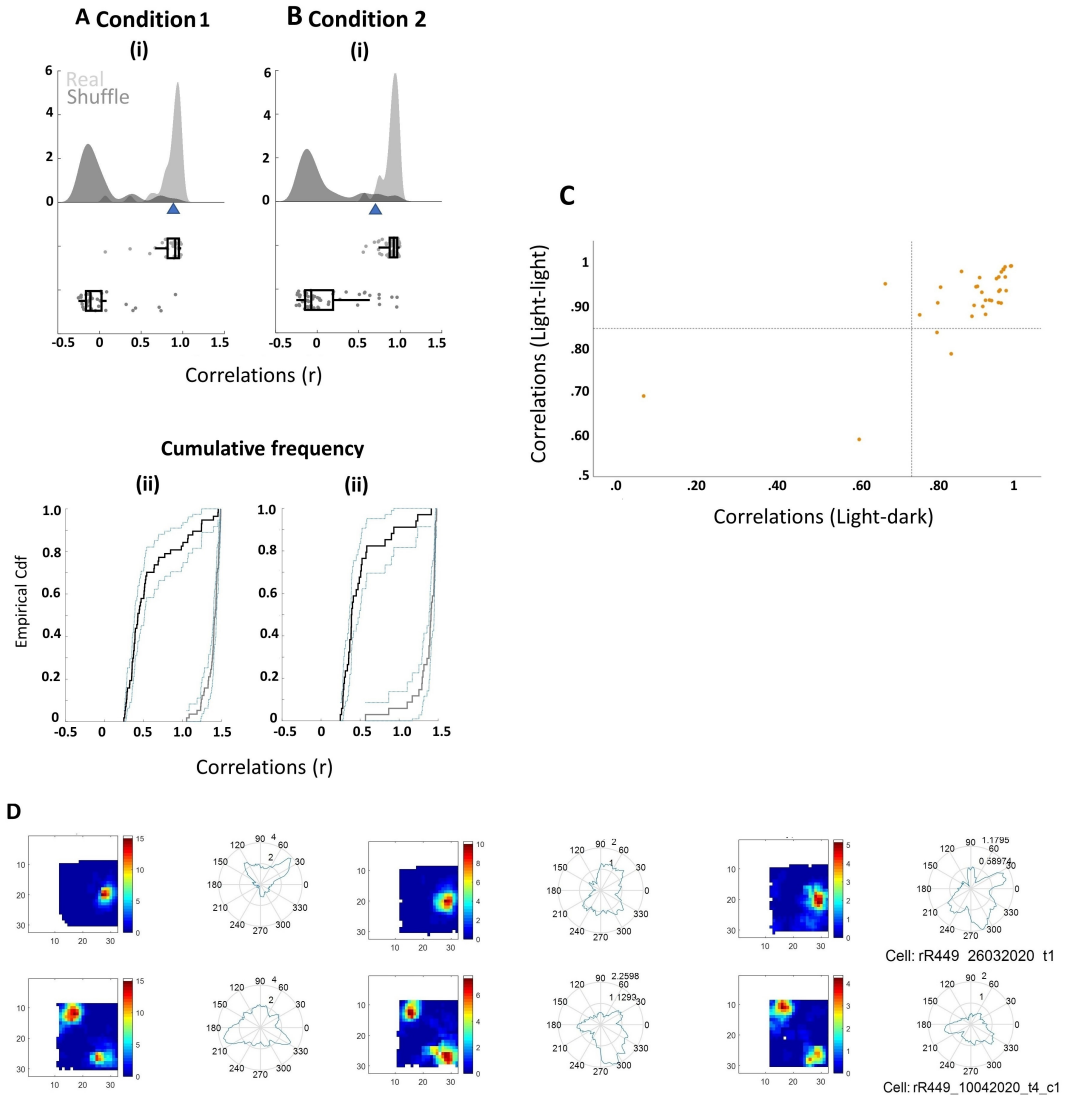


Figure 7.4: **Similar place cell firing across Light-Light and Light-Dark conditions.** **(A)** Condition 1 (Light-Light); **(B)** Condition 2 (Light-Dark). For each condition, the following plots are shown. (i) Distribution of ratemap correlations for all place cells, compared to the control distribution derived by shuffling cell identity. Blue triangles mark the 95^{th} percentile (chance-level criteria that a cell has fields in the same location for each ratemap pair). (ii) Cumulative frequency of the real and shuffled correlation coefficients. Dotted blue lines mark 99% CI. Place cells were more likely than chance to have the same field across both trial pairs. **(C)** Relationships between condition-specific correlations (place cells, n=34). Each marker is the correlation

for a trial pair. x-axis, Condition 1. y-axis, Condition 2. Dashed lines are the 95^{th} percentile threshold as determined by the shuffle distribution for each condition. Correlations clustered in the top right quadrant indicate stable place fields. **(D)** Two place cells recorded across the three trials, in order: Baseline Light, Second Light, Dark. For each trial, the distribution of spatial firing is presented (ratemap and polar plot).

7.4.5.2 Qualitative observations

Qualitatively, few place cells tested in the Dark trial (n=5/34) showed strong suppression of firing in this trial, without place field remapping (recorded from two different animals). For these cells, dark mean firing rates were reduced by more than 50% of baseline rates (average reduction of 65.08±4.24% from the baseline trial; range, 57.46-80.47%; Figure 7.5). Additionally, two place cells exhibited complete suppression of firing (no cluster detected in the dark trial). All these cells with partial or complete silencing were simultaneously recorded in the dark with one or more Theta-by-HD cells drifting slowly CW or CCW, without a significant decrease in firing rate. In the future, it will be important to extend these recordings to include an additional light trial or first conduct recordings in the dark without previous experience of the environment in the light, to determine whether some AV cells may be more dependent on visual inputs (more discussion in the Limitations).

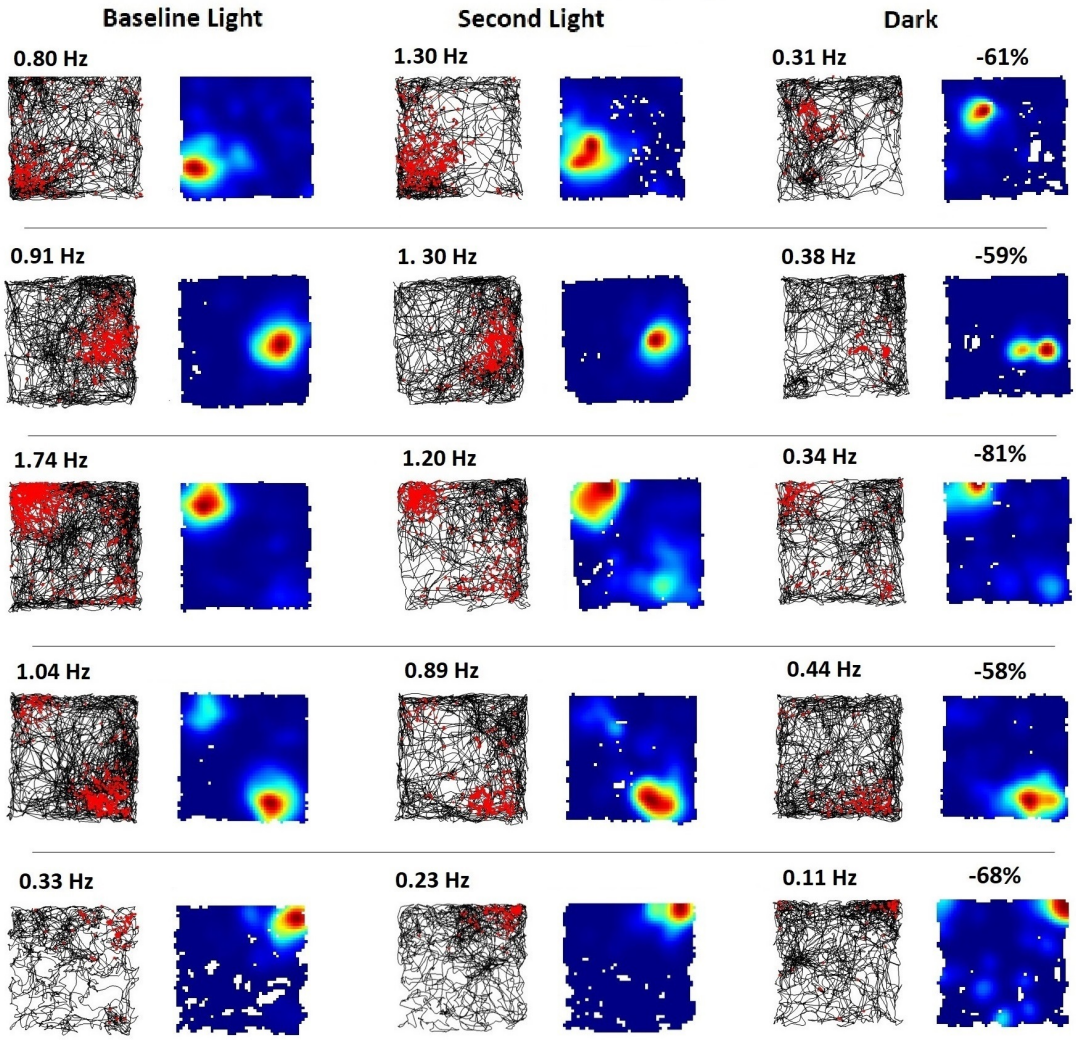


Figure 7.5: **Examples of "dark-off" place cells.** Figure shows the spikemap and ratemp for five place cells that suppressed firing in darkness. Mean firing rate for each trial is reported. Trial name is at the top. Percentages in the rightmost column are the percentage firing rate reduction in the Dark trial compared to Baseline Light trial.

7.5 Discussion

We have examined the stability of AV spatial representations and their dependency on visual input. To do this, we used quantitative methods to correlate firing rate plots across recordings in Light-Light and Light-Dark conditions, and compared between the two. We found that, across both conditions, correlation coefficients were mostly clustered at high values, suggesting that cells could maintain their firing

direction/location across trials irrespective of light condition. We found no difference in correlations between the two conditions. Generally then, the absence of vision did not disrupt spatial stability and firing properties of AV neurons: once the AV spatial map is set up in the light, neurons are able to maintain this pattern also in the absence of vision by relying on internal and non-visual sources of information (Etienne and Jeffery, 2004). Findings accord with the lack of direct visual inputs to AV (Perry and Mitchell, 2019).

7.5.1 Persistence and gradual drift of directional cells in darkness

Both non-rhythmic HD and Theta-by-HD cells maintained a similar direction across Light-Light and Light-Dark conditions. However, comparing distributions of tuning curve correlations revealed that Theta-by-HD cells were distributed more diffusely across both conditions, and this was due to a gradual intra-trial drift rather than abrupt PFD shifts. We found only a slight increase in the amount of intra-trial drift in the Dark compared to Light for both cell groups, indicating only mildly reduced stability in the absence of vision, although Theta-by-HD cells were more heavily impaired, indicating a stronger visual responsiveness. Theta-by-HD cells may receive weaker or more indirect vestibular information from the HD system, in line with their less-anticipatory firing.

For both groups, persistence and gradual drifting of PFDs is consistent with the notion that cells are driven primarily by vestibular inputs (Shinder and Taube, 2010; Stackman and Taube, 1997; Muir et al., 2009; Yoder and Taube, 2009; Stackman et al., 2002), but information about visual landmarks are also integrated to correct errors resulting from inaccurate estimation of AHV during movements (Mizumori and Williams, 1993; Goodridge et al., 1998; McNaughton et al., 2006a; Burak and Fiete, 2009; Etienne and Jeffery, 2004). In the absence of visual landmark stabilization, directional cells were able to maintain their original orientation by integrating vestibular and self-motion cues, as we did not use a disorientation treatment to prevent the animal from using idiothetic cues. Other sources of orienting information include intra-maze non-visual cues, given that in the absence of a reliable visual reference, AD and PoS HD cells have been shown to rely on olfactory and tactile cues to update their orientation, while auditory cues seem to exert a much weaker influence (Zugaro et al., 2000; Goodridge et al., 1998). It seems unlikely that cells used environmental geometry (spatial relations among box or room walls) , since

geometric cues have been shown to influence HD cell firing only when the path integrator is made unreliable by disorientation treatment (Knight et al., 2011).

We additionally hypothesized that the two classes of directional neurons present in AV may not exist in the same continuous attractor network, given that Theta-by-HD cells were more directionally unstable than non-rhythmic HD cells in both light and darkness. To confirm whether Theta-by-HD cells formed a separate attractor ring, or they did not require attractor dynamics, we asked whether these cells behaved as an ensemble during drifting in darkness. Only non-rhythmic HD cells, but not Theta-by-HD cells, maintained stable spatial coupling with one another during ongoing drift, suggesting that the internal network structure was unchanged, even when cells were unstable. See General Discussion.

7.5.2 Place cell stability across trials and in darkness

Place cells also displayed high correlations, indicating highly stable place fields across Light-Light and Light-Dark conditions, with no hint of place field remapping in both conditions, despite few cases (n=7) of rate remapping in darkness. Place fields could have been maintained at similar locations through the integration of idiothetic cues (McNaughton et al., 2006a; Burak and Fiete, 2009), non-visual intra-maze cues (Zhang et al., 2014; Save et al., 2000), and geometric cues about walls/angles. The latter have been shown to provide a reset signal to correct place field drift during path integration also in non-disoriented animals (O'Keefe and Burgess, 1996; Barry et al., 2006; Zhang et al., 2014). While dark testing did not cause place field remapping, the absence of vision reduced the average locational information content and seven place cells suddenly shut-off or decreased firing when room lights were turned off, indicating some sensitivity to visual changes. Likewise, hippocampal place cells have been found to drift in darkness or suddenly quit firing, recovering only during subsequent dark testing O'Keefe (1976). In our study, all place cells that decreased firing were co-recorded with at least one Theta-by-HD cell whose firing was affected by the visual manipulation only in a subtle manner, corroborating our hypothesis of only a weak spatial influence on Theta-by-HD cell firing.

7.5.3 Conclusion

The high stability of AV spatial representations bears strong resemblance to the firing of HD and place cells in other brain regions, which primarily rely on idiothetic information. The extent to which AV cells can be controlled by visual landmarks should be addressed systematically by cue rotation experiments. The next Chapter will focus on bringing together our results from all three experiments. We will consider a network model to answer questions of how different spatial signals recorded in AV arise and what they are for.

7.5.4 Limitations

The analysis in this Chapter revealed high spatial stability across trials for all AV cells. While this automatically implies a high stability of spatial firing within each trial as well, it could have been useful to quantify such intra-trial stability by performing spatial correlations between trial halves.

The task design used in our experiment presents a number of limitations. Our design did not allow us to determine the extent to which AV neurons relied on path integration alone or on a combination of path integration and non-visual information in the Dark trial (Etienne and Jeffery, 2004). Although, it should be noted that our aim was not to test all the possible sensory modalities that cells could use to maintain their firing across trials, but rather to purely investigate the question of whether they could use visual inputs. Since the only difference between light and dark trials was the lack of vision, our results are informative to answer this question and allowed us to conclude that visual perception cannot account for the observed spatial patterns. In the future, dissociating idiothetic and non-visual influence on AV cell spatial representations will require recordings during path integration tasks (dual-chamber task) and non-visual cue manipulation (independent rotations of the arena's floor and walls in light and dark conditions and auditory cues blockade).

Other design limitations include the fact that we could not test all the cells across all trial types, given that dark testing was conducted in only four of the six implanted rats. Additionally, we only performed a single Dark trial that lasted 8 or 16 minutes, and thus we could not determine the duration over which reliance on path integration (or non-visual cues) was successful and whether a switch to other sensory modalities would have occured at longer intervals. Finally, we did not systematically

monitor for the time period between trials, and thus we cannot determine whether place field remapping would occur for longer inter-trial intervals.

8

General Discussion

8.1 Summary of the three experiments

Our work was aimed at investigating and further dissecting the AV-RSC circuit(s), along which two important neural signals for spatial signaling are found, and are combined at the individual cell level: theta and HD. We investigated this interaction both electrophysiologically, by recording neurons from different subregions of RSC and AV, and anatomically, by examining differences in their interconnections. Below is a summary of the main results presented in this thesis:

Experiment 1. Chapter 4. Theta-modulated cells in RSC were predominantly found in gRSC, where they formed a subpopulation of fast-spiking, bursting interneurons (Lomi et al., 2021). AV projections to the two RSC subregions could be differentiated along two separate pathways, AVDM-gRSC and AVVL-gRSC/dRSC. Given that AV represents a key theta relay to the hippocampal formation, these anatomically-segregated pathways could also be functionally distinct and relay different theta signals to gRSC and dRSC. Our combined electrophysiological and anatomical data complement previous studies showing that different RSC subregions map onto different aspects of information processing: gRSC has more extensive connections with subcortical regions of the HD and theta systems, namely AD and AV, as well as with hippocampal formation. dRSC

is partly detached from the hippocampal navigational network and contains HD cells that are sensitive to more primary perceptual information (Jacob et al., 2017; Alexander et al., 2020a).

Experiment 2. Chapters 5 and 6. These results motivated us to then record single units from AV to shine light on how different AV subfields encode and integrate theta and spatial signals, and project this information to RSC. We replicated and extended previous studies by Tsanov et al. (2011) showing the existence in AV of two types of directional signal: a broad one operating at theta frequency (Theta-by-HD), and a more precise one operating independently of theta (non-rhythmic HD). Although our original focus was to record directional neurons, we also recorded place cells, with spatial and temporal firing properties very similar to those of typical hippocampal pyramidal neurons, except for a narrower spike waveform width, likely reflecting differences in thalamic and cortical cell typology (i.e., size of cell bodies and axons, distributions of ion channels and neurotransmitter content). We provided evidence for differences in the anatomical organization of these cells between the two AV subfields that was consistent with their respective projection patterns to different RSC subregions, corroborating our hypothesis of a multifaceted AV-RSC circuit for memory.

Experiment 3. Chapter 7. The spatial firing pattern of non-rhythmic HD, Theta-by-HD and place cells in AV was stable across trials and not disrupted by changes in light condition. Absence of vision did not affect coding of orientation and position, although it had some effect on HD cells' stability, which was stronger for Theta-by-HD cells. During drifting in darkness, Theta-by-HD cell pairs did not show coherence of firing, in contrast to clearer coherence within cell pairs that is seen for most non-rhythmic HD pairs. This is consistent with recordings of theta-modulated HD cells that escape attractor dynamics in regions outside of the main thalamocortical AD circuit (Kornienko et al., 2018; LaChance and Taube, 2022). This may be due to the stronger input that these cells receive from theta (or visual input) as compared to the subcortical HD input. We concluded that AV does not contain a uniform population of directional neurons, but there are two separate networks: the main HD network attractor, and a theta-modulated network that does not necessitate attractor connectivity to generate directional tuning, possibly inheriting directional specificity via excitatory projections from the main HD attractor (see below).

8.2 How do directional cells in AV acquire their specific response properties and what are they for?

In this Section, we advance a network model that can explain formation of directional neurons in AV with firing properties similar to those described in this thesis, namely non-rhythmic HD and Theta-by-HD cells. At the single-cell level, AD-RSC and AV-RSC pathways are known as a HD and a theta relay stream, respectively. In our model, some AV cells receive a strong descending input from the main HD network in RSC and thus are non-rhythmic HD cells; another subpopulation receives strong ascending MMN inputs and thus are theta-modulated cells with no spatial properties, and a third subpopulation receives inputs from both the HD signal and the theta input and thus become Theta-by-HD cells. According to this model, the ascending HD input from AD influences AV firing via an indirect thalamo-cortico-thalamic route. Although a direct projection from AD and AM to AV could drive directional and place modulation of AV firing, in addition to the cortical projection, so far no anatomical and electrophysiological evidence (coordinated cross-correlgram activity) has been reported for intrinsic connectivity between ATN nuclei. Key points of a model instantiating these hypotheses are:

1. A continuous attractor ring of HD cells in AV receives input signaling current HD from a central ring of HD cells upstream in RSC, in turn inherited from the subcortical HD attractor, via AD (Page and Jeffery, 2018). The RSC and AV HD attractors are connected by one-to-one excitatory connections. An attractor architecture represents the predominant model of HD cells (Skaggs et al., 1995; Redish et al., 1996; Zhang, 1996).

2. Theta-modulation of AV cell firing is evoked by a theta input from MMN (Seki and Zyo, 1984). In turn, MMN receives and integrates reciprocal theta signals from VTN (Allen and Hopkins, 1988; Cruce, 1977), hippocampal formation (Allen and Hopkins, 1989; Shibata, 1989; Ishizuka, 2001) and a weaker medial septum input (Gonzalo-Ruiz et al., 1992; Bassant and Poindessous-Jazat, 2001; Kocsis et al., 2001; Kirk et al., 1996; Ruan et al., 2017).

3. Theta-modulated cells in AV that receive the MMN excitatory theta input can be divided into two subpopulations. One receives solely the MMN input. The other receives excitation from both the central HD cell ring within AV, possibly via collateral of thalamocortical glutamatergic projections, and the MMN theta

input. Such input convergence gives rise to theta-modulated cells that undergo directional modulation, without needing an attractor architecture, referred to as Theta-by-HD cells. This agrees with the uncoupling of simultaneously recorded Theta-by-HD cells described in Experiment 3 (Chapter 7).

4. Theta-by-HD cells act as coincidence detectors for the HD input signaling current orientation, and the theta input signaling movements. When the two are paired during locomotion (Type-1 theta states in the LFP), Theta-by-HD cells are activated and can influence post-synaptic targets in RSC. Both populations of non-rhythmic HD and Theta-by-HD cells feed back to RSC, communicating with the main HD network in the cortex.

A schematic of this proposed model is pictured in Figure 8.1. In the next Sections we will propose a function for this network that can explain the formation and function of the different classes of directional neurons in AV. This is followed by a description of the two-stream model of the AV-RSC circuit, along which these neurons are found. According to such a model, the AV-RSC circuit contains two pathways, relaying separate theta and HD information to RSC, and integrating this information, respectively.

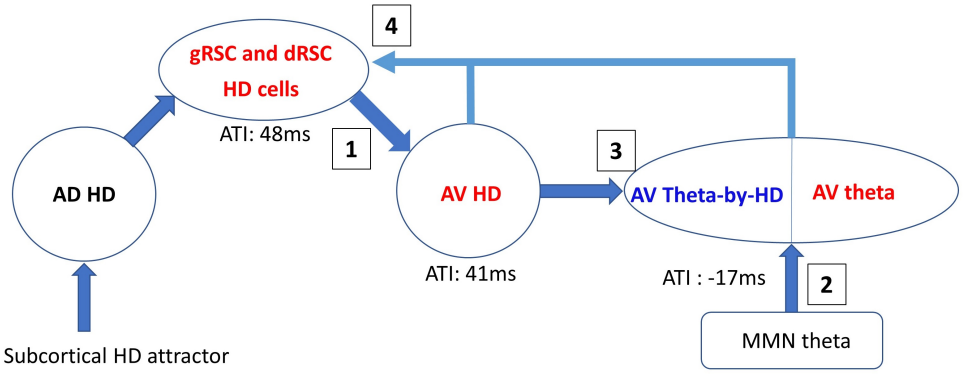


Figure 8.1: **Model schematic of the main features and connectivity of AV directional cells.** Key points of the network model are numbered as in the text. Anticipatory time intervals (ATIs) are reported for non-rhythmic HD cells and Theta-by-HD cells recorded from RSC and AV. RSC values are based on Lozano et al., 2017. As the animal turns its head, activity is updated first in the central HD ring in RSC (inherited from AD); then, after a short interval in the HD ring in AV, and after that in Theta-by-HD cells, whose activity correlates with more present or past heading directions. This notion is based on ATI values that are more anticipatory in RSC (but not in PoS)

compared to AV. The general consensus is that the anterior thalamic-retrosplenial circuit contains two pathways, processing HD information (AD-RSC) and theta inputs (AV-RSC). We suggest that these two pathways meet in AV, where pairing of directional and theta neural signals occur. These signals are relayed back to cortex via AV-RSC pathway(s). Abbreviations: MMN, medial mammillary bodies; gRSC and dRSC, granular and dysgranular retrosplenial cortex; AD, anterodorsal thalamic nucleus; AV, anteroventral thalamic nucleus.

8.2.1 Formation of non-rhythmic HD cells

Our model was investigated by comparing cells' ATIs from different brain regions. The main thalamocortical HD circuit (DTN-LMN-AD-RSC/PoS-MEC) is organized hierarchically, with cells showing different ATIs according to the direction in which vestibular information flows through the system. On average, we found that non-rhythmic HD cells in AV anticipated the heading direction by approximately 42ms. This interval was only slightly smaller than that of putative HD cells previously reported in gRSC, computed using the same analytical approach as in the present thesis (approximately 48ms; Lozano et al., 2017), suggesting a descending influence of RSC projections on AV. Considering the cascade of projections from the DTN-LMN circuit to AD, from AD to RSC (mostly to gRSC) and thence to AV and back to RSC (again, mostly to gRSC), it is conceivable that the central RSC ring (in turn driven by the subcortical HD pathway) transmits and maintains a global HD signal within AV (Figure 8.1). Considering the short latency between RSC and AV HD cell spike discharge (based on ATI values), the hypothesized corticothalamic signal transmission is likely to be fast to ensure reliable feedforward and feedback communication along this loop.

In the future, examining the coordination and interaction of neuronal activity within the AD-RSC-AV-RSC circuit will require lesion data, as well as simultaneous recordings of HD cell ensembles from these regions to perform cross-correlation analysis (Peyrache et al., 2015). Moreover, the question remains of whether ATIs of RSC HD cells might vary as a function of the rostro-caudal location, subregion, and cortical layer in which recordings are conducted (Lozano et al., 2017). This could explain variability of ATIs reported by previous studies of RSC HD cells, ranging approximately from 25 to 50ms (Lozano et al., 2017; Cho and Sharp, 2001). Methodological differences in computing ATIs between studies could also explain this variability. We conclude by noting that it seems unlikely that AV inherits HD signal from other cortical HD components, like the PoS, given that PoS HD cells

encode more past heading directions, with intervals ranging from -15 to 0ms (Lozano et al., 2017; Blair and Sharp, 1995; Blair et al., 1997; Taube and Muller, 1998).

Clearly, given the lack of studies that have recorded from AV after RSC lesions, the idea of inheritance of global directional information from RSC remains to be tested. In the meantime, it could be helpful to consider evidence of AD neural activity when the subcortical directional pathway is lost, as this may offer an *in-vivo* model for the mechanisms driving directional responses in AV, which does not receive inputs from this pathway. Bassett et al. (2007) showed that LMN and DTN damage resulted in the silencing of AD HD cells, possibly reflecting disrupted attractor dynamics required for HD signal generation. On the other hand, after vestibular system damage, AD HD cells lost their directionality but started firing in bursts unrelated to heading direction (Stackman and Taube, 1997; Muir et al., 2009; Yoder and Taube, 2009). This bursting pattern is thought to reflect drifting along the HD ring when its primary driving input (vestibular) is removed.

One study by Blair et al. (1999) observed a gradual emergence of a similar bursting pattern in AD also after bilateral, but not unilateral, electrolytic lesions of the LMN, in apparent conflict with Bassett et al. (2007). Differently from the effects of vestibular damage, such bursting pattern was not irregular but synchronized at theta frequency (6Hz). In lesion animals, theta-bursting cells were often recorded in the same location at which HD cells had been recorded before the lesion, as it would be expected from neurons in a disconnected HD network (like after vestibular damage). One interpretation is that, when deprived of LMN inputs, AD HD cells turn into theta-modulated cells due to a progressive compensatory reorganization of MMN projections, which normally only provide the theta synaptic relay only to AV. A failure of Bassett et al. (2007) to identify theta-modulated cells after DTN and LMN damage, as was the case in Blair et al. (1999) after LMN lesions, could be attributed to the extent of the lesion sites. In Bassett et al. all rats exhibited additional damage in either VTN or MMN, which are part of the theta axis (Vertes et al., 2004; Vertes and Kocsis, 1997). Similarly, vestibular labyrinth damage in (Shinder and Taube, 2010) would have indirectly affected activity along this axis, given the extensive vestibular nuclei projections to VTN. The conclusion from these studies is that DTN-LMN and VTN-MMN projections are part of parallel circuits that confer directional and theta properties to their respective thalamic targets, AD and AV, respectively, making it plausible that AV inherits directional inputs from the AD output (via thalamocortico pathways dependent on AD), as advanced in our model.

8.2.2 Formation of Theta-by-HD cells

Based on our experimental observations, key aspects that a model has to replicate to generate Theta-by-HD cells that receive and integrate inputs from the HD signal and theta inputs are: (1) less anticipatory firing; (2) less-direction-specific activity compared to non-rhythmic HD cells; (3) greater amount of variability of PFDs over time, due to gradual PFD drift. In relation to the first point, we have mentioned above that on average Theta-by-HD lagged spike discharge of non-rhythmic HD cells by approximately 50ms. A key implication of this time delay is that it makes it likely that Theta-by-HD cells arise from the output of theta-modulated cells from MMN and multiple non-rhythmic HD cells within AV. Convergence of inputs from multiple non-rhythmic HD cells that share similar PFDs would result in a lower directional specificity (and greater intra-trial PFD variability) than it would be expected from a single HD cell, while also maintaining a stable direction across trials. Spatial inputs from place cells within the AV may also provide a weak input to the Theta-by-HD cell signal, given that few (n=20) Theta-by-HD cells yielded weak, but reproducible, locational firing. It is possible that the strong anatomical overlap between place cells and Theta-by-HD cells recorded here, both operating at theta frequency and converging on descending theta phases, would allow for these cells to jointly influence common post-synaptic targets in RSC. In this sense, the AV role may be to coordinate these parallel inputs to support early integration of spatial representations and HD information within a theta frequency, in turn laying the basis for downstream higher levels of integration in the cortex, including in RSC. Below, we will show how this can be applied to the formation of conjunctive HD-EBC in dRSC.

8.2.3 What is the functional relevance of a theta-modulated directional signal for spatial processing?

What is the function of HD and place cells modulated by theta in AV? How does this convergence of information processing early on, at the subcortical level, influence hippocampal spatial processing? We will now explore these questions to identify new functional properties of the AV-RSC circuit and discuss future research avenues.

Theoretical models and experimental results indicate that HD system information is essential for grid cell firing (Brandon et al., 2011; Koenig et al., 2011) and to update place and grid cell field activity during path-integration (Winter et al., 2015; Sharp, 1999; McNaughton et al., 1995; Calton et al., 2003; Grieves et al., 2016;

Harland et al., 2017). A key feature of spatial neurons across hippocampal-entorhinal networks, including place and grid cells, is having firing rates strongly entrained by theta oscillations, which is thought to be crucial for their spatial functions (Buzsáki, 2005, 2002; Buzsáki and Moser, 2013). For this reason, it has been proposed that the subcortical HD signal may first need to be converted into a theta signal, and propagated into theta waves, in order to be integrated into downstream spatial networks (Peyrache et al., 2017; Cacucci et al., 2004; Buzsáki, 2005, 2002; Buzsáki and Moser, 2013). The AV could be seen as the first stage of this integration (theta-HD) as well as providing foundations for downstream higher levels of spatial processing in the cortex, where neurons typically express more conjunctive profiles, combining theta and HD signals with place (TPD cells; Cacucci et al., 2004), border (Peyrache et al., 2017), grid (Boccara et al., 2010) and egocentric information (EBC; LaChance and Taube, 2022; Alexander et al., 2020a).

For instance, RSC contains EBC (Alexander et al., 2020a; van Wijngaarden et al., 2020) and dRSC additionally contains conjunctive HD-EBC that combine egocentric boundary information with allocentric directionality (Alexander et al., 2020a). Both pure and conjunctive EBC show theta-modulation in their firing (see Section 2.2.2.4). According to models on spatial coordinate transformations, through combination with allocentric HD information, egocentric representations (EBC) can be anchored to the allocentric reference and be transformed into an allocentric boundary signal (border/BVC; Gofman et al., 2019; Peyrache et al., 2017; McNaughton et al., 1995; Byrne et al., 2007; Bicanski and Burgess, 2020), which in turn constructs hippocampal place fields (Hartley et al., 2000; Burgess et al., 2000). This progressive egocentric-to-allocentric transformation is illustrated in Figure 8.2.

Starting from the notion that subcortical HD information needs to reach, and be compared with, the EBC network within a theta timescale (Alexander et al., 2020a), we propose that AV Theta-by-HD cells could supply the specific directional input to EBC. Conjunctive HD-EBC in dRSC arise from this theta-paced integration, occurring predominantly via the AVVL-dRSC pathway: only AVVL projects to dRSC, and the majority of Theta-by-HD cells were recorded in AVVL (Figure 8.2).

In summary, a theta-modulated HD signal could convey more than just compass information to RSC, and directly participates in RSC ongoing computations. In the example considered here, in the generation of egocentric-to-allocentric transformations, which is a subset of a more general RSC function in memory (Mitchell et al., 2018).

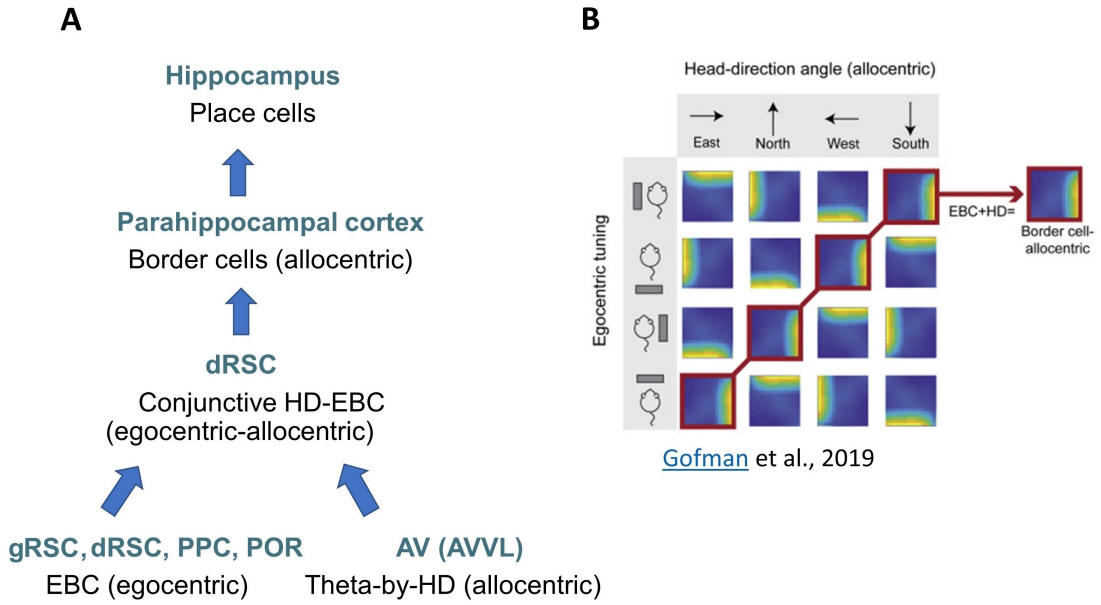


Figure 8.2: **Theta-by-HD cells as fundamental building blocks for allocentric spatial representations in hippocampus: model schematics.** **(A)** Models of spatial coordinate transformations proposed that HD information derived from subcortical pathways can be transformed into an allocentric spatial code for environmental boundaries, through combination with egocentric boundary signals. Egocentric boundary cells (EBC) are found in RSC, posterior parietal cortex (PPC) and postshinal cortex (POR). EBC and Theta-by-HD cells, both being already theta-modulated and converging on descending theta phases, are combined at theta frequencies along the AV-RSC circuit (mostly via AVVL-dRSC, where the majority of these cells were found). This conjunction generates conjunctive HD-EBC in dRSC. **(B)** Boundary related cells with no allocentric HD-component arise from the output of multiple conjunctive HD-EBC with different directional and egocentric properties. Adapted from Gofman et al. (2019). Details in Figure 2.2.

8.3 Two-stream model of the AV-RSC circuit

The general consensus has been that the AV-RSC circuit forms a theta propagating pathway, with a substantial preponderance of theta-modulated cells, while the parallel AD-RSC circuit encompasses the HD system, with a prevalence of directional neurons, ensuring the input to RSC from AV and AD is mainly theta and directional in nature, respectively. The AV receives converging inputs from RSC and MMN, and is directly interconnected with hippocampal formation. RSC corticothalamic pathways

could drive directional firing in AV by virtue of RSC positioning at the top of the hierarchical HD circuit. Projections from MMN and hippocampal regions could provide a route for the passage of theta and spatial signals via the AV.

A first dimension of our results relates to the presence of strong theta activity only in gRSC, but not in dRSC. A second dimension relates to the presence of precisely arranged AV-to-RSC projections. A third dimension relates to the surprising overlap in AV of neural signals related to spatial navigation, other than theta, namely head direction, self-position and head movements, emphasizing a role of the AV-RSC circuit in spatial processing that goes beyond a pure dienchephalic-hippocampal theta relay. Finally, a third dimension relates to the anatomical specificity of these signals within AV. Theta and HD signals are kept mostly separate in AVDM, projecting almost exclusively to gRSC, but get combined to a greater extent in AVVL, more strongly projecting to dRSC. Based on this combined anatomical and electrophysiology data, we propose a new view of the AV-RSC circuit comprising two distinct ascending information streams, whose anatomical and functional properties can be summarized as:

1. **AVDM-gRSC "relay" stream.** We recorded the highest concentration of classic HD (non-theta) and theta cells with no spatial properties in the AVDM subfield, projecting to gRSC, which is also the predominant theta and HD component of RSC. HD and theta signals are also kept separate in gRSC, where large numbers of cells are either theta- of HD-modulated. We suggest that the AVDM-gRSC subcircuit is predominantly involved in the thalamocortical relay of theta and HD signals (Lomi et al., 2021; Jacob et al., 2017). This anatomical organization, together with the overall stronger AV projections to gRSC than dRSC, may help to clarify the observed variations in theta coding between gRSC and dRSC.

2. **AVVL-dRSC/gRSC "integrative" stream.** We recorded the majority of Theta-by-HD and place cells in the AVVL subfield, projecting mostly to dRSC. In dRSC, HD information is also more highly integrated with egocentric signals from visual and parietal regions (Jacob et al., 2017; Alexander et al., 2020a). We suggest that the AVVL-dRSC subcircuit plays a more prominent role in the early integration of spatial signals within a theta frequency and in the coordination of cortical and subcortical systems via the RSC, as discussed above i.e., integration of HD (incoming from subcortical regions via gRSC) and more primary sensory information (from neocortex via dRSC).

8.4 Future works

The results of this thesis complement data from previous lesion studies, which have repeatedly demonstrated that the importance of ATN in spatial cognition cannot be attributed solely to its involvement in processing head orientation (Nelson, 2021). Our results uncovered a crucial role of AV in influencing spatial computations earlier on, at the subcortical level, offering a novel explanation for spared navigation abilities in decorticate rats (Whishaw, 1990), and preserved allocentric spatial memory in rats with full hippocampal ablations (Hollup et al., 2001; Winocur et al., 2005, 2010).

Crucially, findings open new avenues for research. Particularly, the existence of place cells in AV adds to the emerging evidence that processing of spatial location is more widespread than originally thought, occurring as early as the thalamic level. However, we still lack a comprehensive picture of the functional and structural relation between hippocampal-parahippocampal and the thalamic place cell networks. Questions remain as to how place cells in AV are formed, whether they represent spatial information differently from hippocampus, and how they might fit into our two-stream model of AV-RSC interactions. Combined lesion, electrophysiology and behavioural experiments are needed to answer these questions. It will be particularly informative to record place cells simultaneously from AV and hippocampus, compare their firing characteristics and examine remapping in different environments. We expect the locational signal of a given place cell to be environment-specific. We have proposed that HD and place cell systems provide converging inputs to the Theta-by-HD cell signal. Recordings in different environments will also allow us to assess whether locational and directional correlates of Theta-by-HD cells can be dissociated from each other and from place cell ones, as predicted from the current proposal i.e., for the same Theta-by-HD cell, place field remaps but PFD does not change in differently shaped environments.

Finally, our combined electrophysiology and anatomical data fit with a role of AV in imposing firing patterns on RSC and could explain how different information is conveyed along AV-RSC circuit(s) to hippocampus. Nevertheless, actually testing whether AV contributes to drive theta in RSC and hippocampal formation will require causal experiments. To this end, we will need to record from these cortical regions during AV inactivation to determine whether theta, and other spatial profiles such as HD and place cell firing, can be recorded independently of AV. To extend these investigations, pairing them with recordings in behavioural tasks, and comparing

the effects of AD vs AV inactivation both on downstream neurons and on learning abilities will ultimately reveal the specific contribution of AV to spatial learning.

In conclusion, results shine a new light on the importance of the AV-RSC circuit(s) within the broader memory system that receives direct innervation from this pathway. Our experiments lay the basis for exploring exciting new questions on the origin of AV spatial signals and the neural pathways allowing AV to interact with other related spatial networks. Answering these questions is expected to improve our knowledge of the processing systems and mechanisms that underlie spatial cognition and other medial temporal lobe functions.

Appendices

A

Appendices

A.1 General methods

A.1.1 Coordinates verification for AV implants

Prior to conducting Experiment 2, coordinates for AV implants were tested by doing a non-recovery surgery in one non-experimental animal, by use of bilateral neurotoxic lesions (Figure A.1). Microinfusions of 0.12M N-methyl-D-aspartate (NMDA) dissolved in phosphate buffer (pH 7.20) were made using a 1μl Hamilton syringe connected to an infusion pump, over the course of 3 minutes. A volume of 0.12μl was infused per hemisphere. The coordinates were guided based on the neurotracing results of Experiment 1. Since AV tracers were expressed consistently in the same AV subfields across AP -1.44 to -1.92, we tested different AP-coordinates in each hemisphere (-1.6 or -1.9), to determine which may give better data. In the left hemisphere, two injections were made along the same needle tract at coordinates: AP=-1.6; ML=+1.2); DV=3 and 3.6. In the right hemisphere, one injection was made at coordinates: AP=-1.9; ML=-1.5); DV=3.4 . Following histological evaluation, we concluded that the left hemisphere coordinates allowed to target AD and AVDM along the same tract. We used these coordinates for implant surgeries in Experiment 2 (Table 3.1).

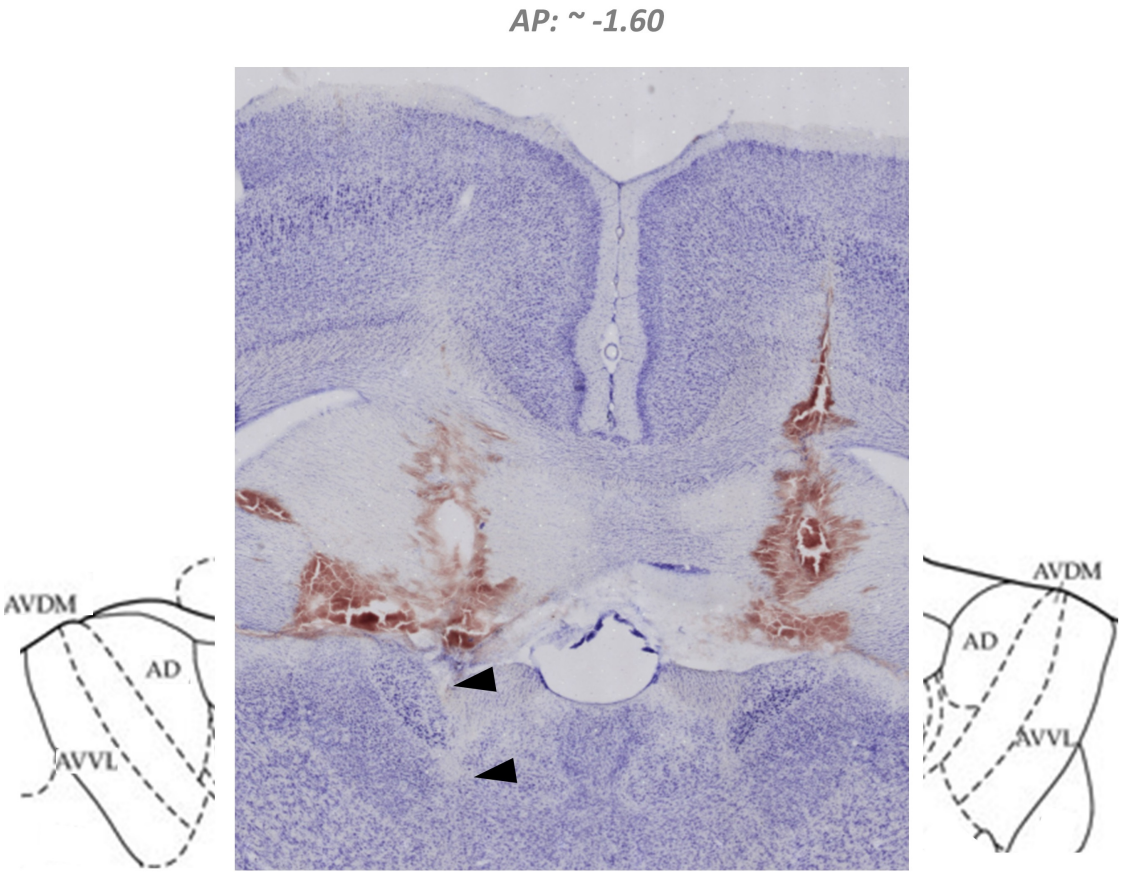


Figure A.1: **Implant coordinates verification.** Cresyl violet-stained coronal section showing the location of NMDA injections. On each side is the schematic drawing of the left and right hemisphere anterior thalamic nuclei for a coronal AP level -1.6 adapted from Paxinos and Watson (2007). Left hemisphere: injections at AP -1.6. Right hemisphere: injection at AP or -1.9. not found within the AV. Black triangles in the left hemisphere mark injections in AD and AVDM. AD and AV are anterodorsal and anteroventral thalamic nucleus; AVDM and AVVL are dorsomedial and ventrolateral subfields of AV.

A.2 Experiment 1: electrophysiology recording experiment

A.2.1 Histological considerations

For RSC implants, in Experiment 1, the AP level of the tetrodes for each rat (n=4) was inferred from the shape of the fibers of the cingulum (Cg), by referencing to the rat atlas (Paxinos and Watson, 2007). Although the shape of the hippocampus would indicate more anterior APs for R887 and R911 (i.e., AP of -4.0mm from bregma), the AP level of the actual tract in the cortex above the hippocampus is more posterior, as the caudal end of Cg disappears at a coronal AP level of -5.5mm. Moreover, for both rats, the two hemispheres are separated by the deep central sulcus, suggesting that recordings in the cortex could not have been taken from APs<-5.5mm (Figure 4.1 in the main text). Hence, given that it is possible that the brain was cut at an angle, we did not use the hippocampus shape as a guide to determine the AP.

For two animals (R602, R911) the electrodes mostly sampled superficial gRSC layers (I-IV), although we cannot exclude potential involvement of other layers. For the remaining two animals (R636, R887), sampling largely included both superficial and deep gRSC layers. These two sets of animals may also have comprised different recording sites within gRSC: while both exhibited sampling of dRSC and gRSC area b, additional gRSC area a sampling may have occurred only for the two animals with deeper implants (see main text Figure 4.1). Additional histological figures for two animals (R602 and R887) are presented in the Supplementary Figure A.2.

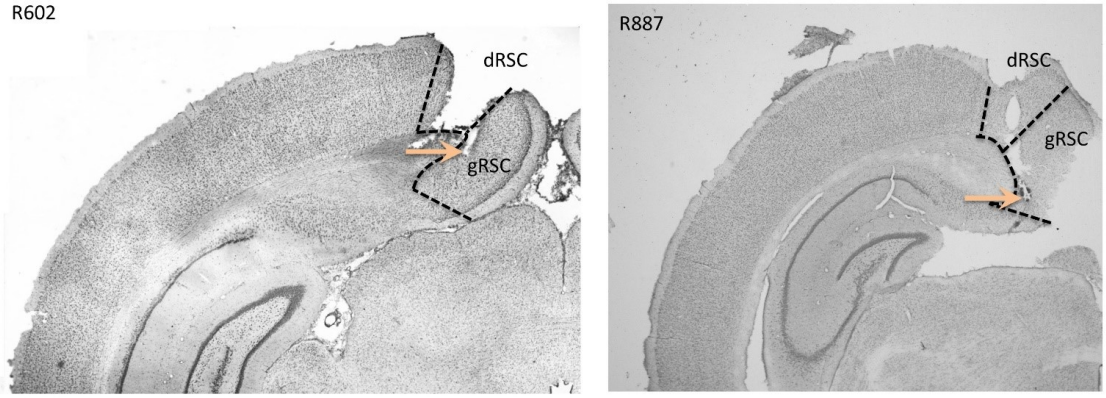


Figure A.2: **Additional RSC histology for R602 and R887.** Photomicrographs of the Nissl-stained coronal sections through the recording site. For each animal, the electrodes tract indicates that electrodes were advanced from dRSC to gRSC. The yellow arrow indicates the final electrode depth (location of electrodes tip on the day of perfusion), located within gRSC. Left, R602 (AP: -5.76); right, R887 (AP: -5.16 or -5.28). Consistent with the visual inspection of the histological slices, the majority of recordings for these two animals were conducted in dRSC. The incidence of theta-modulated cells progressively increased with the advancing of the tetrodes into gRSC. Additionally, for R887 electrodes reached white matter tract, and so no single units were recorded toward the end of recordings.

A.2.2 Phase preference analysis

For Experiment 1, within each animal (single subject analysis), theta-rhythmic cells (see Methods, IC>99^{th} percentile of shuffle distribution) in gRSC exhibited a consistent phase preference, albeit the exact preferred phase is hard to determine because theta was not measured from a fixed reference point across animals, due to different placements of the electrodes. In two animals (R636, R887), LFP-spike coupling occurred on the descending phase just before the trough of the rhythm, with preferred theta phases at 143.49° and 162.04°, and significant R-vectors of 0.75 and 0.34 (Rayleigh test, R636 (n=79): z=9.52; R887 (n=10): z=5.74; all p<0.01). In the remaining two animals (R602, R911), LFP-spike coupling occurred on the ascending phase just before the peak of the rhythm, with means at 308.69° and 343.70°, and significant R-vectors of 0.31 and 0.58 (Rayleigh test, R602 (n= 41): z=3.85, p=0.02; R911 (n=66): z=22.1, p<0.0001). Differences in preferred spiking phases between these two sets of animals are illustrated by the circular distributions (Supplementary Figure A.3). Even by eye, it is clearly apparent that preferred theta phases of theta-rhythmic cells fell in the same 180° hemisphere for two animals (n=89; WW

test, F=4.38, p>0.05), while they fell in the 0/360◦ hemisphere for the other two animals (n=107; F=0.72. p>0.05). The preferred hemisphere is highlighted on each circle. A WW test confirmed that the mean phase of the two sets of animals differed significantly from each other, suggesting firing out of phase (F=164.94, p< 0.001). The dRSC theta-rhythmic cells displayed highly variable phase preference in two animals, indicated by uniform phase distributions (Rayleigh test, R602 (n=86): z=0.03; R636 (n=7): z=1.15; all p>0.05). Only in two cases (R887, R911), dRSC theta-rhythmic cells fired consistently on the same theta phase, with means at 63.41° and 295.15°, and significant R-vectors of 0.63 and 0.89, respectively (Rayleigh test, R887 (n=13): z=5.17; R911 (n=19): z=15.2, all p<0.01). Note that for these two animals, the firing of theta cells converged on the same phase (theta troughs for R887; theta peaks for R911) for gRSC and dRSC recordings (Supplementary Figure A.3).

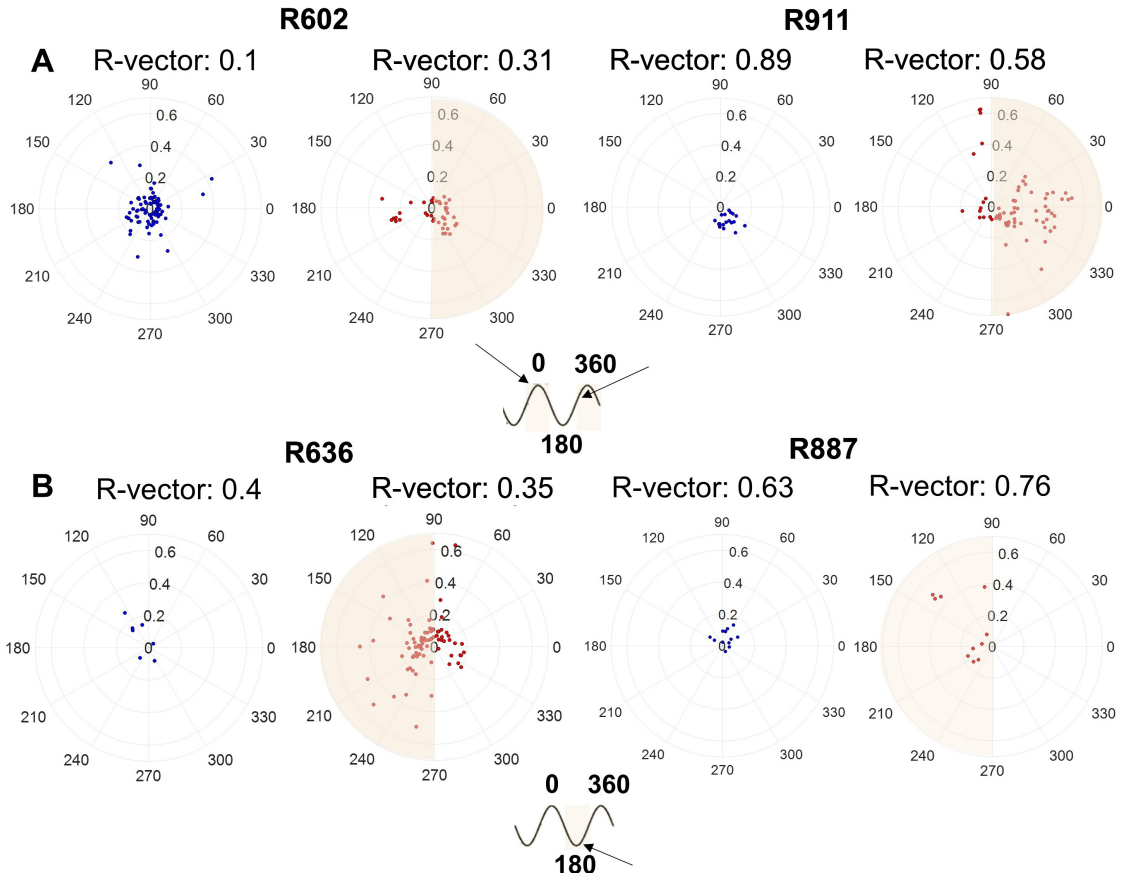


Figure A.3: **Distribution of preferred phases of single neurons.** For each animal, gRSC is shown to the right; dRSC to the left. Rat number at the top. Each marker is the preferred theta phase of a cell, and the radius of each marker is its theta-modulation depth (measured by the index of theta phase-coupling, IC). For each animal, the preferred hemisphere is highlighted. gRSC: in addition to the stronger theta modulation within each cell (markers falling further away from the

centre), across cells there was a more consistent phase preference (unimodal phase distributions within each animal). Distributions were unimodal for all animals (Rayleigh tests, all $p<0.01$). Across all gRSC cells, preferred theta phases converged in the 0° region for two animals **(A)** and in the 180° region for the other two animals **(B)**, suggesting firing on opposite peaks of the cycle between animals. dRSC: cells displayed weaker theta modulation within each cell (markers falling closer to the center). Across cells, phase preference was highly variable in half of the experimental animals (R602, R636). For R887 and R911, theta cell firing converged on a single phase in both gRSC and dRSC. A schematic diagram of results from A and B is shown below each group. A value of 180° was assigned to theta troughs and 0/360° to peaks, corresponding to opposite hemispheres in the circle.

A.3 Experiment 1: retrograde tracer experiment

A.3.1 Injection coordinates

The present section provides a summary of all injection coordinates and tracers used. In the table below, s and d indicate whether the center of the tracer deposit in RSC was located in superficial or deep layers (or both). The different AP-levels of the injections are summarized as caudal, rostral or at electrode level in the main text.

Case No.	**Injection site (electrode level)**	**Weight (g)**	**Laboratory**
222#9	dRSC s + d (-5.0mm, CTB)	297	Aggleton; Cardiff
222#10	dRSC s + d (-5.0mm, CTB)	306	Aggleton; Cardiff
077941#13	gRSC d (-5.5mm, CTB)	286	Aggleton; Cardiff
077942#14	gRSC d (-5.5mm, CTB)	227	Aggleton; Cardiff
878	dRSC s + d (-5.5mm, Ctb-488)	Unknown	Jeffery; London
878	gRSC s (d)(-5.5mm, Ctb-594)	Unknown	Jeffery; London
731	dRSC s + d (-5.5mm, FG)	Unknown	Jeffery; London
731	gRSC s + d (-5.5mm, Ctb-594)	Unknown	Jeffery; London
730	dRSC d (-5.5mm, Ctb-594)	Unknown	Jeffery; London
730	gRSC s + d (-5.55mm, FG)	Unknown	Jeffery; London
717	dRSC/M2 s + d (-5.55mm, FG)	Unknown	Jeffery; London
729	dRSC s + d (-5.5mm, FG)	Unknown	Jeffery; London
682	gRSC s (d) (-5.5mm, Ctb-594)	Unknown	Jeffery; London
Case No.	**Injection site (rostral/caudal)**	**Weight (g)**	**Laboratory**
187#9	gRSC d (s) (Rostral, BDA)	293	Aggleton; Cardiff
64#3	dRSC/M2/V2 s + d (Rostral + caudal, FB)	Unknown	Aggleton; Cardiff
172#27	dRSC (M2/V2), s + d (Rostral + caudal, FB)	Unknown	Aggleton; Cardiff
172#28	dRSC (M2/V2), s + d (Rostral + caudal, FB)	Unknown	Aggleton; Cardiff
225#4	dRSC s + d (-3.30/3.80mm, CTB)	291	Aggleton; Cardiff

225#12	dRSC s + d/gRSC d (-3.80/4.55/5.30mm, CTB)	294	Aggleton; Cardiff
223#1	dRSC s + d (-3.50/4.50mm, CTB)	321	Aggleton; Cardiff
223#4	dRSC s + d/gRSC d (-4.5mm, CTB)	329	Aggleton; Cardiff
227#22	dRSC s + d (-3.30mm, FB)	463	Aggleton; Cardiff
227#22	dRSC d (-6.80mm, CTB)	463	Aggleton; Cardiff
227#24	dRSC s + d (-3.30mm, FB)	508	Aggleton; Cardiff
227#24	gRSC d (-6.80mm, CTB)	508	Aggleton; Cardiff
227#16	dRSC d (-3.30mm, CTB)	606	Aggleton; Cardiff
227#16	dRSC s + d/gRSC d (-6.50mm, FB)	606	Aggleton; Cardiff
227#202	gRSC (dRSC), s + d (-6.3/-6.8mm), CTB)	519	Aggleton; Cardiff
227#204	gRSC s + d (-6.3/-6.8mm), CTB)	614	Aggleton; Cardiff

Table A.1: **List of all injection coordinates.** Thirteen retrograde tracer injections (n=10 animals) targeted RSC at approximately the same AP levels as the recording sites (-5.5 and -5.8 from bregma). Sixteen retrograde tracer injections (n=13 animals) targeted portions of RSC > 0.5mm rostral or caudal to the electrophysiology recording sites. AP levels determined from sections. Where the AP level is extensive, we report whether the injection targeted rostral or caudal sites, without specifying the exact AP of each injection. Weight refers to weight in grams at time of surgery. Tracers are as follows. FB, fast blue; CTB, cholera toxin subunit b; BDA, biotinylated dextran amine; FG, fluorogold.

A.3.2 Injection sites for injections made at more rostral and caudal RSC locations

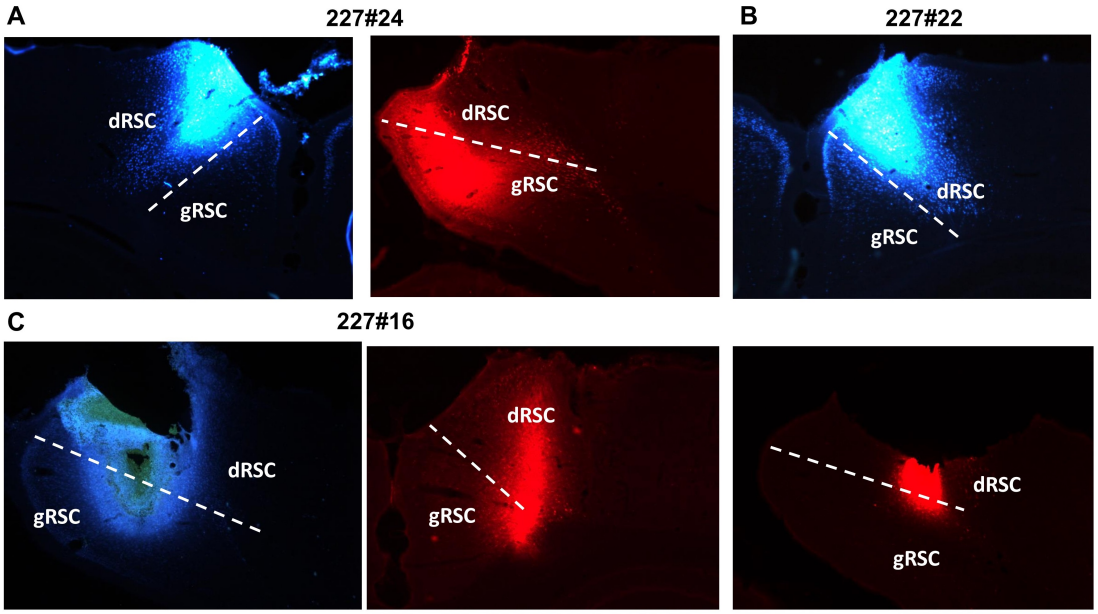


Figure A.4: **Dual retrograde tracer injections at different AP levels in the RSC.** **(A)** 227#24 Right, caudal CTB injection in gRSC (mainly deep layers); left, rostral fast blue (FB) injection in dRSC (both superficial and deep layers). **(B)** 227#22 Both injections centered in dRSC. Top, rostral FB injection (superficial and deep layers of dRSC); bottom, caudal cholera toxin subunit b (CTB) injection (deep layers of dRSC). **(C)** 227#16 Right, rostral CTB injection mainly confined to dRSC (deep layer); left, caudal FB injection in both dRSC (superficial and deep layers) and gRSC (deep layers).

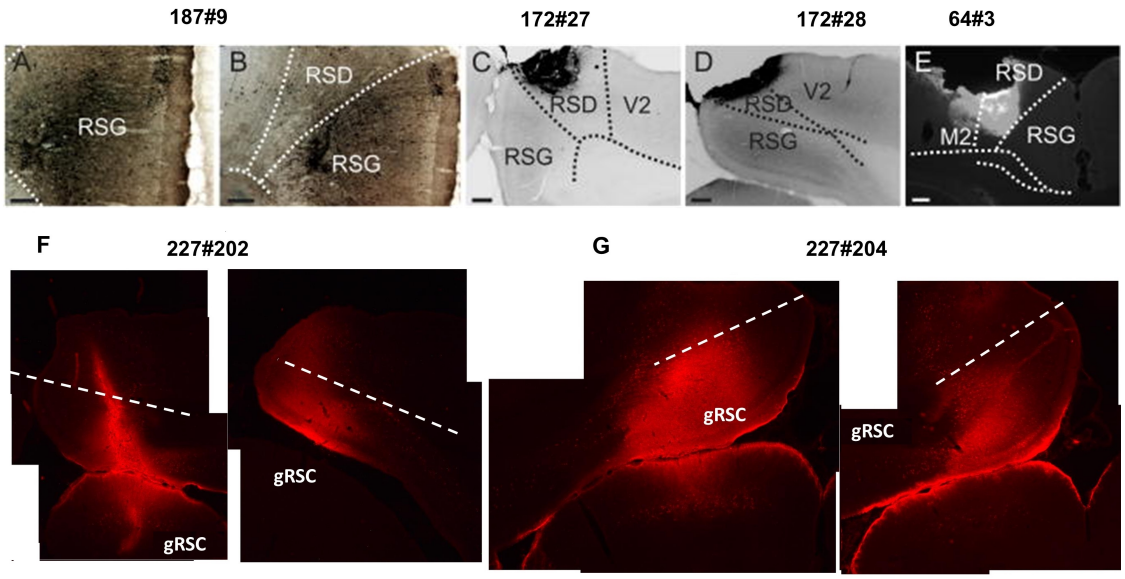


Figure A.5: **Single retrograde tracer injection in either gRSC or dRSC.** **(A-B)** 187#9 Brightfield images of the biotinylated dextran amine (BDA) injection site centered in gRSC (largely deep), adapted from Mathiasen et al. (2017). **(C-D-E)** Inverted greyscale fluorescence images of FB tracer injection in dRSC, adapted from Mathiasen et al. (2017). All layers seemingly involved. **(F-G)** 227#202, 227#204. Two CTB injection cases in caudal gRSC, all layers (superficial and deep) involved with possible weak dRSC involvement in case #202.

A.4 Experiment 2

A.4.1 Theta-by-HD do not show phase coding of HD

By comparing global and intrinsic theta frequencies for cells that displayed a significant spike time-LFP relationship (place cells; Theta-by-HD cells), we revealed a phase precession phenomena, stronger for place cells. Although an average Theta-by-HD cells fired at a rate faster than theta (phase precessed), these cells did not display phase coding of HD (Figure A.6), raising questions of what spatial dimensions is phase coded by these cells.

Phase coding was shown by plotting HD on the x-axis, shifted so the PFD is centered at zero on the x-axis, and theta phase on the y-axis. This was done separately for CW and CCW spikes to avoid raw values to cancel each other out. For a phase processing HD cell, we expect a negative linear relationship for CW turns (when

approaching the PFD from the left, phases should decrease as HD values become larger) but positive for CCW turns. Separate linear regression models were fitted to CW and CCW data and slopes were derived to quantify the rate of precession. The circular-circular correlation coefficient (matlab function circ_corrcc in the circular statistics toolbox) informs us of the error in the best fit line. The corresponding p-value was used to identify cells that were significantly phase precessing (p-value<0.01). In no instance the relationship between HD and theta phases was significant.

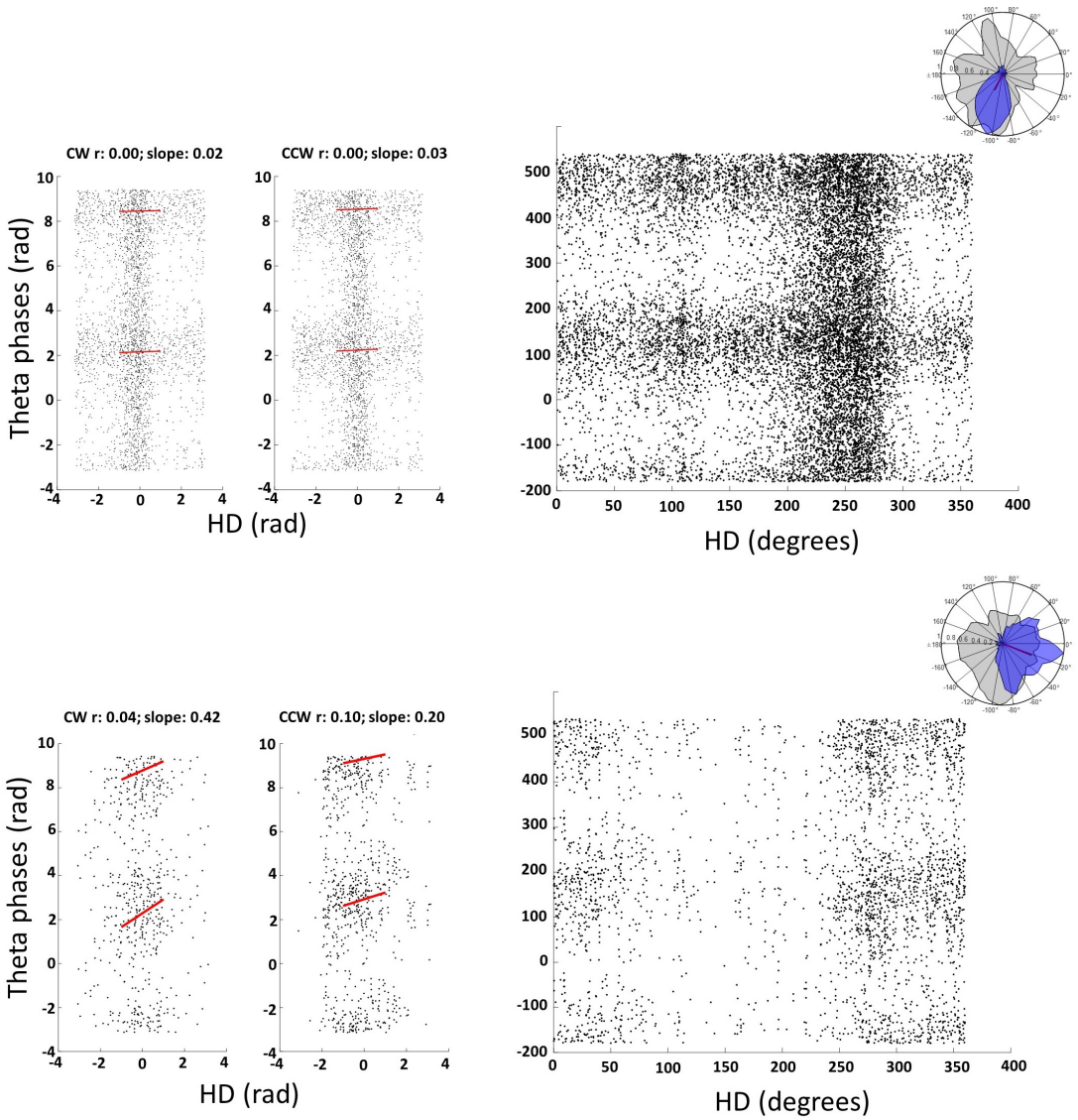


Figure A.6: Plots of theta phase vs HD for two representative Theta-by-HD cells. Right, theta phase (degrees) vs HD (degrees) for all spikes combined. Left, theta phase (radians) vs HD (radians), with PFD centered at zero, for CW (AHV>60°/s) and CCW (AHV<-60°/s) spikes. Phases are double plotted on the y-axis by generating a second set of phases, 360° offset from the first. The best fit line (red) measures the

slope of the precession rate. Cells are Theta-by-HD cells, in that they have a preferred theta phase and a PFD (reflected in the cross pattern in the spikes). For both cells, the low slope values, positive in both turn directions, indicate no significant phase coding. Circular-circular correlations and slopes are reported for each plot. Polar plots of directional tuning curve (blue) and dwelltime curve (gray) are shown at the top.

A.4.2 Differences in firing properties between narrow and broad spiking cells

We hypothesized that broad spiking cells recorded from AV might display stronger signs of hippocampal association compared to the narrow ones. In line with this prediction, broad spiking cells were more likely to fire locked to theta and display spatial correlates compared to narrow ones (Figure A.7, in red). By contrast, cells with HD, linear- and angular velocity-modulation were no more likely to be found in broad spiking cells than in narrow spiking cells (Figure A.7, in black). Additionally, we compared firing properties of cells in the two groups using multiple WRS tests. IC and locational information content were higher for broad spiking cells than narrow ones (IC: 0.18±0.02 vs 0.11±0.01; z=3.519,p<0.0001 . Locational info: 0.77±0.09 vs 0.54±0.03; z=3.191, p<0.01). The two groups had the same directional information content (0.72±0.1 vs 0.64±0.04) and angular velocity-modulation (0.22±0.02 vs 0.23±0.01; all$p$>0.1). Linear velocity-modulation was higher for narrow spiking cells than broad ones (0.46±0.03 vs 0.56±0.02; z=-6.919, p<0.0001), consistent with reports that hippocampal speed cells are interneurons. Results fit with our conclusion, explained in the main text, that AV neurons with broad spikes are more hippocampally-related than narrow ones, which instead encode place and theta signals only weakly.

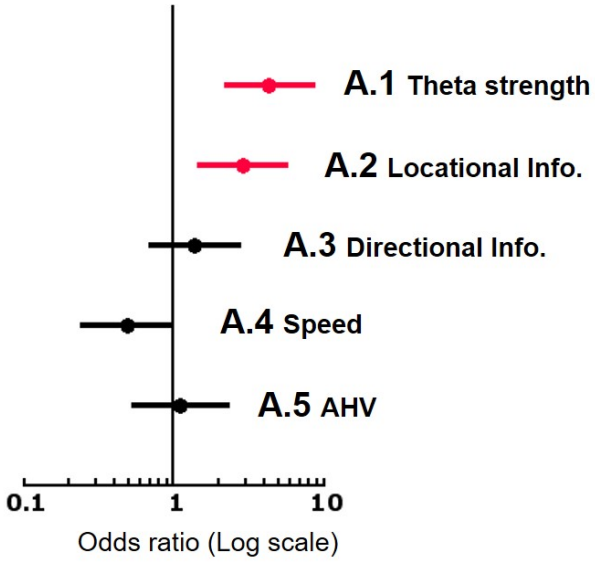


Figure A.7: Broad and narrow spiking cells have distinct firing properties. Log scale odds ratio±confidence interval, representing the odds that a specific firing property co-occurs with broad waveform, compared to the odds of that property co-occurring with narrow waveform for all AV units. 1=no effect. Odds and p-values were calculated with Fisher exact test. Hippocampus-related spiking patterns, namely theta- and spatial-modulation (in red, $p<0.0001$) were more likely to be found in broad spiking cells, and occurred independently from directional, linear- and angular velocity-modulation.

A.4.3 Visualization of spatial firing distributions

Figure A.9 displays spatial ratemaps constructed for eight different directional ranges for a (A) non-rhythmic HD and (B) Theta-by-HD cell, with locational-independent firing. Examples of place cells with (C) direction-independent firing and (D) passing the directionality threshold based on tuning curve R-vector are also displayed.

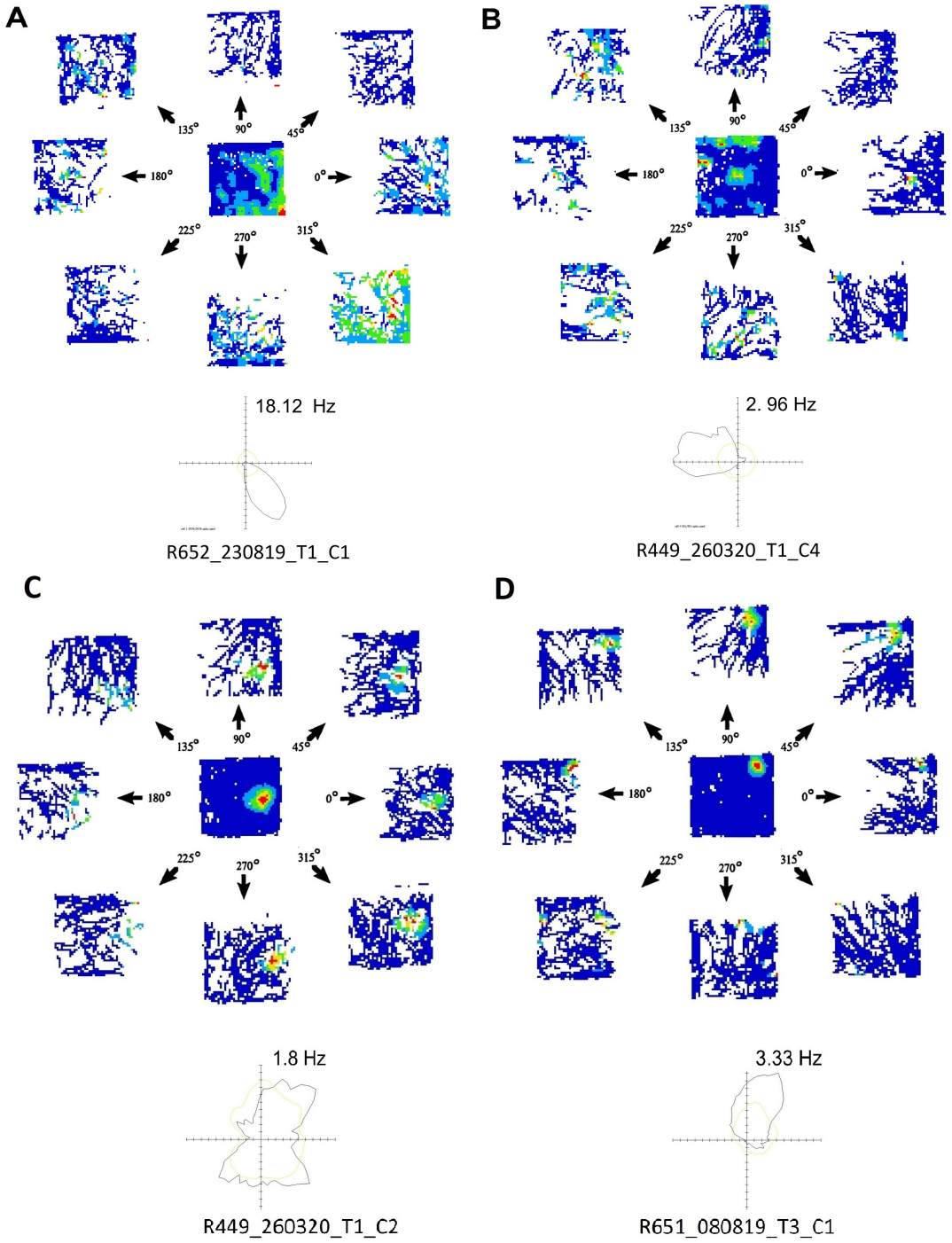


Figure A.9: **Analysis of locational firing for different orientations compared between cell groups.** Ratemaps show firing rate as a function of locational bins. The central ratemap is direction-independent; the surrounding ratemaps are plotted using only those samples from when the rat was facing a 45° directional range, noted next to each map. The respective polar plots of firing rate (Hz) vs HD (degrees) are presented at the bottom. Directional peak rate (Hz) and cell ID are reported. Cells are as follows: **(A)** non-rhythmic HD cell; **(B)** Theta-by-HD; For these cells, firing increases at a specific direction, associated to the peak of the polar plot, irrespective of locational bins. **(C)** Place cell with direction-independent firing rates. Firing increases at a specific location for all directional ranges. **(D)** Place cell with directional modulation. For this cell, firing increases at a specific location and direction. However, note that not all the locational bins were well sampled at all directional ranges, due to a tendency of the animal to approach the place field from a specific direction. This is also reflected in the polar plots as a greater overlap between the observed tuning curve (black line) and the expected tuning curve based on the proportion of time the animal spent facing each directional bin (yellow line; computed according to (Muller et al., 1994)). Place cell directionality could be explained by this sampling bias.

Bibliography

Addante, R. J., Watrous, A. J., Yonelinas, A. P., Ekstrom, A. D., and Ranganath, C. (2011). Prestimulus theta activity predicts correct source memory retrieval. *Proceedings of the National Academy of Sciences*, 108(26):10702–10707.

Aggleton, J. P. and Brown, M. W. (1999). Episodic memory, amnesia, and the hippocampal-anterior thalamic axis. *The Behavioral and Brain Sciences*, 22(3):425–489.

Aggleton, J. P., Hunt, P. R., Nagle, S., and Neave, N. (1996). The effects of selective lesions within the anterior thalamic nuclei on spatial memory in the rat. *Behavioural Brain Research*, 81(1-2):189–198.

Aggleton, J. P., O'Mara, S. M., Vann, S. D., Wright, N. F., Tsanov, M., and Erichsen, J. T. (2010). Hippocampal–anterior thalamic pathways for memory: uncovering a network of direct and indirect actions. *The European Journal of Neuroscience*, 31(12):2292–2307.

Aggleton, J. P., Pralus, A., Nelson, A. J. D., and Hornberger, M. (2016). Thalamic pathology and memory loss in early Alzheimer's disease: moving the focus from the medial temporal lobe to Papez circuit. *Brain: A Journal of Neurology*, 139(Pt 7):1877–1890.

Aggleton, J. P., Yanakieva, S., Sengpiel, F., and Nelson, A. J. (2021). The separate and combined properties of the granular (area 29) and dysgranular (area 30) retrosplenial cortex. *Neurobiology of Learning and Memory*, 185:107516.

Akaike, H. (1974). A new look at the statistical model identification. *IEEE Transactions on Automatic Control*, 19(6):716–723.

Albo, Z., Viana Di Prisco, G., and Vertes, R. P. (2003). Anterior thalamic unit discharge profiles and coherence with hippocampal theta rhythm. *Thalamus & Related Systems*, 2(2):133–144.

Alexander, A. S., Carstensen, L. C., Hinman, J. R., Raudies, F., Chapman, G. W., and Hasselmo, M. E. (2020a). Egocentric boundary vector tuning of the retrosplenial cortex. *Science Advances*, 6(8):eaaz2322.

Alexander, A. S. and Nitz, D. A. (2015). Retrosplenial cortex maps the conjunction of internal and external spaces. *Nature Neuroscience*, 18(8):1143–1151.

Alexander, A. S. and Nitz, D. A. (2017). Spatially Periodic Activation Patterns of Retrosplenial Cortex Encode Route Sub-spaces and Distance Traveled. *Current Biology*, 27(11):1551–1560.e4.

Alexander, A. S., Rangel, L. M., Tingley, D., and Nitz, D. A. (2018). Neurophysiological signatures of temporal coordination between retrosplenial cortex and the hippocampal formation. *Behavioral Neuroscience*, 132(5):453–468.

Alexander, A. S., Tung, J. C., Chapman, G. W., Shelley, L. E., Hasselmo, M. E., and Nitz, D. A. (2020b). Adaptive integration of self-motion and goals in posterior parietal cortex. *bioRxiv*, page 2020.12.19.423589.

Allen, G. V. and Hopkins, D. A. (1988). Mamillary body in the rat: A cytoarchitectonic, golgi, and ultrastructural study. *Journal of Comparative Neurology*, 275(1):39–64.

Allen, G. V. and Hopkins, D. A. (1989). Mamillary body in the rat: topography and synaptology of projections from the subicular complex, prefrontal cortex, and midbrain tegmentum. *The Journal of Comparative Neurology*, 286(3):311–336.

Amaral, D. and Lavenex, P. (2007). Hippocampal neuroanatomy. In *The hippocampus book*, pages 37–114. Oxford University Press, New York, NY, US.

Anderson, M. I. and Jeffery, K. J. (2003). Heterogeneous modulation of place cell firing by changes in context. *The Journal of Neuroscience: The Official Journal of the Society for Neuroscience*, 23(26):8827–8835.

Arcelli, P., Frassoni, C., Regondi, M. C., De Biasi, S., and Spreafico, R. (1997). GABAergic neurons in mammalian thalamus: a marker of thalamic complexity? *Brain Research Bulletin*, 42(1):27–37.

Ardid, S., Vinck, M., Kaping, D., Marquez, S., Everling, S., and Womelsdorf, T. (2015). Mapping of Functionally Characterized Cell Classes onto Canonical Circuit Operations in Primate Prefrontal Cortex. *Journal of Neuroscience*, 35(7):2975–2991.

Arleo, A., Déjean, C., Allegraud, P., Khamassi, M., Zugaro, M. B., and Wiener, S. I. (2013). Optic flow stimuli update anterodorsal thalamus head direction neuronal activity in rats. *The Journal of Neuroscience*, 33(42):16790–16795.

Aronov, D., Nevers, R., and Tank, D. W. (2017). Mapping of a non-spatial dimension by the hippocampal–entorhinal circuit. *Nature*, 543(7647):719–722.

Auger, S. and Maguire, E. (2018). Dissociating Landmark Stability from Orienting Value Using Functional Magnetic Resonance Imaging. *Journal of Cognitive Neuroscience*, 30:1–17.

Auger, S. D. and Maguire, E. A. (2013). Assessing the mechanism of response in the retrosplenial cortex of good and poor navigators. *Cortex; a Journal Devoted to the Study of the Nervous System and Behavior*, 49(10):2904–2913.

Auger, S. D., Mullally, S. L., and Maguire, E. A. (2012). Retrosplenial Cortex Codes for Permanent Landmarks. *PLOS ONE*, 7(8):e43620.

Auger, S. D., Zeidman, P., and Maguire, E. A. (2015). A central role for the retrosplenial cortex in de novo environmental learning. *eLife*, 4:e09031.

Barnett, S. C., Parr-Brownlie, L. C., Perry, B. A. L., Young, C. K., Wicky, H. E., Hughes, S. M., McNaughton, N., and Dalrymple-Alford, J. C. (2021). Anterior thalamic nuclei neurons sustain memory. *Current Research in Neurobiology*, 2:100022.

Barry, C., Hayman, R., Burgess, N., and Jeffery, K. J. (2007). Experience-dependent rescaling of entorhinal grids. *Nature Neuroscience*, 10(6):682–684.

Barry, C., Lever, C., Hayman, R., Hartley, T., Burton, S., O'Keefe, J., Jeffery, K., and Burgess, N. (2006). The boundary vector cell model of place cell firing and spatial memory. *Reviews in the Neurosciences*, 17(1-2):71–97.

Bassant, M.-H. and Poindessous-Jazat, F. (2001). Ventral tegmental nucleus of Gudden: A pontine hippocampal theta generator? *Hippocampus*, 11(6):809–813.

Bassett, J. P. and Taube, J. S. (2001). Neural Correlates for Angular Head Velocity in the Rat Dorsal Tegmental Nucleus. *Journal of Neuroscience*, 21(15):5740–5751.

Bassett, J. P., Tullman, M. L., and Taube, J. S. (2007). Lesions of the Tegmentomammillary Circuit in the Head Direction System Disrupt the Head Direction Signal in the Anterior Thalamus. *The Journal of Neuroscience*, 27(28):7564–7577.

Bassett, J. P., Wills, T. J., and Cacucci, F. (2018). Self-Organized Attractor Dynamics in the Developing Head Direction Circuit. *Current Biology*, 28(4):609–615.e3.

Belchior, H., Lopes-dos-Santos, V., Tort, A. B. L., and Ribeiro, S. (2014). Increase in hippocampal theta oscillations during spatial decision making. *Hippocampus*, 24(6):693–702.

Berens, P. (2009). CircStat: A MATLAB Toolbox for Circular Statistics. *Journal of Statistical Software*, 31(1):1–21. Number: 1.

Bicanski, A. and Burgess, N. (2016). Environmental Anchoring of Head Direction in a Computational Model of Retrosplenial Cortex. *Journal of Neuroscience*, 36(46):11601–11618.

Bicanski, A. and Burgess, N. (2020). Neuronal vector coding in spatial cognition. *Nature Reviews Neuroscience*, 21(9):453–470.

Blair, H. T., Cho, J., and Sharp, P. E. (1998). Role of the Lateral Mammillary Nucleus in the Rat Head Direction Circuit: A Combined Single Unit Recording and Lesion Study. *Neuron*, 21(6):1387–1397.

Blair, H. T., Cho, J., and Sharp, P. E. (1999). The Anterior Thalamic Head-Direction Signal Is Abolished by Bilateral But Not Unilateral Lesions of the Lateral Mammillary Nucleus. *The Journal of Neuroscience*, 19(15):6673–6683.

Blair, H. T., Lipscomb, B. W., and Sharp, P. E. (1997). Anticipatory Time Intervals of Head-Direction Cells in the Anterior Thalamus of the Rat: Implications for Path Integration in the Head-Direction Circuit. *Journal of Neurophysiology*, 78(1):145–159.

Blair, H. T. and Sharp, P. E. (1995). Anticipatory head direction signals in anterior thalamus: evidence for a thalamocortical circuit that integrates angular head motion to compute head direction. *The Journal of Neuroscience*, 15(9):6260–6270.

Blair, H. T. and Sharp, P. E. (1996). Visual and vestibular influences on head-direction cells in the anterior thalamus of the rat. *Behavioral Neuroscience*, 110(4):643–660.

Bland, B. H., Konopacki, J., Kirk, I. J., Oddie, S. D., and Dickson, C. T. (1995). Discharge patterns of hippocampal theta-related cells in the caudal diencephalon of the urethan-anesthetized rat. *Journal of Neurophysiology*, 74(1):322–333.

Boccara, C. N., Sargolini, F., Thoresen, V. H., Solstad, T., Witter, M. P., Moser, E. I., and Moser, M.-B. (2010). Grid cells in pre- and parasubiculum. *Nature Neuroscience*, 13(8):987–994.

Bohbot, V. D., Copara, M. S., Gotman, J., and Ekstrom, A. D. (2017). Low-frequency theta oscillations in the human hippocampus during real-world and virtual navigation. *Nature Communications*, 8:14415.

Bonnevie, T., Dunn, B., Fyhn, M., Hafting, T., Derdikman, D., Kubie, J. L., Roudi, Y., Moser, E. I., and Moser, M.-B. (2013). Grid cells require excitatory drive from the hippocampus. *Nature Neuroscience*, 16(3):309–317.

Borst, J. G., Leung, L. W., and MacFabe, D. F. (1987). Electrical activity of the cingulate cortex. II. Cholinergic modulation. *Brain Research*, 407(1):81–93.

Bowman, A. W. and Azzalini, A. (1997). *Applied Smoothing Techniques for Data Analysis: The Kernel Approach with S-Plus Illustrations*. Oxford Statistical Science Series. Oxford University Press, Oxford, New York.

Braak, H. and Braak, E. (1991). Neuropathological stageing of Alzheimer-related changes. *Acta Neuropathologica*, 82(4):239–259.

Brandon, M. P., Bogaard, A. R., Libby, C. P., Connerney, M. A., Gupta, K., and Hasselmo, M. E. (2011). Reduction of theta rhythm dissociates grid cell spatial periodicity from directional tuning. *Science (New York, N.Y.)*, 332(6029):595–599.

Brandon, M. P., Bogaard, A. R., Schultheiss, N. W., and Hasselmo, M. E. (2013). Segregation of cortical head direction cell assemblies on alternating theta cycles. *Nature Neuroscience*, 16(6):739–748.

Brandon, M. P., Koenig, J., Leutgeb, J. K., and Leutgeb, S. (2014). New and distinct hippocampal place codes are generated in a new environment during septal inactivation. *Neuron*, 82(4):789–796.

Brennan, E. K., Jedrasiak-Cape, I., Kailasa, S., Rice, S. P., Sudhakar, S. K., and Ahmed, O. J. (2021). Thalamus and claustrum control parallel layer 1 circuits in retrosplenial cortex. *eLife*, 10:e62207. Publisher: eLife Sciences Publications, Ltd.

Brennan, E. K., Sudhakar, S. K., Jedrasiak-Cape, I., John, T. T., and Ahmed, O. J. (2020). Hyperexcitable Neurons Enable Precise and Persistent Information Encoding in the Superficial Retrosplenial Cortex. *Cell Reports*, 30(5):1598–1612.e8.

Bubb, E. J., Kinnavane, L., and Aggleton, J. P. (2017). Hippocampal–diencephalic–cingulate networks for memory and emotion: An anatomical guide. *Brain and Neuroscience Advances*, 1:2398212817723443.

Buckley, M. J. and Mitchell, A. S. (2016). Retrosplenial Cortical Contributions to Anterograde and Retrograde Memory in the Monkey. *Cerebral Cortex (New York, N.Y.: 1991)*, 26(6):2905–2918.

Buckwalter, J. A., Parvizi, J., Morecraft, R. J., and Van Hoesen, G. W. (2008). Thalamic Projections to the Posteromedial Cortex in the Macaque. *The Journal of Comparative Neurology*, 507(5):1709–1733.

Burak, Y. and Fiete, I. R. (2009). Accurate Path Integration in Continuous Attractor Network Models of Grid Cells. *PLOS Computational Biology*, 5(2):e1000291.

Burgess, N., Barry, C., and O'Keefe, J. (2007). An oscillatory interference model of grid cell firing. *Hippocampus*, 17(9):801–812.

Burgess, N., Cacucci, F., Lever, C., and O'keefe, J. (2005). Characterizing multiple independent behavioral correlates of cell firing in freely moving animals. *Hippocampus*, 15(2):149–153.

Burgess, N., Jackson, A., Hartley, T., and O'Keefe, J. (2000). Predictions derived from modelling the hippocampal role in navigation. *Biological Cybernetics*, 83(3):301–312.

Burgess, N., Maguire, E. A., and O'Keefe, J. (2002). The human hippocampus and spatial and episodic memory. *Neuron*, 35(4):625–641.

Burgess, N. and O'Keefe, J. (2011). Models of place and grid cell firing and theta rhythmicity. *Current Opinion in Neurobiology*, 21(5):734–744.

Bush, D., Ólafsdóttir, H. F., Barry, C., and Burgess, N. (2022). Ripple band phase precession of place cell firing during replay. *Current Biology*, 32(1):64–73.e5.

Butler, W. N., Smith, K. S., van der Meer, M. A. A., and Taube, J. S. (2017). The Head-Direction Signal Plays a Functional Role as a Neural Compass during Navigation. *Current biology: CB*, 27(9):1259–1267.

Buzsáki, G. (2002). Theta Oscillations in the Hippocampus. *Neuron*, 33(3):325–340.

Buzsáki, G. (2005). Theta rhythm of navigation: link between path integration and landmark navigation, episodic and semantic memory. *Hippocampus*, 15(7):827–840.

Buzsáki, G., Lai-Wo S., L., and Vanderwolf, C. H. (1983). Cellular bases of hippocampal EEG in the behaving rat. *Brain Research Reviews*, 6(2):139–171.

Buzsáki, G. and Moser, E. I. (2013). Memory, navigation and theta rhythm in the hippocampal-entorhinal system. *Nature Neuroscience*, 16(2):130–138.

Byrne, P., Becker, S., and Burgess, N. (2007). Remembering the past and imagining the future. *Psychological review*, 114(2):340–375.

Cacucci, F., Lever, C., Wills, T. J., Burgess, N., and O'Keefe, J. (2004). Theta-modulated place-by-direction cells in the hippocampal formation in the rat. *The Journal of Neuroscience*, 24(38):8265–8277.

Calton, J. L., Stackman, R. W., Goodridge, J. P., Archey, W. B., Dudchenko, P. A., and Taube, J. S. (2003). Hippocampal Place Cell Instability after Lesions of the Head Direction Cell Network. *Journal of Neuroscience*, 23(30):9719–9731.

Caplan, J. B., Madsen, J. R., Raghavachari, S., and Kahana, M. J. (2001). Distinct patterns of brain oscillations underlie two basic parameters of human maze learning. *Journal of Neurophysiology*, 86(1):368–380.

Caplan, J. B., Madsen, J. R., Schulze-Bonhage, A., Aschenbrenner-Scheibe, R., Newman, E. L., and Kahana, M. J. (2003). Human Oscillations Related to Sensorimotor Integration and Spatial Learning. *Journal of Neuroscience*, 23(11):4726–4736.

Cenquizca, L. and Swanson, L. (2007). Spatial Organization of Direct Hippocampal Field CA1 Axonal Projections To the Rest of the Cerebral Cortex. *Brain research reviews*, 56:1–26.

Chambers, A. R., Berge, C. N., and Vervaeke, K. (2021). Cell-type-specific silence in thalamocortical circuits precedes hippocampal sharp-wave ripples. *bioRxiv*, page 2021.05.05.442741.

Chen, L. L., Lin, L. H., Barnes, C. A., and McNaughton, B. L. (1994a). Head-direction cells in the rat posterior cortex. II. Contributions of visual and ideothetic information to the directional firing. *Experimental Brain Research*, 101(1):24–34.

Chen, L. L., Lin, L. H., Green, E. J., Barnes, C. A., and McNaughton, B. L. (1994b). Head-direction cells in the rat posterior cortex. I. Anatomical distribution and behavioral modulation. *Experimental Brain Research*, 101(1):8–23.

Cho, J. and Sharp, P. (2001). Head direction, place, and movement correlates for cells in the rat retrosplenial cortex. *Behavioral neuroscience*, 115:3–25.

Christiansen, K., Dillingham, C. M., Wright, N. F., Saunders, R. C., Vann, S. D., and Aggleton, J. P. (2016). Complementary subicular pathways to the anterior thalamic nuclei and mammillary bodies in the rat and macaque monkey brain. *The European Journal of Neuroscience*, 43(8):1044–1061.

Clark, B. J., Bassett, J. P., Wang, S. S., and Taube, J. S. (2010). Impaired head direction cell representation in the anterodorsal thalamus after lesions of the retrosplenial cortex. *The Journal of Neuroscience*, 30(15):5289–5302.

Clark, B. J., Sarma, A., and Taube, J. S. (2009). Head Direction Cell Instability in the Anterior Dorsal Thalamus after Lesions of the Interpeduncular Nucleus. *The Journal of Neuroscience*, 29(2):493–507.

Clark, B. J. and Taube, J. S. (2011). Intact Landmark Control and Angular Path Integration by Head Direction Cells in the Anterodorsal Thalamus After Lesions of the Medial Entorhinal Cortex. *Hippocampus*, 21(7):767–782.

Climer, J. R., DiTullio, R., Newman, E. L., Hasselmo, M. E., and Eden, U. T. (2015). Examination of rhythmicity of extracellularly recorded neurons in the entorhinal cortex. *Hippocampus*, 25(4):460–473.

Cooper, B. G., Manka, T. F., and Mizumori, S. J. Y. (2001). Finding your way in the dark: The retrosplenial cortex contributes to spatial memory and navigation without visual cues. *Behavioral Neuroscience*, 115(5):1012–1028.

Cooper, B. G. and Mizumori, S. J. (1999). Retrosplenial cortex inactivation selectively impairs navigation in darkness. *Neuroreport*, 10(3):625–630.

Cooper, B. G. and Mizumori, S. J. (2001). Temporary inactivation of the retrosplenial cortex causes a transient reorganization of spatial coding in the hippocampus. *The Journal of Neuroscience*, 21(11):3986–4001.

Cruce, J. A. (1977). An autoradiographic study of the descending connections of the mammillary nuclei of the rat. *The Journal of Comparative Neurology*, 176(4):631–644.

Csicsvari, J., Hirase, H., Czurkó, A., Mamiya, A., and Buzsáki, G. (1999). Oscillatory Coupling of Hippocampal Pyramidal Cells and Interneurons in the Behaving Rat. *The Journal of Neuroscience*, 19(1):274–287.

Czajkowski, R., Sugar, J., Zhang, S.-J., Couey, J. J., Ye, J., and Witter, M. P. (2013). Superficially Projecting Principal Neurons in Layer V of Medial Entorhinal Cortex in the Rat Receive Excitatory Retrosplenial Input. *Journal of Neuroscience*, 33(40):15779–15792.

De Biasi, S., Arcelli, P., and Spreafico, R. (1994). Parvalbumin immunoreactivity in the thalamus of guinea pig: light and electron microscopic correlation with gamma-aminobutyric acid immunoreactivity. *The Journal of Comparative Neurology*, 348(4):556–569.

Deshmukh, S. S., Yoganarasimha, D., Voicu, H., and Knierim, J. J. (2010). Theta modulation in the medial and the lateral entorhinal cortices. *Journal of Neurophysiology*, 104(2):994–1006.

Dillingham, C. M., Milczarek, M. M., Perry, J. C., Frost, B. E., Parker, G. D., Assaf, Y., Sengpiel, F., O'Mara, S. M., and Vann, S. D. (2019). Mammillothalamic disconnection alters hippocampo-cortical oscillatory activity and microstructure: Implications for diencephalic amnesia. *Journal of Neuroscience*.

Dillingham, C. M. and Vann, S. D. (2019). Why Isn't the Head Direction System Necessary for Direction? Lessons From the Lateral Mammillary Nuclei. *Frontiers in Neural Circuits*, 13:60.

Doeller, C. F., Barry, C., and Burgess, N. (2010). Evidence for grid cells in a human memory network. *Nature*, 463(7281):657–661.

Douchamps, V., Jeewajee, A., Blundell, P., Burgess, N., and Lever, C. (2013). Evidence for Encoding versus Retrieval Scheduling in the Hippocampus by Theta Phase and Acetylcholine. *Journal of Neuroscience*, 33(20):8689–8704.

Dragoi, G. and Buzsáki, G. (2006). Temporal Encoding of Place Sequences by Hippocampal Cell Assemblies. *Neuron*, 50(1):145–157.

Dudchenko, P. A., Goodridge, J. P., and Taube, J. S. (1997). The effects of disorientation on visual landmark control of head direction cell orientation. *Experimental Brain Research*, 115(2):375–380.

Dumont, J. R., Amin, E., Poirier, G. L., Albasser, M. M., and Aggleton, J. P. (2012). Anterior thalamic nuclei lesions in rats disrupt markers of neural plasticity in distal limbic brain regions. *Neuroscience*, 224:81–101.

Dupire, A., Kant, P., Mons, N., Marchand, A. R., Coutureau, E., Dalrymple-Alford, J., and Wolff, M. (2013). A role for anterior thalamic nuclei in affective cognition: Interaction with environmental conditions. *Hippocampus*, 23(5):392–404.

Duvelle, l., Grieves, R. M., Hok, V., Poucet, B., Arleo, A., Jeffery, K. J., and Save, E. (2019). Insensitivity of Place Cells to the Value of Spatial Goals in a Two-Choice Flexible Navigation Task. *Journal of Neuroscience*, 39(13):2522–2541.

Ebbesen, C. L., Reifenstein, E. T., Tang, Q., Burgalossi, A., Ray, S., Schreiber, S., Kempter, R., and Brecht, M. (2016). Cell Type-Specific Differences in Spike Timing and Spike Shape in the Rat Parasubiculum and Superficial Medial Entorhinal Cortex. *Cell Reports*, 16(4):1005–1015.

Ekstrom, A. D., Kahana, M. J., Caplan, J. B., Fields, T. A., Isham, E. A., Newman, E. L., and Fried, I. (2003). Cellular networks underlying human spatial navigation. *Nature*, 425(6954):184–188. Bandiera_abtest: a Cg_type: Nature Research Journals Number: 6954 Primary_atype: Research Publisher: Nature Publishing Group.

Eliav, T., Geva-Sagiv, M., Yartsev, M. M., Finkelstein, A., Rubin, A., Las, L., and Ulanovsky, N. (2018). Nonoscillatory Phase Coding and Synchronization in the Bat Hippocampal Formation. *Cell*, 175(4):1119–1130.e15.

Epstein, R. A., Patai, E. Z., Julian, J. B., and Spiers, H. J. (2017). The cognitive map in humans: Spatial navigation and beyond. *Nature Neuroscience*, 20(11):1504–1513.

Etienne, A. S. and Jeffery, K. J. (2004). Path integration in mammals. *Hippocampus*, 14(2):180–192.

Etienne, A. S., Maurer, R., and Séguinot, V. (1996). Path integration in mammals and its interaction with visual landmarks. *The Journal of Experimental Biology*, 199(Pt 1):201–209.

Etienne, A. S., Teroni, E., Hurni, C., and Portenier, V. (1990). The effect of a single light cue on homing behaviour of the golden hamster. *Animal Behaviour*, 39(1):17–41.

Fanselow, E. E., Sameshima, K., Baccala, L. A., and Nicolelis, M. A. L. (2001). Thalamic bursting in rats during different awake behavioral states. *Proceedings of the National Academy of Sciences of the United States of America*, 98(26):15330–15335.

Fenton, A. A., Kao, H.-Y., Neymotin, S. A., Olypher, A., Vayntrub, Y., Lytton, W. W., and Ludvig, N. (2008). Unmasking the CA1 Ensemble Place Code by Exposures to Small and Large Environments: More Place Cells and Multiple, Irregularly Arranged, and Expanded Place Fields in the Larger Space. *Journal of Neuroscience*, 28(44):11250–11262.

Fernández-Ruiz, A., Oliva, A., Nagy, G. A., Maurer, A. P., Berényi, A., and Buzsáki, G. (2017). Entorhinal–CA3 dual-input control of spike timing in the hippocampus by theta-gamma coupling. *Neuron*, 93(5):1213–1226.e5.

Fischer, L. F., Mojica Soto-Albors, R., Buck, F., and Harnett, M. T. (2020). Representation of visual landmarks in retrosplenial cortex. *eLife*, 9:e51458.

Fisher, N. I. (1993). *Statistical Analysis of Circular Data*. Cambridge University Press, Cambridge.

Fox, S. E., Wolfson, S., and Ranck, J. B. (1986). Hippocampal theta rhythm and the firing of neurons in walking and urethane anesthetized rats. *Experimental Brain Research*, 62(3):495–508.

Frank, L. M., Brown, E. N., and Wilson, M. A. (2001). A Comparison of the Firing Properties of Putative Excitatory and Inhibitory Neurons From CA1 and the Entorhinal Cortex. *Journal of Neurophysiology*, 86(4):2029–2040.

Frost, B. E., Martin, S. K., Cafalchio, M., Islam, M. N., Aggleton, J. P., and O'Mara, S. M. (2021). Anterior Thalamic Inputs Are Required for Subiculum Spatial Coding, with Associated Consequences for Hippocampal Spatial Memory. *Journal of Neuroscience*, 41(30):6511–6525.

Fyhn, M., Hafting, T., Treves, A., Moser, M.-B., and Moser, E. I. (2007). Hippocampal remapping and grid realignment in entorhinal cortex. *Nature*, 446(7132):190–194.

Gabriel, M. (1993). Discriminative Avoidance Learning: A Model System. In Vogt, B. A. and Gabriel, M., editors, *Neurobiology of Cingulate Cortex and Limbic Thalamus: A Comprehensive Handbook*, pages 478–523. Birkhäuser, Boston, MA.

Gabriel, M., Sparenborg, S. P., and Stolar, N. (1987). Hippocampal control of cingulate cortical and anterior thalamic information processing during learning in rabbits. *Experimental Brain Research*, 67(1):131–152.

Gaffan, E. A., Gaffan, D., and Hodges, J. R. (1991). Amnesia following damage to the left fornix and to other sites. A comparative study. *Brain: A Journal of Neurology*, 114 (Pt 3):1297–1313.

Gallistel, C. R. (1990). *The organization of learning*. The organization of learning. The MIT Press, Cambridge, MA, US. Pages: viii, 648.

Games, P. A., Keselman, H. J., and Clinch, J. J. (1979). Tests for homogeneity of variance in factorial designs. *Psychological Bulletin*, 86(5):978–984.

Gardner, R. J., Hermansen, E., Pachitariu, M., Burak, Y., Baas, N. A., Dunn, B. A., Moser, M.-B., and Moser, E. I. (2022). Toroidal topology of population activity in grid cells. *Nature*, 602(7895):123–128.

Gener, T., Perez-Mendez, L., and Sanchez-Vives, M. V. (2013). Tactile modulation of hippocampal place fields. *Hippocampus*, 23(12):1453–1462.

Giocomo, L. M., Stensola, T., Bonnevie, T., Van Cauter, T., Moser, M.-B., and Moser, E. I. (2014). Topography of head direction cells in medial entorhinal cortex. *Current Biology: CB*, 24(3):252–262.

Góis, Z. H. T. D. and Tort, A. B. L. (2018). Characterizing Speed Cells in the Rat Hippocampus. *Cell Reports*, 25(7):1872–1884.e4.

Gofman, X., Tocker, G., Weiss, S., Boccara, C. N., Lu, L., Moser, M.-B., Moser, E. I., Morris, G., and Derdikman, D. (2019). Dissociation between Postrhinal Cortex and Downstream Parahippocampal Regions in the Representation of Egocentric Boundaries. *Current Biology*, 29(16):2751–2757.e4.

Golob, E. J. and Taube, J. S. (1997). Head direction cells and episodic spatial information in rats withoutahippocampus. *Proceedings of the National Academy of Sciences of the United States of America*, 94(14):7645–7650.

Golob, E. J., Wolk, D. A., and Taube, J. S. (1998). Recordings of postsubiculum head direction cells following lesions of the laterodorsal thalamic nucleus. *Brain Research*, 780(1):9–19.

Gonzalo-Ruiz, A., Alonso, A., Sanz, J. M., and Llinás, R. R. (1992). Afferent projections to the mammillary complex of the rat, with special reference to those from surrounding hypothalamic regions. *The Journal of Comparative Neurology*, 321(2):277–299.

Gonzalo-Ruiz, A., Sanz, J. M., and Lieberman, A. R. (1996). Immunohistochemical studies of localization and co-localization of glutamate, aspartate and GABA in the anterior thalamic nuclei, retrosplenial granular cortex, thalamic reticular nucleus and mammillary nuclei of the rat. *Journal of Chemical Neuroanatomy*, 12(2):77–84.

Goodridge, J. P., Dudchenko, P. A., Worboys, K. A., Golob, E. J., and Taube, J. S. (1998). Cue control and head direction cells. *Behavioral Neuroscience*, 112(4):749–761.

Goodridge, J. P. and Taube, J. S. (1995). Preferential use of the landmark navigational system by head direction cells in rats. *Behavioral Neuroscience*, 109(1):49–61.

Goodridge, J. P. and Taube, J. S. (1997). Interaction between the postsubiculum and anterior thalamus in the generation of head direction cell activity. *The Journal of Neuroscience*, 17(23):9315–9330.

Gothard, K. M., Skaggs, W. E., and McNaughton, B. L. (1996). Dynamics of Mismatch Correction in the Hippocampal Ensemble Code for Space: Interaction between Path Integration and Environmental Cues. *Journal of Neuroscience*, 16(24):8027–8040.

Greenstein, Y. J., Pavlides, C., and Winson, J. (1988). Long-term potentiation in the dentate gyrus is preferentially induced at theta rhythm periodicity. *Brain Research*, 438(1-2):331–334.

Grieves, R. M., Jedidi-Ayoub, S., Mishchanchuk, K., Liu, A., Renaudineau, S., and Jeffery, K. J. (2020). The place-cell representation of volumetric space in rats. *Nature Communications*, 11(1):789.

Grieves, R. M., Jenkins, B. W., Harland, B. C., Wood, E. R., and Dudchenko, P. A. (2016). Place field repetition and spatial learning in a multicompartment environment. *Hippocampus*, 26(1):118–134.

Hafting, T., Fyhn, M., Bonnevie, T., Moser, M.-B., and Moser, E. I. (2008). Hippocampus-independent phase precession in entorhinal grid cells. *Nature*, 453(7199):1248–1252.

Hafting, T., Fyhn, M., Molden, S., Moser, M.-B., and Moser, E. I. (2005). Microstructure of a spatial map in the entorhinal cortex. *Nature*, 436(7052):801–806.

Hangya, B., Borhegyi, Z., Szilágyi, N., Freund, T. F., and Varga, V. (2009). GABAergic neurons of the medial septum lead the hippocampal network during theta activity. *The Journal of Neuroscience*, 29(25):8094–8102.

Harding, A., Halliday, G., Caine, D., and Kril, J. (2000). Degeneration of anterior thalamic nuclei differentiates alcoholics with amnesia. *Brain: A Journal of Neurology*, 123 (Pt 1):141–154.

Hargreaves, E. L., Yoganarasimha, D., and Knierim, J. J. (2007). Cohesiveness of spatial and directional representations recorded from neural ensembles in the anterior thalamus, parasubiculum, medial entorhinal cortex, and hippocampus. *Hippocampus*, 17(9):826–841.

Harland, B., Contreras, M., Souder, M., and Fellous, J.-M. (2021). Dorsal CA1 hippocampal place cells form a multi-scale representation of megaspace. *Current biology: CB*, 31(10):2178–2190.e6.

Harland, B., Grieves, R. M., Bett, D., Stentiford, R., Wood, E. R., and Dudchenko, P. A. (2017). Lesions of the Head Direction Cell System Increase Hippocampal Place Field Repetition. *Current Biology*, 27(17):2706–2712.e2.

Hartley, T., Burgess, N., Lever, C., Cacucci, F., and O'Keefe, J. (2000). Modeling place fields in terms of the cortical inputs to the hippocampus. *Hippocampus*, 10(4):369–379.

Hartley, T., Lever, C., Burgess, N., and O'Keefe, J. (2014). Space in the brain: how the hippocampal formation supports spatial cognition. *Philosophical Transactions of the Royal Society B: Biological Sciences*, 369(1635):20120510.

Hasselmo, M. E. (2005). What is the function of hippocampal theta rhythm?–Linking behavioral data to phasic properties of field potential and unit recording data. *Hippocampus*, 15(7):936–949.

Hasselmo, M. E., Bodelón, C., and Wyble, B. P. (2002). A proposed function for hippocampal theta rhythm: separate phases of encoding and retrieval enhance reversal of prior learning. *Neural Computation*, 14(4):793–817.

Hasselmo, M. E. and Eichenbaum, H. (2005). Hippocampal mechanisms for the context-dependent retrieval of episodes. *Neural Networks: The Official Journal of the International Neural Network Society*, 18(9):1172–1190.

Haugland, K. G., Sugar, J., and Witter, M. P. (2019). Development and topographical organization of projections from the hippocampus and parahippocampus to the retrosplenial cortex. *European Journal of Neuroscience*, 50(1):1799–1819.

Henze, D. A., Borhegyi, Z., Csicsvari, J., Mamiya, A., Harris, K. D., and Buzsáki, G. (2000). Intracellular features predicted by extracellular recordings in the hippocampus in vivo. *Journal of Neurophysiology*, 84(1):390–400.

Hill, A. J. and Best, P. J. (1981). Effects of deafness and blindness on the spatial correlates of hippocampal unit activity in the rat. *Experimental Neurology*, 74(1):204–217.

Hindley, E., Nelson, A., Aggleton, J., and Vann, S. (2014). The rat retrosplenial cortex is required when visual cues are used flexibly to determine location. *Behavioural Brain Research*, 263(100):98–107.

Hinman, J. R., Brandon, M. P., Climer, J. R., Chapman, G. W., and Hasselmo, M. E. (2016). Multiple running speed signals in medial entorhinal cortex. *Neuron*, 91(3):666–679.

Hinman, J. R., Chapman, G. W., and Hasselmo, M. E. (2019). Neuronal representation of environmental boundaries in egocentric coordinates. *Nature Communications*, 10(1):2772.

Hölscher, C., Anwyl, R., and Rowan, M. J. (1997). Stimulation on the Positive Phase of Hippocampal Theta Rhythm Induces Long-Term Potentiation That Can Be Depotentiated by Stimulation on the Negative Phase in Area CA1 In Vivo. *Journal of Neuroscience*, 17(16):6470–6477.

Hok, V., Jacob, P.-Y., Bordiga, P., Truchet, B., Poucet, B., and Save, E. (2018). A spatial code in the dorsal lateral geniculate nucleus. *bioRxiv*, page 473520.

Hollup, S. A., Kjelstrup, K. G., Hoff, J., Moser, M.-B., and Moser, E. I. (2001). Impaired Recognition of the Goal Location during Spatial Navigation in Rats with Hippocampal Lesions. *The Journal of Neuroscience*, 21(12):4505–4513.

Huang, L.-W., Simonnet, J., Nassar, M., Richevaux, L., Lofredi, R., and Fricker, D. (2017). Laminar Localization and Projection-Specific Properties of Presubicular Neurons Targeting the Lateral Mammillary Nucleus, Thalamus, or Medial Entorhinal Cortex. *eNeuro*, 4(2):ENEURO.0370–16.2017.

Huerta, P. T. and Lisman, J. E. (1993). Heightened synaptic plasticity of hippocampal CA1 neurons during a Cholinergically induced rhythmic state. *Nature*, 364(6439):723–725.

Huerta, P. T. and Lisman, J. E. (1995). Bidirectional synaptic plasticity induced by a single burst during cholinergic theta oscillation in CA1 in vitro. *Neuron*, 15(5):1053–1063.

Huerta, P. T. and Lisman, J. E. (1996). Synaptic plasticity during the cholinergic theta-frequency oscillation in vitro. *Hippocampus*, 6(1):58–61.

Hyman, J. M., Wyble, B. P., Goyal, V., Rossi, C. A., and Hasselmo, M. E. (2003). Stimulation in hippocampal region CA1 in behaving rats yields long-term potentiation when delivered to the peak of theta and long-term depression when delivered to the trough. *The Journal of Neuroscience*, 23(37):11725–11731.

Ishizuka, N. (2001). Laminar organization of the pyramidal cell layer of the subiculum in the rat. *The Journal of Comparative Neurology*, 435(1):89–110.

Jacob, P.-Y., Casali, G., Spieser, L., Page, H., Overington, D., and Jeffery, K. (2017). An independent, landmark-dominated head direction signal in dysgranular retrosplenial cortex. *Nature neuroscience*, 20(2):173–175.

Jacob, P.-Y., Van Cauter, T., Poucet, B., Sargolini, F., and Save, E. (2020). Medial entorhinal cortex lesions induce degradation of CA1 place cell firing stability when self-motion information is used. *Brain and Neuroscience Advances*, 4:2398212820953004.

Jacobs, J., Weidemann, C. T., Miller, J. F., Solway, A., Burke, J. F., Wei, X.-X., Suthana, N., Sperling, M. R., Sharan, A. D., Fried, I., and Kahana, M. J. (2013). Direct recordings of grid-like neuronal activity in human spatial navigation. *Nature Neuroscience*, 16(9):1188–1190. Number: 9 Publisher: Nature Publishing Group.

Jankowski, M. M., Islam, M. N., Wright, N. F., Vann, S. D., Erichsen, J. T., Aggleton, J. P., and O'Mara, S. M. (2014). Nucleus reuniens of the thalamus contains head direction cells. *eLife*, 3:e03075.

Jankowski, M. M. and O'Mara, S. M. (2015). Dynamics of place, boundary and object encoding in rat anterior claustrum. *Frontiers in Behavioral Neuroscience*, 9.

Jankowski, M. M., Passecker, J., Islam, M. N., Vann, S., Erichsen, J. T., Aggleton, J. P., and O'Mara, S. M. (2015). Evidence for spatially-responsive neurons in the rostral thalamus. *Frontiers in Behavioral Neuroscience*, 9.

Jankowski, M. M., Ronnqvist, K. C., Tsanov, M., Vann, S. D., Wright, N. F., Erichsen, J. T., Aggleton, J. P., and O'Mara, S. M. (2013). The anterior thalamus provides a subcortical circuit supporting memory and spatial navigation. *Frontiers in Systems Neuroscience*, 7:45.

Jeffery, K. J. (1998). Learning of landmark stability and instability by hippocampal place cells. *Neuropharmacology*, 37(4-5):677–687.

Jeffery, K. J. (2007). Integration of the sensory inputs to place cells: what, where, why, and how? *Hippocampus*, 17(9):775–785.

Jeffery, K. J. and Anderson, M. I. (2003). Dissociation of the geometric and contextual influences on place cells. *Hippocampus*, 13(7):868–872.

Jeffery, K. J., Donnett, J. G., Burgess, N., and O'Keefe, J. M. (1997). Directional control of hippocampal place fields. *Experimental Brain Research*, 117(1):131–142.

Jeffery, K. J., Donnett, J. G., and O'Keefe, J. (1995). Medial septal control of theta-correlated unit firing in the entorhinal cortex of awake rats. *Neuroreport*, 6(16):2166–2170.

Jeffery, K. J., Grieves, R., and Donnett, J. (2018). Chapter 5 - Recording the Spatial Mapping Cells: Place, Head Direction, and Grid Cells. In Manahan-Vaughan, D., editor, *Handbook of Behavioral Neuroscience*, volume 28 of *Handbook of Neural Plasticity Techniques*, pages 95–121. Elsevier.

Jeffery, K. J. and O'Keefe, J. M. (1999). Learned interaction of visual and idiothetic cues in the control of place field orientation. *Experimental Brain Research*, 127(2):151–161.

Jeffery, K. J., Page, H. J. I., and Stringer, S. M. (2016). Optimal cue combination and landmark-stability learning in the head direction system. *The Journal of Physiology*, 594(22):6527–6534.

Jenkins, T. A., Dias, R., Amin, E., and Aggleton, J. P. (2002a). Changes in Fos expression in the rat brain after unilateral lesions of the anterior thalamic nuclei. *The European Journal of Neuroscience*, 16(8):1425–1432.

Jenkins, T. A., Dias, R., Amin, E., Brown, M. W., and Aggleton, J. P. (2002b). Fos Imaging Reveals that Lesions of the Anterior Thalamic Nuclei Produce Widespread Limbic Hypoactivity in Rats. *The Journal of Neuroscience*, 22(12):5230–5238.

Jinno, S., Klausberger, T., Marton, L. F., Dalezios, Y., Roberts, J. D. B., Fuentealba, P., Bushong, E. A., Henze, D., Buzsáki, G., and Somogyi, P. (2007). Neuronal Diversity in GABAergic Long-Range Projections from the Hippocampus. *Journal of Neuroscience*, 27(33):8790–8804.

Jones, B. F. and Witter, M. P. (2007). Cingulate cortex projections to the parahippocampal region and hippocampal formation in the rat. *Hippocampus*, 17(10):957–976.

Jones, E. G. (1985). *The Thalamus*. Springer US.

Jones, M. W. and Wilson, M. A. (2005). Phase precession of medial prefrontal cortical activity relative to the hippocampal theta rhythm. *Hippocampus*, 15(7):867–873.

Kadir, S. N., Goodman, D. F. M., and Harris, K. D. (2014). High-dimensional cluster analysis with the Masked EM Algorithm. *Neural computation*, 26(11):2379–2394.

Kay, K., Chung, J. E., Sosa, M., Schor, J. S., Karlsson, M. P., Larkin, M. C., Liu, D. F., and Frank, L. M. (2020). Constant Sub-second Cycling between Representations of Possible Futures in the Hippocampus. *Cell*, 180(3):552–567.e25.

Keene, C. S. and Bucci, D. J. (2008). Contributions of the retrosplenial and posterior parietal cortices to cue-specific and contextual fear conditioning. *Behavioral Neuroscience*, 122(1):89–97.

Kempter, R., Leibold, C., Buzsáki, G., Diba, K., and Schmidt, R. (2012). Quantifying circular-linear associations: hippocampal phase precession. *Journal of Neuroscience Methods*, 207(1):113–124.

Keshavarzi, S., Bracey, E. F., Faville, R. A., Campagner, D., Tyson, A. L., Lenzi, S. C., Branco, T., and Margrie, T. W. (2021a). Multisensory coding of angular head velocity in the retrosplenial cortex. *Neuron*, page S0896627321008461.

Keshavarzi, S., Bracey, E. F., Faville, R. A., Campagner, D., Tyson, A. L., Lenzi, S. C., Branco, T., and Margrie, T. W. (2021b). The retrosplenial cortex combines internal and external cues to encode head velocity during navigation. *bioRxiv*, page 2021.01.22.427789.

King, C., Recce, M., and O'Keefe, J. (1998). The rhythmicity of cells of the medial septum/diagonal band of Broca in the awake freely moving rat: relationships with behaviour and hippocampal theta. *The European Journal of Neuroscience*, 10(2):464–477.

Kirk, I. J., Oddie, S. D., Konopacki, J., and Bland, B. H. (1996). Evidence for Differential Control of Posterior Hypothalamic, Supramammillary, and Medial Mammillary Theta-Related Cellular Discharge by Ascending and Descending Pathways. *The Journal of Neuroscience*, 16(17):5547–5554.

Kjelstrup, K. B., Solstad, T., Brun, V. H., Hafting, T., Leutgeb, S., Witter, M. P., Moser, E. I., and Moser, M.-B. (2008). Finite scale of spatial representation in the hippocampus. *Science (New York, N.Y.)*, 321(5885):140–143.

Knierim, J. J., Kudrimoti, H. S., and McNaughton, B. L. (1995). Place cells, head direction cells, and the learning of landmark stability. *The Journal of Neuroscience: The Official Journal of the Society for Neuroscience*, 15(3 Pt 1):1648–1659.

Knierim, J. J., Kudrimoti, H. S., and McNaughton, B. L. (1998). Interactions Between Idiothetic Cues and External Landmarks in the Control of Place Cells and Head Direction Cells. *Journal of Neurophysiology*, 80(1):425–446.

Knight, R., Hayman, R., Ginzberg, L. L., and Jeffery, K. (2011). Geometric Cues Influence Head Direction Cells Only Weakly in Nondisoriented Rats. *Journal of Neuroscience*, 31(44):15681–15692.

Knight, R., Piette, C. E., Page, H., Walters, D., Marozzi, E., Nardini, M., Stringer, S., and Jeffery, K. J. (2014). Weighted cue integration in the rodent head direction system. *Philosophical Transactions of the Royal Society B: Biological Sciences*, 369(1635):20120512.

Knill, D. C. and Pouget, A. (2004). The Bayesian brain: the role of uncertainty in neural coding and computation. *Trends in Neurosciences*, 27(12):712–719.

Kocsis, B., Di Prisco, G. V., and Vertes, R. P. (2001). Theta synchronization in the limbic system: the role of Gudden's tegmental nuclei. *The European Journal of Neuroscience*, 13(2):381–388.

Kocsis, B. and Vertes, R. P. (1994). Characterization of neurons of the supramammillary nucleus and mammillary body that discharge rhythmically with the hippocampal theta rhythm in the rat. *The Journal of Neuroscience*, 14(11 Pt 2):7040–7052.

Koenig, J., Linder, A. N., Leutgeb, J. K., and Leutgeb, S. (2011). The spatial periodicity of grid cells is not sustained during reduced theta oscillations. *Science (New York, N.Y.)*, 332(6029):592–595.

Kornienko, O., Latuske, P., Bassler, M., Kohler, L., and Allen, K. (2018). Non-rhythmic head-direction cells in the parahippocampal region are not constrained by attractor network dynamics. *eLife*, 7:e35949.

Korotkova, T., Ponomarenko, A., Monaghan, C. K., Poulter, S. L., Cacucci, F., Wills, T., Hasselmo, M. E., and Lever, C. (2018). Reconciling the different faces of hippocampal theta: The role of theta oscillations in cognitive, emotional and innate behaviors. *Neuroscience and Biobehavioral Reviews*, 85:65–80.

Kropff, E., Carmichael, J. E., Moser, M.-B., and Moser, E. I. (2015). Speed cells in the medial entorhinal cortex. *Nature*, 523(7561):419–424.

LaChance, P. A. and Taube, J. S. (2022). Spatial context and the functional role of the postrhinal cortex. *Neurobiology of Learning and Memory*, 189:107596.

LaChance, P. A., Todd, T. P., and Taube, J. S. (2019). A sense of space in postrhinal cortex. *Science*, 365(6449).

Lambrey, S., Amorim, M.-A., Samson, S., Noulhiane, M., Hasboun, D., Dupont, S., Baulac, M., and Berthoz, A. (2008). Distinct visual perspective-taking strategies involve the left and right medial temporal lobe structures differently. *Brain*, 131(2):523–534.

Larson, J. and Lynch, G. (1986). Induction of synaptic potentiation in hippocampus by patterned stimulation involves two events. *Science (New York, N.Y.)*, 232(4753):985–988.

Larson, J. and Munkácsy, E. (2015). Theta-Burst LTP. *Brain research*, 1621:38–50.

Larson, J., Wong, D., and Lynch, G. (1986). Patterned stimulation at the theta frequency is optimal for the induction of hippocampal long-term potentiation. *Brain Research*, 368(2):347–350.

Leutgeb, S., Leutgeb, J. K., Barnes, C. A., Moser, E. I., McNaughton, B. L., and Moser, M.-B. (2005). Independent Codes for Spatial and Episodic Memory in Hippocampal Neuronal Ensembles. *Science (New York, N.Y.)*, 309(5734):619–623.

Leutgeb, S., Ragozzino, K. E., and Mizumori, S. J. Y. (2000). Convergence of head direction and place information in the CA1 region of hippocampus. *Neuroscience*, 100(1):11–19.

Lever, C., Burton, S., Jeewajee, A., O'Keefe, J., and Burgess, N. (2009). Boundary Vector Cells in the Subiculum of the Hippocampal Formation. *The Journal of Neuroscience*, 29(31):9771–9777.

Lever, C., Wills, T., Cacucci, F., Burgess, N., and O'Keefe, J. (2002). Long-term plasticity in hippocampal place-cell representation of environmental geometry. *Nature*, 416(6876):90–94.

Lewicki, M. S. (1998). A review of methods for spike sorting: the detection and classification of neural action potentials. *Network (Bristol, England)*, 9(4):R53–78.

Lomi, E., Mathiasen, M. L., Cheng, H. Y., Zhang, N., Aggleton, J. P., Mitchell, A. S., and Jeffery, K. J. (2021). Evidence for two distinct thalamocortical circuits in retrosplenial cortex. *Neurobiology of Learning and Memory*, 185:107525.

Long, X. and Zhang, S.-J. (2021). A novel somatosensory spatial navigation system outside the hippocampal formation. *Cell Research*, pages 1–15.

Lozano, Y. R., Page, H., Jacob, P.-Y., Lomi, E., Street, J., and Jeffery, K. (2017). Retrosplenial and postsubicular head direction cells compared during visual landmark discrimination. *Brain and Neuroscience Advances*, 1.

M. Aghajan, Z., Schuette, P., Fields, T. A., Tran, M. E., Siddiqui, S. M., Hasulak, N. R., Tcheng, T. K., Eliashiv, D., Mankin, E. A., Stern, J., Fried, I., and Suthana, N. (2017). Theta Oscillations in the Human Medial Temporal Lobe during Real-World Ambulatory Movement. *Current Biology*, 27(24):3743–3751.e3.

Madl, T., Franklin, S., Chen, K., Montaldi, D., and Trappl, R. (2014). Bayesian Integration of Information in Hippocampal Place Cells. *PLOS ONE*, 9(3):e89762.

Maguire, E. A. (2001). The retrosplenial contribution to human navigation: a review of lesion and neuroimaging findings. *Scandinavian Journal of Psychology*, 42(3):225–238.

Mao, D., Kandler, S., McNaughton, B. L., and Bonin, V. (2017). Sparse orthogonal population representation of spatial context in the retrosplenial cortex. *Nature Communications*, 8(1):243.

Mao, D., Molina, L. A., Bonin, V., and McNaughton, B. L. (2020). Vision and Locomotion Combine to Drive Path Integration Sequences in Mouse Retrosplenial Cortex. *Current Biology*, 30(9):1680–1688.e4.

Mao, D., Neumann, A. R., Sun, J., Bonin, V., Mohajerani, M. H., and McNaughton, B. L. (2018). Hippocampus-dependent emergence of spatial sequence coding in retrosplenial cortex. *Proceedings of the National Academy of Sciences of the United States of America*, 115(31):8015–8018.

Marchette, S. A., Vass, L. K., Ryan, J., and Epstein, R. A. (2014). Anchoring the neural compass: coding of local spatial reference frames in human medial parietal lobe. *Nature Neuroscience*, 17(11):1598–1606.

Markus, E. J., Barnes, C. A., McNaughton, B. L., Gladden, V. L., and Skaggs, W. E. (1994). Spatial information content and reliability of hippocampal CA1 neurons: Effects of visual input. *Hippocampus*, 4(4):410–421.

Markus, E. J., Qin, Y. L., Leonard, B., Skaggs, W. E., McNaughton, B. L., and Barnes, C. A. (1995). Interactions between location and task affect the spatial and directional firing of hippocampal neurons. *Journal of Neuroscience*, 15(11):7079–7094.

Marozzi, E., Ginzberg, L. L., Alenda, A., and Jeffery, K. J. (2015). Purely Translational Realignment in Grid Cell Firing Patterns Following Nonmetric Context Change. *Cerebral Cortex*, 25(11):4619–4627.

Mathiasen, M. L., Dillingham, C. M., Kinnavane, L., Powell, A. L., and Aggleton, J. P. (2017). Asymmetric cross-hemispheric connections link the rat anterior thalamic nuclei with the cortex and hippocampal formation. *Neuroscience*, 349:128–143.

McCormick, D. A., Connors, B. W., Lighthall, J. W., and Prince, D. A. (1985). Comparative electrophysiology of pyramidal and sparsely spiny stellate neurons of the neocortex. *Journal of Neurophysiology*, 54(4):782–806.

McFarland, W. L., Teitelbaum, H., and Hedges, E. K. (1975). Relationship between hippocampal theta activity and running speed in the rat. *Journal of Comparative and Physiological Psychology*, 88(1):324–328.

McNaughton, B. L., Barnes, C. A., Gerrard, J. L., Gothard, K., Jung, M. W., Knierim, J. J., Kudrimoti, H., Qin, Y., Skaggs, W. E., Suster, M., and Weaver, K. L. (1996). Deciphering the hippocampal polyglot: the hippocampus as a path integration system. *The Journal of Experimental Biology*, 199(Pt 1):173–185.

McNaughton, B. L., Barnes, C. A., and O'Keefe, J. (1983). The contributions of position, direction, and velocity to single unit activity in the hippocampus of freely-moving rats. *Experimental Brain Research*, 52(1):41–49.

McNaughton, B. L., Battaglia, F. P., Jensen, O., Moser, E. I., and Moser, M.-B. (2006a). Path integration and the neural basis of the 'cognitive map'. *Nature Reviews Neuroscience*, 7(8):663–678.

McNaughton, B. L., Chen, L. L., and Markus, E. J. (1991). "Dead reckoning," landmark learning, and the sense of direction: a neurophysiological and computational hypothesis. *Journal of Cognitive Neuroscience*, 3(2):190–202.

McNaughton, B. L., Knierim, J. J., and Wilson, M. A. (1995). Vector encoding and the vestibular foundations of spatial cognition: Neurophysiological and computational mechanisms. In *The cognitive neurosciences*, pages 585–595. The MIT Press, Cambridge, MA, US.

McNaughton, N., Ruan, M., and Woodnorth, M.-A. (2006b). Restoring theta-like rhythmicity in rats restores initial learning in the Morris water maze. *Hippocampus*, 16(12):1102–1110.

Meer, M. A. A. v. d. and Redish, A. D. (2011). Theta Phase Precession in Rat Ventral Striatum Links Place and Reward Information. *Journal of Neuroscience*, 31(8):2843–2854.

Mehta, M. R., Lee, A. K., and Wilson, M. A. (2002). Role of experience and oscillations in transforming a rate code into a temporal code. *Nature*, 417(6890):741–746.

Meibach, R. C. and Siegel, A. (1977). Subicular projections to the posterior cingulate cortex in rats. *Experimental Neurology*, 57(1):264–274.

Miller, A. M., Mau, W., and Smith, D. M. (2019). Retrosplenial Cortical Representations of Space and Future Goal Locations Develop with Learning. *Current Biology*, 29(12):2083–2090.e4.

Miller, J. F., Neufang, M., Solway, A., Brandt, A., Trippel, M., Mader, I., Hefft, S., Merkow, M., Polyn, S. M., Jacobs, J., Kahana, M. J., and Schulze-Bonhage, A. (2013). Neural activity in human hippocampal formation reveals the spatial context of retrieved memories. *Science*, 342(6162):1111–1114.

Mitchell, A. S., Czajkowski, R., Zhang, N., Jeffery, K., and Nelson, A. J. D. (2018). Retrosplenial cortex and its role in spatial cognition. *Brain and Neuroscience Advances*, 2.

Mitchell, A. S. and Dalrymple-Alford, J. C. (2005). Dissociable memory effects after medial thalamus lesions in the rat. *The European Journal of Neuroscience*, 22(4):973–985.

Mitchell, A. S. and Dalrymple-Alford, J. C. (2006). Lateral and anterior thalamic lesions impair independent memory systems. *Learning & Memory*, 13(3):388–396.

Mitchell, S. J., Rawlins, J. N., Steward, O., and Olton, D. S. (1982). Medial septal area lesions disrupt theta rhythm and cholinergic staining in medial entorhinal cortex and produce impaired radial arm maze behavior in rats. *The Journal of Neuroscience*, 2(3):292–302.

Mizumori, S. J., Perez, G. M., Alvarado, M. C., Barnes, C. A., and McNaughton, B. L. (1990). Reversible inactivation of the medial septum differentially affects two forms of learning in rats. *Brain Research*, 528(1):12–20.

Mizumori, S. J. and Williams, J. D. (1993). Directionally selective mnemonic properties of neurons in the lateral dorsal nucleus of the thalamus of rats. *Journal of Neuroscience*, 13(9):4015–4028.

Mizuseki, K. and Buzsáki, G. (2013). Preconfigured, skewed distribution of firing rates in the hippocampus and entorhinal cortex. *Cell Reports*, 4(5):1010–1021.

Mizuseki, K., Royer, S., Diba, K., and Buzsáki, G. (2012). Activity Dynamics and Behavioral Correlates of CA3 and CA1 Hippocampal Pyramidal Neurons. *Hippocampus*, 22(8):1659–1680.

Mizuseki, K., Sirota, A., Pastalkova, E., and Buzsáki, G. (2009). Theta oscillations provide temporal windows for local circuit computation in the entorhinal-hippocampal loop. *Neuron*, 64(2):267–280.

Moita, M. A. P., Rosis, S., Zhou, Y., LeDoux, J. E., and Blair, H. T. (2004). Putting Fear in Its Place: Remapping of Hippocampal Place Cells during Fear Conditioning. *Journal of Neuroscience*, 24(31):7015–7023.

Morel, A., Magnin, M., and Jeanmonod, D. (1997). Multiarchitectonic and stereotactic atlas of the human thalamus. *The Journal of Comparative Neurology*, 387(4):588–630.

Morris, R. G. M. (1981). Spatial localization does not require the presence of local cues. *Learning and Motivation*, 12(2):239–260.

Morris, R. G. M., Schenk, F., Tweedie, F., and Jarrard, L. E. (1990). Ibotenate Lesions of Hippocampus and/or Subiculum: Dissociating Components of Allocentric Spatial Learning. *The European Journal of Neuroscience*, 2(12):1016–1028.

Moser, E. I. and Moser, M.-B. (2008). A metric for space. *Hippocampus*, 18(12):1142–1156.

Muir, G. M., Brown, J. E., Carey, J. P., Hirvonen, T. P., Della Santina, C. C., Minor, L. B., and Taube, J. S. (2009). Disruption of the Head Direction Cell Signal after Occlusion of the Semicircular Canals in the Freely Moving Chinchilla. *The Journal of Neuroscience*, 29(46):14521–14533.

Muller, R., Bostock, E., Taube, J., and Kubie, J. (1994). On the directional firing properties of hippocampal place cells. *The Journal of Neuroscience*, 14(12):7235–7251.

Muller, R. U. and Kubie, J. L. (1987). The effects of changes in the environment on the spatial firing of hippocampal complex-spike cells. *The Journal of Neuroscience*, 7(7):1951–1968.

Murakami, T., Yoshida, T., Matsui, T., and Ohki, K. (2015). Wide-field Ca2+ imaging reveals visually evoked activity in the retrosplenial area. *Frontiers in Molecular Neuroscience*, 8.

Neitz, J. and Jacobs, G. H. (1986). Reexamination of spectral mechanisms in the rat (Rattus norvegicus). *Journal of Comparative Psychology*, 100(1):21–29.

Nelson, A. (2021). The anterior thalamic nuclei and cognition: A role beyond space? *Neuroscience & Biobehavioral Reviews*, 126.

Nelson, A. J. D., Powell, A. L., Holmes, J. D., Vann, S. D., and Aggleton, J. P. (2015). What does spatial alternation tell us about retrosplenial cortex function? *Frontiers in Behavioral Neuroscience*, 9.

Newman, E. L. and Hasselmo, M. E. (2014). Grid cell firing properties vary as a function of theta phase locking preferences in the rat medial entorhinal cortex. *Frontiers in Systems Neuroscience*, 8:193.

O'Keefe, J. (1976). Place units in the hippocampus of the freely moving rat. *Experimental Neurology*, 51(1):78–109.

O'Keefe, J. and Burgess, N. (1996). Geometric determinants of the place fields of hippocampal neurons. *Nature*, 381(6581):425–428.

O'Keefe, J., Burgess, N., Donnett, J. G., Jeffery, K. J., and Maguire, E. A. (1998). Place cells, navigational accuracy, and the human hippocampus. *Philosophical Transactions of the Royal Society B: Biological Sciences*, 353(1373):1333–1340.

O'Keefe, J. and Conway, D. H. (1978). Hippocampal place units in the freely moving rat: why they fire where they fire. *Experimental Brain Research*, 31(4):573–590.

O'Keefe, J. and Dostrovsky, J. (1971). The hippocampus as a spatial map. Preliminary evidence from unit activity in the freely-moving rat. *Brain Research*, 34(1):171–175.

O'Keefe, J. and Nadel, L. (1978). *The Hippocampus as a Cognitive Map*. Oxford: Clarendon Press. Accepted: 2016-10-08T00:43:54Z.

O'Keefe, J. and Recce, M. L. (1993). Phase relationship between hippocampal place units and the EEG theta rhythm. *Hippocampus*, 3(3):317–330.

O'Keefe, J. and Speakman, A. (1987). Single unit activity in the rat hippocampus during a spatial memory task. *Experimental Brain Research*, 68(1):1–27.

Olsen, G. M., Ohara, S., Iijima, T., and Witter, M. P. (2017). Parahippocampal and retrosplenial connections of rat posterior parietal cortex. *Hippocampus*, 27(4):335–358.

Olvera-Cortés, E., Cervantes, M., and González-Burgos, I. (2002). Place-learning, but not cue-learning training, modifies the hippocampal theta rhythm in rats. *Brain Research Bulletin*, 58(3):261–270.

O'Mara, S. M., Rolls, E. T., Berthoz, A., and Kesner, R. P. (1994). Neurons responding to whole-body motion in the primate hippocampus. *The Journal of Neuroscience*, 14(11 Pt 1):6511–6523.

Opalka, A. N., Huang, W.-q., Liu, J., Liang, H., and Wang, D. V. (2020). Hippocampal Ripple Coordinates Retrosplenial Inhibitory Neurons during Slow-Wave Sleep. *Cell Reports*, 30(2):432–441.e3.

Page, H. J. I. and Jeffery, K. J. (2018). Landmark-Based Updating of the Head Direction System by Retrosplenial Cortex: A Computational Model. *Frontiers in Cellular Neuroscience*, 12.

Papez, J. W. (1937). A proposed mechanism of emotion. *Archives of Neurology & Psychiatry*, 38:725–743.

Paré, D., Dossi, R. C., and Steriade, M. (1991). Three types of inhibitory postsynaptic potentials generated by interneurons in the anterior thalamic complex of cat. *Journal of Neurophysiology*, 66(4):1190–1204.

Patai, E. Z., Javadi, A.-H., Ozubko, J. D., O'Callaghan, A., Ji, S., Robin, J., Grady, C., Winocur, G., Rosenbaum, R. S., Moscovitch, M., and Spiers, H. J. (2019). Hippocampal and Retrosplenial Goal Distance Coding After Long-term Consolidation of a Real-World Environment. *Cerebral Cortex*, 29(6):2748–2758.

Pavlides, C., Greenstein, Y. J., Grudman, M., and Winson, J. (1988). Long-term potentiation in the dentate gyrus is induced preferentially on the positive phase of theta-rhythm. *Brain Research*, 439(1-2):383–387.

Paxinos, G. and Watson, C. (2007). *The Rat Brain in Stereotaxic Coordinates: Hard Cover Edition*. Academic Press, Amsterdam ; Boston, 6th edition edition.

Perry, B. A. L., Lomi, E., and Mitchell, A. S. (2021). Thalamocortical interactions in cognition and disease: the mediodorsal and anterior thalamic nuclei. *Neuroscience & Biobehavioral Reviews*, 130:162–177.

Perry, B. A. L., Mercer, S. A., Barnett, S. C., Lee, J., and Dalrymple-Alford, J. C. (2018). Anterior thalamic nuclei lesions have a greater impact than mammillothalamic tract lesions on the extended hippocampal system. *Hippocampus*, 28(2):121–135.

Perry, B. A. L. and Mitchell, A. S. (2019). Considering the Evidence for Anterior and Laterodorsal Thalamic Nuclei as Higher Order Relays to Cortex. *Frontiers in Molecular Neuroscience*, 12:167.

Peyrache, A., Lacroix, M. M., Petersen, P. C., and Buzsáki, G. (2015). Internally organized mechanisms of the head direction sense. *Nature Neuroscience*, 18(4):569–575.

Peyrache, A., Schieferstein, N., and Buzsáki, G. (2017). Transformation of the head-direction signal into a spatial code. *Nature Communications*, 8(1):1752.

Pothuizen, H., Aggleton, J., and Vann, S. (2008). Do rats with retrosplenial cortex lesions lack direction? *The European journal of neuroscience*, 28:2486–98.

Pothuizen, H., Davies, M., Albasser, M., Aggleton, J., and Vann, S. (2009). Granular and dysgranular retrosplenial cortices provide qualitatively different contributions to spatial working memory: Evidence from immediate-early gene imaging in rats. *The European journal of neuroscience*, 30:877–88.

Pothuizen, H. H. J., Davies, M., Aggleton, J. P., and Vann, S. D. (2010). Effects of selective granular retrosplenial cortex lesions on spatial working memory in rats. *Behavioural Brain Research*, 208(2):566–575.

Poulter, S., Lee, S. A., Dachtler, J., Wills, T. J., and Lever, C. (2021). Vector trace cells in the subiculum of the hippocampal formation. *Nature Neuroscience*, 24(2):266–275.

Powell, A., Connelly, W. M., Vasalauskaite, A., Nelson, A. J. D., Vann, S. D., Aggleton, J. P., Sengpiel, F., and Ranson, A. (2020). Stable Encoding of Visual Cues in the Mouse Retrosplenial Cortex. *Cerebral Cortex*, 30(8):4424–4437.

Preston-Ferrer, P., Coletta, S., Frey, M., and Burgalossi, A. (2016). Anatomical organization of presubicular head-direction circuits. *eLife*, 5:e14592.

Pérez-Escobar, J. A., Kornienko, O., Latuske, P., Kohler, L., and Allen, K. (2016). Visual landmarks sharpen grid cell metric and confer context specificity to neurons of the medial entorhinal cortex. *eLife*, 5:e16937.

Quirk, G. J., Muller, R. U., Kubie, J. L., and Ranck, J. B. (1992). The positional firing properties of medial entorhinal neurons: description and comparison with hippocampal place cells. *The Journal of Neuroscience*, 12(5):1945–1963.

Raji, C. A., Lopez, O. L., Kuller, L. H., Carmichael, O. T., and Becker, J. T. (2009). Age, Alzheimer disease, and brain structure. *Neurology*, 73(22):1899–1905.

Redish, A. D., Elga, A. N., and Touretzky, D. S. (1996). A coupled attractor model of the rodent head direction system. *Network: Computation in Neural Systems*, 7(4):671–685.

Reed, J. M. and Squire, L. R. (1997). Impaired recognition memory in patients with lesions limited to the hippocampal formation. *Behavioral Neuroscience*, 111(4):667–675.

Richard, G. R., Titiz, A., Tyler, A., Holmes, G. L., Scott, R. C., and Lenck-Santini, P.-P. (2013). Speed modulation of hippocampal theta frequency correlates with spatial memory performance. *Hippocampus*, 23(12):1269–1279.

Robertson, R. G., Rolls, E. T., Georges-François, P., and Panzeri, S. (1999). Head direction cells in the primate pre-subiculum. *Hippocampus*, 9(3):206–219.

Robinson, S., Keene, C. S., Iaccarino, H. F., Duan, D., and Bucci, D. J. (2011). Involvement of retrosplenial cortex in forming associations between multiple sensory stimuli. *Behavioral Neuroscience*, 125(4):578–587.

Robinson, S., Todd, T. P., Pasternak, A. R., Luikart, B. W., Skelton, P. D., Urban, D. J., and Bucci, D. J. (2014). Chemogenetic Silencing of Neurons in Retrosplenial Cortex Disrupts Sensory Preconditioning. *Journal of Neuroscience*, 34(33):10982–10988.

Rotenberg, A. and Muller, R. U. (1997). Variable place-cell coupling to a continuously viewed stimulus: evidence that the hippocampus acts as a perceptual system. *Philosophical Transactions of the Royal Society B: Biological Sciences*, 352(1360):1505–1513.

Royer, S., Sirota, A., Patel, J., and Buzsáki, G. (2010). Distinct Representations and Theta Dynamics in Dorsal and Ventral Hippocampus. *Journal of Neuroscience*, 30(5):1777–1787.

Ruan, M., Young, C. K., and McNaughton, N. (2017). Bi-Directional Theta Modulation between the Septo-Hippocampal System and the Mammillary Area in Free-Moving Rats. *Frontiers in Neural Circuits*, 11.

Rubin, A., Yartsev, M. M., and Ulanovsky, N. (2014). Encoding of Head Direction by Hippocampal Place Cells in Bats. *Journal of Neuroscience*, 34(3):1067–1080.

Sambeth, A., Meeter, M., and Blokland, A. (2009). Hippocampal theta frequency and novelty. *Hippocampus*, 19(4):407–408.

Sargolini, F., Fyhn, M., Hafting, T., McNaughton, B. L., Witter, M. P., Moser, M.-B., and Moser, E. I. (2006). Conjunctive Representation of Position, Direction, and Velocity in Entorhinal Cortex. *Science*, 312(5774):758–762.

Save, E., Cressant, A., Thinus-Blanc, C., and Poucet, B. (1998). Spatial firing of hippocampal place cells in blind rats. *The Journal of Neuroscience*, 18(5):1818–1826.

Save, E., Nerad, L., and Poucet, B. (2000). Contribution of multiple sensory information to place field stability in hippocampal place cells. *Hippocampus*, 10(1):64–76.

Savelli, F., Yoganarasimha, D., and Knierim, J. J. (2008). Influence of boundary removal on the spatial representations of the medial entorhinal cortex. *Hippocampus*, 18(12):1270–1282.

Seki, M. and Zyo, K. (1984). Anterior thalamic afferents from the mamillary body and the limbic cortex in the rat. *The Journal of Comparative Neurology*, 229(2):242–256.

Shapiro, M. L., Tanila, H., and Eichenbaum, H. (1997). Cues that hippocampal place cells encode: dynamic and hierarchical representation of local and distal stimuli. *Hippocampus*, 7(6):624–642.

Sharp, P. E. (1999). Complimentary roles for hippocampal versus subicular/entorhinal place cells in coding place, context, and events. *Hippocampus*, 9(4):432–443.

Sharp, P. E. and Green, C. (1994). Spatial correlates of firing patterns of single cells in the subiculum of the freely moving rat. *The Journal of Neuroscience*, 14(4):2339–2356.

Sharp, P. E., Tinkelman, A., and Cho, J. (2001). Angular velocity and head direction signals recorded from the dorsal tegmental nucleus of gudden in the rat: implications for path integration in the head direction cell circuit. *Behavioral Neuroscience*, 115(3):571–588.

Sharp, P. E. and Turner-Williams, S. (2005). Movement-related correlates of single-cell activity in the medial mammillary nucleus of the rat during a pellet-chasing task. *Journal of Neurophysiology*, 94(3):1920–1927.

Sherrill, K. R., Erdem, U. M., Ross, R. S., Brown, T. I., Hasselmo, M. E., and Stern, C. E. (2013). Hippocampus and Retrosplenial Cortex Combine Path Integration Signals for Successful Navigation. *The Journal of Neuroscience*, 33(49):19304–19313.

Shibata, H. (1989). Descending projections to the mammillary nuclei in the rat, as studied by retrograde and anterograde transport of wheat germ agglutinin-horseradish peroxidase. *The Journal of Comparative Neurology*, 285(4):436–452.

Shibata, H. (1992). Topographic organization of subcortical projections to the anterior thalamic nuclei in the rat. *The Journal of Comparative Neurology*, 323(1):117–127.

Shibata, H. (1993a). Direct projections from the anterior thalamic nuclei to the retrohippocampal region in the rat. *The Journal of Comparative Neurology*, 337(3):431–445.

Shibata, H. (1993b). Efferent projections from the anterior thalamic nuclei to the cingulate cortex in the rat. *The Journal of Comparative Neurology*, 330(4):533–542.

Shibata, H. (1994). Terminal distribution of projections from the retrosplenial area to the retrohippocampal region in the rat, as studied by anterograde transport of biotinylated dextran amine. *Neuroscience Research*, 20(4):331–336.

Shibata, H., Honda, Y., Sasaki, H., and Naito, J. (2009). Organization of intrinsic connections of the retrosplenial cortex in the rat. *Anatomical Science International*, 84(4):280.

Shibata, H., Kondo, S., and Naito, J. (2004). Organization of retrosplenial cortical projections to the anterior cingulate, motor, and prefrontal cortices in the rat. *Neuroscience Research*, 49(1):1–11.

Shibata, H. and Naito, J. (2005). Organization of anterior cingulate and frontal cortical projections to the anterior and laterodorsal thalamic nuclei in the rat. *Brain Research*, 1059(1):93–103.

Shibata, H. and Yoshiko, H. (2015). Thalamocortical projections of the anteroventral thalamic nucleus in the rabbit. *Journal of Comparative Neurology*, 523(5):726–741.

Shinder, M. E. and Taube, J. S. (2010). Differentiating ascending vestibular pathways to the cortex involved in spatial cognition. *Journal of Vestibular Research: Equilibrium & Orientation*, 20(1):3–23.

Silverman, B. W. (1986). *Density Estimation for Statistics and Data Analysis*. CRC Press.

Skaggs, W., McNaughton, B., and Gothard, K. (1992). An Information-Theoretic Approach to Deciphering the Hippocampal Code. In *Advances in Neural Information Processing Systems*, volume 5. Morgan-Kaufmann.

Skaggs, W. E., Knierim, J. J., Kudrimoti, H. S., and McNaughton, B. L. (1995). A model of the neural basis of the rat's sense of direction. *Advances in Neural Information Processing Systems*, 7:173–180.

Skaggs, W. E. and McNaughton, B. L. (1996). Replay of neuronal firing sequences in rat hippocampus during sleep following spatial experience. *Science (New York, N.Y.)*, 271(5257):1870–1873.

Skaggs, W. E., McNaughton, B. L., Wilson, M. A., and Barnes, C. A. (1996). Theta phase precession in hippocampal neuronal populations and the compression of temporal sequences. *Hippocampus*, 6(2):149–172.

Solstad, T., Boccara, C. N., Kropff, E., Moser, M.-B., and Moser, E. I. (2008). Representation of geometric borders in the entorhinal cortex. *Science (New York, N.Y.)*, 322(5909):1865–1868.

Spalla, D., Treves, A., and Boccara, C. N. (2021). Angular and Linear Speed Cells in the Parahippocampal Circuits. *bioRxiv*, page 2021.01.28.428631.

Stackman, R. W., Clark, A. S., and Taube, J. S. (2002). Hippocampal Spatial Representations Require Vestibular Input. *Hippocampus*, 12(3):291–303.

Stackman, R. W., Golob, E. J., Bassett, J. P., and Taube, J. S. (2003). Passive Transport Disrupts Directional Path Integration by Rat Head Direction Cells. *Journal of Neurophysiology*, 90(5):2862–2874.

Stackman, R. W. and Taube, J. S. (1997). Firing Properties of Head Direction Cells in the Rat Anterior Thalamic Nucleus: Dependence on Vestibular Input. *The Journal of Neuroscience*, 17(11):4349–4358.

Stackman, R. W. and Taube, J. S. (1998). Firing Properties of Rat Lateral Mammillary Single Units: Head Direction, Head Pitch, and Angular Head Velocity. *Journal of Neuroscience*, 18(21):9020–9037.

Steriade, M. (1997). Synchronized activities of coupled oscillators in the cerebral cortex and thalamus at different levels of vigilance. *Cerebral Cortex (New York, N.Y.: 1991)*, 7(6):583–604.

Stewart, M. and Fox, S. E. (1991). Hippocampal theta activity in monkeys. *Brain Research*, 538(1):59–63.

Sugar, J., Witter, M. P., van Strien, N. M., and Cappaert, N. L. M. (2011). The retrosplenial cortex: intrinsic connectivity and connections with the (para)hippocampal region in the rat. An interactive connectome. *Frontiers in Neuroinformatics*, 5:7.

Sutherland, R. J. and Hoesing, J. M. (1993). Posterior Cingulate Cortex and Spatial Memory: A Microlimnology Analysis. In Vogt, B. A. and Gabriel, M., editors, *Neurobiology of Cingulate Cortex and Limbic Thalamus: A Comprehensive Handbook*, pages 461–477. Birkhäuser, Boston, MA.

Sutherland, R. J. and Rodriguez, A. J. (1989). The role of the fornix/fimbria and some related subcortical structures in place learning and memory. *Behavioural Brain Research*, 32(3):265–277.

Suzuki, K., Yamadori, A., Hayakawa, Y., and Fujii, T. (1998). Pure Topographical Disorientation Related to Dysfunction of the Viewpoint Dependent Visual System. *Cortex*, 34(4):589–599.

Szymusiak, R. and Nitz, D. (2003). Chronic recording of extracellular neuronal activity in behaving animals. *Current Protocols in Neuroscience*, 6:6.16.

Takahashi, N., Kawamura, M., Shiota, J., Kasahata, N., and Hirayama, K. (1997). Pure topographic disorientation due to right retrosplenial lesion. *Neurology*, 49(2):464–469.

Talk, A., Kang, E., and Gabriel, M. (2004). Independent generation of theta rhythm in the hippocampus and posterior cingulate cortex. *Brain Research*, 1015(1-2):15–24.

Tan, H., Bassett, J., O'Keefe, J., Cacucci, F., and Wills, T. (2015). The Development of the Head Direction System before Eye Opening in the Rat. *Current Biology*, 25(4):479–483.

Taube, J. S. (1995). Head direction cells recorded in the anterior thalamic nuclei of freely moving rats. *The Journal of Neuroscience*, 15(1 Pt 1):70–86.

Taube, J. S. (2007). The Head Direction Signal: Origins and Sensory-Motor Integration. *Annual Review of Neuroscience*, 30(1):181–207.

Taube, J. S. and Burton, H. L. (1995). Head direction cell activity monitored in a novel environment and during a cue conflict situation. *Journal of Neurophysiology*, 74(5):1953–1971.

Taube, J. S. and Muller, R. U. (1998). Comparisons of head direction cell activity in the postsubiculum and anterior thalamus of freely moving rats. *Hippocampus*, 8(2):87–108.

Taube, J. S., Muller, R. U., and Ranck, J. B. (1990a). Head-direction cells recorded from the postsubiculum in freely moving rats. I. Description and quantitative analysis. *The Journal of Neuroscience*, 10(2):420–435.

Taube, J. S., Muller, R. U., and Ranck, J. B. (1990b). Head-direction cells recorded from the postsubiculum in freely moving rats. II. Effects of environmental manipulations. *The Journal of Neuroscience*, 10(2):436–447.

Taube, J. S., Wang, S. S., Kim, S. Y., and Frohardt, R. J. (2013). Updating of the spatial reference frame of head direction cells in response to locomotion in the vertical plane. *Journal of Neurophysiology*, 109(3):873–888.

Taylor, C. C. (2008). Automatic bandwidth selection for circular density estimation. *Computational Statistics & Data Analysis*, 52(7):3493–3500.

Tolman, E. C. (1948). Cognitive maps in rats and men. *Psychological Review*, 55(4):189–208.

Tsanov, M., Chah, E., Vann, S. D., Reilly, R. B., Erichsen, J. T., Aggleton, J. P., and O'Mara, S. M. (2011). Theta-Modulated Head Direction Cells in the Rat Anterior Thalamus. *Journal of Neuroscience*, 31(26):9489–9502.

Tsanov, M., Chah, E., Wright, N., Vann, S. D., Reilly, R., Erichsen, J. T., Aggleton, J. P., and O'Mara, S. M. (2010). Oscillatory Entrainment of Thalamic Neurons by Theta Rhythm in Freely Moving Rats. *Journal of Neurophysiology*, 105(1):4–17.

Tsivilis, D., Vann, S. D., Denby, C., Roberts, N., Mayes, A. R., Montaldi, D., and Aggleton, J. P. (2008). A disproportionate role for the fornix and mammillary bodies in recall versus recognition memory. *Nature Neuroscience*, 11(7):834–842.

Ulanovsky, N. and Moss, C. F. (2007). Hippocampal cellular and network activity in freely moving echolocating bats. *Nature Neuroscience*, 10(2):224–233.

Unal, G., Crump, M. G., Viney, T. J., Éltes, T., Katona, L., Klausberger, T., and Somogyi, P. (2018). Spatio-temporal specialization of GABAergic septo-hippocampal neurons for rhythmic network activity. *Brain Structure & Function*, 223(5):2409–2432.

Unal, G., Joshi, A., Viney, T. J., Kis, V., and Somogyi, P. (2015). Synaptic Targets of Medial Septal Projections in the Hippocampus and Extrahippocampal Cortices of the Mouse. *The Journal of Neuroscience*, 35(48):15812–15826.

van Groen, T., Kadish, I., and Wyss, J. M. (1999). Efferent connections of the anteromedial nucleus of the thalamus of the rat. *Brain Research Reviews*, 30(1):1–26.

van Groen, T., Kadish, I., and Wyss, J. M. (2004). Retrosplenial cortex lesions of area Rgb (but not of area Rga) impair spatial learning and memory in the rat. *Behavioural Brain Research*, 154(2):483–491.

van Groen, T. and Wyss, J. M. (1990a). The connections of presubiculum and parasubiculum in the rat. *Brain Research*, 518(1-2):227–243.

van Groen, T. and Wyss, J. M. (1990b). Connections of the retrosplenial granular a cortex in the rat. *The Journal of Comparative Neurology*, 300(4):593–606.

van Groen, T. and Wyss, J. M. (1990c). The postsubicular cortex in the rat: characterization of the fourth region of the subicular cortex and its connections. *Brain Research*, 529(1-2):165–177.

van Groen, T. and Wyss, J. M. (1992). Connections of the retrosplenial dysgranular cortex in the rat. *The Journal of Comparative Neurology*, 315(2):200–216.

Van Groen, T. and Wyss, J. M. (1995). Projections from the anterodorsal and anteroventral nucleus of the thalamus to the limbic cortex in the rat. *The Journal of Comparative Neurology*, 358(4):584–604.

Van Groen, T. and Wyss, J. M. (2003). Connections of the retrosplenial granular b cortex in the rat. *The Journal of Comparative Neurology*, 463(3):249–263.

van Strien, N. M., Cappaert, N. L. M., and Witter, M. P. (2009). The anatomy of memory: an interactive overview of the parahippocampal-hippocampal network. *Nature Reviews. Neuroscience*, 10(4):272–282.

van Wijngaarden, J. B., Babl, S. S., and Ito, H. T. (2020). Entorhinal-retrosplenial circuits for allocentric-egocentric transformation of boundary coding. *eLife*, 9:e59816.

Vanderwolf, C. H. (1969). Hippocampal electrical activity and voluntary movement in the rat. *Electroencephalography and Clinical Neurophysiology*, 26(4):407–418.

Vann, S. D. (2005). Transient spatial deficit associated with bilateral lesions of the lateral mammillary nuclei. *The European Journal of Neuroscience*, 21(3):820–824.

Vann, S. D. (2009). Gudden's ventral tegmental nucleus is vital for memory: re-evaluating diencephalic inputs for amnesia. *Brain: A Journal of Neurology*, 132(Pt 9):2372–2384.

Vann, S. D. (2018). Lesions within the head direction system reduce retrosplenial c-fos expression but do not impair performance on a radial-arm maze task. *Behavioural Brain Research*, 338:153–158.

Vann, S. D. and Aggleton, J. P. (2002). Extensive cytotoxic lesions of the rat retrosplenial cortex reveal consistent deficits on tasks that tax allocentric spatial memory. *Behavioral Neuroscience*, 116(1):85–94.

Vann, S. D. and Aggleton, J. P. (2004). Testing the importance of the retrosplenial guidance system: effects of different sized retrosplenial cortex lesions on heading direction and spatial working memory. *Behavioural Brain Research*, 155(1):97–108.

Vann, S. D. and Aggleton, J. P. (2005). Selective dysgranular retrosplenial cortex lesions in rats disrupt allocentric performance of the radial-arm maze task. *Behavioral Neuroscience*, 119(6):1682–1686.

Vann, S. D., Saunders, R. C., and Aggleton, J. P. (2007). Distinct, parallel pathways link the medial mammillary bodies to the anterior thalamus in macaque monkeys. *The European Journal of Neuroscience*, 26(6):1575–1586.

Vantomme, G., Rovó, Z., Cardis, R., Béard, E., Katsioudi, G., Guadagno, A., Perrenoud, V., Fernandez, L. M. J., and Lüthi, A. (2020). A Thalamic Reticular Circuit for Head Direction Cell Tuning and Spatial Navigation. *Cell Reports*, 31(10):107747.

Vedder, L. C., Miller, A. M. P., Harrison, M. B., and Smith, D. M. (2017). Retrosplenial Cortical Neurons Encode Navigational Cues, Trajectories and Reward Locations During Goal Directed Navigation. *Cerebral Cortex (New York, N.Y.: 1991)*, 27(7):3713–3723.

Vertes, R. P., Albo, Z., and Viana Di Prisco, G. (2001). Theta-rhythmically firing neurons in the anterior thalamus: implications for mnemonic functions of Papez's circuit. *Neuroscience*, 104(3):619–625.

Vertes, R. P., Hoover, W. B., and Viana Di Prisco, G. (2004). Theta rhythm of the hippocampus: subcortical control and functional significance. *Behavioral and Cognitive Neuroscience Reviews*, 3(3):173–200.

Vertes, R. P. and Kocsis, B. (1997). Brainstem-diencephalo-septohippocampal systems controlling the theta rhythm of the hippocampus. *Neuroscience*, 81(4):893–926.

Viney, T. J., Salib, M., Joshi, A., Unal, G., Berry, N., and Somogyi, P. (2018). Shared rhythmic subcortical GABAergic input to the entorhinal cortex and presubiculum. *eLife*, 7:e34395. Publisher: eLife Sciences Publications, Ltd.

Vogt, B. A. and Miller, M. W. (1983). Cortical connections between rat cingulate cortex and visual, motor, and postsubicular cortices. *The Journal of Comparative Neurology*, 216(2):192–210.

Vogt, B. A., Pandya, D. N., and Rosene, D. L. (1987). Cingulate cortex of the rhesus monkey: I. Cytoarchitecture and thalamic afferents. *The Journal of Comparative Neurology*, 262(2):256–270.

Wang, C., Chen, X., Lee, H., Deshmukh, S. S., Yoganarasimha, D., Savelli, F., and Knierim, J. J. (2018). Egocentric coding of external items in the lateral entorhinal cortex. *Science*, 362(6417):945–949.

Warburton, E. C., Baird, A., Morgan, A., Muir, J. L., and Aggleton, J. P. (2001). The Conjoint Importance of the Hippocampus and Anterior Thalamic Nuclei for Allocentric Spatial Learning: Evidence from a Disconnection Study in the Rat. *Journal of Neuroscience*, 21(18):7323–7330.

Warburton, E. C., Baird, A. L., Morgan, A., Muir, J. L., and Aggleton, J. P. (2000). Disconnecting hippocampal projections to the anterior thalamus produces deficits on tests of spatial memory in rats. *The European Journal of Neuroscience*, 12(5):1714–1726.

Welday, A. C., Shlifer, I. G., Bloom, M. L., Zhang, K., and Blair, H. T. (2011). Cosine Directional Tuning of Theta Cell Burst Frequencies: Evidence for Spatial Coding by Oscillatory Interference. *Journal of Neuroscience*, 31(45):16157–16176.

Wesierska, M., Adamska, I., and Malinowska, M. (2009). Retrosplenial cortex lesion affected segregation of spatial information in place avoidance task in the rat. *Neurobiology of Learning and Memory*, 91(1):41–49.

Whishaw, I. Q. (1990). The decorticate rat. In *The cerebral cortex of the rat*, pages 239–267. The MIT Press, Cambridge, MA, US.

Whishaw, I. Q., Maaswinkel, H., Gonzalez, C. L., and Kolb, B. (2001). Deficits in allothetic and idiothetic spatial behavior in rats with posterior cingulate cortex lesions. *Behavioural Brain Research*, 118(1):67–76.

Wilber, A. A., Clark, B. J., Forster, T. C., Tatsuno, M., and McNaughton, B. L. (2014). Interaction of egocentric and world-centered reference frames in the rat posterior parietal cortex. *The Journal of Neuroscience*, 34(16):5431–5446.

Wilent, W. B. and Nitz, D. A. (2007). Discrete Place Fields of Hippocampal Formation Interneurons. *Journal of Neurophysiology*, 97(6):4152–4161.

Winocur, G., Moscovitch, M., Fogel, S., Rosenbaum, R. S., and Sekeres, M. (2005). Preserved spatial memory after hippocampal lesions: effects of extensive experience in a complex environment. *Nature Neuroscience*, 8(3):273–275.

Winocur, G., Moscovitch, M., Rosenbaum, R. S., and Sekeres, M. (2010). An investigation of the effects of hippocampal lesions in rats on pre- and postoperatively acquired spatial memory in a complex environment. *Hippocampus*, 20(12):1350–1365.

Winson, J. (1978). Loss of hippocampal theta rhythm results in spatial memory deficit in the rat. *Science (New York, N.Y.)*, 201(4351):160–163.

Winter, S. and Taube, J. (2014). Head Direction Cells: From Generation to Integration. In *Space, Time and Memory in the Hippocampal Formation*, page 24.

Winter, S. S., Clark, B. J., and Taube, J. S. (2015). Spatial navigation. Disruption of the head direction cell network impairs the parahippocampal grid cell signal. *Science (New York, N.Y.)*, 347(6224):870–874.

Witter, M. P. and Moser, E. I. (2006). Spatial representation and the architecture of the entorhinal cortex. *Trends in Neurosciences*, 29(12):671–678.

Witter, M. P., Ostendorf, R. H., and Groenewegen, H. J. (1990). Heterogeneity in the Dorsal Subiculum of the Rat. Distinct Neuronal Zones Project to Different Cortical and Subcortical Targets. *The European Journal of Neuroscience*, 2(8):718–725.

Wood, E. R., Dudchenko, P. A., and Eichenbaum, H. (1999). The global record of memory in hippocampal neuronal activity. *Nature*, 397(6720):613–616.

Wright, N. F., Erichsen, J. T., Vann, S. D., O'Mara, S., and Aggleton, J. P. (2010). Parallel but separate inputs from limbic cortices to the mammillary bodies and anterior thalamic nuclei in the rat. *The Journal of comparative neurology*, 518(12):2334–2354.

Yamawaki, N., Li, X., Lambot, L., Ren, L. Y., Radulovic, J., and Shepherd, G. M. G. (2019). Long-range inhibitory intersection of a retrosplenial thalamocortical circuit by apical tuft-targeting CA1 neurons. *Nature Neuroscience*, 22(4):618–626.

Yamawaki, N., Radulovic, J., and Shepherd, G. M. G. (2016). A Corticocortical Circuit Directly Links Retrosplenial Cortex to M2 in the Mouse. *Journal of Neuroscience*, 36(36):9365–9374.

Yan, Y., Burgess, N., and Bicanski, A. (2021). A model of head direction and landmark coding in complex environments. *PLOS Computational Biology*, 17(9):e1009434.

Yartsev, M. M. and Ulanovsky, N. (2013). Representation of three-dimensional space in the hippocampus of flying bats. *Science (New York, N.Y.)*, 340(6130):367–372.

Yartsev, M. M., Witter, M. P., and Ulanovsky, N. (2011). Grid cells without theta oscillations in the entorhinal cortex of bats. *Nature*, 479(7371):103–107.

Yin, A., Tseng, P. H., Rajangam, S., Lebedev, M. A., and Nicolelis, M. a. L. (2018). Place Cell-Like Activity in the Primary Sensorimotor and Premotor Cortex During Monkey Whole-Body Navigation. *Scientific Reports*, 8(1):9184.

Yoder, R. M., Clark, B. J., Brown, J. E., Lamia, M. V., Valerio, S., Shinder, M. E., and Taube, J. S. (2011a). Both visual and idiothetic cues contribute to head direction cell stability during navigation along complex routes. *Journal of Neurophysiology*, 105(6):2989–3001.

Yoder, R. M., Clark, B. J., and Taube, J. S. (2011b). Origins of Landmark Encoding in the Brain. *Trends in neurosciences*, 34(11):561–571.

Yoder, R. M., Peck, J. R., and Taube, J. S. (2015). Visual Landmark Information Gains Control of the Head Direction Signal at the Lateral Mammillary Nuclei. *Journal of Neuroscience*, 35(4):1354–1367.

Yoder, R. M. and Taube, J. S. (2009). Head Direction Cell Activity in Mice: Robust Directional Signal Depends on Intact Otolith Organs. *Journal of Neuroscience*, 29(4):1061–1076.

Yoder, R. M. and Taube, J. S. (2014). The vestibular contribution to the head direction signal and navigation. *Frontiers in Integrative Neuroscience*, 8.

Yoganarasimha, D., Yu, X., and Knierim, J. J. (2006). Head Direction Cell Representations Maintain Internal Coherence during Conflicting Proximal and Distal Cue Rotations: Comparison with Hippocampal Place Cells. *Journal of Neuroscience*, 26(2):622–631.

Young, C. K. and McNaughton, N. (2009). Coupling of theta oscillations between anterior and posterior midline cortex and with the hippocampus in freely behaving rats. *Cerebral Cortex*, 19(1):24–40.

Zakowski, W., Zawistowski, P., Braszka, u., and Jurkowlaniec, E. (2017). The effect of pharmacological inactivation of the mammillary body and anterior thalamic nuclei on hippocampal theta rhythm in urethane-anesthetized rats. *Neuroscience*, 362:196–205.

Zar, J. H. (2010). *Biostatistical Analysis*. Prentice Hall.

Zhang, K. (1996). Representation of spatial orientation by the intrinsic dynamics of the head-direction cell ensemble: a theory. *Journal of Neuroscience*, 16(6):2112–2126.

Zhang, N., Grieves, R. M., and Jeffery, K. J. (2021). Environment symmetry drives a multidirectional code in rat retrosplenial cortex. *bioRxiv*, page 2021.08.22.457261.

Zhang, S., Schönfeld, F., Wiskott, L., and Manahan-Vaughan, D. (2014). Spatial representations of place cells in darkness are supported by path integration and border information. *Frontiers in Behavioral Neuroscience*, 8.

Zhou, T. L., Tamura, R., Kuriwaki, J., and Ono, T. (1999). Comparison of medial and lateral septal neuron activity during performance of spatial tasks in rats. *Hippocampus*, 9(3):220–234.

Zugaro, M. B., Berthoz, A., and Wiener, S. I. (2001). Background, but not foreground, spatial cues are taken as references for head direction responses by rat anterodorsal thalamus neurons. *The Journal of Neuroscience*, 21(14):RC154.

Zugaro, M. B., Tabuchi, E., and Wiener, S. I. (2000). Influence of conflicting visual, inertial and substratal cues on head direction cell activity. *Experimental Brain Research*, 133(2):198–208.